QUASI-STATIC BUBBLE SHAPE ANALYSIS IN THE DEVELOPMENT OF MODELS FOR ADIABATIC AND DIABATIC GROWTH AND DEPARTURE

By FRÉDÉRIC J. LESAGE, B.Sc., M.Sc.

A Thesis Submitted to the School of Graduate Studies in Partial Fulfilment of the Requirements for the Degree Doctor of Philosophy

DOCTOR OF PHILOSOPHY (2011) McMaster University
(Mechanical Engineering) Hamilton, Ontario

TITLE: Quasi-Static Bubble Shape Analysis in the Development of Models for Adiabatic and Diabatic Growth and Departure

AUTHOR: Frédéric J. Lesage, B.Sc., M.Sc.

SUPERVISOR: Dr. J. S. Cotton, Associate Professor
Dr. A. J. Robinson, Adjunct Professor

NUMBER OF PAGES: xxiv, 241

ABSTRACT

In an effort to better understand the physical mechanisms responsible for pool boiling heat transfer, an analytical model is developed that better describes the changing shape and size of a growing bubble. Indeed, any analysis of thermal transport due to nucleate pool boiling requires bubble frequency predictions which are intimately linked to bubble volume. The model is developed and validated for quasi-static bubble growth due to gas injection and for bubble growth due to vaporization within the heat-transfer controlled growth regime; it highlights the need to include the asymmetric nature of growing bubbles when modeling bubble growth.

In addition, a numerical study of quasi-static bubble shape for both adiabatic bubble growth and vapour bubble growth provides insight into the dependence the bubble shape evolution has on the Bond number. In so doing, bubble profiles generated from a numerical treatment of the Capillary equation are benchmarked to quasi-static gas injected bubble formations and to heat-transfer controlled vapour bubble formations.

The numerical treatment of bubble shape evolution leads to a simplifying bubble geometry for low Bond number applications. The geometric model accounts for bubble shape transformation throughout the bubble growth cycle including the necking phenomenon. An analytical model of quasi-static adiabatic bubble growth is accordingly developed based on the proposed low Bond number geometric model; it is coupled with a geometric detachment relation and a force

balance detachment criterion that are dependent on the Bond number. The resulting predicted bubble growth characteristics, such as profile, volume, centre of gravity and aspect ratio, are validated with the benchmarked numerical treatment of the problem.

Furthermore, the low Bond number geometric model is applied to bubble growth due to vaporization. In order to solve the mass-energy balance at the vapour bubble interface, a spherical surface area is commonly assumed. This leads to the need for correction factors and provides little insight into the physical mechanism responsible for bubble shape. In this study, the transitioning shape of a vapour bubble is considered in the integral analysis of the interfacial mass-energy balance. The model predicts the following bubble growth characteristics: profile, volume, centre of gravity, and aspect ratio.

ACKNOWLEDGMENTS

It is with great pleasure that I gratefully and humbly thank my supervisors Dr. James S. Cotton and Dr. Anthony J. Robinson for having guided me throughout this project. Their intellect and motivation to progress in the field of Mechanical Engineering have been a true source of inspiration.

I express deep gratitude to Sergio Di Bari and Samuel Siedel for their expertise in bubble image capturing and their valuable collaborative support.

I appreciatively thank the department administrative staff for their professionalism and kind manner.

I extend my deepest and warmest thank you to my devoted parents Marie-Madeleine and Christian, to my loving wife Sarah and to my adoring children: Jacob, Chloe, Zachary, Madeleine and Mackenzie.

TABLE OF CONTENTS

List of Figures

List of Tables

Nomenclature

Symbol	Quantity	SI Unit
A	Surface area	m^2
AR	Arbitrary region	-
AR	Aspect ratio	-
Bo_b	Bond number with characteristic length *b*	-
b	Orifice radius; Cavity radius	m
c_p	Specific heat at constant pressure	$J\text{-}kg^{-1}K^{-1}$
C	Centre curvature with necking	m
CoG	Centre of gravity	m
d	Thermal boundary layer thickness affected by bubble	m
D	Diameter	m
F	Force	N
g	Gravitational constant	$m\text{-}s^{-2}$
H	Vertical position of centre of gravity	m
h	Height; Height of bubble neck; Height of conical frustum	m
h_{lv}	Latent heat of evaporation	$J\text{-}kg^{-1}$
Ja	Jakob number	-
k	Thermal conductivity	$W\text{-}m^{-1}K^{-1}$

L_l	Laplace length: $\sqrt{\dfrac{\sigma}{(\rho_l-\rho_v)g}}$	m
MR	Material region	-
m	Mass in bubble	kg
P	Pressure	N-m^{-2}
R_1, R_2	Principle radii of curvature	m
R	Bubble radius	m
$\vec{r}$	Position vector	m
s	$\sqrt{R^2-b^2}$	m
T	Temperature profile	K
t	Time	s
t_b	Characteristic time: $\dfrac{2}{3}\pi b^3/\dot{V}$	s
t_{Ja}	$b^2/\left(\alpha\pi^3 Ja^2\right)$	s
$\vec{u}$	MR fluid velocity	m-s^{-1}
u_r, u_θ, u_ϕ	Spherical coordinates of MR fluid velocity	-
V	Volume	m^3
$\dot{V}$	Flow rate	m^{3}s^{-1}
$\dot{V}_{cr}$	Critical Flow rate $\dfrac{\pi}{100}\sqrt{\dfrac{b^3\sigma}{5\rho_v}}$	m^{3}s^{-1}
$\vec{v}$	Fluid velocity	m-s^{-1}
w	Width	m

$\vec{w}$	Surface velocity	m-s^{-1}
W	Work	J
y	Perpendicular distance from nucleation cavity	m
z	h_{bub} - y	m
α	Contact angle	rad
α	Thermal diffusivity	m^2 s^{-1}
β	Growth parameter	-
δ	Thermal boundary layer thickness	m
μ	Viscosity	kg-m^{-1}s^{-1}
Θ	Temperature profile	K
θ_1, θ_2	Arc angles	rad
ρ	Fluid density	kg-m^{-3}
ρ_l	Density of liquid	kg-m^{-3}
ρ_v	Density of vapour	kg-m^{-3}
σ	Surface tension	N-m^{-1}
τ	Viscous stress	N-m^{-2}
ψ	Temporal limit angle $\pi - \alpha$	rad
Ψ	Bubble degree of sphericity	-
ζ	Perpendicular distance from the bubble interface	m
ξ	Fluid depth	m

Superscripts

$\bar{\bar{P}}$	Normalized pressure $P/(2\sigma/R_o)$
$\bar{R}_i^{-1}$	Normalized principal radius $\bar{R}_i^{-1} = \dfrac{R_o}{R_i}$
$\hat{t}$	Normalized time: t/t_{Ja}
t^*	Normalized time: t/t_b
t'	Normalized time: ${}^*\dot{V}\cdot t$
${}^*V$	Normalized volume : $\dfrac{V}{\frac{2}{3}\pi b^3}$
$\dot{V}^¢$	Normalized flow rate: $\dot{V}/\dot{V}_{cr}$
$\bar{\delta}$	Normalized thermal boundary layer thickness $\bar{\delta} = \dfrac{\delta}{\sqrt{\alpha\pi t_{Ja}}}$
$\tilde{\zeta}$	Normalized length: ζ/L_l
ζ^*	Normalized length: ζ/b
ζ^+	Normalized length: ζ/ζ_d
$\dot{\zeta}$	Derivative with respect to time: $\dfrac{d\zeta}{dt}$

Subscripts

amb	Ambient
b	Buoyancy
bub	Bubble
c	Capillary

cr	Critical
d	Detachment
dp	Submerged depth
eq	Equivalent
face	Interface
frustum	Conical frustum
g	Growth period
gm	Gas momentum
hemi	Hemisphere
hydro	Hydrostatic
i	Coordinate index
l	Liquid
m	Measured
min	Minimum
mod	Modified
neck	Bubble neck
NG	Numerically generated
o	Initial condition; Apex origin
P	Pressure
pr	Predicted
sat	Saturated
sph	Sphere
tr	Truncated

wall	Wall
v	Gas/vapour
w	Waiting period
z	Vertical component
∞	Far field

1. INTRODUCTION

Many industrial practices create large amounts of heat. Thermal control of the site, industrial instruments and electrical components is vital to the industries running capacity and is managed with heat exchangers. For this reason, industrial needs have motivated a large number of studies of the underlying physics of nucleate pool boiling and forced convection boiling for their capacity to generate high heat transfer rates. The common goal of these studies is to, through a deeper understanding of the fundamental mechanisms that govern boiling, effectively apply pool boiling and forced convection boiling to diverse industrial processes that require the removal of large amounts of heat or that require a near constant temperature boundary condition.

In particular, whether in pool boiling or convective boiling applications, the extremely high heat transfer rates associated with the nucleate pool boiling phenomenon are intimately linked to the vapour bubbles which form, grow and depart at the heated surface. Energy is introduced into the liquid by conduction from the heated solid surface and is stored within a thin thermal boundary layer adjacent to that surface. This stored energy is ultimately used to vaporize the liquid and cause bubbles to form and grow. In addition to evaporative cooling effects, fluid motions induced by bubble activity disrupt the thermal boundary layer in the vicinity of the bubbles causing enhanced mixing and improved heat transfer in these regions (Dhir, 1991). As detailed by Dhir (2006), in the past a number of purely empirical and mechanism-based correlations have been developed for predicting nucleate pool boiling heat transfer rates. The empirical approach has resulted in correlations which show different functional dependence on the important boiling parameters. Very often, the predictive capabilities of the empirical correlations fall off rapidly once outside of the range in which the correlations were developed.

Mechanism-based correlations combine information about the underlying sub-phenomena including, but not limited to, bubble waiting time, growth times, heat flux contributions of the micro layer and transient conduction. This is combined with information about the active site density and natural convection to predict the boiling heat transfer rates. A particularly insightful and practical model was put forth by Judd & Hwang (1976). Here, the contributions of transient conduction through the liquid, micro layer evaporation and natural convection during single bubble events were combined with information about the bubble emission frequency in an attempt to formulate a straightforward and mechanistic model which could predict the wall heat fluxes during boiling.

An alternative approach is the development of accurate numerical simulations of boiling (Dhir, 2006). In fact, the beginning of this century has seen a notable increase in the number of archival publications related to numerical modelling of heterogeneous bubble growth in partial nucleate boiling along with many other boiling scenarios such as convective boiling, bubble merger and boiling in mini/micro channels (Bai & Fujita, 2000; Robinson & Judd, 2001;

Yoon *et al*., 2001; Genske & Stephan, 2006; Fuchs *et al*., 2006; Wu *et al.*, 2007; Mukherjee & Kandlikar, 2007; Stephan & Fuchs, 2009; Robinson *et al.*, 2010).

Due to the highly non-linear, transient multi-physics phenomenon involving the coupled interaction of three phases with extreme gradients, in particular near the triple contact line, the computational expense is very high. As a result, the numerical models must incorporate some simplifying assumptions which largely depend on the aim of the particular investigation. For example, in Bai & Fujita (2000), Yoon *et al.* (2001), Genske & Stephan (2006), Fuchs *et al.* (2006), Wu *et al.* (2007), Mukherjee & Kandlikar (2007) and Stephan & Fuchs (2009), the simulated bubbles were initially unrealistically large compared with that of an actual nucleation cavity to ensure that the vapour temperature remains at the saturation temperature corresponding with the system pressure during the entire growth period. This assumption can be rationalized in these cases since the primary focus was on the bubble dynamics and heat transfer for bubbles growing in the thermally controlled bubble growth domain.

Robinson & Judd (2001) developed a model in which bubble growth on a heated surface was initiated from a sub-micron nucleus. The numerical simulation was able to resolve bubble growth over several time and length scales due to a hemispherical bubble shape assumption, which allowed the moving interface to be tracked without skewing of the mesh, as well as the implementation of a 4^{th} order Runge-Kutta scheme. The mathematical modelling of the problem resulted in a set of three coupled differential equations; one for the time rate of change of the vapour temperature, one for the time rate of change of the radius and one for the interface velocity. Even though this methodology provided the required temporal and spatial resolution for numerically simulating heterogeneous bubble growth over many time and length scales, the equation set is only valid for hemispherical bubbles such as those measured experimentally by Lee & Merte (1996) in their microgravity experiments. A similar numerical method was employed by Robinson *et al.* (2010) for spherically symmetric bubble expansion in an initially uniform superheated and unbounded liquid. However, the equation set is only valid for spherical bubbles.

Recalling that a common goal of these investigations is to gain a deeper understanding of the fundamental mechanisms responsible for bubble growth, the present work of this document exposes the need for more accurate bubble shape modeling. In particular, bubbles are commonly assumed to be spherical despite clear evidence that a bubble experiences a drastic shape transition during its growth cycle.

In this work, bubble growth models highlighting the importance of shape modeling when predicting bubble growth characteristics are presented. To facilitate the model development, the mechanics of bubble growth are initially examined by considering adiabatic bubble growth and then diabatic bubble growth. The benefits are twofold: firstly, an industrial application using an analytical model can adapt its operating conditions in parallel with changing environmental parameters. Secondly, an analytical model provides more insight into the mechanisms at work during bubble growth.

In particular, chapter 4 derives a bubble geometric detachment relation based on a mass balance at detachment. This provides analytical closure to the bubble growth problem when including the observed necking phenomenon in the geometric model. This relation is strictly derived from bubble geometry and the principle of conservation of mass and does not require any force balance. This proposed bubble geometric detachment relation was first experimentally observed by Oguz & Prosperetti (1993). The developed bubble growth model is validated for gas injected adiabatic quasi-static bubble growth from a submerged orifice.

The adopted geometric model is, in chapter 5, appropriately applied to bubble growth due to vaporization on a heated plane, that is to say, nucleate bubble growth. In a collaborative effort with INSA Lyon, the model is experimentally validated for heat-induced vapour bubble growth conditions in which the bubble base is fixed to an artificial nucleation site and in which micro-layer vaporization is negligible.

All of the bubble growth results presented in this work require a bubble geometric model. This allows for integral analysis over the surface of the bubble when analytically solving the conservation equations. It also allows for forces acting on the bubble, represented as vectors having magnitude and direction, to be evaluated. In this particular work, spherical bubble geometry has not been assumed, rather a bubble geometric model that changes in shape and in size as is observed in reality is adopted. This novel approach builds on past analytical models; in order to alleviate the complexity in the analysis, many previous works make spherical assumptions when analysing data and developing numerical, empirical or analytical models.

In an effort to better understand bubble shape behaviour, the physical mechanisms dictating bubble deviation from a spherical shape is investigated in chapter 3 by quantifying the magnitude of the bubble's spherical tendencies as the bubble's degree of sphericity. Similarly, the bubble's tendency to be a truncated spherical shape is quantified in terms of, as introduced in this work, the bubble degree of Modified sphericity. To this end, a numerical procedure is detailed solving the capillary equation providing the bubble profile from which bubble shape analysis may be performed.

This numerical treatment of the Capillary equation providing bubble profiles has been benchmarked for quasi-static adiabatic bubble growth for both a fixed and growing foot radius by Gerlach *et al.* (2005) and for bubble growth due to gas diffusion by Mori & Baines (2001). In this study, this same numerical simulation of the pressure balance experienced by a bubble during bubble growth is benchmarked for bubble growth due to vaporization with a fixed foot radius and bubble growth due to gas injection with a fixed foot radius. Furthermore, the Bond number, with the fixed foot radius as its characteristic length, is identified as the principle parameter responsible for a bubble's deviation from a sphericity of unity. In the following chapter 2, a review of the primary contributions in bubble growth modeling relating to nucleate boiling on a superheated plane are outlined.

A common theme throughout this work is the importance in properly modeling bubble shape prior to modeling bubble growth. In particular, the majority of the contributions to the understanding of nucleate boiling on a heated plane assume the individual bubbles to be spherical with exception to microgravity consideration in which the bubbles are correctly assumed to be hemispherical. However, a spherical bubble assumption on a heated plane clearly misrepresents the bubble shape thereby requiring the model to adjust with empirically deduced correction factors. The correction factors often only apply to the conditions in which they were deduced and provide little insight into the mechanisms responsible for bubble growth.

2. LITERATURE REVIEW

It is the goal of this study to provide a geometric starting point in the modeling of bubble growth that more accurately describes bubble shape during quasi-static bubble growth. In what follows is an account of important contributions which are in fact the building blocks of this study.

2.1. Early Bubble Growth Models

It was common practice in early bubble growth models to make the two following assumptions.

1. Bubble growth was assumed to be spherical from inception to departure. In this way, all bubble characteristics, such as volume, surface area, centre of gravity, centre of curvature, etc... , could be deduced from a single parameter: bubble radius.

2. A bubble growth parameter β was introduced such that the bubble radius growth curve be the following root function,

2-1 $$R = 0.5\beta\sqrt{t}\,.$$

The most commonly used bubble growth models would incorporate Equation 2-1 with the parameter $\beta = 4\left(\frac{\alpha}{\pi}\right)^{\frac{1}{2}} Ja$, which was proposed by (Fritz &

Ende, 1936), or the parameter $\beta = 4\left(\frac{3\alpha}{\pi}\right)^{\frac{1}{2}} Ja$, proposed by (Plesset & Zwick, 1954), or again the parameter $\beta = 5(\alpha)^{\frac{1}{2}}(Ja)^{\frac{3}{2}}$, proposed by (Cole & Shulman, 1966) in which *Ja* is the Jakob number.

Physically, the Jakob number represents the ratio of sensible to latent energy injected into the bubble from its surroundings. These different β factors were empirically developed and would fall off rapidly once outside the range in which the correlations were developed. Furthermore, the models provide little insight into the physical mechanisms at work during bubble growth.

In order to predict the bubble detachment diameter, Eq. 2-1 was combined with a simple force model that did not include the necking phenomenon and that was derived through empirical means. Kiper (1971) predicted a minimum bubble detachment diameter of $D_{\min} = 0.935 Ja^{\frac{4}{3}}$ when using the parameter $\beta = 4\left(\frac{\alpha}{\pi}\right)^{\frac{1}{2}} Ja$, $D_{\min} = 1.95 Ja^{\frac{4}{3}}$ when using the parameter $\beta = 4\left(\frac{3\alpha}{\pi}\right)^{\frac{1}{2}} Ja$ and $D_{\min} = 2.7 Ja$ when using the parameter $\beta = 5(\alpha)^{\frac{1}{2}}(Ja)^{\frac{3}{2}}$. The minimum diameter predictions proposed by Kiper (1971) were validated using data from Cole & Shulman (1966).

The shortcomings of these early models were a fixed spherical geometry and bubble detachment diameters based on empirical results. These are aspects of bubble growth theory with potential for improvement since a fixed spherical bubble does not respect the observed physical realities of a growing bubble on a heated plane.

2.2. Rayleigh Equation

The most fundamental equation describing spherical bubble growth is the Rayleigh equation (Rayleigh, 1917; Plesset & Zwick, 1954; Scriven, 1959; Plesset & Prosperetti, 1977; Prosperetti, 1982). It is often used as a starting point in the development of numerical models of bubble growth (Oguz & Prosperetti, 1993; Robinson *et al.*, 2010).

Due to the importance of this equation in bubble growth modeling, it is developed fully from the principle of conservation of mass (detailed in Appendix 7.5). The following two definitions (Panton, 1993) are used in the terminology of this text:

1. A Material Region, noted *MR*, is a region whose surface moves with the local velocity of the material. That is to say for an *MR*, $\vec{v} = \vec{w}$ in which $\vec{v}$ is the fluid velocity and $\vec{w}$ is the surface velocity of the bulk.

2. An Arbitrary Region, noted *AR*, is a region whose surface may or may not move with the local velocity of the material. That is to say, for an *AR*, $\vec{v}$ and $\vec{w}$ are not necessarily equal.

The conservation of mass principle implies that the change of mass inside a control volume is due to any flux in or out of that control volume. Expressed as an equation, the conservation of mass principle states that the rate of change of mass per unit volume for a control volume is equal to the rate of increase of volume occupied by the mass,

2-2 $$\frac{d\rho}{dt}+\vec{\nabla}\cdot\rho\vec{u}=0\,.$$

In the above, ρ represents the fluid density, $\vec{u}$ represents the fluid velocity for an *MR*. Equation 2-2 is often referred to as the continuity equation and is developed fully in Appendix 7.5. For steady state incompressible flow this Eq. 2-2 is reduced to $\vec{\nabla}\cdot\vec{u}=0$, which in spherical coordinates becomes,

2-3 $$\frac{1}{r}\frac{\partial}{\partial r}\left(r^2u_r\right)+\frac{1}{\sin\phi}\frac{\partial u_\theta}{\partial\theta}+\frac{1}{r\sin\phi}\frac{\partial}{\partial\phi}\left(u_\phi\sin\phi\right)=0$$

in which *r* is the position coordinate.

Since a growing bubble in quiescent liquid is commonly assumed to be symmetrical about the vertical axis due to the absence of any cross flow, any derivation with respect to φ or θ is zero. Equation 2-3 reduces to,

2-4 $$\frac{1}{r}\frac{\partial}{\partial r}\left(r^2u_r\right)=0$$

implying that r^2u_r is a function of time only and therefore constant with respect to position.

The fluid velocity for an *MR* at the bubble interface ($r = R$) is equal to the rate of change of the bubble radius with respect to time implying,

2-5 $$u_R = \frac{dR}{dt}.$$

This coupled with the fact that r^2u_r is constant with respect to position implies the following equality,

2-6 $$r^2u_r = R^2u_R = R^2\frac{dR}{dt}$$

yielding,

2-7 $$u_r = \frac{R^2}{r^2}\frac{dR}{dt}.$$

Differentiating the above with respect to time and with respect to position yields,

2-8 $$\frac{du_r}{dt} = \frac{1}{r^2}\left(2R\left(\frac{dR}{dt}\right)^2 + R^2\frac{d^2R}{dt^2}\right)$$

and

2-9 $$\frac{du_r}{dr} = -\frac{2R^2}{r^3}\frac{dR}{dt}.$$

Substituting Equations 2-8 and 2-9 into the *r*-direction Navier-Stokes equation for motion,

2-10 $$\frac{du_r}{dt} + u_r\frac{du_r}{dr} = -\frac{1}{\rho_l}\frac{dP}{dr} + \frac{\mu}{\rho_l}\left(\frac{1}{r^2}\frac{d}{dr}\left(r^2\frac{du_r}{dr}\right) - \frac{2u_r}{r^2}\right)$$

reduces the above to,

2-11 $$\frac{2R}{r^2}\left(\frac{dR}{dt}\right)^2 + \frac{R^2}{r^2}\frac{d^2R}{dt^2} - \frac{2R^4}{r^5}\left(\frac{dR}{dt}\right)^2 = -\frac{1}{\rho_l}\frac{dP}{dr}.$$

Finally, integrating Eq. 2-11 from the bubble boundary *R* to the liquid bulk, noted ∞, reduces Eq. 2-11 to,

2-12 $$R\frac{d^2R}{dt^2} + \frac{3}{2}\left(\frac{dR}{dt}\right)^2 = \frac{p_R - p_\infty}{\rho_l}.$$

The Young-Laplace balance of pressure (detailed in the forthcoming Eq. 3-10), $p_v - p_l = \frac{2\sigma}{R} - \tau_{rr}$ in which τ_{rr} is the viscous term, coupled with Stoke's assumption, $\tau_{rr} = -\frac{4\mu}{R}\frac{dR}{dt}$ (Panton, 1996), and Eq. 2-12 yields the extended form of the Rayleigh equation, 2-13 $$R\frac{d^2R}{dt^2}+\frac{3}{2}\left(\frac{dR}{dt}\right)^2=\frac{1}{\rho_l}\left(p_v-p_\infty-\frac{2\sigma}{R}-\frac{4\mu}{R}\frac{dR}{dt}\right).$$

It should be noted that the more commonly used form of the Rayleigh equation assumes quasi-static growth thereby making the viscous term (the last term on the right hand side of Eq. 2-13) negligible,

2-14 $$R\frac{d^2R}{dt^2}+\frac{3}{2}\left(\frac{dR}{dt}\right)^2=\frac{1}{\rho_l}\left(p_v-p_\infty-\frac{2\sigma}{R}\right).$$

The above governing equation relates the bubble radius rate of change directly with the pressure inside the bubble, the pressure outside the bubble and the surface tension. It applies to spherical bubble growth for Newtonian fluids in which the cavity interface does not contribute to any exchange of mass (Prosperetti, 1982). It is once again noted that a limiting factor of the model is the spherical assumption as it would not physically apply to bubble growth on a heated plane since such a bubble is visibly not spherical.

The Rayleigh equation can be solved numerically for simplified cases with given initial and boundary conditions within the heat-transfer controlled bubble growth regime. It can be solved analytically within the inertia controlled bubble growth regime.

In the *inertia controlled* bubble growth regime, the temperature is considered uniform and thermal effects on growth rate are negligible. Bubble growth is governed by its momentum's ability to drive adjacent fluid outwards.

In the *heat-transfer controlled* bubble growth regime (often referred to as the *thermally controlled* regime or again the *diffusion controlled* regime) the vapour bubble pressure is near the bulk fluid pressure minimizing inertia effects on bubble growth. In the heat-transfer controlled regime, bubble growth is attributed to heat transport to the bubble interface causing vaporization (Carey, 1992; Brennan, 2005).

In particular, in the inertia controlled regime, the Clapeyron equation which assumes thermodynamic equilibrium for the pressure, entropy, temperature and volume of a liquid-vapour interface (Faghri & Zhang, 2006),

2-15 $$\frac{dp}{dT} = \frac{h_{lv}}{\left(\frac{1}{\rho_v} - \frac{1}{\rho_l}\right) T_{sat}}$$

can be applied to the Rayleigh equation and solved as follows.

By assuming the liquid specific volume to be negligible relative to the vapour specific volume and applying the working conditions of a spherical vapour bubble in a superheated liquid, the Clapeyron equation can be expressed as,

2-16 $$p_v - p_l = \frac{\rho_v h_{lv} \left(T_\infty - T_{sat}\right)}{T_{sat}}.$$

With the above and the condition that the initial bubble radius be zero, the Rayleigh equation solves for the bubble radius such that, 2-17 $$R = t\sqrt{\frac{2\rho_v h_{lv}\left(T_\infty - T_{sat}\right)}{3\rho_l T_{sat}}}.$$

Equation 2-17 represents the bubble growth radius at time *t* for spherical inertia-controlled bubble growth in a superheated liquid.

In the present study, a full shape growth history providing all bubble growth characteristics for heat-transfer controlled bubble growth on a heated plane is developed by adopting non-spherical bubble geometry. The geometric model is based on the results of a numerical study of bubble shape detailed in chapter 3.

2.3. Bubble Detachment

In order to estimate bubble detachment radius Fritz (1935) postulated that bubble detachment would occur when the buoyancy and surface tension effects balance. In considering the bubble to be spherical yet growing from an orifice of radius *b*, Fritz (1935) equated the buoyancy with the capillary force (a detailed account of the capillary force for a cavity radius *b* is found in section 4.3),

2-18 $$\rho_l g\left(\frac{4}{3}\pi R_d^3\right) = 2\pi\sigma b.$$

Isolating R_d yields a bubble detachment radius for a spherical bubble (Fritz, 1935), 2-19 $$R_d = \left(\frac{3\sigma b}{2\rho_l g} \right)^{\frac{1}{3}}.$$

It is important to note that Eq. 2-18 yielding Eq. 2-19 is geometrically contradictory. In particular, the left hand side of Eq. 2-18 is a buoyancy force for a sphere and the right hand side is the capillary force for a bubble with a foot radius *b* and therefore a non spherical shape. The Fritz (1935) detachment radius has proven itself useful for its predictive capabilities but does not provide an accurate account of bubble shape.

In the present study, a similar force balance is adopted and validated in section 4.3 using a geometric model in which no bubble shape contradictions arise.

2.3.1. Bond number

In nucleate boiling, a bubble grows and detaches; and then, this ebullition cycle repeats. Typically, two factors are considered to dictate the thermal transport resulting from this phenomenon: bubble detachment volume and the ebullition cycle frequency. However, the frequency of bubble detachment is dependent on the volume that the bubble attains. A model's ability to predict heat transfer due to boiling is therefore limited to its ability to predict bubble detachment volume. To this end, many empirical correlations have been developed predicting bubble detachment diameter in which the bubble is assumed to be spherical. The non dimensional Bond number with characteristic length equal to the detachment diameter is often central to the correlation. It represents a ratio of gravitational to surface tension forces and is defined as,

2-20 $$Bo_{D_d} = \frac{g(\rho_l - \rho_v) D_d^2}{\sigma}.$$

Fritz (1935) developed the following empirical correlation for the bubble detachment diameter of a vapour bubble growing from a heated plane in which θ is the contact angle,

2-21 $$\sqrt{Bo_{D_d}} = 0.0208\theta.$$

For bubble growth in a uniformly heated liquid and a constant heated plane temperature, Zuber (1959) developed the following empirical correlation,

2-22 $$\sqrt{Bo_{D_d}} = \left(\frac{\sigma}{g(\rho_l - \rho_v)} \right)^{-1/6} \left(\frac{6k_l (T_{wall} - T_{sat})}{q''} \right)^{1/3}.$$

Cole & Shulman (1966) and Cole (1967) proceeded to develop a correlation relating the detachment diameter Bond number to the wall temperature Jakob number for a bubble growing from a heated plane. The non dimensional wall superheat Jakob number is defined as,

2-23 $$Ja = \frac{\rho_l c_p (T_{wall} - T_{sat}(P_\infty))}{\rho_v h_{lv}}.$$

The resulting empirical correlation was simply, 2-24 $$\sqrt{Bo_{D_d}} = 0.04Ja\ .$$

In a comprehensive study comparing bubble detachment correlations with available data in the literature, Jensen & Memmel (1986) concluded that an empirical correlation developed by Kuteladze & Gogonin (1979) had the best fit with a standard deviation of 45.4 %. Jensen & Memmel (1986) refined the Kuteladze & Gogonin (1979) correlation to a standard deviation of 44.4% in presenting the following empirical correlation for bubble detachment diameter,

2-25 $$\sqrt{Bo_{D_d}} = 0.19\left(1.8 + 10^5\left(\frac{Ja}{\Pr_l}\right)\left(\frac{g\rho_l\left(\rho_l-\rho_v\right)}{\mu_l^2}\right)^{-1}\left(\frac{\sigma}{g\left(\rho_l-\rho_v\right)}\right)^{-3/2}\right)^{2/3}\ .$$

The importance in these above mentioned bubble detachment empirical correlations lies in that they all incorporate the non dimensional Bond number implying that the Bond number plays a central role in bubble growth analysis.

It is commonly observed that under the same operating conditions, different nucleation sites on a heated plane will produce bubbles at different frequencies and thus at different detachment volumes (Carey, 1992). Therefore, the characteristics of the nucleation cavity, namely its orifice size, play an important role in bubble detachment volume. Despite this, the empirical correlations of Eq. 2-21 to Eq. 2-25 do not incorporate cavity size in the bubble detachment correlations. Understandably, such a correspondence between bubble detachment volume and the radius of the cavity from which the bubble grows is not easily validated; this is due to the typically minute size of a nucleation site.

An anomaly in these correlations is that the bubble is assumed to be spherical, implying an infinitesimally small point of contact with the heated plane, while the empirical correlations incorporating the Bond number imply that the surface tension plays a central role. Since the surface tension is a consequence of contact between the bubble and the heated plane, the empirical correlations themselves suggest that the bubble shape is not spherical and has a significant contact with the bubble growth site further suggesting that the nucleation cavity size should be incorporated into bubble growth modeling.

In this study, the importance of the Bond number on bubble growth characteristics is strongly recognized in the bubble shape analysis. Furthermore, the proposed bubble geometry includes bubble foot contact with the heated plane justifying the importance of the surface tension in bubble growth and detachment.

In an effort to identify the Bond number as a parameter of the experimental conditions rather than a combination of the experimental conditions and the experimental results, in their bubble pinch-off study of adiabatic bubble growth, Quan & Hua (2008) defined the Bond number with characteristic length equal to the orifice radius rather than the bubble detachment radius. Similarly, in the present study, the characteristic length of the Bond number is set to be the radius of the cavity from which the bubble is issuing in order to include cavity size in the bubble shape analysis. The cavity/orifice radius is noted b and the non dimensional Bond number with characteristic length equal to b is defined

2-26 $$Bo_b = \frac{g\left(\rho_l - \rho_v\right)b^2}{\sigma}.$$

In order to validate elementary results relating bubble growth and detachment characteristics to the cavity radius, controlled bubble growth experiments are necessary in which the parameters influencing the bubble are limited and in which the bubble is large enough to image process the observed bubble growth. Recently, Siedel *et al.* (2008) conducted bubble growth experiments particularly well adapted to such model validations. In particular, *n*-pentane vapour bubbles growing from a constant temperature low superheat plane were observed and image processed in which the growth operating conditions yielded quasi-static bubble growth from a large 90 µm radius nucleation cavity. In these bubble growth experiments, the bubble foot remained fixed to the perimeter of the cavity from inception to detachment. These novel results effectively reduce the number of varying parameters in bubble shape and growth analysis. In this way, validating data for this study's shape analysis of vapour bubble growth that incorporates the nucleation site radius is provided.

2.4. Adiabatic Bubble Growth

In an important study of adiabatic bubble growth, Oguz & Prosperetti (1993) adopted a numerical model based on that of Davidson & Schuler (1960) which approximates the bubble as spherical during its growth period. In this way, Oguz & Prosperetti (1993) were able to combine the Rayleigh equation with empirical relations for spherical bubbles to develop an approximate model for bubble detachment size.

In order for Oguz & Prosperetti (1993) to fully develop their model to the point of bubble detachment, a criterion for detachment of a needle injected vapour bubble was developed. Adopted through observation, it was stated that at the moment of detachment, the centre of curvature of the bubble is of the order of the bubble radius plus the needle tip radius,

2-27 $$C_d \approx R_d + b$$

in which C_d is the centre of curvature at detachment, b is the orifice radius and R_d is the detachment radius.

Equation 2-27 is helpful in reducing the number of unknowns in an analytical attempt to solve the bubble growth problem. It is however, an empirical find lacking any physical reasoning.

In the present study, a similar bubble geometric detachment relation based on a proposed geometric model and the principle of conservation of mass is developed.

2.5. Vapour Bubble Growth

Han & Griffith (1965) observed that the rapid early stage of bubble growth is such that a large portion of the thermal layer is translated vertically upwards thereby supporting a one-dimensional temperature profile.

Based on this observation, Mikic & Rohsenow (1969) presented an analytical model for vapour bubble growth from a heated plane by considering a two part one-dimensional transient conduction temperature profile detailed in the following section 2.5.1 and resulting in

2-28
$$\begin{aligned} T(y,t) = T_\infty + (T_{wall} - T_\infty)\left(1 - erf\left(\frac{y}{\sqrt{4\alpha(t+t_w)}}\right)\right) \\ + (T_{sat} - T_{wall})\left(1 - erf\left(\frac{y}{\sqrt{4\alpha t}}\right)\right) \end{aligned}.$$

2.5.1. Temperature Profile of Mikic & Rohsenow (1969)

The temperature profile of Mikic & Rohsenow (1969) is built on the following assumption. Once a vapour bubble detaches from a nucleation site, a vapour pocket is entrapped in the cavity from which the bubble grows. A superheated layer forms adjacent to the surface due to the no slip condition. This superheated layer then provides the energy needed to generate bubble growth due to vaporization. During the bubble growth period, the temperature within the superheated layer decreases in a non-uniform manner.

The period of time in which the heated plate induces the super heated layer prior to nucleation is referred to as the bubble growth waiting period and its time length is noted t_w; t_w shall be referred to as the waiting time. In the discussion that follows, time $-t_w$ corresponds to the beginning of the waiting period and time *0* corresponds to the end of the waiting period and subsequently to the beginning of the bubble growth period.

The temperature profile is solved for as a function of time and of position and is noted $T(y,t)$. The perpendicular distance from the bubble interface on the heated plane is noted *y*. During the waiting period, the temperature profile is solved for assuming that the bubble interface remains level with the heated plane.

The initial and boundary conditions are identified as follows:

During the waiting period, $-t_w < t \le 0$,

2-29
$$\begin{aligned} &T(y_\infty, t) = T_\infty \\ &T(y, -t_w) = T_\infty \\ &T(0,t) = T_{wall} \end{aligned} .$$

During the bubble growth period, that is to say $0 < t \le t_d$, in which t_d is the time at bubble detachment, the temperature at the bubble interface (corresponding to $y = 0$) is taken to be the fluid saturation temperature yielding boundary conditions,

2-30
$$\begin{aligned} &T(y_\infty, t) = T_\infty \\ &T(0,t) = T_{sat} \end{aligned} .$$

These boundary conditions, for both the waiting period and the growth period, are illustrated in Figure 2-1.

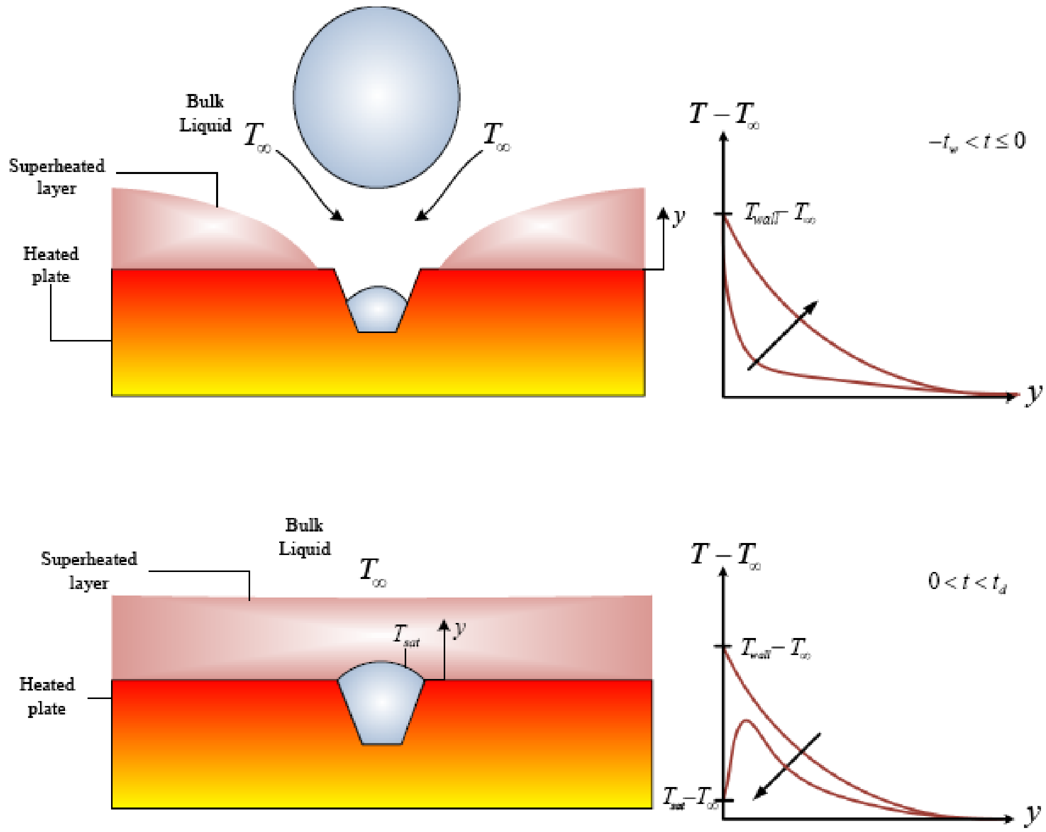

Figure 2-1: Schematic representation of the adopted boundary conditions in the solution procedure of the Heat Equation. (*Top)* Boundary conditions during the waiting period, $-t_w < t \le 0$. *(Bottom)* Boundary conditions during the growth period, $0 < t < t_d$. The arrows indicate the advancement of time.

For convenience in the calculations, the temperature profile is defined relative to the bulk temperature such that,

2-31 $\theta(y,t) = T(y,t) - T_\infty$.

The corresponding boundary conditions for the waiting period, in which $-t_w < t < 0$, are

2-32 $$\begin{aligned}&\theta(y_\infty,t)=0\\&\theta(y,-t_w)=0\\&\theta(0,t)=T_{wall}-T_\infty\end{aligned}$$

and for the growth period, in which $0<t\le t_d$, the boundary conditions are,

2-33 $$\begin{aligned}&\theta(y_\infty,t)=0\\&\theta(0,t)=T_{sat}-T_\infty\end{aligned}.$$

In the forthcoming arguments, the temperature profile is developed by coupling the solutions to the heat equation for the waiting period and for the growth period, noted θ_w and θ_g respectively, such that

2-34 $$\theta(y,t)=\theta_w(y,t)+\theta_g(y,t).$$

2.5.1.1. Waiting Period Temperature Profile

The boundary conditions for the waiting period temperature profile $\theta_w(y,t)$ are those of the temperature profile, listed in Eq. 2-32, since the growth period has not yet influenced the temperature profile.

The one dimensional heat equation representing the energy balance between the heated wall and the adjacent liquid in terms of $\theta_w=\theta_w(y,t)$ is,

2-35 $$\frac{\partial\theta_w}{\partial t}=\alpha\frac{\partial^2\theta_w}{\partial^2 y}.$$

The solution procedure to Eq. 2-35 requires reducing the heat equation to an ordinary differential equation by applying the following change of variables,

2-36 $$\eta = \frac{y}{\sqrt{4\alpha\left(t+t_w\right)}}.$$

A simple calculation of the partial derivatives of θ_w,

2-37 $$\frac{\partial\theta_w}{\partial t} = \frac{\partial\theta_w}{\partial\eta}\left(-\frac{y}{2t\sqrt{4\alpha(t+t_w)}}\right) = -\frac{\eta}{2\left(t+t_w\right)}\frac{\partial\theta_w}{\partial\eta}$$

and

2-38 $$\frac{\partial^2\theta_w}{\partial y^2} = \frac{1}{\sqrt{4\alpha\left(t+t_w\right)}}\frac{\partial}{\partial y}\left(\frac{\partial\theta_w}{\partial\eta}\right) = \frac{1}{4\alpha\left(t+t_w\right)}\frac{\partial^2\theta_w}{\partial\eta^2},$$

substituted into Eq. 2-35, yields the heat equation as the following ordinary differential equation,

2-39 $$\frac{\partial\theta_w}{\partial\eta} = -\frac{1}{2\eta}\frac{\partial^2\theta_w}{\partial\eta^2}.$$

From the definition of η in Eq. 2-36,

2-40 $$\begin{aligned} &\eta\left(y,-t_w\right) = \lim_{t\to -t_w^+}\frac{y}{\sqrt{4\alpha\left(t+t_w\right)}} = \eta_\infty \\ &\eta\left(y_\infty,t\right) = \eta_\infty \\ &\eta\left(0,t\right) = 0 \end{aligned}.$$

The boundary conditions are subsequently expressed in terms of η,

$$
\begin{aligned}
&\theta_w\left(\eta(y,-t_w)\right)=\theta_w\left(\eta_\infty\right)=0\\
&\theta_w\left(\eta(y_\infty,t)\right)=\theta_w\left(\eta_\infty\right)=0 \qquad \text{2-41}\\
&\theta_w\left(\eta(0,t)\right)=\theta_w\left(0\right)=T_{wall}-T_\infty
\end{aligned}
$$

which simplifies to the following two conditions,

$$
\begin{aligned}
&\theta_w\left(\eta_\infty\right)=0\\
&\theta_w\left(0\right)=T_w-T_\infty
\end{aligned}. \qquad \text{2-42}
$$

Equation 2-35 is now expressed as a first order differential equation by defining θ_w' as the first order derivative of θ_w, that is to say $\theta_w'=\frac{d\theta_w}{d\eta}$. The heat equation is reduced to,

$$\theta_w'=-\frac{1}{2\eta}\frac{\partial\theta_w'}{\partial\eta}. \qquad \text{2-43}$$

Straightforward integration of Eq. 2-43 yields, $\ln\theta_w'=-\eta^2+\ln K$ in of which *K* is a constant dependent on the boundary condition. Rearranging in order to isolate θ_w' yields,

$$\theta_w'=Ke^{-\eta^2}. \qquad \text{2-44}$$

Integrating with use of the boundary conditions solves for the unknown *K*, 2-45 $$\int_{\theta_w(0)}^{\theta_w(\eta_\infty)} d\theta_w = K\int_0^\infty e^{-\eta^2} d\eta \,.$$

As detailed in Appendix 7.8, the integral on the right hand side of Eq. 2-45 is simply,

2-46 $$\int_0^\infty e^{-\eta^2} d\eta = \frac{\sqrt{\pi}}{2} \,.$$

Equation 2-45 combined with the boundary conditions of Eq. 2-42 solve for *K*,

2-47 $$\theta_w(\eta_\infty) - \theta_w(0) = K\frac{\sqrt{\pi}}{2} \Rightarrow K = -\frac{2}{\sqrt{\pi}}(T_{wall} - T_\infty) \,,$$

reducing Eq. 2-44 to,

2-48 $$\frac{d\theta_w}{d\eta} = -\frac{2}{\sqrt{\pi}}(T_{wall} - T_\infty)e^{-\eta^2} \,.$$

Integrating once more from 0 to η, considering once again the boundary condition that $\theta_w(0) = T_{wall} - T_\infty$, yields

2-49 $$\theta_w(\eta) = (T_{wall} - T_\infty)\left(1 - \frac{2}{\sqrt{\pi}}\int_0^\eta e^{-\eta^2}\right) .$$

Defining the *erf* function as $erf\left(\eta\right)=\frac{2}{\sqrt{\pi}}\int_0^{\eta}e^{-\eta^2}d\eta$, and substituting in $\eta=\frac{y}{\sqrt{4\alpha\left(t+t_w\right)}}$, yields the temperature profile for the waiting period as a function of time,

$$\text{2-50} \qquad \theta_w\left(y,t\right)=\left(T_{wall}-T_\infty\right)\left(1-erf\left(\frac{y}{\sqrt{4\alpha\left(t+t_w\right)}}\right)\right).$$

Figure 2-2 illustrates the predicted temperature profile during the waiting period, given in Eq. 2-50, for a fluid at saturation temperature. The input conditions used are those of the experiments performed by Samuel Siedel (detailed in section 3.4). In particular, the wall superheat is 2.1 K and the working fluid properties are those of *n*-pentane with a saturation temperature of 35.7 °C. The waiting period is chosen arbitrarily to be t_w = 0.001 *sec.* and is purely for illustrative purposes.

In the graphical representation of Figure 2-2, the upper-horizontal frame axis corresponds to the wall temperature and the lower-horizontal corresponds to the liquid saturation temperature. The graphical representation of the temperature profile during the waiting period illustrates that the thermal boundary layer thickness increases with time and that the temperature of the fluid transitions from close to wall temperature to fluid saturation temperature within the thermal boundary layer.

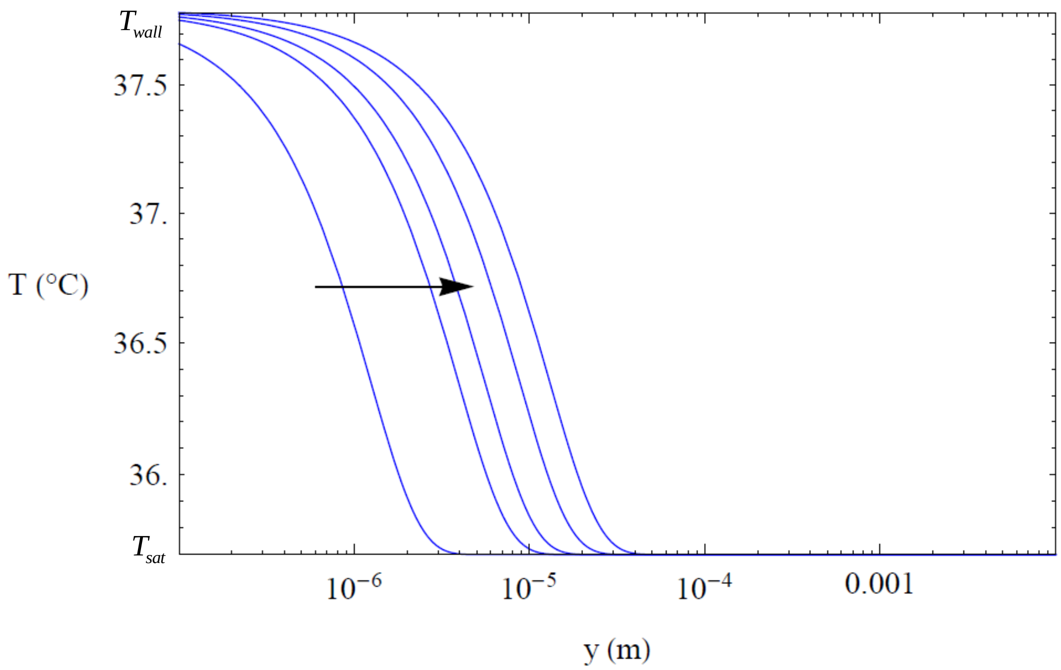

Figure 2-2: Graphical representation of the predicted temperature profile during the waiting period, $-t_w < t < 0$. The arrow indicts the advancement of time.

2.5.1.2. Growth Period Temperature Profile

The end of the waiting period implies the beginning of the bubble growth period. Bubble growth causes the temperature profile to change. As the bubble grows, it draws heat from its surroundings through vaporization, and as it departs, it causes an influx of cooler fluid near the heated plate.

The boundary conditions for the growth period, stated earlier in Eq. 2-30, are solved for by considering the growth period temperature profile definition of Eq. 2-34, the boundary conditions of Eq. 2-33 and by solving for $\theta_w\left(y_\infty, t\right)$ and $\theta_w\left(0, t\right)$ with Eq. 2-50.

From Eq. 2-50, $\theta_w\left(y_\infty,t\right)=0$ (refer to the definition of the *erf* function and the integral of Appendix 7.8 for *y* approaching infinity) and $\theta_w\left(0,t\right)=T_{wall}-T_{sat}$.

The boundary conditions for the growth period temperature profile are therefore,

2-51 $$\begin{aligned}\theta_g\left(y_\infty,t\right)&=\theta\left(y_\infty,t\right)-\theta_w\left(y_\infty,t\right)=0\\ \theta_g\left(0,t\right)&=\theta\left(0,t\right)-\theta_w\left(0,t\right)=T_{sat}-T_{wall}\end{aligned}.$$

The one dimensional heat equation representing the energy balance between the bubble interface and the adjacent liquid in terms of $\theta_g=\theta_g\left(y,t\right)$ is,

2-52 $$\frac{\partial\theta_g}{\partial t}=\alpha\frac{\partial^2\theta_g}{\partial^2 y}.$$

The solution procedure requires reducing the heat equation to an ordinary differential equation by applying the following change of variables,

2-53 $$\eta=\frac{y}{\sqrt{4\alpha t}}.$$

It is noted that the waiting time is appropriately absent from the solution procedure of the growth period temperature profile.

In a similar approach as to the calculation of the previous section, the heat equation is solved as an ordinary differential equation with respect to η, 2-54 $$\frac{\partial \theta_g}{\partial \eta} = -\frac{1}{2\eta}\frac{\partial^2 \theta_g}{\partial \eta^2}$$

of which the boundary conditions are,

2-55 $$\begin{aligned} &\theta_g\left(\eta(y_\infty, t)\right) = \theta_g\left(\eta_\infty\right) = 0 \\ &\theta_g\left(\eta(0,t)\right) = \theta_g\left(0\right) = T_{sat} - T_{wall} \end{aligned}.$$

Solving the above heat equation with these boundary conditions in the same manner as in the previous section yields the temperature profile for the growth period,

2-56 $$\theta_g\left(y,t\right) = \left(T_{sat} - T_{wall}\right)\left(1 - erf\left(\frac{y}{\sqrt{4\alpha t}}\right)\right).$$

Combining Eq. 2-56 with Eq. 2-50 yields the final form of the temperature profile adjacent to the heated plane,

2-57 $$\begin{aligned} \theta\left(y,t\right) = &\left(T_{wall} - T_\infty\right)\left(1 - erf\left(\frac{y}{\sqrt{4\alpha\left(t + t_w\right)}}\right)\right) \\ &+ \left(T_{sat} - T_{wall}\right)\left(1 - erf\left(\frac{y}{\sqrt{4\alpha t}}\right)\right) \end{aligned}.$$

In an attempt to account for the moving vapour-liquid boundary, Mikic & Rohsenow (1969) proposed a shape factor value of $\sqrt{3}$. In assuming the bubble to be spherical throughout its growth, they solved the interfacial mass-energy balance (detailed in Eq. 5-3: $h_{lv}\rho_v \frac{dV}{dt} = k_l \int \nabla \cdot \vec{T} dA$) with the temperature profile of Eq. 2-28 and included an unknown constant, noted *C*, into the solution,

$$\text{2-58} \qquad \rho_v h_{lv} \frac{dR}{dt} = Ck\left(\frac{T_{wall} - T_{sat}}{\sqrt{\alpha \pi t}} - \frac{T_{wall} - T_{\infty}}{\sqrt{\alpha \pi \left(t + t_w\right)}} \right).$$

The constant *C* was solved to be $\sqrt{3}$ by equating the above with the limiting solution of spherical bubble growth in an infinite uniformly superheated liquid (Plesset & Zwick, 1954),

$$\text{2-59} \qquad h_{lv}\rho_v \frac{dR}{dt} = \sqrt{3}k \frac{T_{\infty} - T_v}{\sqrt{\alpha \pi t}}$$

and setting the bubble vapour temperature to the liquid saturation temperature.

A similar development, yielding a similar result, uses the spherical bubble growth in a uniformly superheated pool analysis of Forster & Zuber (1954) to deduce $\pi / 2$ as the value of the constant *C*.

In the Mikic & Rohsenow (1969) analysis, the bubble volume is calculated by assuming the bubble to be a perfect sphere and by integrating Eq. 2-58 thereby solving for the bubble radius,

$$\text{2-60} \qquad R = \frac{2}{\pi}\sqrt{3} Ja \sqrt{\pi \alpha t \left(1 - \frac{T_{wall} - T_{\infty}}{T_{wall} - T_{sat}} \left(\sqrt{1 + \frac{t_w}{t}} - \sqrt{\frac{t_w}{t}} \right) \right)}.$$

The importance in the result of Eq. 2-60 relative to the general study of this document is that the bubble is spherical during its entire growth cycle yet sitting on a heated plane.

In a similar study, Han & Griffith (1965) linearized the temperature profile and assumed the bubble to grow spherically on the heated plane. The resulting bubble radius growth curve,

2-61
$$R = b + \frac{\varphi_s \varphi_c}{\varphi_v} \frac{c_p \rho_l \left(T_{wall} - T_{sat}\right)\sqrt{\pi \alpha t_w}}{h_{lv}\rho_v} \left(\begin{array}{l} 2erfc\left(\sqrt{\frac{\pi t_w}{4t}}\right) - \frac{4t}{\pi t_w} erf\left(\sqrt{\frac{\pi t_w}{4t}}\right) \\ -\frac{4}{\pi} e^{-\frac{\pi t_w}{4t}} \sqrt{\frac{t}{t_w}} + \frac{2}{\pi}\sqrt{\frac{t}{t_w}} \end{array} \right) + \varphi_b \frac{h_v \left(T_{wall} - T_{sat}\right)}{h_{lv}\rho_v \varphi_v} t$$

includes many shape correction terms. In particular, φ_c is a curvature factor such that $1 < \varphi_c < \sqrt{3}$ and h_v is the heat transfer coefficient deduced empirically. Also, φ_s, φ_v and φ_b are the surface, base and volume factors respectively and are dependent of the contact angle. Physically, a spherical bubble resting on a plane would necessarily have a contact angle of zero. However, it is understood that the contact angle is measured when observing the bubble’s actual shape on the plane and that in the Han & Griffith (1965) model development, spherical bubble growth has been assumed in order to ease the calculations. In doing so, the physical significance of the terms is lost.

Van Stralen & Sluyter (1969) developed a spherical equivalent radius growth model for a heat-transfer controlled vapour bubble growing on a heated plane. It was assumed that a thin thermal layer providing the necessary latent heat of vaporization was driven outwards by the growing bubble. The resulting equivalent radius growth curve was found to be,

2-62 $$R = \frac{1.954 B c_p \rho_l e^{\sqrt{t/t_d}} \sqrt{t\alpha}\left(T_{wall} - T_{sat}\right)}{h_{lv}\rho_v}.$$

In the above B is an empirical growth parameter with a maximum value of 1 and t_d is the time of bubble detachment. In addition, Van Stralen *et al.* (1975) put forth a bubble equivalent radius growth curve for either the inertia-controlled or the heat-transfer controlled growth regimes such that the spherical equivalent radius growth curve was,

2-63 $$R = \frac{R_1 R_2}{R_1 + R_2}$$

in which,

2-64 $$R_1 = 0.8165 t \sqrt{\frac{\rho_v h_{lv}\left(T_{wall} - T_{sat}\right) e^{-\sqrt{t/t_d}}}{\rho_l T_{sat}}}$$

and

2-65 $$R_2 = 1.9544\left(\begin{array}{c}\left(1.3908\dfrac{R_2(t_d)}{Ja\sqrt{\alpha t}} - 0.1908\,\mathrm{Pr}_l^{-1/6}\right)e^{-\sqrt{t/t_d}} \\ +\dfrac{T_\infty - T_{sat}}{T_{wall} - T_{sat}}\end{array}\right)Ja\sqrt{\alpha t} + 0.3730\,\mathrm{Pr}_l^{-1/6}\,e^{-\frac{1}{2}\sqrt{t/t_d}}\,Ja\sqrt{\alpha t}\,.$$

More recently, Zhao *et al.* (2002) solved for the bubble radius of an individual growing bubble on a heated plane by considering the bubble to be a hemisphere sitting on a microlayer situated between it and the heated plane. The energy-mass balance is assumed to take place at the bubble-microlayer interface resulting in the following bubble radius growth curve,

2-66 $$R = \frac{2k\left(T_{wall} - T_{sat}\right)}{\rho_v h_{lv}\sqrt{0.64\dfrac{c_p \mu_l \alpha}{k_l}}}t^{1/2}\,.$$

The presence of 0.64 in the root denominator is the result of an empirical estimation of the microlayer thickness when compared with the experimental results of Cooper *et al.* (1978).

A recurring theme in all of the above mentioned studies is oversimplified bubble geometry compensated with corrective empirical shape factors. In this study, a bubble geometry transitioning in shape and size is adopted throughout the model development providing a model of bubble growth on a heated plane that more accurately describes the trends of bubble growth characteristics during the growth cycle.

2.5.2. Waiting Time

The waiting time is defined as the time necessary to initiate bubble growth. It is a required input for some of the previously mentioned models of vapour bubble growth on a heated plane. This is due to the fact that the waiting time is intimately linked with the amount of energy that is available for latent heat vaporization in the superheated layer adjacent to the plane. For a given wall superheat, the longer the waiting time the more energy injected into the superheated layer. For this reason, Han & Griffith (1965) solved for the waiting time in the following way.

The waiting time was conveniently identified as the moment in which the fluid adjacent to the heated plane is brought to the temperature of the bubble, noted T_{bub} (Scriven, 1959). This temperature was identified by use of the Clapeyron equation (Eq. 2-15) in which the Young-Laplace equation was applied without the viscous term (detailed in the forthcoming Eq. 3-10), $p_v - p_l = 2\sigma / R$. By assuming the incipient hemispherical bubble to be of radius equal to the cavity radius, by considering the temperature differential to be $T_{bub} - T_\infty$ and by taking the liquid specific volume to be negligible in comparison with the vapour specific volume, the following relation was established, 2-67 $$\frac{2\sigma}{b}=\frac{h_{lv}\left(T_{bub}-T_{\infty}\right)}{\left(\frac{1}{\rho_v}\right)T_{sat}}.$$

The temperature identifying the end of the waiting period was therefore identified as,

2-68 $$T_{bub}=T_{\infty}+\frac{2\sigma T_{sat}}{b\rho_v h_{lv}}.$$

The waiting time was solved for by setting the temperature of the fluid adjacent to the heated plane to the bubble vapour temperature. This is due to occur at time zero, corresponding to the beginning of bubble growth. The waiting time is therefore calculated by setting the temperature of Eq. 2-50 to T_{bub} at time $t=0$ and isolating t_w,

2-69 $$T_{bub}=T_{\infty}+\left(T_{wall}-T_{\infty}\right)\left(1-erf\left(\frac{y}{\sqrt{4\alpha t_w}}\right)\right).$$

However, since the right hand side of the above equation contains an *erf* function, it is necessary to approximate it as a linear function in order to isolate t_w. Approximating the *erf* function to the first term of its polynomial expansion, $erf(\zeta)=\frac{2\zeta}{\sqrt{\pi}}-\frac{2\zeta^3}{3\sqrt{\pi}}+\frac{\zeta^5}{5\sqrt{\pi}}-\frac{\zeta^7}{21\sqrt{\pi}}+\frac{x^9}{108\sqrt{\pi}}+o\left(\zeta^{11}\right)$, Eq. 2-69 reduces to

$$T_{bub} = T_{\infty} + \left(T_{wall} - T_{\infty}\right)\left(1 - \frac{y}{\sqrt{\alpha \pi t_w}}\right). \quad (2\text{-}70)$$

In order to illustrate the validity of the linear form of the *erf* function in the context of the temperature profile, Figure 2-3 illustrates that the thermal boundary layer is well approximated with the linear form of the *erf* function; it is particularly well approximated for the higher temperatures near the heated plane. The input values used in Figure 2-3 are those in which the working fluid is *n*-pentane and the wall superheat is 2.1 K. In Figure 2-3, y represents the perpendicular distance from the heated plane. The input waiting time is calculated from Han & Griffith (1965) in the forthcoming Eq. 2-72, however, the purpose of Figure 2-3 is meant to be illustrative of the linear *erf* approximation.

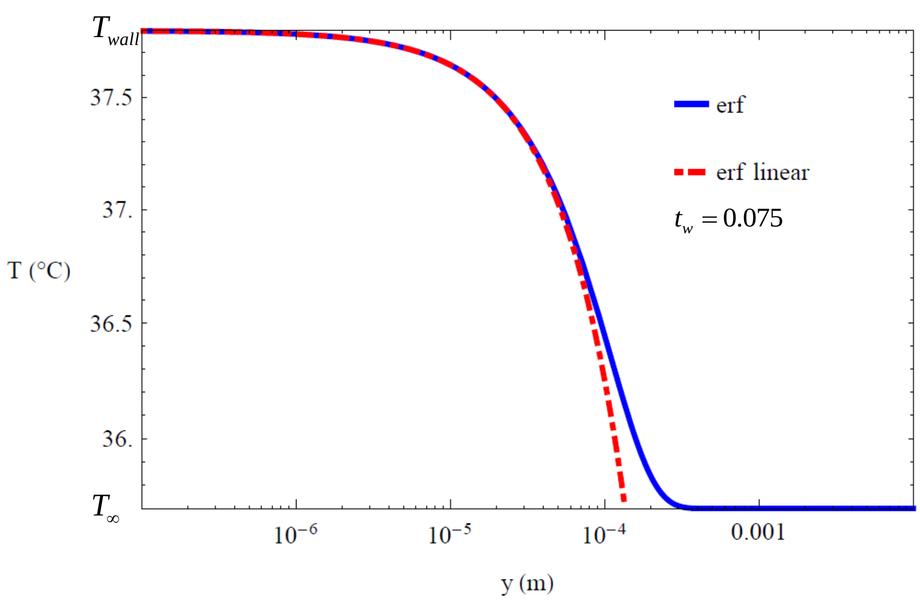

Figure 2-3: Comparison of the temperature profile generated using the *erf* function versus using the linear approximation of the *erf* function.

Combining Eq. 2-68 with Eq. 2-70 yields,

2-71 $$\frac{2\sigma T_{sat}}{b\rho_v h_{lv}} = \left(T_{wall} - T_\infty\right)\left(1 - \frac{y}{\sqrt{\alpha\pi t_w}}\right).$$

Han & Griffith (1965) further assume that the incipient hemispherical bubble was isolated by an isothermal layer at the bubble vapour temperature in which there occurs tangential conduction causing the bubble to grow. The distance from the top point of this conduction layer to the heated plate was approximated to $\frac{3}{2}b$. Therefore, Han & Griffith (1965) solved Eq. 2-71 for $y = \frac{3}{2}b$ expressing the waiting time in terms of the wall temperature and the fluid properties as,

2-72 $$t_w = \frac{9b^2}{4\alpha\pi}\left(1 - \frac{2\sigma T_{sat}}{b\rho_v h_{lv}\left(T_{wall} - T_\infty\right)}\right)^{-2}.$$

Similarly, Mikic & Rohsenow (1969) solved Eq. 2-71 for $y = b$ yielding the waiting time,

2-73 $$t_w = \frac{b^2}{\alpha\pi}\left(1 - \frac{2\sigma T_{sat}}{b\rho_v h_{lv}\left(T_{wall} - T_\infty\right)}\right)^{-2}.$$

2.5.3. Boundary Layer Thickness

As illustrated in Figure 2-3, the boundary layer thickness can be approximated as the distance from the heated plane in which the temperature profile reaches bulk fluid temperature (Han & Griffith, 1965). The boundary layer thickness, noted δ, can be solved for by setting the temperature of Eq. 2-50 to the bulk fluid temperature at time zero: $\theta(\delta, t_w) = 0$. In using the linearized *erf* function, Eq. 2-50 reduces to,

$$0 = \left(T_{wall} - T_\infty\right)\left(1 - \frac{\delta}{\sqrt{\alpha \pi t_w}}\right). \tag{2-74}$$

Isolating δ in the above yields the following approximate thermal boundary layer at the end of the waiting time,

$$\delta = \sqrt{\alpha \pi t_w}. \tag{2-75}$$

2.6. Asymmetric Bubble Growth

In an effort to further understand the shape behaviour of a bubble during its growth evolution, Lesage *et al.* (2009) proposed a model including the acceleration term that is due to an asymmetric gain of mass.

In particular, for approximately hemispherical bubble growth, the sum of the forces acting on the bubble was deemed negligible compared with the asymmetric term making the momentum due to centre of gravity motion non-negligible. For non-hemispherical bubble growth, this component in the equation of motion was deemed very significant during the initial rapid growth phase as a bubble transitions from a near hemisphere to a truncated spherical geometry.

An equation describing the bubble radius growth cycle was developed by solving the integral form of the momentum equation and conserving the term representing the asymmetric gain of mass. The model was developed by first expressing the principle of conservation of mass in the form of an equation of motion for the centre of mass of an arbitrary bulk as detailed in Panton (1996),

2-76 $$m\dot{\vec{H}} = \int \rho \vec{v} dV - \int \rho \vec{n} \cdot (\vec{v} - \vec{w})(\vec{r} - \vec{H}) dS \ .$$

The first term on the right hand side represents the momentum of the vapour bubble and the second term represents the momentum due to the movement of the centre of gravity of the bubble resulting from an asymmetric gain or loss of mass from the region. The importance of this expression lies in the fact that the product of the mass and the instantaneous rate of change of the bubble's centre of mass is not necessarily equal to the momentum of the bubble.

An example of this would be a quiescent liquid drop on a superheated surface in which evaporation only occurs along the bottom portion of the drop. Since the liquid within the drop has no bulk velocity its momentum is zero. However, if the drop is vaporizing asymmetrically, the centre of gravity will move and this can be described by the asymmetric loss term provided that sufficient information is available to model the vaporization dynamics and drop geometry.

Similarly, from the momentum principle, a general expression for the motion of the centre of mass of an arbitrary bulk of variable mass growing asymmetrically was detailed (Panton, 1996),

$$\text{2-77} \qquad m\ddot{\vec{H}} = -\int \rho\vec{n}\cdot(\vec{v}-\vec{w})(\vec{v}-\dot{\vec{H}})dS - \frac{d}{dt}\int \rho\vec{n}\cdot(\vec{v}-\vec{w})(\vec{r}-\vec{H})dS + \sum \vec{F}\ .$$

In the above equation, the first and last terms on the right hand side account for the momentum of the gas/vapour crossing the interface and the sum of the forces acting on the bubble respectively. The second term on the right hand side, however, was typically unaccounted for in all prior bubble growth models in that it accounts for the acceleration of the centre of mass due to asymmetric growth. In particular, the integral $\int \rho\vec{n}\cdot(\vec{v}-\vec{w})(\vec{v}-\dot{\vec{H}})dS$, represents the momentum that leaves the bubble with mass flux $\rho\vec{n}\cdot(\vec{v}-\vec{w})$ and the second of the above integrals, $\frac{d}{dt}\int \rho\vec{n}\cdot(\vec{v}-\vec{w})(\vec{r}-\vec{H})dS$, accounts for the movement of the centre of mass due to asymmetric mass loss or gain. With this, Lesage *et al.* (2009) considered a scenario to exemplify the significance of their modelling approach in which a bubble grows in microgravity initiating from a small nucleation site on a superheated surface. Bubble growth was considered to initiate at the end of a waiting time and to grow as a near perfect hemisphere as is the case with the space microgravity experiments of Lee & Merte (1996). For this particular scenario, Robinson (2002) showed that during the early growth stages, the thermal boundary layer adjacent to the heated surface was very large compared with the size of the bubble. Therefore, the superheat around the bubble dome was nearly constant and vaporization could be approximated as uniform over the bubble surface. It was argued that if this were approximately the case, then the mass flux $\rho\vec{n}\cdot(\vec{v}-\vec{w})$ could be integrated over the vapour-liquid surface area, noted *A*, establishing the following uniform vaporization condition,

2-78 $$-\rho\vec{n}\cdot(\vec{v}-\vec{w})=\frac{\dot{m}}{A}.$$

Lesage *et al.* (2009) showed that Eq. 2-77 combined with Eq. 2-78, the fact that $s=0$ for a hemispherical bubble (implying that the centre of curvature sits at the foot of the bubble), the symmetry of the problem and the fact that the linear momentum was assumed negligible the equation of motion for the centre of gravity (Eq. 2-77) simplified to,

2-79 $$m\ddot{H}=\dot{m}(v_z-\dot{H})+\frac{1}{8}\frac{d}{dt}\left(\dot{m}R\right)+\sum F\ .$$

In the microgravity scenario the buoyancy force is zero due to the absence of gravity. Due to the geometry of the bubble the contact pressure force and the capillary force were shown to be equal and offsetting which cause the sum of the forces to be exactly zero. This was provided that the drag force could be considered very small, which in this case was rational since the expansion was almost radially symmetric making the liquid flow quasi-irrotational. With this, Lesage *et al.* (2009) obtained the following expression,

2-80 $$m\ddot{R} = -\frac{2}{3}\dot{m}\dot{R} + \frac{1}{3}\ddot{m}R\,.$$

The main result of this scenario was that the linear momentum of the bubble is zero, in that it was not a force imbalance that caused the centre of gravity to accelerate. That is to say, as illustrated below, the motion of the centre of gravity was solely described by geometric and mass transfer factors as opposed to mechanistic influences.

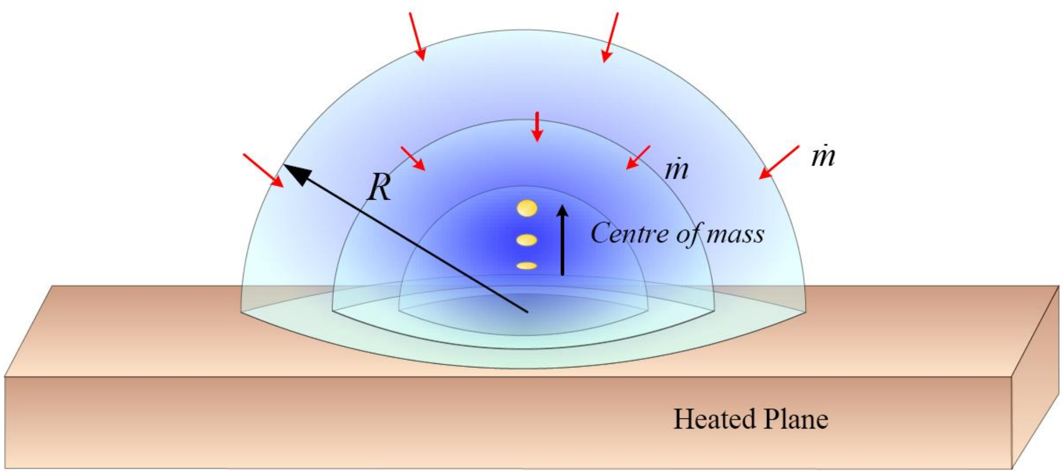

Figure 2-4 : Hemispherical bubble growth due to vaporization at the liquid-vapour interface.

Furthermore, Lesage *et al.* (2009) developed an equation of motion for bubble formation due to a constant flow rate gas injection through a submerged orifice in which the bubble foot was assumed to stay fixed to the perimeter of the issuing cavity. The model was based on the asymmetric mass flux. In particular, the linear momentum of the gas bubble growing in a quasi-static formation was considered to be negligibly small and as such the bulk linear momentum term of Eq. 2-76 was neglected reducing Eq. 2-76 to,

$$\text{2-81} \qquad m\dot{H} = -\int_A \rho\left(v_z - w\right)(r_z - H)dS \, .$$

The above simply states that the momentum of the centre of gravity of the bubble is solely due to the asymmetric mass flux term. In the treatment of quasi-static gas injected bubble growth from a submerged orifice, it was assumed that the mass flux be uniform making Eq. 2-78 applicable. With this assumption, Lesage *et al.* (2009) successfully reduced Eq. 2-81 with the hemispherical inception condition to the following relation which expresses the bubble radius as a function of time in implicit terms,

$$\text{2-82} \qquad t = \frac{\pi b^2}{3\dot{V}}\left[\frac{4R^3}{3b^2} + 5R + \sqrt{R^2 - b^2}\left(\frac{4R^2}{3b^2} + \frac{17}{3}\right) - \frac{19}{3}b\right].$$

It is important to recall that the above non-empirical analytical result was developed neglecting bulk linear momentum and thus only considering the momentum due to the asymmetric gain of mass. The model was shown to have predictive capabilities for quasi-static low Bond number bubble growth thereby highlighting the role of the momentum due to the motion of the centre of gravity resulting from an asymmetric gain of mass.

The model is limited by the geometric shape of the bubble in that it was assumed to remain a section of a sphere with a bubble foot attached to the orifice. The lack of inclusion of the necking phenomenon implies that the model is not able to predict the bubble's centre of gravity correctly. This is due to the fact that the necking phenomenon near the end stage of bubble growth causes the bubble's centre of gravity to increase rapidly. This common shortcoming in analytical models attempting to describe bubble growth as spherical or truncated spherical is often compensated by the inclusion of empirical constants adjusting the results to the validating data. However, even with the inclusion of an empirical constant, any model with a spherical or truncated spherical geometric assumption that does not include the necking phenomenon cannot predict a centre of gravity vertical component to surpass the magnitude of the bubble radius. Otherwise, the result would be in contradiction with its own geometric model. It is however observed to be consistently true that the centre of gravity vertical component surpasses the radius in magnitude (Duhar &Colin, 2006; Di Bari & Robinson, 2009) once again highlighting the importance of accurate bubble shape modeling.

In the present study, the importance in understanding bubble shape prior to any bubble growth model development is highlighted. Bubble modeling in this study begins with an appropriate geometric bubble shape and is followed by the physical mechanics affecting the bubble during its growth cycle as it continues to change in shape.

3. NUMERICAL STUDY OF BUBBLE SPHERICITY

3.1. Introduction

In this chapter, bubble degree of sphericity is investigated by first benchmarking a numerical procedure for adiabatic bubble growth and for bubble growth due to vaporization and then by analysing the results of numerically generated bubble profiles under varying operating conditions. In particular, the Bond number as defined in Eq. 2-26 is varied with respect to the gravitational field strength and then varied with respect to the characteristic length. The shape evolution is observed to be dependent on the Bond number exposing the physical mechanisms quantified by the Bond number as the dictating factor in a bubble's deviation from a spherical shape. This is found to be true irrespective of the size of the bubble. By introducing the notion of modified sphericity, the behaviour of a bubble's growth shape is shown to be a transition from hemispherical to spherical with an elongation due to neck formation near the end of the growth cycle. In addition, the magnitude of this elongation is shown to be dependent on the Bond number.

In this numerical study the validity of assuming a sphericity of unity is investigated and the physical mechanism that promotes deviation from sphericity of unity is identified. Furthermore, a detailed shape analysis leads to a bubble geometry postulation for low Bond number applications. With exception of the microgravity conditions, the low Bond number geometric postulation considers the bubble to be hemispherical at inception transitioning to spherical with a growing cylindrical neck driving the bulk of the bubble upwards. In the microgravity consideration, the buoyancy force is negligable and therefore the Bond number – being efffectively a ratio of the buoyancy to surface tension forces – does not play an important role in the microgravity bubble evolution. For this reason, the bubble shape evolution dependance on the Bond number postulated in this work does not apply to microgravity considerations.# This would then make the

3.2. Degree of sphericity

A numerical procedure is developed with the objective of measuring shape behaviour of a bubble during its growth cycle and at detachment.

A convenient way to quantify the spherical behaviour of a bubble is to evaluate its degree of sphericity. The bubble degree of sphericity, noted Ψ, is the ratio of the bubble's volume equivalent spherical area to the bubble's actual surface area. It is solved for by first evaluating the radius of a volume equivalent sphere, noted R_{eq} defined as,

3-1 $$R_{eq} = V_{sph}^{-1}\left(V_m\right) = \sqrt[3]{\frac{\frac{3}{4}V_m}{\pi}}$$

in which V_{sph}^{-1} is the inverse function of $V_{sph}\left(R\right) = \frac{4}{3}\pi R^3$ and V_m is the measured volume. The area of the volume equivalent sphere is noted A_{eq} and defined as, 3-2 $$A_{eq} = A_{sph} \circ V_{sph}^{-1}(V_m)$$

in which $A_{sph}(R) = 4\pi R^2$. The ratio of A_{eq} to A_m yields the bubble degree of sphericity,

3-3 $$\Psi = \frac{A_{sph} \circ V_{sph}^{-1}(V_m)}{A_m} = \frac{\left(6\sqrt{\pi}V_m\right)^{2/3}}{A_m}$$

in which A_m is the bubble's measured surface area including the bubble foot area.

An illustrative example is the degree of sphericity of the unit cube. Figure 3-1 illustrates that despite having the same volume, the unit cube appears to have a larger surface area than its volume equivalent sphere of radius $\sqrt[3]{\frac{3}{4\pi}}$ with coinciding centre. Indeed, the degree of sphericity for the unit cube is calculated from Eq. 3-3 to be $\Psi = (\pi/6)^{1/3} = 0.806$. This result implies that the surface area of the unit cube's volume equivalent sphere is less than the surface area of the unit cube.

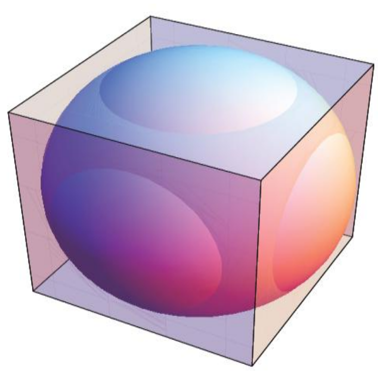

Figure 3-1: The unit cube and its volume equivalent sphere with coinciding centres.

It is important to note that if the bubble's entire surface area is considered, its maximum possible sphericity is unity corresponding to a perfect sphere. In most if not all of the available data, an equivalent radius to that of a sphere of equal volume is used as the physical parameter from which the bubble growth characteristics are measured. This implies that the available data already has made a result influencing geometric assumption when providing measurements of bubble growth characteristics. The numerical procedure described in the following section provides the bubble's surface area and the bubble's volume measured from the bubble's image processed contour. This makes it possible to experimentally benchmark a numerical solution of the bubble profile. From these results, the bubble degree of sphericity is investigated.

3.3. Numerical Model of Bubble Profile

Bubble profile simulations are run by solving the capillary equation numerically yielding the bubble contour from which the sphericity of a bubble is obtained. In this process, a frustum geometric analysis of the bubble's profile is applied. The solution procedure is benchmarked against image processing results of two sets of experiments:

1. Gas injected adiabatic bubble growth with a fixed foot radius and a constant volumetric flow rate.

2. Bubble growth due to vaporization from a heated plane with a constant superheat and fixed foot radius.

The Capillary equation is the result of a pressure balance during the quasi-static bubble formation in which the interfacial pressure balance is dictated by the Young-Laplace equation. A full development of the capillary equation follows.

3.3.1. The Young-Laplace Equation

The application of the Young-Laplace equation to bubble growth is used to predict the difference between the external and internal pressures across the vapour-liquid bubble interface thereby relating this pressure difference to the surface tension. It is developed here in a similar fashion as to Faghri & Zhang (2006).

Consider the infinitesimal interfacial segment illustrated in Figure 3-2 in which the area of the curved surface is expanding outwards. The *x* direction length of the infinitesimal segment increases as does the *y* direction length. These lengths, noted *x* and *y*, are considered to be arc lengths with associated angles θ_2 and θ_1 respectively and associated radii R_2 and R_1 respectively. The radii R_2 and R_1 are the principal radii of curvature of the infinitesimal surface since their respective principal directions *x* and *y* are perpendicular.

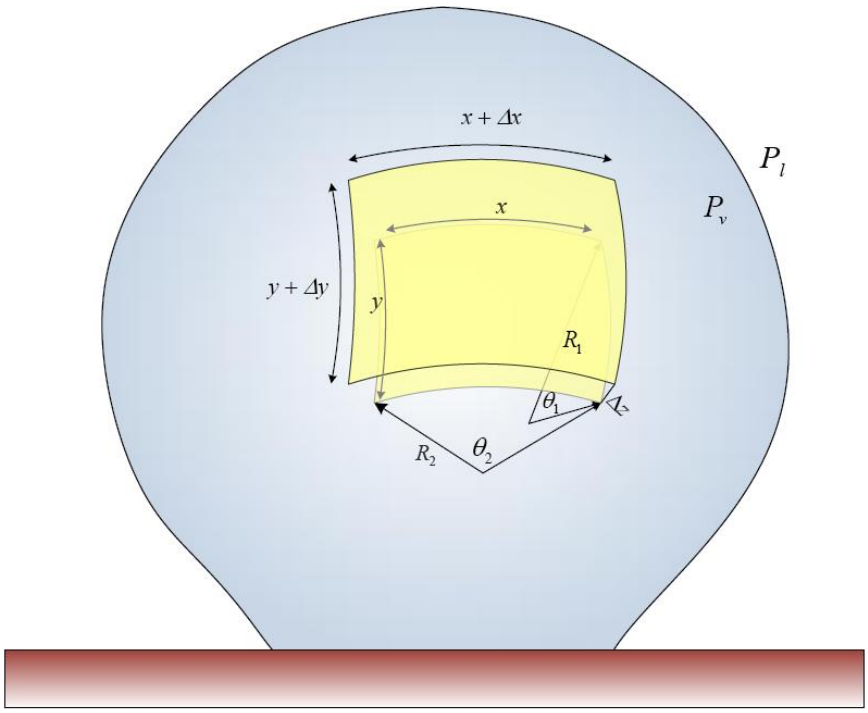

Figure 3-2: Arbitrarily curved surface with two radii of curvature.

For an arbitrarily curved surface with two radii of curvature R_1 and R_2, an infinitesimal area on a curved surface is approximated by its length times its width as if it were a flat surface. An infinitesimal variation in the area ΔA is thus approximated in the following way in which second order length variations are considered to be negligible.

3-4 $$\Delta A = (x + \Delta x)(y + \Delta y) + xy = y\Delta x + x\Delta y$$

By definition of surface tension, noted σ, the work done on the system in order to increase the area by an amount ΔA is, 3-5 $$W = \sigma \Delta A \Delta z$$

in which Δz is normal to the *x*-*y* plane.

This results in a pressure difference across the surface, noted $\Delta P_{face} = P_{v,face} - P_{l,face}$ and a viscous stress term normal to the surface, noted τ. This interfacial pressure difference is often referred to as the capillary pressure. The force acting on the system is thus resulting from the sum of the pressure difference across the normal surface and the shear stress on that surface,

3-6 $$W = \left(\Delta P_{face} + \tau\right) xy \,.$$

Combining Eq. 3-5 and Eq. 3-6 above in terms of the infinitesimal lengths illustrated in Figure 3-2 establishes the following work balance,

3-7 $$\left(\Delta P_{face} xy + \tau xy\right)\Delta z = \sigma\left(y\Delta x + x\Delta y\right).$$

Relating the arc lengths to their respective angles illustrated in Figure 3-2 yields the following relations between the principal radii of curvature and their arc lengths,

3-8 $$\begin{aligned} \theta_1 &= \frac{y}{R_1} = \frac{y+\Delta y}{R_1+\Delta z} \Rightarrow \Delta y = \frac{y\Delta z}{R_1} \\ \theta_2 &= \frac{x}{R_2} = \frac{x+\Delta x}{R_2+\Delta z} \Rightarrow \Delta x = \frac{x\Delta z}{R_2} \end{aligned} \,.$$

Substituting the Δx and Δy terms from Eq. 3-8 into Eq. 3-7 yields, 3-9 $$\left(\Delta P_{face}+\tau\right)xy\Delta z=\sigma\left(y\frac{x\Delta z}{R_2}+x\frac{y\Delta z}{R_1}\right)$$

which when simplified provides the final form of the Young-Laplace Equation,

3-10 $$\Delta P_{face}=\sigma\left(\frac{1}{R_2}+\frac{1}{R_1}\right)-\tau\ .$$

The above Young-Laplace equation describing the infinitesimal segment interfacial pressure balance may be applied to a pressure balance at any interfacial point over the entire bubble in the development of the capillary equation.

3.3.2. Capillary Equation

The capillary equation is a result of a balance of pressure at the bubble interface. It is developed here in a similar fashion as to Mori & Baines (2001), Gerlach *et al.* (2005), and Di Marco *et al.* (2005).

Consider a coordinate system such that the origin is situated at the bubble's apex and such that the *z*-axis is positive in the downward direction as is illustrated in the Figure 3-3. In Figure 3-3, ξ represents the liquid submerged depth of the plane, z_{dp} represents the liquid submerged depth of the bubble apex and *b* represents the cavity radius on which the bubble foot sits.

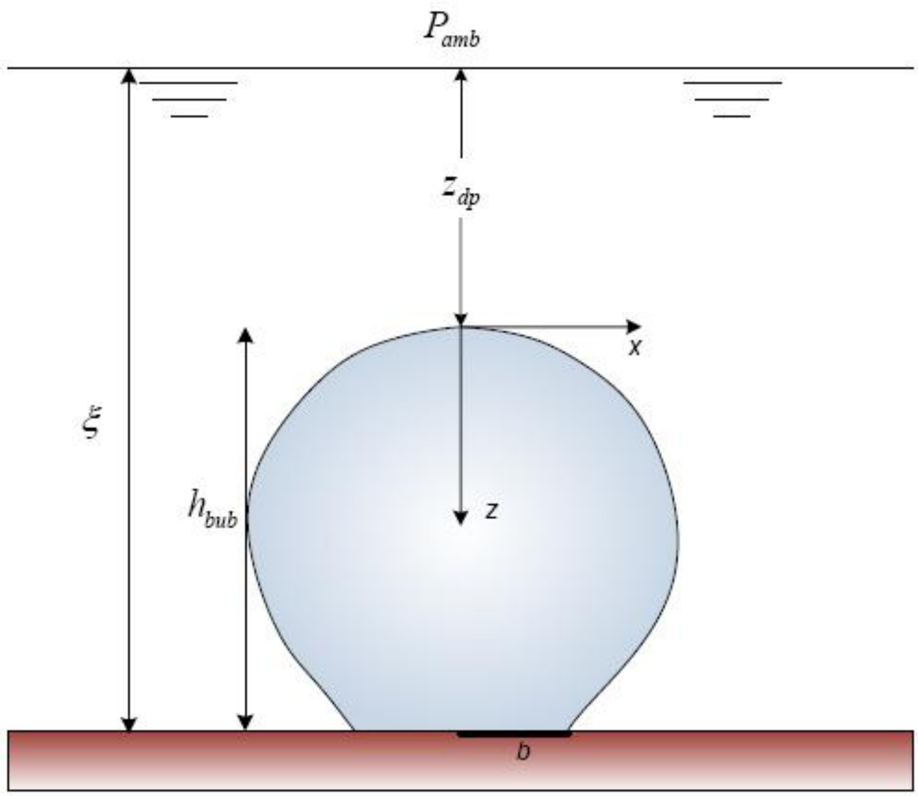

Figure 3-3: Coordinate system used when developing the capillary equation.

Within the quasi-static regime, it is assumed that the viscous stresses are negligible thereby considering the pressure balance at the interface as described by the Young-Laplace equation (Eq. 3-10) without the viscous term τ. Therefore, the pressure balance at any given position can be expressed as,

3-11 $$P_v(z) - P_l(z) = \sigma\left(\frac{1}{R_1(z)} + \frac{1}{R_2(z)}\right).$$

By including the hydrostatic pressures, the vapour pressure and the liquid pressure are expressed in terms of their respective pressures at the apex such that, 3-12 $$P_v(z) = P_v(0) + \rho_v gz$$

and

3-13 $$P_l(z) = P_l(0) + \rho_l gz\,.$$

Due to symmetry at the bubble's apex, the pressure difference at the apex origin, in which z = 0, is easily found from Eq. 3-11 to be,

3-14 $$P_v(0) - P_l(0) = \frac{2\sigma}{R_o}$$

in which R_o is the principal radius of curvature at the apex origin.

Subtracting Eq. 3-13 from Eq. 3-12, combining the resulting equation with Eq. 3-11 and Eq. 3-14 and dividing all terms by σ yields the following form of the capillary equation,

3-15 $$\frac{1}{R_1} + \frac{1}{R_2} = \frac{2}{R_o} - \frac{(\rho_l - \rho_v)gz}{\sigma}\,.$$

The above relation holds at any point along the bubble interface at a vertical distance z from the apex origin. The last term on the right hand side appropriately becomes less significant as the point along the profile approaches the apex origin at which time the bubble is more spherical. Conversely, this term becomes more significant as z increases, implying that the hydrostatic pressure becomes more influential near the base of the bubble. Therefore, the magnitude of the last term on the right hand side of Eq. 3-15, representing the buoyancy force to surface tension at that point, dictates bubble shape.

The pressure change that the bubble experiences from hemispherical inception to detachment is evaluated by taking the ratio of the pressure of the incipient bubble at the apex and the pressure of the detaching bubble at the apex. From Eq. 3-11 and referring to Figure 3-3 the pressure in the gas bubble at the apex origin is easily shown to be

3-16 $$P_{v,o} = \frac{2\sigma}{R_o} + P_{atm} + \rho_l g\left(\xi - h_{bub}\right).$$

The ratio of the gas pressure at the apex origin at bubble inception to the gas pressure at the apex origin at bubble detachment is therefore,

3-17 $$\frac{P_{v,hemi}}{P_{v,d}} = \frac{\dfrac{2\sigma}{b} + P_{atm} + \rho_l g\left(\xi - b\right)}{\dfrac{2\sigma}{R_d} + P_{atm} + \rho_l g\left(\xi - h_{bub,d}\right)}.$$

Equation 3-17 dissolves to unity for bubble growth in an infinite body of liquid since $P_{atm} + \rho_l g\xi$ becomes the dominate term of both the denominator and the numerator. This in turn implies that, for ideal gases, the ratio of the gas densities at inception and at departure are of the same order.

The radii of curvature may be defined in terms of x and z as, $R_1 = \left(1+z'^2\right)^{3/2} / z''$ and $R_2 = x\left(1+z'^2\right)^{1/2} / z'$ (Gerlach *et al.*, 2005). Combining with Eq. 3-15 provides the following final form of the capillary equation to which a numerical treatment is applied,

3-18 $$\frac{z''}{\left(1+z'^2\right)^{3/2}}+\frac{z'}{x\left(1+z'^2\right)^{1/2}}=\frac{2}{R_o}-\frac{\left(\rho_l-\rho_v\right)g}{\sigma}z \quad .$$

By multiplying all terms by the cavity radius, the above is conveniently normalized and expressed in terms of the Bond number with the cavity radius as its characteristic length,

3-19 $$Bo_b=\frac{\left(\rho_l-\rho_v\right)gb^2}{\sigma} \quad .$$

The normalized term $\zeta^*=\zeta/b$ and the non-dimensional derivatives are transformed such that $\frac{dz}{dx}=\frac{dz^*}{dx^*}$ and $\frac{d^2z}{dx^2}=\frac{1}{b}\frac{d^2z^*}{dx^{*2}}$ thereby respecting the infinitesimal normalized length scale, $dz^*=dz/b$. Equation 3-18 is expressed in non-dimensional terms,

3-20 $$\frac{z^{*\prime\prime}}{\left(1+z^{*\prime 2}\right)^{3/2}}+\frac{z^{*\prime}}{x^*\left(1+z^{*\prime 2}\right)^{1/2}}=\frac{2}{R_o^*}-Bo_b z^* .$$

The solution to the above is not only dependent on the Laplace length $L_l=\left(\left(\rho_l-\rho_v\right)g/\sigma\right)^{-1/2}$ which would make it only dependent on fluid properties and gravitational field strength, but also on the bubble foot radius. This is due to the fact that for a fixed bubble foot radius there is only one possible value of R_o^* yielding a solution to the above capillary equation. This was highlighted by Gerlach *et al.* (2005) who identified the foot radius and the Laplace constant as the only parameters of which quasi-static bubble shape is dependent. Gerlach *et al.* (2005) did not go on to evaluate the influence that these parameters have on bubble shape.

In this study, the influence of these parameters on quasi-static bubble formation is investigated by identifying the Bond number with characteristic length equal to the fixed bubble foot radius, $Bo_b = L_l^{-2} b^2$, as the dependent parameter. The Bond number has physical meaning in that it is the ratio of a characteristic buoyancy force to surface tension providing insight into the physical mechanism influencing bubble shape.

To this end, Eq. 3-20 is solved numerically assuming that the bubble foot is fixed to the orifice (or nucleation site) perimeter. For this reason, a contact point with the cavity perimeter is used making the solution dependent on the cavity radius. A fixed bubble foot to the perimeter has been observed in numerous adiabatic bubble growth experiments such as those observed in Di Bari & Robinson (2009) and has also been observed in the heat-induced *n*-pentane vapour bubble growth experiments of Siedel *et al.* (2008). Furthermore, as previously stated, ebullition cycle frequency from a uniformly heated plane varies from one nucleation site to another (Incorpera *et al.*, 2007). This implies that the nucleation cavity size influences bubble growth and detachment making cavity radius an appropriate parameter in the bubble profile solution procedure.

An interpolation code, using *Mathematica* software, numerically solves the capillary equation expressed as an ordinary differential equation in which *z* is a function of *x*. The boundary conditions are $z(0)=0$ and $z'(0)=0$ at the apex as illustrated in Figure 3-4. It is important to note that the downward *z* axis of Figure 3-3 is represented as the horizontal axis of Figure 3-4 illustrating that *x* is expressed as a function of *z* in the solution procedure of the forthcoming Eq. 3-23.

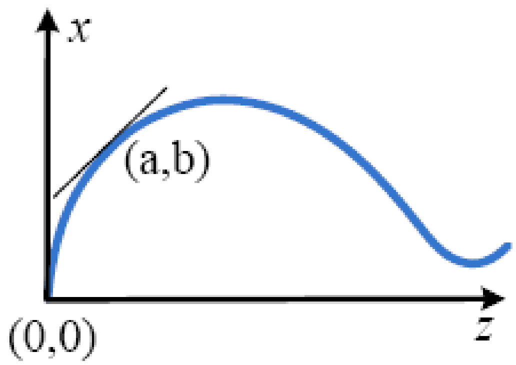

Figure 3-4: Arbitrary bubble profile produced when solving the capillary equation; bubble apex is at (0,0).

The initial condition in the solution procedure is an arbitrary principal radius of curvature at the apex origin, noted R_o. The equation is then solved for *z* by interpolation up until the point on the bubble profile in which $z'=1$. This point is identified as (a,b) in Figure 3-4. Recalling that the solution of Eq. 3-18 yields a solution to *z* in terms of *x*, if the numerical treatment continues beyond the point

(a,b), an error is produced as the slope of the tangent to the curve $\frac{dz}{dx}$ approaches infinity. It is therefore necessary to repeat the numerical treatment of the capillary equation with *x* expressed as a function of *z*. In this way, no error is generated since, with exception to the apex origin $(0,0)$, x is a well defined function of z despite that *z* may not be a well defined function of *x*. To this end, care is taken expressing Eq. 3-18 as a function of *z* rather than *x* by noting that the chain rule and product rule imply, respectively,

3-21 $$z'(x) = \frac{1}{x'(z)}$$

and

3-22 $$z''(x) = -\frac{x''(z)}{\left(x'(z)\right)^3}.$$

Substituting the above into Eq. 3-18 yields the capillary equation of which the solution yields *x* as a function of *z*,

3-23 $$\frac{1}{x\left(1+x'^2\right)^{1/2}} - \frac{x''}{\left(1+x'^2\right)^{3/2}} = \frac{2}{R_o} - \frac{\left(\rho_l - \rho_v\right)g}{\sigma} z.$$

Equation 3-23 is conveniently normalized by multiplying all terms by the cavity radius *b* yielding the following form in which the normalized terms are noted $\zeta^* = \zeta / b$, 3-24 $$\frac{1}{x^*\left(1+x^{*\prime 2}\right)^{1/2}}-\frac{x^{*\prime\prime}}{\left(1+x^{*\prime 2}\right)^{3/2}}=\frac{2}{R_o^*}-Bo_b z^* .$$

The point (a,b) of the numerical treatment of Eq. 3-18 is used as the initial condition for a numerical treatment of Eq. 3-23. Once again, it is noted that this chain of events is necessary since the solution in terms of $z(x)$ is not a proper function beyond (a,b); and $x(z)$ does not yield a solution at the apex origin since the slope of the tangent to the curve $x(z)$ is not well defined at the apex origin. However, the apex origin provides the overall initial condition for the numerical treatment making it necessary to include both Eq. 3-18 and Eq. 3-23 in the solution procedure. For an arbitrary principal radius of curvature at the apex, the solution procedure provides a bubble profile that is not necessarily in contact with the perimeter of the cavity. Through iteration, a single R_o is found yielding one possible profile in which the bubble base is in contact with the cavity perimeter.

The above described procedure solves the capillary equation and yields a bubble profile for a chosen bubble height.

As previously discussed, the significance of the last term on the right hand side of Eq. 3-24 is that the relative magnitude of the buoyancy force to surface tension affects bubble deformation. In particular, the more influence this term has on the relation, the more deformed from spherical the bubble will be. This is quantified in terms of the Bond number and the forthcoming arguments shall show that small Bond numbers yield more spherical bubbles and that large Bond numbers yield more elongated bubbles irrespective of size.

3.4. Benchmarking the Numerical Procedure

The bubble profiles resulting from the described procedure described in section 3.4 are benchmarked to two test cases:

1. Adiabatic quasi-static bubble growth due to gas injection with a constant flow rate in which the bubble foot is fixed to the perimeter of the submerged orifice.

2. Bubble growth due to vaporization within the heat transfer controlled growth regime in which the bubble foot is fixed to the perimeter of the nucleation cavity.

These benchmarking results of the numerical treatment of the capillary equation build on the results of Mori & Baines (2001) and of Gerlach *et al.* (2005). Gerlach *et al.* (2005) compared the resulting profile of the solution to the capillary equation with image processed bubble profiles. The images were taken during bubble formation due to constant injected air at 0.01 ml/min into water through an orifice of radius 0.259 mm with a bubble foot fixed to the orifice perimeter. Mori & Baines (2001) compared the numerical solution of the capillary equation to bubble growth contours due to gas diffusion. In these gas diffusion experiments, bubble formation takes place at an artificial nucleation cavity of radius 1.04 mm in saturated carbonated water. The present investigation builds on these works by testing the ability of the capillary equation to accurately predict the bubble profiles of bubble growth due to vaporization. The heat-transfer controlled bubble growth regime resulting from a constant and low superheat provides the vapour bubble test case in which the vapour bubble growth is most quasi-static (Carey, 1992).

3.4.1. Adiabatic Bubble Growth

The adiabatic bubble growth test case is a result of a collaborative effort with Trinity College Dublin in which Sergio Di Bari performed the following experiments.

Images of bubbles growing from a submerged orifice at the bottom of a small Perspex basin made large enough such that the influence of the side walls can be considered negligible are captured with digital video footage with high spatial and temporal resolution operating up to 1000 frames/second. The top of the vessel is open to the atmosphere and the vessel is partially filled with pre-boiled and distilled water at room temperature to a height of 21 mm above the base. A *Hamilton 1750 CX 500 lw/Stop(1/4-28)* with an inner volume of 500µl syringe is used to issue air at a flow rate controlled by a Kd Scientific Model 200 syringe pump. Air bubbles are injected through an aluminum orifice at a constant volumetric flow rate of 10 ml/h into an otherwise quiescent pool of water at room temperature with an orifice radius of 0.525 mm. The experiment is repeated for an orifice radius of 0.8 mm.

The first of the adiabatic test cases is illustrated in Figure 3-5 showing a comparison of the measured bubble contours from the images captured during bubble formation from a 0.8 mm orifice at 10 ml/h. The numerical simulation deviates slightly from the measured contour near detachment along the wall of the neck. Otherwise the numerical solution is within the uncertainty of the measurements of the processed bubble images in which the uncertainty is set to ± 1 pixel length. The uncertainty in the *x*-direction and the *y*-direction are represented by the height and width of the diamond coordinate point plot marker of the measured bubble profile. It is important to note that the bubble foot is fixed to the orifice perimeter and that the bubble height is measured along the horizontal *y* axis. Furthermore, the bubble is symmetric about the *y* axis due to the absence of cross flow. It is also assumed that any fluid flow induced by bubble formation is negligible due to the quasi-static nature of the growth.

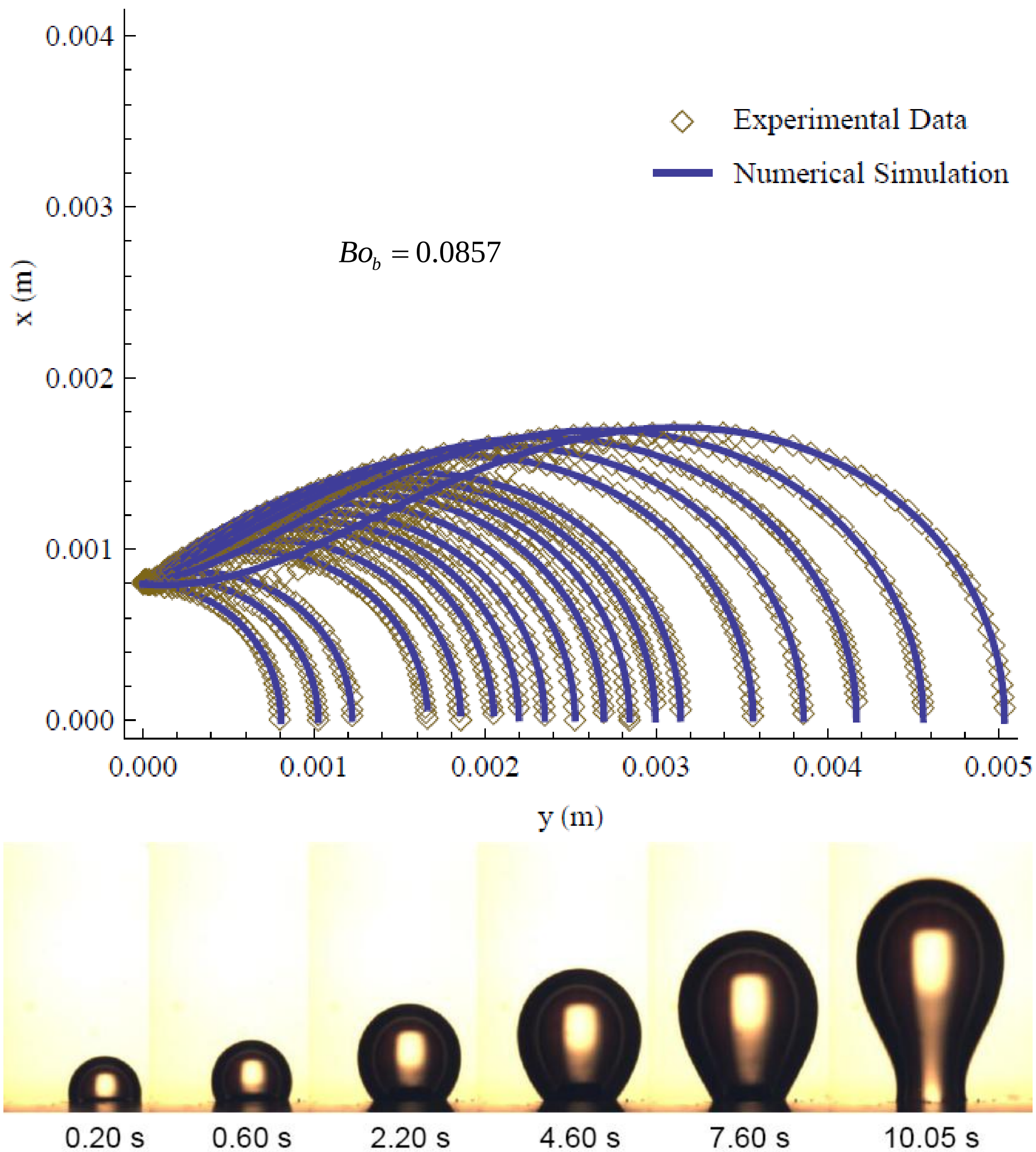

Figure 3-5: Bubble profiles during bubble evolution as predicted by the solution of the capillary equation compared with adiabatic gas injected bubble growth profiles from an orifice of radius 0.8 mm and an injection rate of 10 ml/h.

The second of the adiabatic test cases is illustrated in Figure 3-6 showing a comparison of the measured bubble contours from the images captured during bubble formation from a 0.525 mm orifice at 10 ml/h. Once again, the bubble profile resulting from the numerical simulation only deviates outside of the uncertainty range of ± 1 pixel length along the bubble neck in the last frame prior to departure.

It is important to note that the non-dimensional Bond number with characteristic length equal to the orifice radius is smaller for the more spherical bubbles of Figure 3-6 than the less spherical profiles of Figure 3-5. This phenomenon is investigated thoroughly in this study.

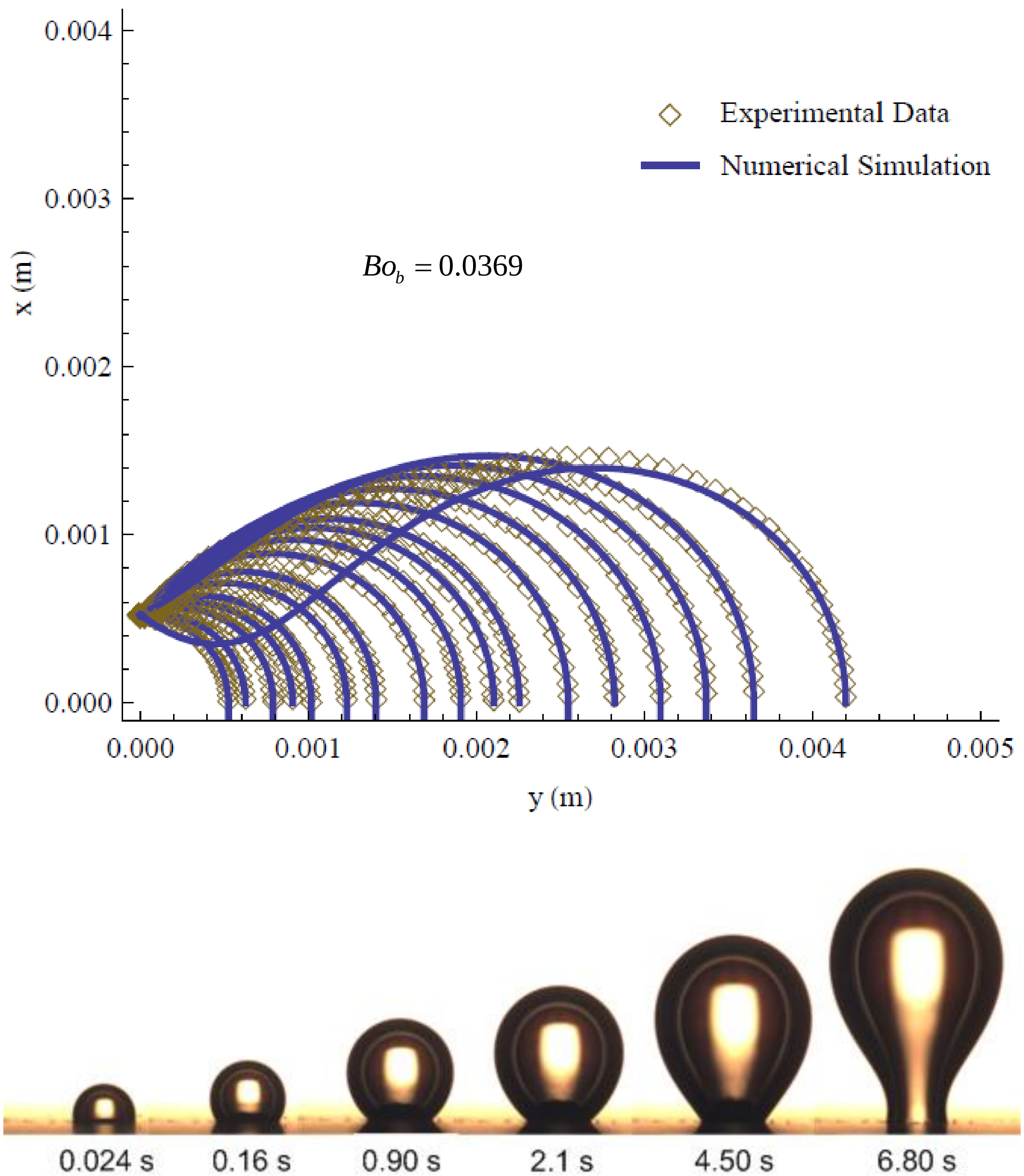

Figure 3-6: Bubble profiles during bubble evolution as predicted by the solution of the capillary equation compared with adiabatic gas injected bubble growth profiles from an orifice of radius 0.525mm and an injection rate of 10 ml/h.

3.4.2. Bubble Growth due to Vaporization

The bubble growth due to vaporization test case is a result of a collaborative effort with INSA Lyon in which Samuel Siedel performed the following experiments.

Bubble growth from a copper heated plate is filmed with a *Photon Fastcam 1024 PCI* high speed camera recording images of single bubble growth up to 3000 fps. The plate is polished in order to minimize nucleation near the 90 μm radius artificial nucleation site. Also, the plate is made 40 μm thin favouring a radial temperature drop and thereby preventing nucleation on the edges of the plate. The working fluid is degassed *n*-pentane contained in a tank of dimensions 250 × 250 × 180 mm^3. Due to the high thermal diffusivity of copper (approximately 1.1×10^{-4} m^2/s) and the small size of the growing bubble (0.5 mm maximum radius) in comparison to the 2.5 mm radius copper pin on which it sits, less than 1% of the heat flux to the bubble from the heated plate is of the form of latent heat transfer (Siedel *et al*., 2008). For this reason, the local heat flux variations are deemed negligible and the wall temperature is assumed to be constant and homogeneous favouring the heat-transfer controlled bubble growth regime for low wall superheats (Carey, 1992). The result is bubble formation due to vaporization with a bubble foot fixed to the perimeter of the nucleation cavity. The experiment is repeated for constant wall superheats of 2.1 K and 4.7 K in which the saturation temperature of *n*-pentane is 35.7 ^{o}C at 1 bar.

Although the bubble profile resulting from the numerical treatment of the capillary equation has been validated for gas injection and gas diffusion bubble formation scenarios by Gerlach *et al.* (2005) and Mori & Baines (2001) respectively, the numerical treatment of the capillary equation has not been, to the best of the author's knowledge, validated for bubble formation due to vaporization as it is in the forthcoming result.

With exception to the neck profiles in the final frames, Figure 3-7 and Figure 3-8 illustrate that the bubble profiles resulting from the numerical treatment of the capillary equation are within the ± 1 pixel uncertainty with the experimentally observed profiles of the heat-induced vapour bubble formations resulting from the constant wall superheats of 4.7 K and 2.1 K.

It is important to note that the foot of the bubble base remains fixed to the nucleation site allowing the model to produce a unique solution for each bubble profile. It is also noted that the Bond number with characteristic length equal to the nucleation site radius for both illustrations is the same since only one working fluid and one cavity are considered. Highlighted in the forthcoming sections of this document is that similar Bond numbers, despite varying working conditions, provide bubbles of similar shape.

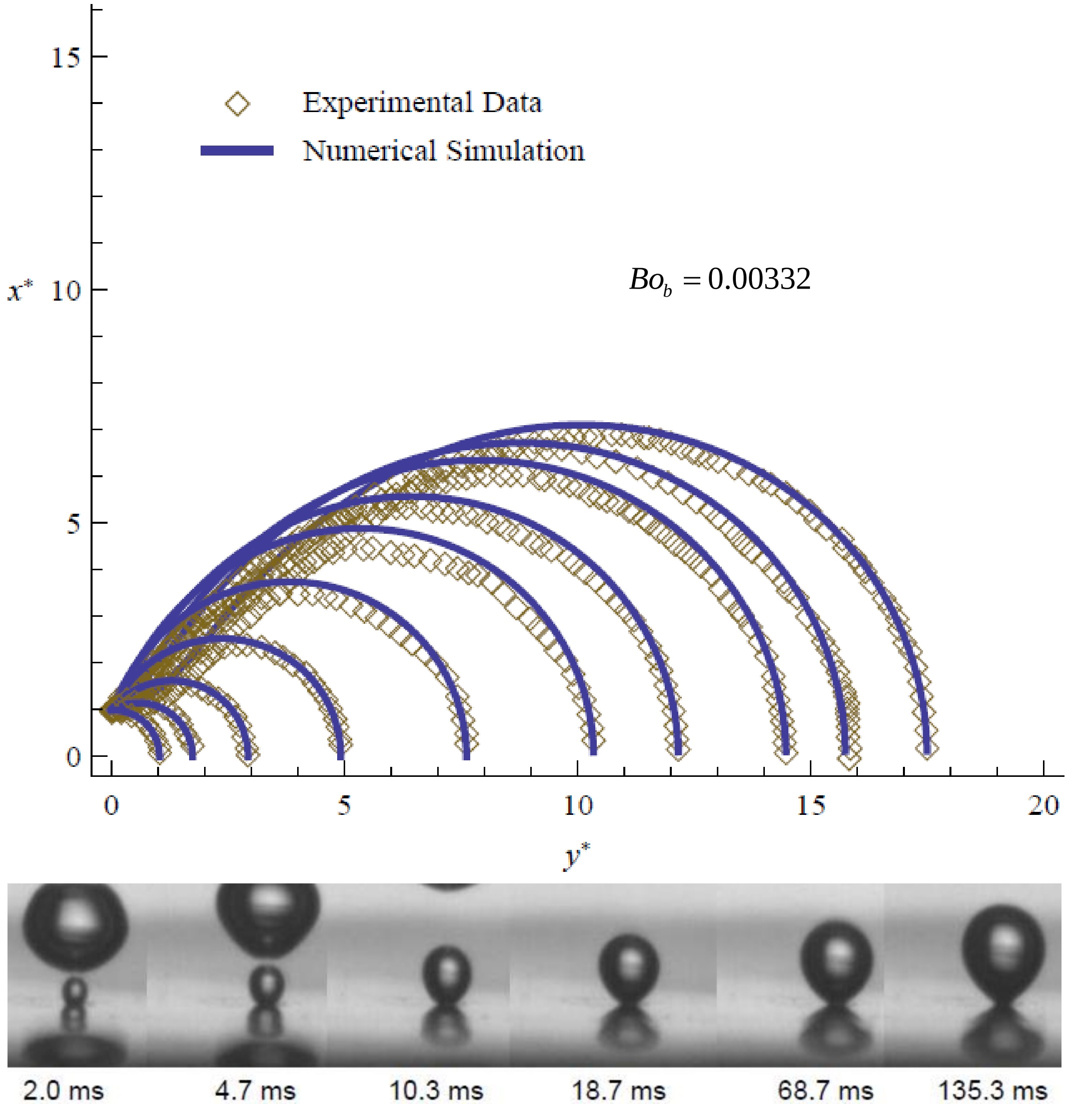

Figure 3-7: Bubble profile during bubble evolution as predicted by the solution of the capillary equation compared with bubble growth due to vaporization profiles from a nucleation site radius of 90 μm and a wall superheat of 4.7 K.

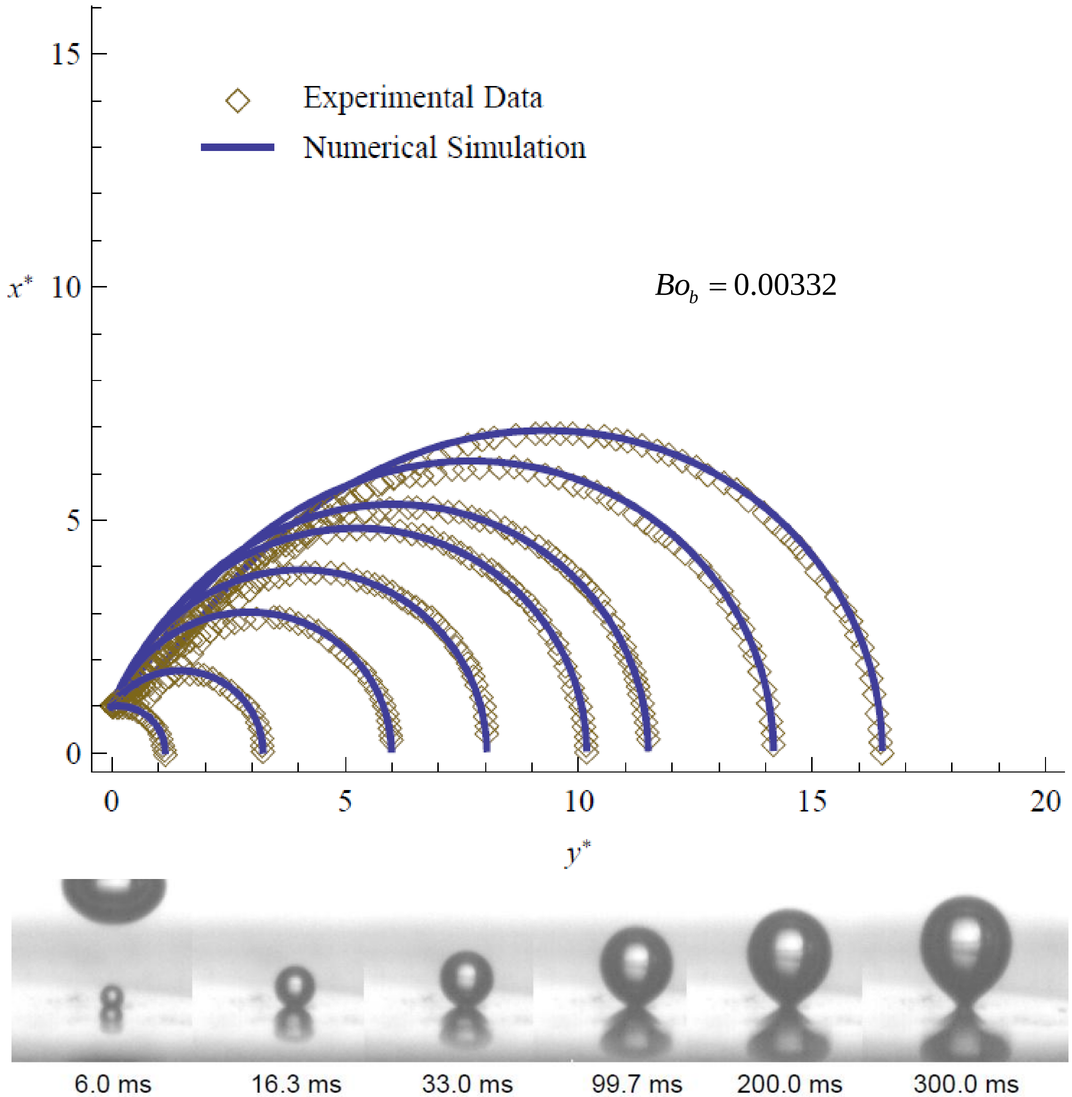

Figure 3-8: Bubble profiles during bubble evolution as predicted by the solution of the capillary equation compared with bubble growth due to vaporization profiles from a nucleation site radius of 90 μm and a wall superheat of 2.1 K.

3.5. Contact angle analysis

For any liquid, gas and substrate combination at equilibrium, a surface tension balance exists that is dependent on the liquid's affinity to the solid. This phenomenon is known as the wettability of the liquid for a substrate and is quantified by the Young contact angle, noted α_Y, illustrated in Figure 3-9.

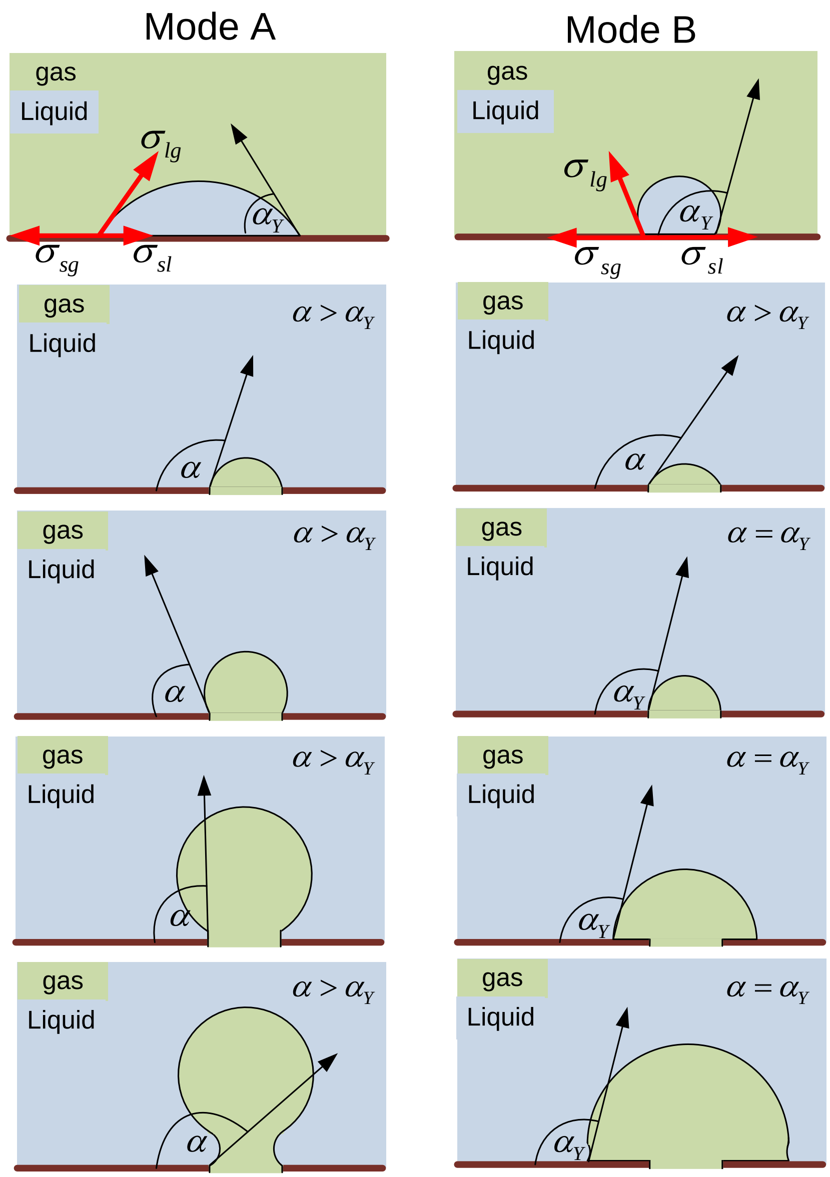

Figure 3-9: (*Left*) Mode A gas/vapour bubble growth in a wetting liquid. (*Right*) Mode B: gas/vapour bubble growth in a non-wetting liquid.

In the case of gas/vapour bubble growth issuing from an orifice, there are two modes of growth possible relative to the contact angle: Mode A and Mode B (Gerlach *et al.*, 2005).

In Mode A, the Young contact angle (contact angle at equilibrium) remains inferior to the instantaneous contact angle throughout the growth of the bubble. This is attributed to the liquids strong affinity for the surface and as such the bubble foot is prevented from expanding outwards.

Conversely, in Mode B, the liquid has a weak affinity for the surface and it yields to the gas bubble's expansion. In this mode, during the bubble growth cycle, the instantaneous contact angle equals the Young contact angle and the bubble foot expands to a radius greater than that of the orifice.

In this study, Mode A bubble growth is considered. For this reason, the benchmark experiments use liquids and substrates in which the wettebility is such that the bubble foot remains fixed to the orifice. In this mode, the contact angle varies throughout the growth cycle due to the fixed foot radius. In particular, the contact angle is large as the bubble emerges from the orifice decreasing during mid growth and increasing near detachment. A comparison of the measured contact angles with the numerically generated contact angles for the given conditions detailed in section 3.4.1 is provided in Figure 3-10 and Figure 3-11.

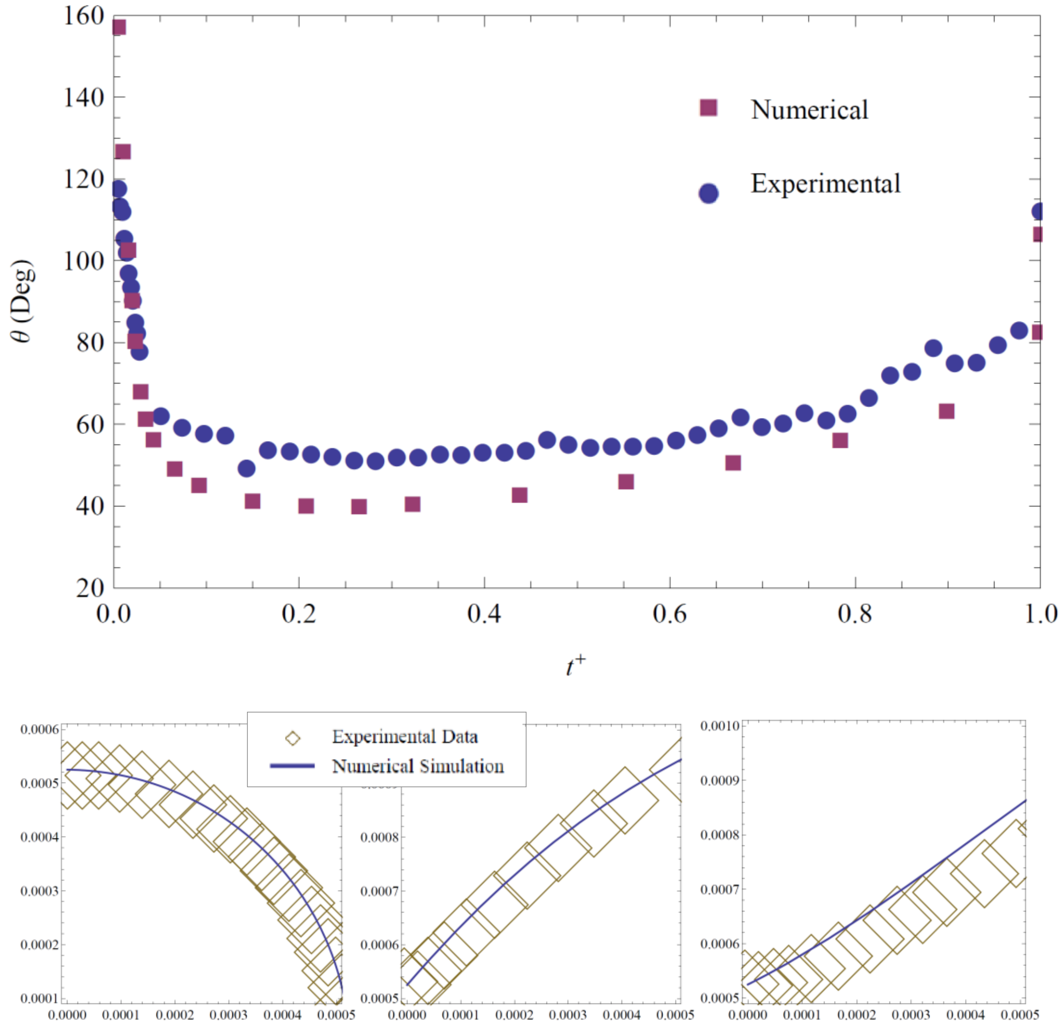

Figure 3-10: (*Top*) Bubble contact angle evolution as predicted by the solution of the capillary equation compared with adiabatic gas injected bubble measurements from an orifice of radius 0.525 mm and an injection rate of 10 ml/h. (*Bottom*) Near orifice comparison of numerical and experimental results.

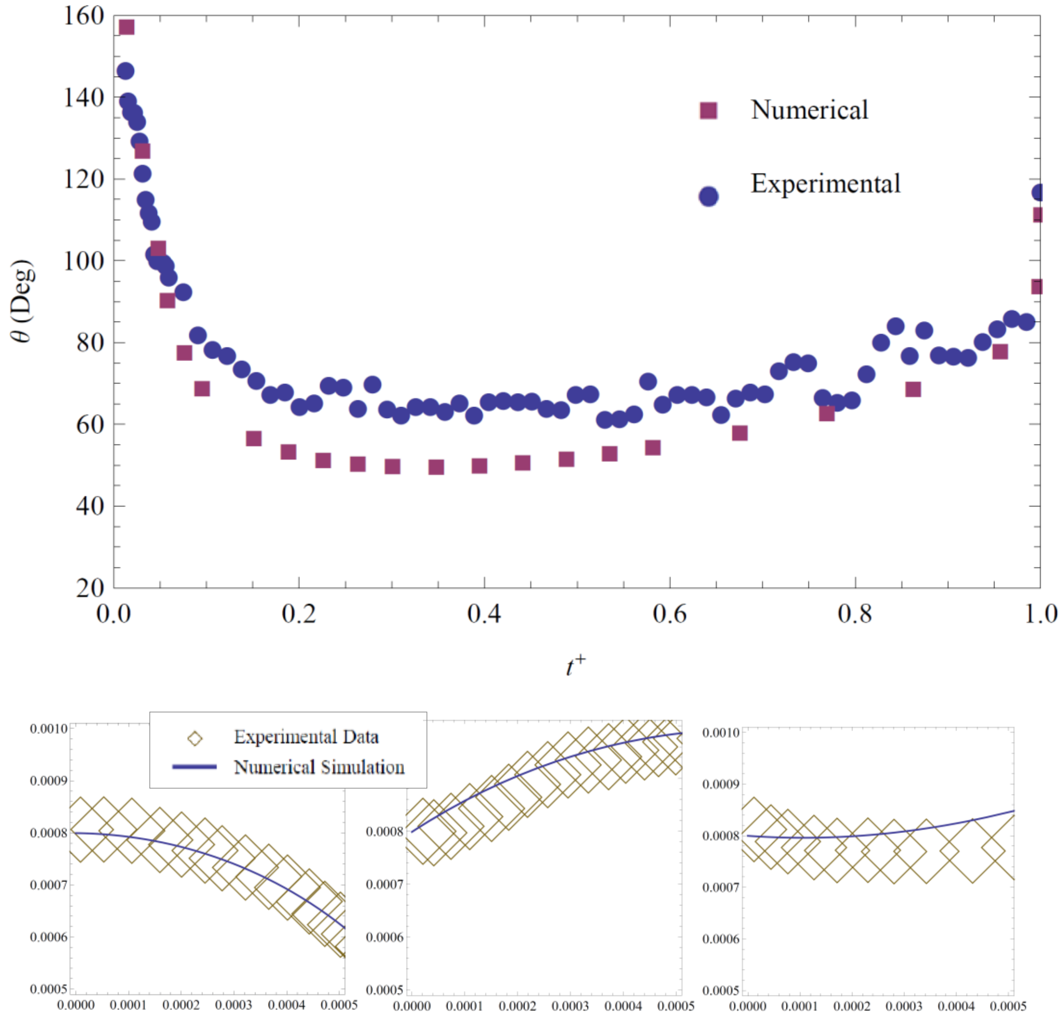

Figure 3-11: (*Top*) Bubble contact angle evolution as predicted by the solution of the capillary equation compared with adiabatic gas injected bubble measurements from an orifice of radius 0.8 mm and an injection rate of 10 ml/h. (*Bottom*) Near orifice comparison of numerical and experimental results.

3.6. Bubble Volume, Area and Centre of Gravity from Bubble Profile

In this study, a purpose built *Mathematica* code is written in order to define the coordinates of the bubble contour enabling the measurement of the bubble volume, surface area and centre of gravity. The bubble profiles to which the code is applied are the result of the numerical simulation of the capillary equation and the result of image processing of captured bubble growth images. *Mathematica* software is used to identify a finite number of coordinate points of the vapour-liquid interface detailed in Appendix 7.2. This code approximates the bubble volume, bubble vapour-liquid surface area and the bubble centre of gravity by defining frustum cones as illustrated in Figure 3-12. The following describes the procedure in detail.

Two arbitrary points on the bubble contour are identified as $\left(x_i, y_i\right)$ and $\left(x_{i+1}, y_{i+1}\right)$ representing two sequential points in a series of points defining the bubble profile.

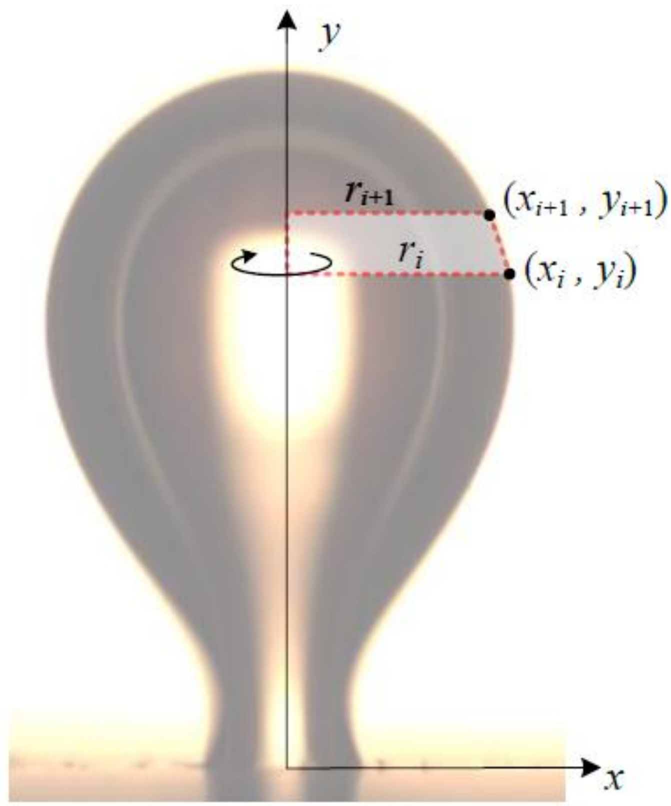

Figure 3-12: Coordinate system used in the code for approximating the bubble volume, vapour-liquid surface area and centre of gravity. Background bubble image captured by Sergio Di Bari.

A rotation about the vertical axis of a lateral section identified by two sequential bubble contour points defines a frustum cone. This conical frustum is illustrated in Figure 3-13. All necessary information in solving for the conical frustum's surface area, volume and centre of gravity are deduced from two coordinate points (x_{i+1}, y_{i+1}) and (x_i, y_i).

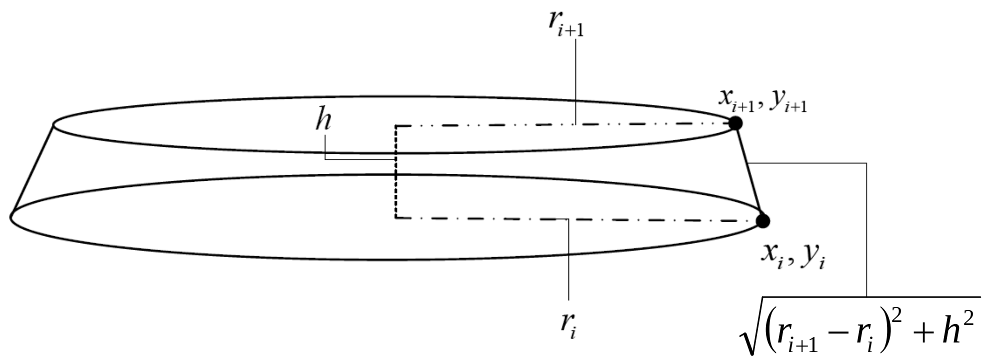

Figure 3-13: Frustum cone resulting from the coordinate points identified along the contour of the bubble.

The height of the cone, the base radius and the top radius are defined in terms of the point coordinates as, respectively,

3-25
$$\begin{aligned} h &= y_{i+1} - y_i \\ r_i &= x_i \\ r_{i+1} &= x_{i+1} \end{aligned} .$$

The liquid-vapour area is approximated by considering the lateral area of an interface segment of two adjacent coordinate points and integrating about the central vertical axis. This yields the area of the conical frustum,

3-26
$$A_{frustum} = \pi(r_{i+1} + r_i)\sqrt{(r_{i+1} - r_i)^2 + h^2} .$$

The sum of Eq. 3-26 over all interface coordinate points represents the sum of the generated conical frustum surface areas and thus yields the total liquid-vapour surface area of the bubble, 3-27 $$A_{bub} = \pi \sum_{i=1}^{n-1} \left(x_{i+1} + x_i \right) \sqrt{(x_i - x_{i+1})^2 + (y_{i+1} - y_i)^2} \, .$$

Similarly, the volume of the conical frustum illustrated in Figure 3-13 is the area of the segment integrated about the central vertical axis,

3-28 $$V_{frustum} = \frac{1}{3} \pi h \left(r_{i+1}^2 + r_{i+1} r_i + r_i^2 \right).$$

The sum of Eq. 3-28 over all interface coordinate points represents the sum of the generated conical frustum volumes and thus yields the total volume of the bubble,

3-29 $$V_{bub} = \frac{1}{3} \pi \sum_{i=1}^{n-1} \left(y_{i+1} - y_i \right) \left(x_{i+1}^2 + x_{i+1} x_i + x_i^2 \right) .$$

By the definition of the centre of mass, the centre of gravity of the conical frustum illustrated in Figure 3-13 is found by dividing the weighted integral of *y* over the frustum yielding a centre of gravity along the vertical axis,

3-30 $$\begin{aligned} CoG_{frustum} &= \frac{1}{V_{frustum}} \int_0^h \pi \left(r_i - \left(r_{i+1} - r_i \right) \frac{y}{h} \right)^2 y dy \\ &= \frac{h \left(r_{i+1}^2 + 2 r_{i+1} r_i + 3 r_i^2 \right)}{4 \left(r_{i+1}^2 + r_{i+1} r_i + r_i^2 \right)} \end{aligned} .$$

The sum of the above over all interface coordinate points represents the sum of the generated conical frustum centre of gravity vertical positions and thus yields the centre of gravity of the bubble,

$$CoG_{bubble} = \sum_{i=1}^{n-1} \left(y_{i+1} - y_i \right) \frac{\left(x_{i+1}^2 + 2x_{i+1}x_i + 3x_i^2 \right)}{4\left(x_{i+1}^2 + x_{i+1}x_i + x_i^2 \right)} . \tag{3-31}$$

It is noted that Equation 3-31 is in fact the calculation of the centre of mass of the bubble. However, in a uniform gravitational field the above calculation yields the mean location of the gravitational force acting on the bubble. All gravitational fields in this document shall be considered constant over the mass distribution of the bubble making the terms *Centre of Mass* and *Centre of Gravity* interchangeable (Serway, 1982).

For each bubble profile obtained throughout this chapter, either through numerical simulation or through image processing of captured bubble images, the frustum calculated bubble volume and bubble liquid-vapour surface area shall be used to calculate the bubble degree of sphericity and the bubble degree of Modified sphericity defined in sections 3.2 and 3.7 respectively.

3.7. Numerical Simulations: Results and Discussion

Having benchmarked the numerical procedure in its capacity to accurately predict bubble contours during bubble formation, numerical simulations are run in an effort to isolate the physical mechanism causing a bubble’s shape to deviate from a sphericity of unity. The following table presents the conditions for which the numerical simulations in this section are run and their resulting Bond number.

Table 3-1 : Bond number for conditions tested

Cavity radius b (mm)	Gravitational Constant g (m/s²)	$Bo_b = \frac{(\rho_l - \rho_v) g b^2}{\sigma}$
1	0.1	0.00137
1	1	0.0137
1	2	0.0273
1	9.807	0.134
1	20	0.273
1	40	0.546
0.1	9.807	0.00134
0.25	9.807	0.00837
0.5	9.807	0.0335
1.5	9.807	0.134
2.25	9.807	0.678

3.7.1. Numerical Solution Bubble Growth Cycle

The numerical treatment of the capillary equation is used to solve for the contour of air bubble growth in water with a fixed bubble foot radius at terrestrial conditions. Numerical computations are run for increasingly large bubbles until no solution to the capillary equation is possible for the specified bubble foot radius. This ultimate frame in the numerical simulation's bubble growth cycle is the predicted bubble growth profile at detachment for this model (Gerlach *et al.*, 2005). This is illustrated in the Figure 3-14 which shows the family of solutions that is generated by the capillary equation. One solution can be distinguished by the contact angle of the foot radius. In the case of Mode A bubble growth, the bubble foot stays fixed to the orifice perimeter and therefore the unique solution within the family is chosen as that which the bubble foot radius is equal to the cavity radius.

Within the family of solutions to the capillary equation there exists a solution with a minimal inner foot radius. This solution represents the minimal contact with the surface that is capable of contouring the buoyancy of the bubble in order to keep the bubble fixed its cavity. As the bubble grows, the buoyancy term becomes more prominent and the minimum foot radius required to counter the buoyancy increases. For Mode A bubble growth, when the minimum foot radius in the family of solutions is equal to the cavity radius, the detachment frame has been attained and any length step forward will yield a family of solutions in which the minimum foot radius is larger than the cavity radius meaning that the bubble has detached.

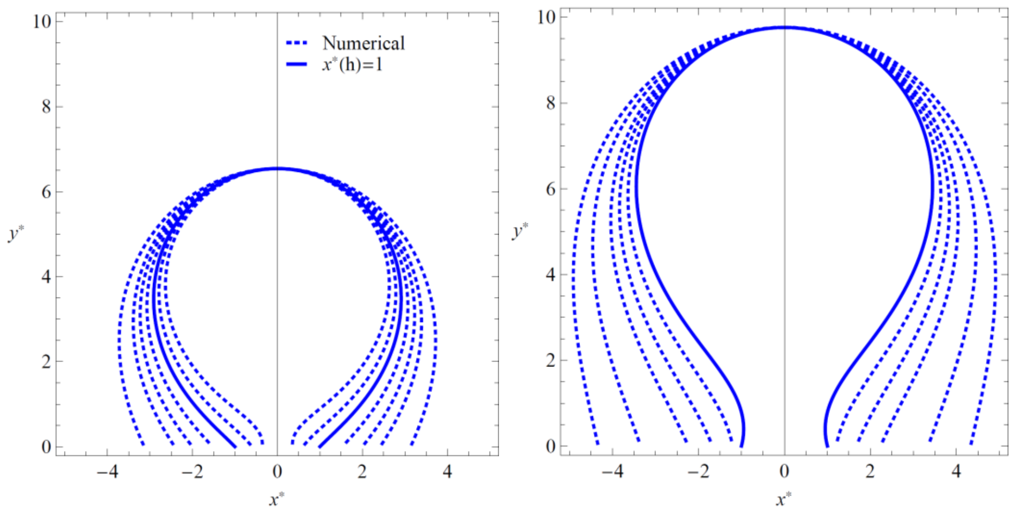

Figure 3-14: (*Left*) Family of solutions to the capillary equation for a given height prior to detachment. (*Right*) Family of solutions to the capillary equation at detachment.

To illustrate this, in Figure 3-15, the last frame profile on the numerical treatment is compared with the measured profiles from the adiabatic bubble growth test cases near detachment. In addition, Figure 3-16 compares the last frame profile of the numerical treatment with the measured profiles from the diabatic vapour bubble growth test cases near detachment.

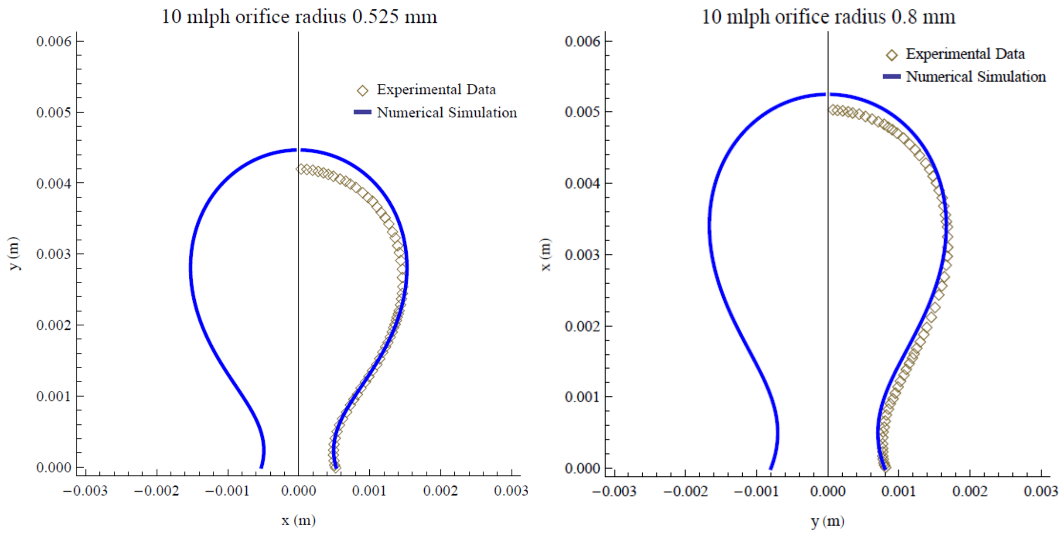

Figure 3-15: Measurements from the last captured image prior to detachment compared with the largest bubble profile produced from the numerical computation of the Capillary equation for a gas injected bubble with a foot radius of 0.525 mm *(Left)* and for a gas injected bubble with a foot radius of 0.8 mm *(Right)*.

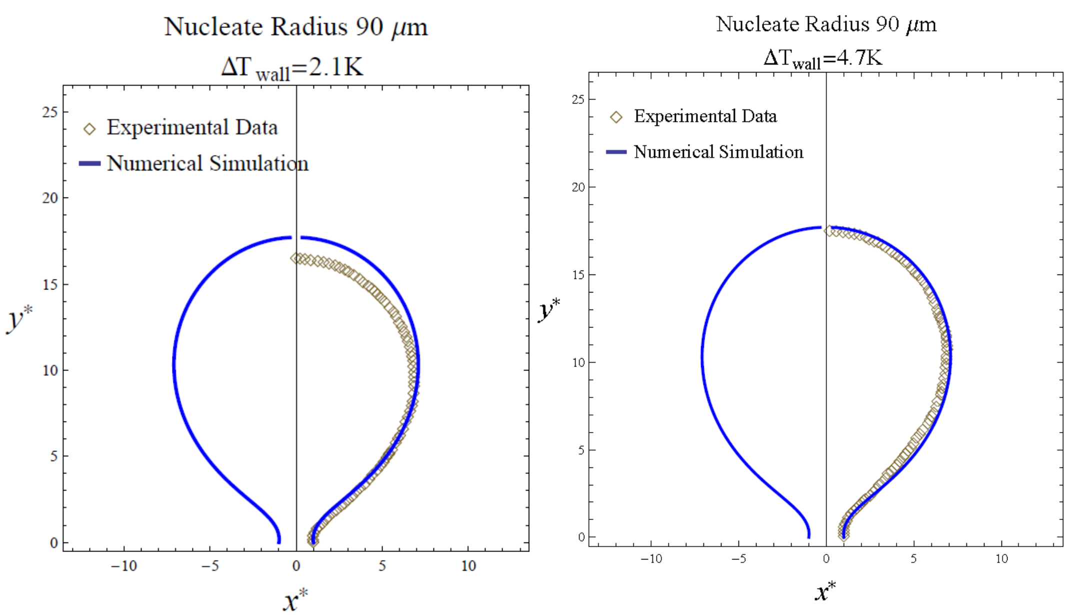

Figure 3-16: Measurements from the last captured image prior to detachment compared with the largest bubble profile produced from the numerical computation of the Capillary equation for an *n*-pentane vapour bubble from a nucleation cavity of 90 µm on a heated plane with superheat 2.1 K *(Left)* and 4.7 K *(Right)*.

This detachment postulate implies that running the simulations for bubble profiles that increase in size until no computational solution is possible provides the bubble profiles for the entire bubble growth cycle where the no solution length step implies detachment.

In this way, the bubble growth cycle for the numerically generated bubble profiles is defined and normalized by defining *Growth Cycle** as the ratio of the numerically generated bubble height, noted h_{bub}, to its height near detachment, noted $h_{bub;d}$, yielding the following definition,

3-32 $$Growth\,Cycle^{*} = \frac{h_{bub}}{h_{bub;d}}.$$

The growth cycle is therefore complete and the bubble is near detachment once *Growth Cycle** attains unity. Recalling that the Capillary equation is not dependent on time, it is noted that *Growth Cycle** is a non-dimensional height scale rather than a time scale.

3.7.2. Bubble Growth Cycle for Terrestrial Gravity

A sample of the solutions to the capillary equation providing the bubble profiles throughout the bubble growth cycle is illustrated in Figure 3-17. Air bubble growth in water is simulated for terrestrial conditions. The simulations are repeated for increasing bubble foot radius (ranging from 0.1 mm to 2.25 mm), fixed fluid properties and terrestrial gravitational field strength.

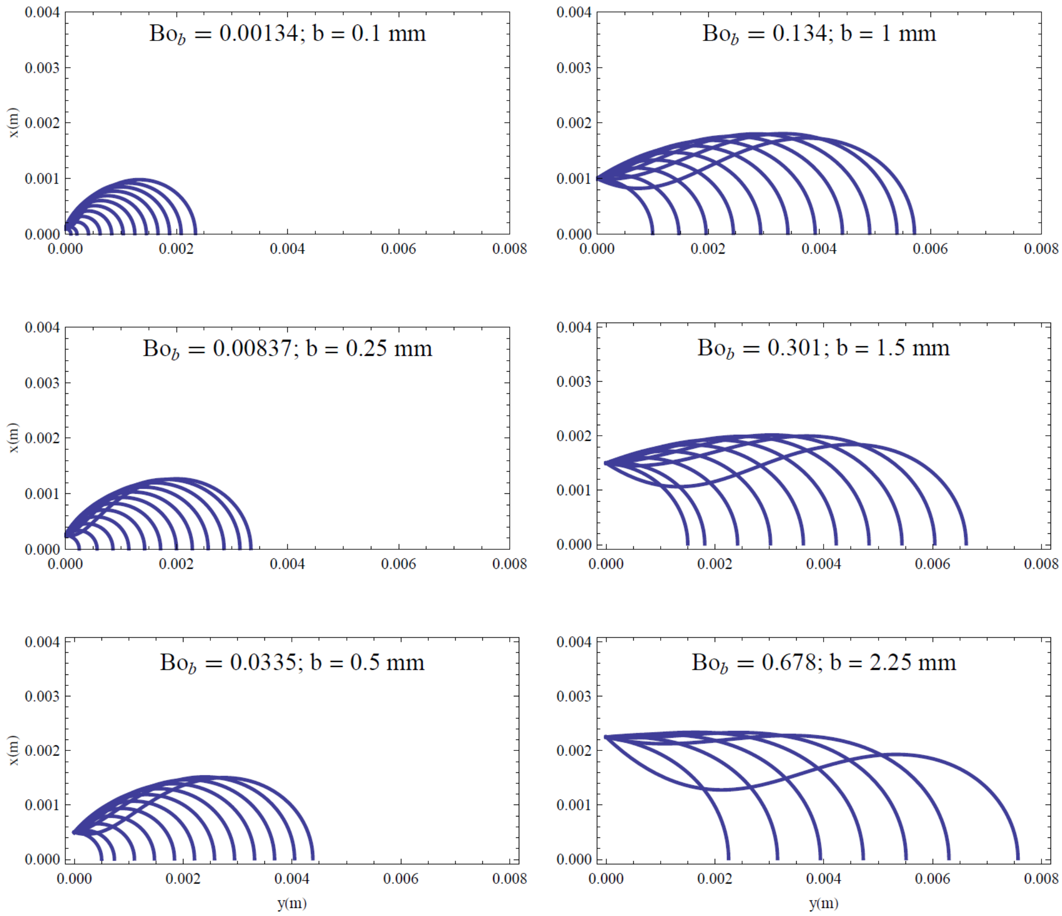

Figure 3-17 : Bubble profile evolution with Bond number varying with respect to the bubble foot radius.

Figure 3-17 shows that an increase in Bond number corresponds with a decrease in the spherical shape of the bubble. In particular, for constant fluid properties and terrestrial gravitational conditions, an increase in Bond number is a result of an increase in the orifice radius from which the bubble is growing.

For this particular scenario in which the gravitational field strength is constant, an increase in bubble foot radius implies larger bubbles growing taller thereby experiencing weakened hydrostatic pressure and thus being more influenced by the force of buoyancy. This causes them to elongate and to deviate from a sphericity of unity. The fixed gravitational field strength with increasing bubble foot radius increases the Bond number implying that larger Bond numbers yield less spherical bubbles.

3.7.3. Bubble Growth Cycle for Increasing Gravitational Constant

Numerical computations are run generating bubble contours during bubble formation with a fixed foot radius of 1mm and fixed fluid properties in which air is the gas make up of the bubble and water is the surrounding liquid. The simulations are repeated for increasing values of the gravitational constant ranging from 0.1 m/s² to 40 m/s².

In this series of simulations, the bubble foot radius is constant and the gravitational field strength is increased thereby increasing the Bond number.

Figure 3-18 illustrates the results showing that, in keeping with the previous section's results, a smaller Bond number, in this case resulting from smaller gravitational field strength, yields a more spherical bubble.

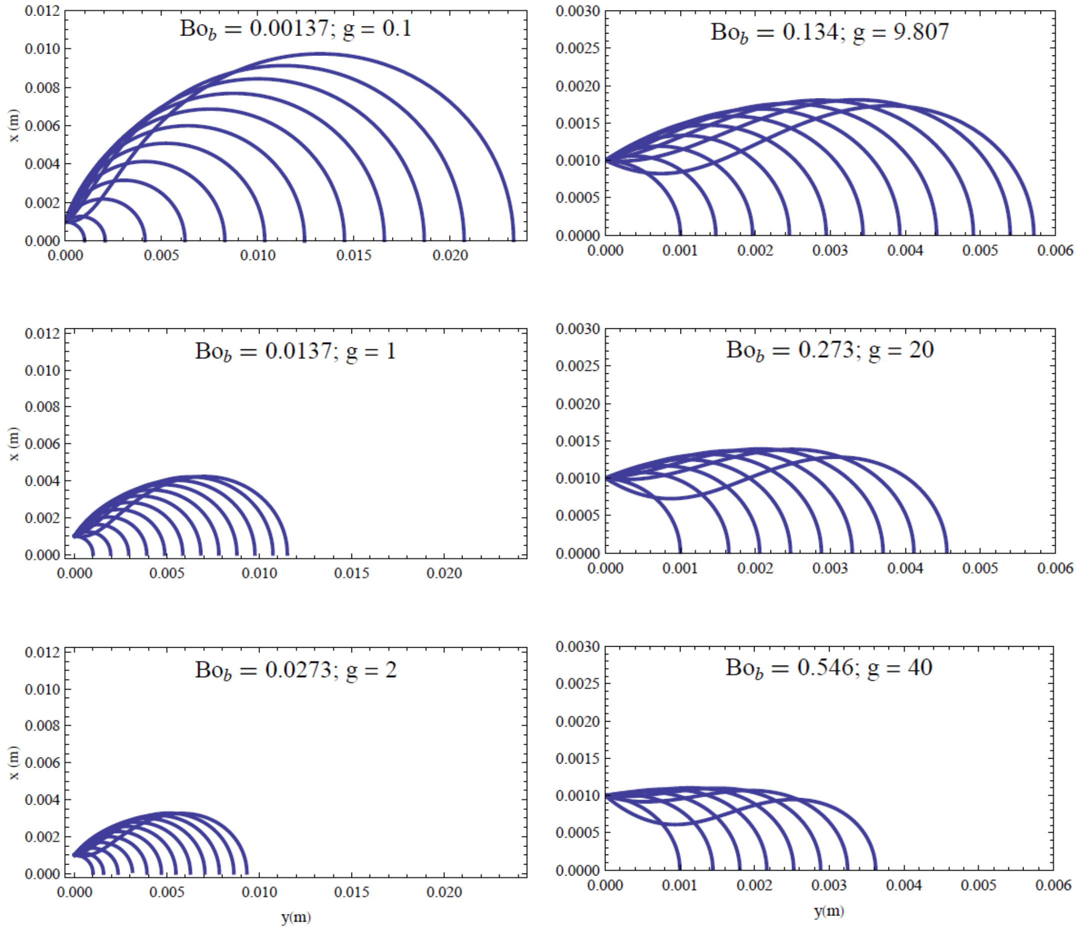

Figure 3-18 : Bubble profile evolution for a fixed foot radius of 1mm and a Bond number varying with respect to the gravitational constant. Note the scale difference in the two columns.

The results of the simulations of Figure 3-18 and the simulations of Figure 3-17 can be summarized for constant fluid properties in the following table in which the terms *small*, *large, spherical* and *non-spherical* are used rather loosely. These characteristics will be quantified more precisely in the following sections in terms of the bubble degree of sphericity relative to the Bond number.

Table 3-2 : Bubble characteristics relative to Bond number				
Parameter	Figure 3-17 results		Figure 3-18 results	
g	Terrestrial	Terrestrial	Small	Large
b	Small	Large	1 mm	1 mm
$Bo_b = \frac{g(\rho_l - \rho_v)}{\sigma}$	Small	Large	Small	Large
Bubble Profile	Spherical	Non-spherical	Spherical	Non-spherical
Bubble Volume	Small	Large	Large	Small

The commonality between the simulations of Figure 3-18 and the simulations of Figure 3-17, as highlighted in the above table, is that a decrease in Bond number implies an increase in bubble spherical shape tendencies implying that the bubble shape is dictated by the Bond number $Bo_b = \frac{g(\rho_l - \rho_v)b^2}{\sigma}$.

For strictly terrestrial conditions, the bubble volume appears to be only dependent on the Bond number as was observed by Mori & Baines (2001). However, a small Bond number resulting from a small gravitational constant yields a much larger bubble than the same Bond number due to a small bubble foot radius. The bubble volume relative to the Bond number is investigated in the following section.

3.7.4. Bubble Volume Evolution

The bubble's volume throughout the bubble growth cycle with respect to the Bond number is investigated. In what follows, the growth cycle of the numerically simulated bubble profile is generated up until the computations no longer provide a solution to the capillary equation; refer to section 0.

In Figure 3-19 the bubble volume evolution resulting from the numerically generated bubble profiles is illustrated for a fixed bubble foot radius of 1 mm in which the Bond number is varied by varying the gravitational constant only. The fluid properties are that of air in water. Figure 3-20 compares the bubble profiles near detachment for decreasing Bond numbers due to decreasing gravitational field strengths. The results show that for weaker gravitational field strengths, corresponding to smaller Bond numbers, the bubble grows more spherical than for strong gravitational field strengths corresponding to larger Bond numbers.

This result can be attributed to the fact that for weaker gravitational forces, bubble detachment is delayed due to weakened buoyancy allowing the bubble to grow larger; the weakened buoyancy does not cause a significant bubble elongation that would otherwise deform the bubble.

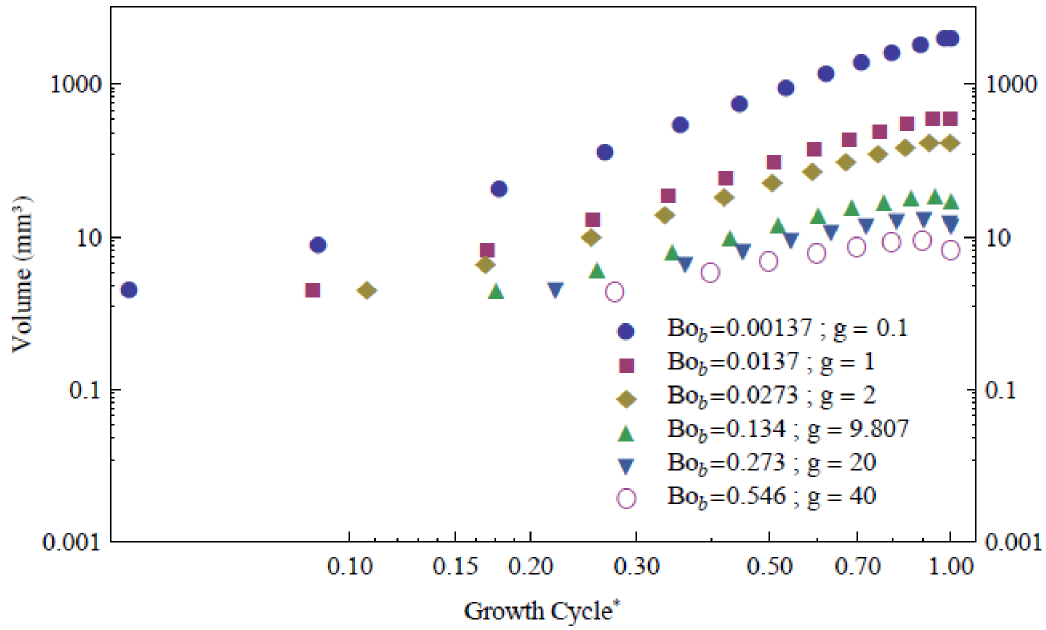

Figure 3-19 : Bubble volume evolution from numerical simulations for a fixed foot radius of 1mm and a Bond number varying with respect to the gravitational constant.

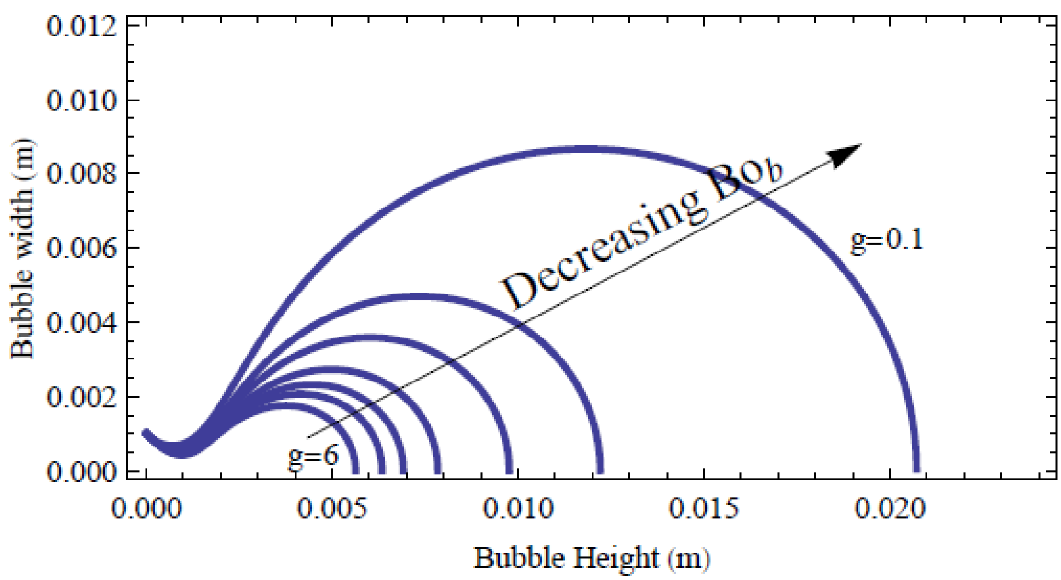

Figure 3-20 : Bubble profile near detachment for a fixed foot radius of 1mm and a Bond number decreasing due to a decreasing gravitational field strength: 6, 4, 3, 2, 1, 0.5 and 0.1 (m/s²).

In Figure 3-21, the bubble volume evolution resulting from the numerically generated bubble profiles is illustrated for terrestrial conditions in which the Bond number is varied by varying the bubble foot radius only. The fluid properties are that of air in water. Figure 3-22 compares the bubble profiles near detachment for decreasing Bond numbers due to decreasing bubble foot radii.

The results show that for larger bubble foot radii, as a result of a larger orifice or a larger nucleation site, and corresponding to larger Bond numbers, the bubble grows to a larger volume with a less spherical shape than for smaller bubble foot radii corresponding to smaller Bond numbers.

This result can be attributed to the fact that for terrestrial conditions, a larger orifice (or nucleation site) yields a larger hemispherical bubble than a smaller cavity. The larger bubble grows and experiences a smaller hydrostatic pressure than a smaller bubble since the former's apex is less submerged. This effect subsequently elongates the larger bubble since the buoyancy force is relatively strong. Conversely, bubbles growing from smaller cavities with smaller Bond numbers experience a weakened capillary force due to the shortened cavity perimeter. This implies that for a smaller cavity, the capillary force is not sufficiently strong to counter the buoyancy force that is necessary for bubble deformation and that the bubble will detach prior to significant bubble deformation; this also implies that the bubble will detach at a smaller volume than for larger cavity radii. It is important to note that, once again, for the smaller Bond numbers, the bubble profiles are more spherical. The Bond number dictates shape but not volume.

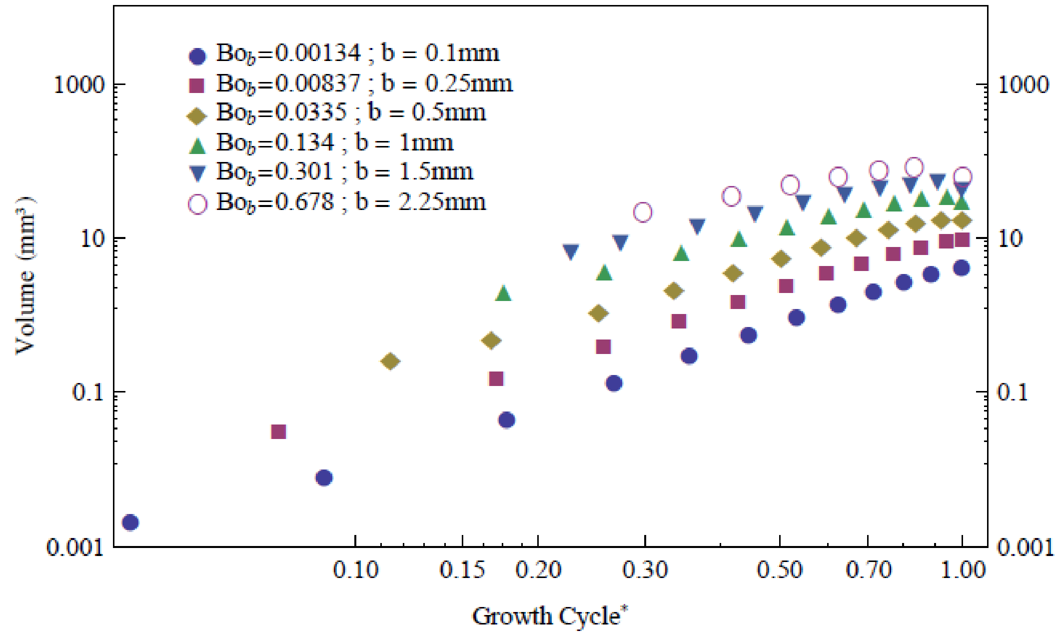

Figure 3-21 : Bubble volume evolution from numerical simulations at terrestrial conditions and a Bond number varying with respect to bubble foot radius.

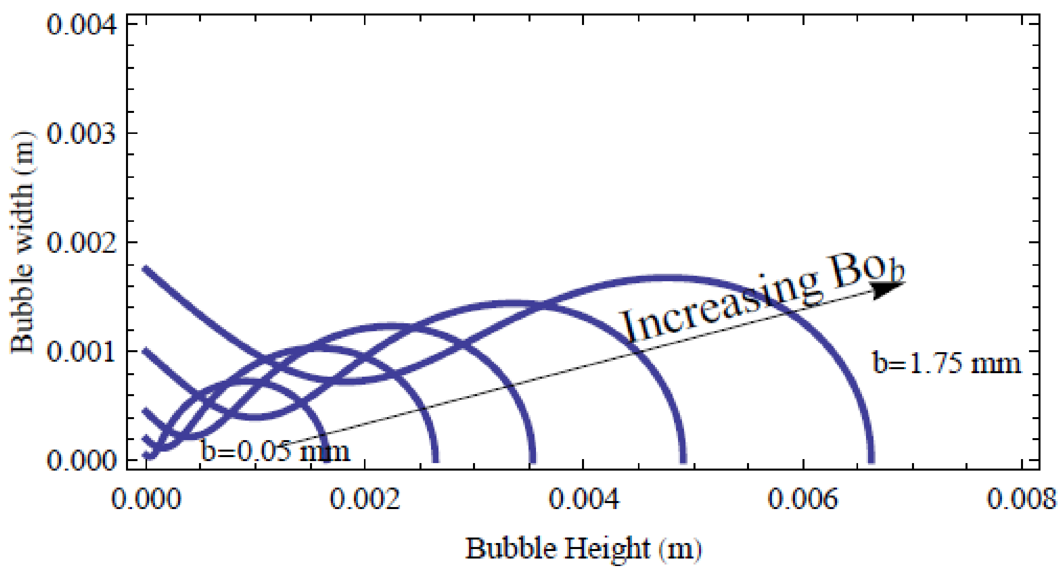

Figure 3-22 : Bubble profile near detachment for terrestrial conditions and a Bond number increasing due to an increasing cavity radius: 0.05, 0.2, 0.4, 1.0 and 1.75 (mm).

In general, Figure 3-19 to Figure 3-22 compare bubble volume, during bubble growth evolution and near detachment, indicating the Bond number Bo_b for the given conditions. It is shown that a decrease in Bo_b implies a more spherical bubble shape irrespective of size.

3.7.5. Bubble Vapour-Liquid Surface Area Evolution

In order to be able to quantify the influence of the Bond number on bubble shape, the bubble's degree of sphericity is investigated. To this end, the bubble vapour-liquid surface area generated from the numerically simulated bubble profiles is evaluated.

In Figure 3-23, the vapour-liquid surface area evolution resulting from the numerically generated bubble profiles is illustrated for a fixed bubble foot radius of 1 mm in which the Bond number is varied by varying the gravitational constant only. The fluid properties are that of air in water.

In Figure 3-24, the vapour-liquid surface area evolution resulting from the numerically generated bubble profiles is illustrated for terrestrial conditions in which the Bond number is varied by varying the bubble foot radius only. The fluid properties are that of air in water.

The results show similar trends as to the volume growth curves.

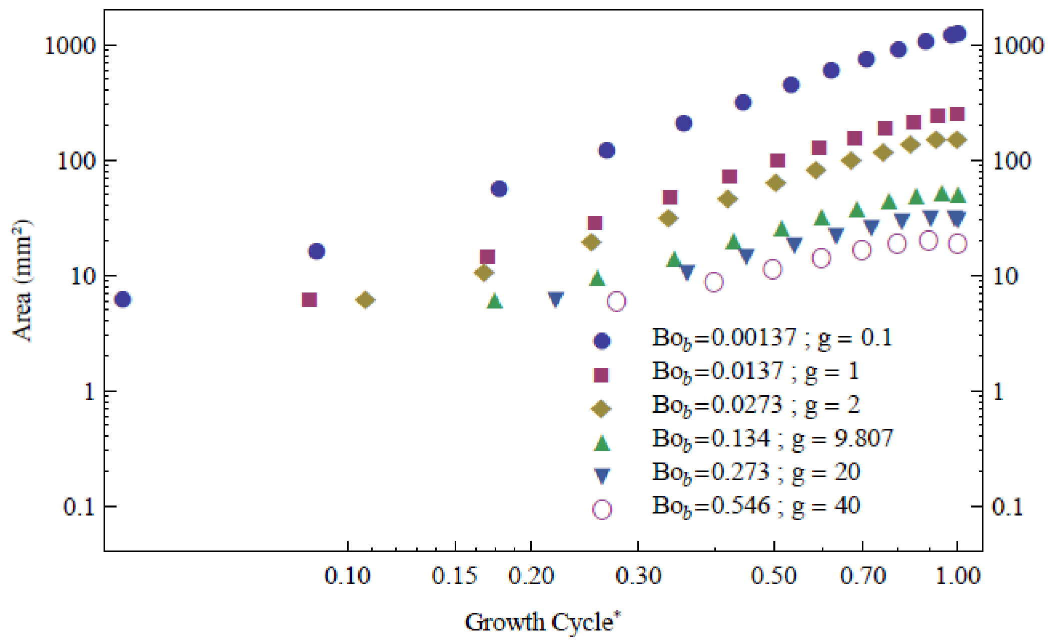

Figure 3-23 : Bubble gas-liquid surface area evolution from numerical simulations for a fixed foot radius of 1mm and a Bond number varying with respect to the gravitational constant.

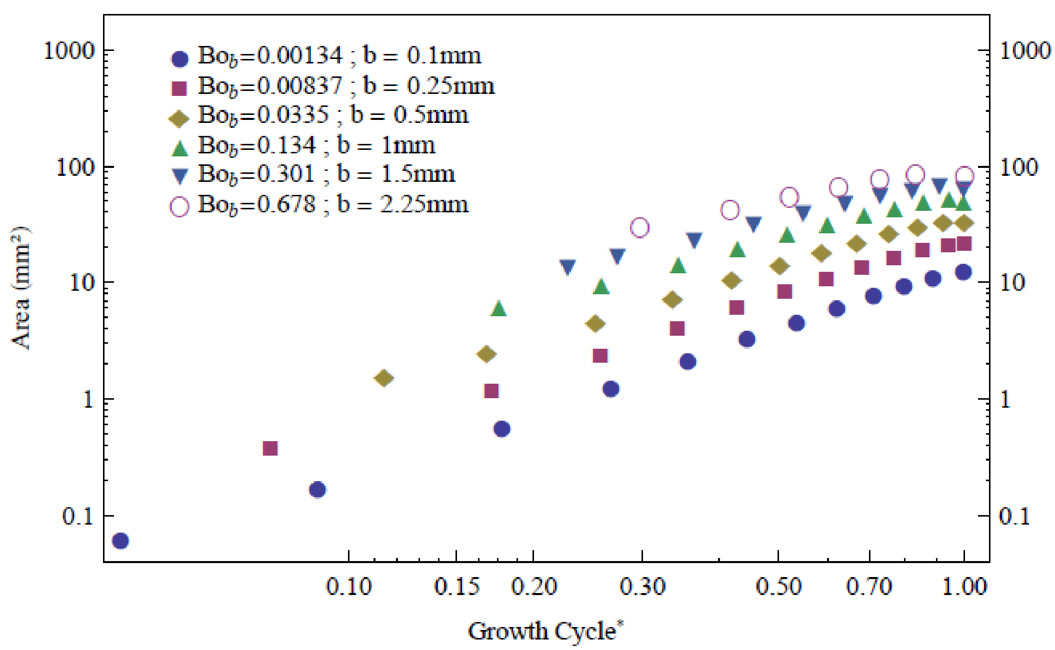

Figure 3-24 : Bubble gas-liquid surface area evolution from numerical simulations at terrestrial gravity and a Bond number varying with respect to bubble foot radius.

3.7.6. Bubble Centre of Gravity Evolution

In this document, all gravitational fields are assumed uniform making the terms *Centre of mass* and *Centre of gravity* interchangeable. For this reason, the derivation of the centre of gravity of a bubble, meaning the mean location of the gravitational force acting on the bubble, is simply the derivation of the Centre of mass of a bubble growing in a uniform gravitational field.

In Figure 3-25, the bubble centre of gravity evolution resulting from the numerically generated bubble profiles is illustrated for a fixed bubble foot radius of 1 mm in which the Bond number is varied by varying the gravitational field strength only. The fluid properties are that of air in water.

The results show that a decrease in gravitational field strength increases the vertical position of the centre of gravity of the bubble. This is to be expected since such a gravitational field strength decrease was previously observed to increase the volume of the bubble.

In Figure 3-26, the bubble centre of gravity evolution resulting from the numerically generated bubble profiles is illustrated for terrestrial conditions in which the Bond number is varied by varying the bubble foot radius only. The fluid properties are that of air in water.

The results show that an increase in bubble foot radius implies an increase in Centre of gravity vertical position. Once again, this is to be expected since it was previously observed that an increase in orifice radius yields an increase in bubble volume.

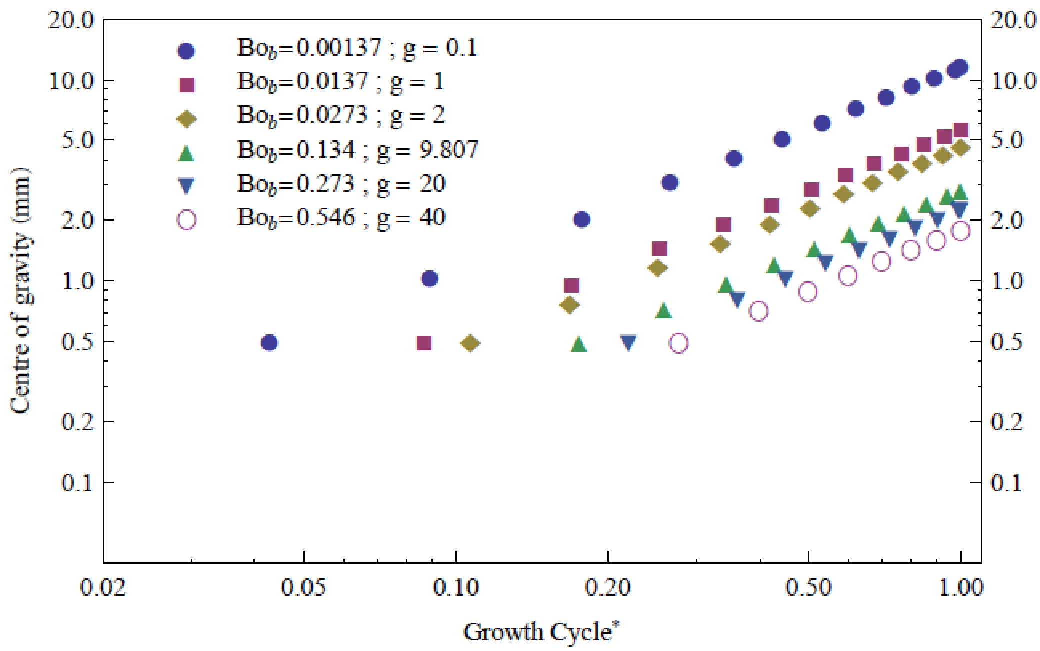

Figure 3-25 : Bubble centre of gravity evolution from numerical simulations for a fixed foot radius of 1mm and a Bond number varying with respect to the gravitational constant.

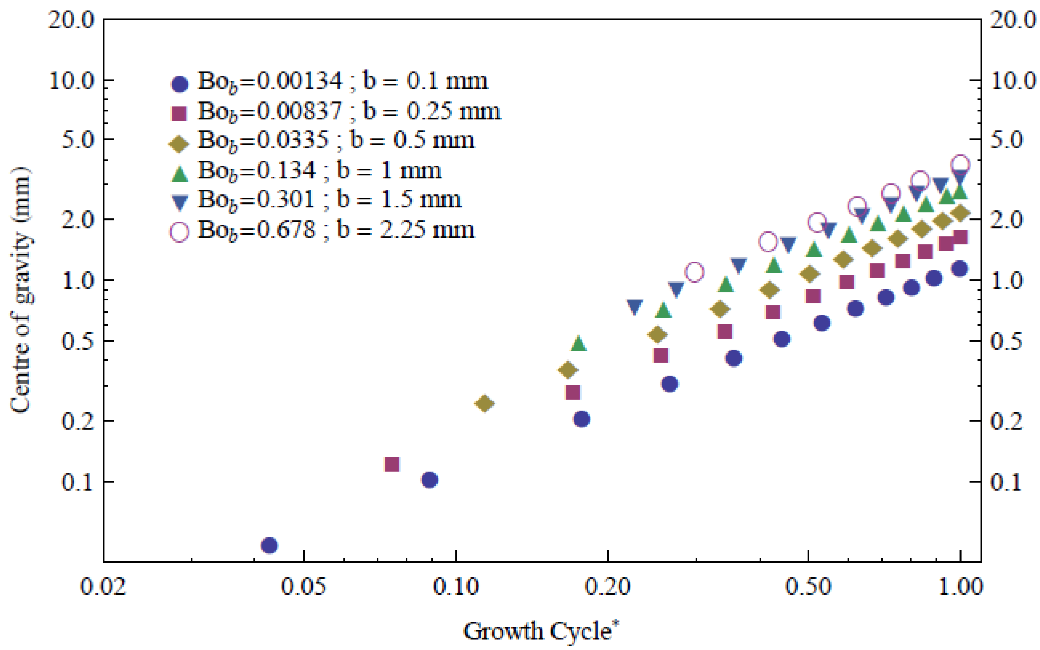

Figure 3-26 : Bubble centre of gravity evolution from numerical simulations at terrestrial gravity and a Bond number varying with respect to bubble foot radius.

3.7.7. Bubble Aspect Ratio Evolution

Thus far, the increasing Bond number due to an increase in gravitational field strength and the increasing Bond number due to an increase in bubble foot radius have had inverse effects on the bubble growth characteristics of bubble volume, vapour-liquid surface area and centre of gravity. Conversely, the increasing Bond number due to an increase in gravitational field strength and the increasing Bond number due to an increase in bubble foot radius have had parallel effects on the bubbles shape tendencies (refer to Figure 3-17 and Figure 3-18). It is therefore necessary to define a bubble characteristic that quantifies the shape of the bubble irrespective of size.

To this end, the simple and commonly used Aspect Ratio of the numerically simulated bubble is investigated. The Aspect Ratio, noted *AR*, as defined by Iacono *et al.* (2006) and Chen *et al.* (2007), is simply the ratio of the major axis length h_{bub} to the minor axis length w_{bub}. These lengths are illustrated in Figure 3-27 for an arbitrary bubble. The *AR* is sometimes referred to as the bubble shape factor and noted σ (Nieuwland *et al.*, 1996).

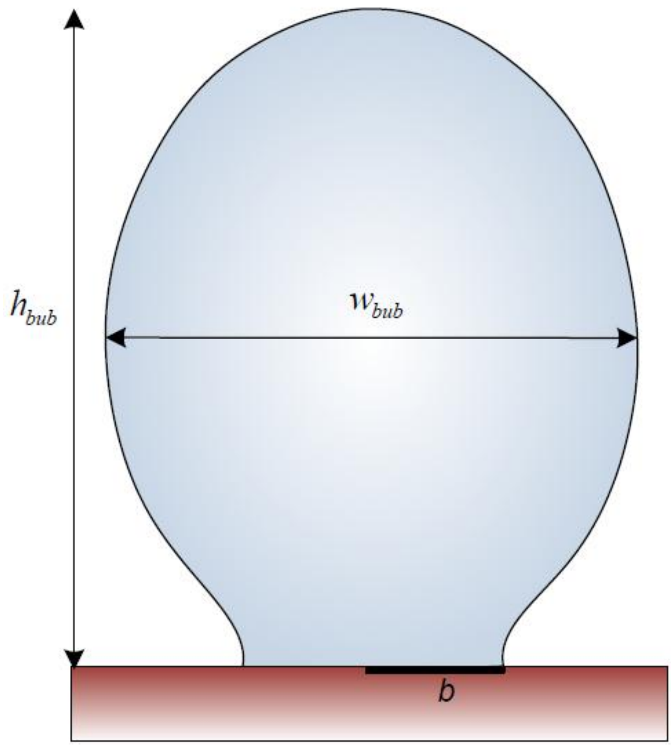

Figure 3-27 : Shematic representation of the major axis length of an arbitrary bubble, noted h_{bub}, and the minor axis length, noted w_{bub}.

The Aspect Ratio is defined as,

3-33: $$AR = \frac{h_{bub}}{w_{bub}}.$$

In Figure 3-28, the bubble *AR* evolution resulting from the numerically generated bubble profiles is illustrated for a fixed bubble foot radius of 1 mm in which the Bond number is varied by varying the gravitational field strength only. The fluid properties are that of air in water.

In Figure 3-29, the bubble *AR* evolution resulting from the numerically generated bubble profiles is illustrated for terrestrial conditions in which the Bond number is varied by varying the bubble foot radius only. The fluid properties are that of air in water.

The results are significant in that they show similar bubble *AR* trends for varying Bond numbers irrespective of the manner in which the Bond number is varied. Figure 3-28 shows increased *AR* values near detachment for higher Bond numbers due to increased gravitational field strengths. Similarly, Figure 3-29 shows increased *AR* values near detachment for higher Bond numbers due to increased orifice radii. In particular, for smaller Bond numbers, irrespective of bubble size, the bubble *AR* is closer to unity throughout the bubble growth cycle and near detachment than for larger Bond numbers.

Recalling that a perfect sphere has an *AR* of unity, the upward *AR* trends illustrated in Figure 3-28 and Figure 3-29 during early growth correspond to the bubble transitioning from hemispherical to spherical. During mid growth, an *AR* of unity is obtained corresponding to the most spherical shape attained during the bubble growth cycle. From this point onwards to detachment, the *AR* continues to increase for values greater than unity. This is attributed to bubble elongation due to the necking phenomenon. In addition to this, the deviation from an *AR* of unity during the bubble growth cycle is more prominent for larger Bond numbers and is independent of bubble volume.

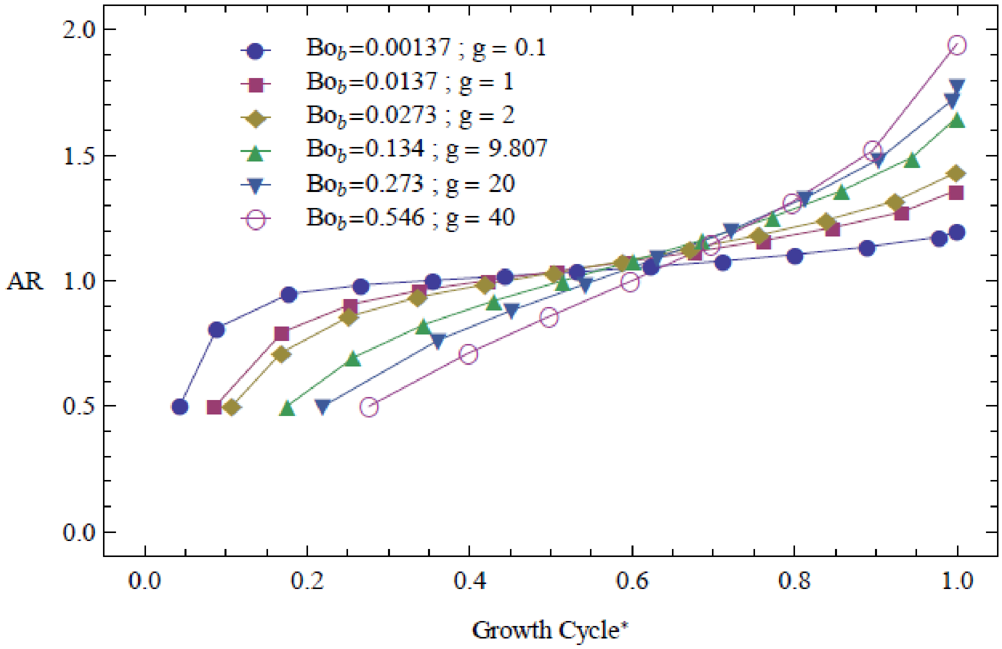

Figure 3-28 : Bubble aspect ratio evolution from numerical simulations for a fixed foot radius of 1mm and a Bond number varying with respect to the gravitational constant.

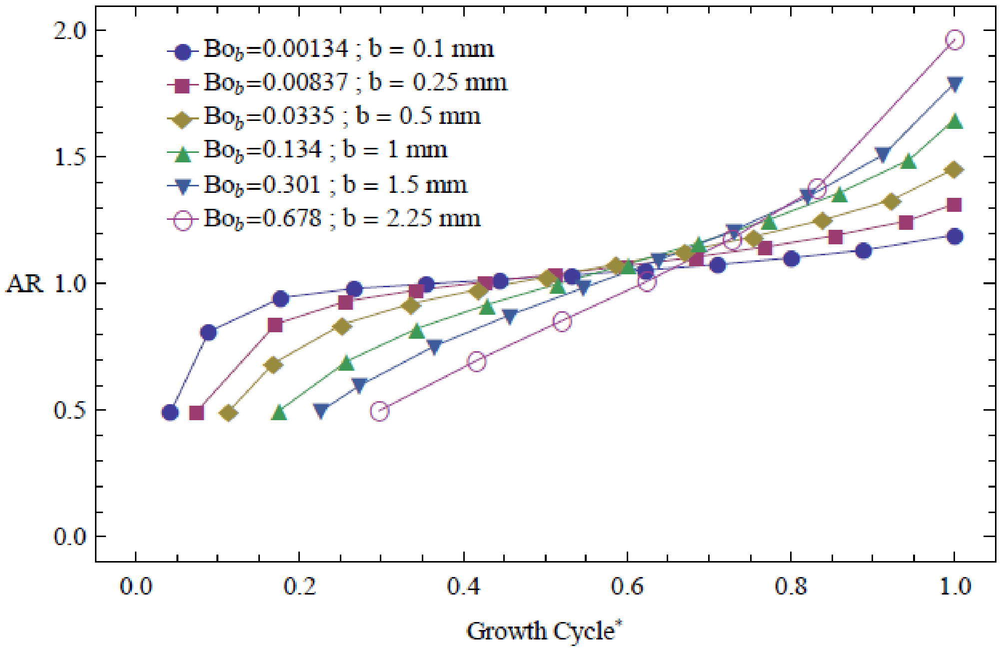

Figure 3-29 : Bubble aspect ratio evolution from numerical simulations at terrestrial gravity and a Bond number varying with respect to bubble foot radius.

The results illustrated in Figure 3-28 and Figure 3-29 lead to the postulation that deviation from a spherical shape for quasi-static bubble growth is intimately linked to the ratio of the surface tension to buoyancy forces, that is to say, to the Bond number. The influence of the Bond number on the bubble degree of sphericity is investigated in the following sections.

3.7.8. Bubble Deformation with respect to Bond Number

The influence of the Bond number on the bubble shape highlighted in the previous section's *AR* investigation can best be illustrated with a non-dimensional comparison of bubble profiles for varying Bond numbers. In the normalized bubble profiles illustrated in Figure 3-30, the Bond number is varied due to a change in the gravitational field strength with a fixed bubble foot radius of 1 mm. The profile comparisons are repeated with terrestrial gravity conditions, the results of which are also illustrated in Figure 3-30, for varying Bond numbers due to a varying orifice radius. The fluid properties are that of air in water.

The vertical *y*-axis is normalized by identifying the bubble height, noted h_{bub}, resulting from the numerically generated bubble profile sequence, as the characteristic length. This characteristic length divides the vertical component of the bubble contour as well as its horizontal component yielding vertical and horizontal normalized lengths.

Since the Capillary equation is not dependent on time, the terms *Early Growth*, *Mid Growth* and *Late Growth* are defined in the following non temporal way. In Figure 3-30, the term *Early Growth* makes reference to the most hemispherical bubble profile generated by the numerical computations for the given conditions. *Early Growth* therefore corresponds to the bubble profile in which,

3-34 $$\frac{h_{bub}}{w_{bub}} = \frac{1}{2}.$$

The term *Mid Growth* is set to be the moment in which the bubble height, resulting from the numerically generated bubble contour, is half the detachment bubble height, noted $h_{bub;d}$. In particular, for *Mid Growth*

3-35 $$Growth\,Cycle^{*} = \frac{h_{bub}}{h_{bub;d}} = \frac{1}{2}.$$

It is noted once more that the numerical simulation detachment profile corresponds to the last possible solution computed by the numerical treatment.

The term *Late Growth* is defined as the frame in which the bubble height generated from the numerical simulations attains its maximum height in the growth cycle. Therefore, *Late Growth* implies that *Growth Cycle** has attained unity,

3-36 $$Growth\,Cycle^{*} = \frac{h_{bub}}{h_{bub;d}} = 1.$$

The results illustrated in Figure 3-30 show that a relatively strong gravitational field imposes an inward constraint on the bubble thereby causing the bubble shape to deviate from a spherical shape. Conversely, a weak gravitational field favours a more spherical bubble shape for *Mid Growth* to *Late Growth* and a more hemispherical shape for *Early Growth*.

The results show similar behaviour when the bubble foot radius is varied. A larger foot radius yields a bubble profile that is more “bullet” shaped than spherical at *Mid Growth* and then elongated with neck formation at *Late Growth*. A small bubble foot radius yields a more spherical bubble shape for *Mid Growth* to *Late Growth* and a more hemispherical shape for *Early Growth* when compared with the bubble profiles of larger bubble foot radii.

Summarizing, a small Bond number, resulting from a weak gravitational field strength or a small cavity radius, favours a truncated spherical shape transitioning from hemispherical to spherical. A large Bond number, resulting from a strong gravitational field or a large cavity radius favours an elongated bubble shape transitioning from hemispherical to oblique with a strong neck formation. This analysis shows a bubble shape dependence on the Bond number:

$$Bo_b = \frac{g\left(\rho_l - \rho_v\right)b^2}{\sigma}.$$

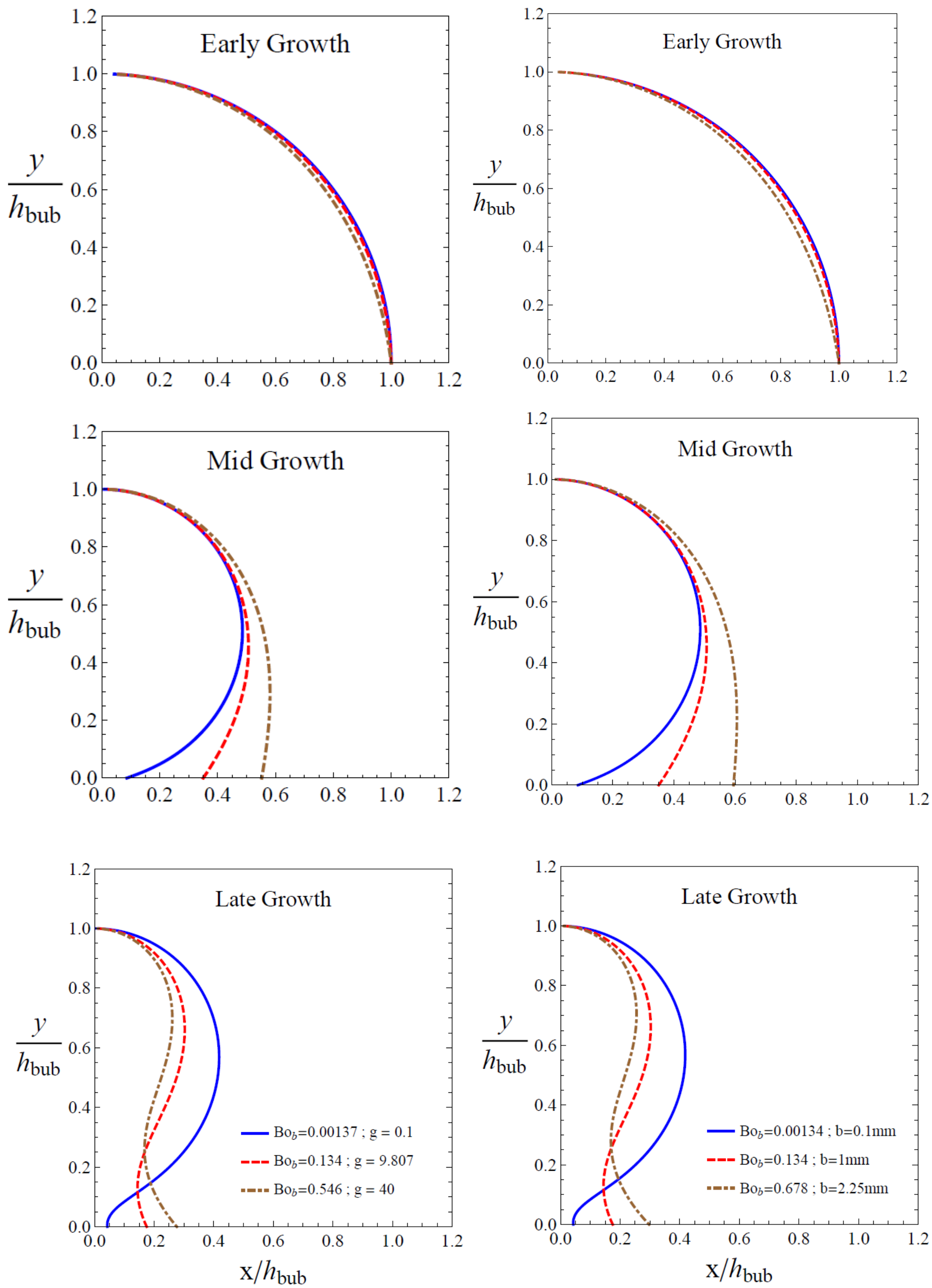

Figure 3-30 : Comparison of normalized bubble profiles in *Early*, *Mid* and *Late Growth* for (*Left)* varying gravitational field strengths and a bubble foot radius of 1mm and *(Right)* varying orifice radii under terrestrial conditions.

3.7.9. Bubble Degree of sphericity during Bubble Growth

Having established the presence of a relationship between the Bond number and the bubble profile produced, the bubble degree of sphericity as a function of the Bond number is investigated. Analysis of the bubble degree of sphericity quantifies the Bond number's influence on the bubble shape, as did the *AR*, while providing more insight than the *AR* into the actual shape of the bubble. As previously mentioned in section 3.2, the bubble degree of sphericity is the ratio of the bubble's spherical volume equivalent area to its measured surface area.

In Figure 3-31, the bubble degree of sphericity evolution resulting from the numerically generated bubble profiles is illustrated for a fixed bubble foot radius of 1 mm in which the Bond number is varied by varying the gravitational field strength only. The fluid properties are that of air in water.

In Figure 3-32, the bubble degree of sphericity evolution resulting from the numerically generated bubble profiles is illustrated for terrestrial conditions in which the Bond number is varied by varying the bubble foot radius only. The fluid properties are that of air in water.

The results show similar trends for all Bond numbers tested. Generally, during early growth, a bubble's degree of sphericity increases towards unity. Recalling that the maximum attainable degree of sphericity is unity corresponding to a perfect sphere, this is attributed to a transitioning phase from hemispherical to spherical. During mid growth, a maximum sphericity is attained representing the bubble's most spherical shape followed by a decrease in sphericity. The end stage decrease in sphericity is attributed to neck formation causing the bubble to elongate and become more oblique.

Furthermore, the results show that the deviations from sphericity during the mid and late stages of the bubble formation are more pronounced for larger Bond numbers. In addition, the maximum attainable degree of sphericity is less for bubble growth with larger Bond numbers.

In keeping with the *AR* investigation, the bubble degree of sphericity dependence on the Bond number is consistent for Bond numbers varying due to a change in gravitational field strength and for Bond numbers varying due to base radius variations. In general, a small Bond number, resulting from a weak gravitational field strength or a small cavity radius, yields a degree of sphericity that is closer to unity throughout the growth cycle than large Bond numbers.

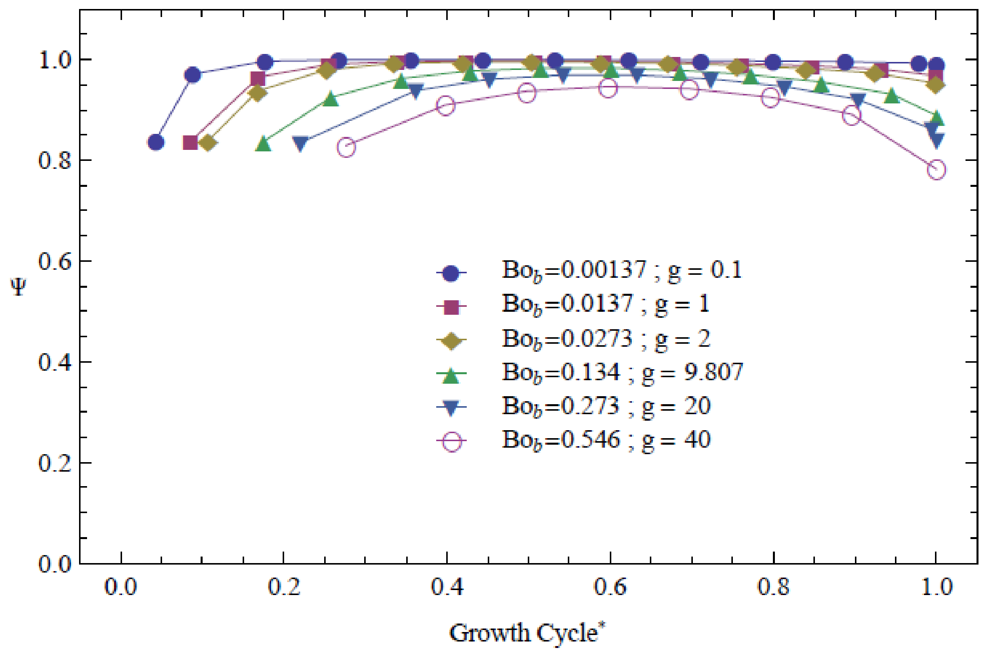

Figure 3-31 : Bubble degree of sphericity evolution from numerical simulations for a fixed foot radius of 1mm and a Bond number varying with respect to the gravitational constant.

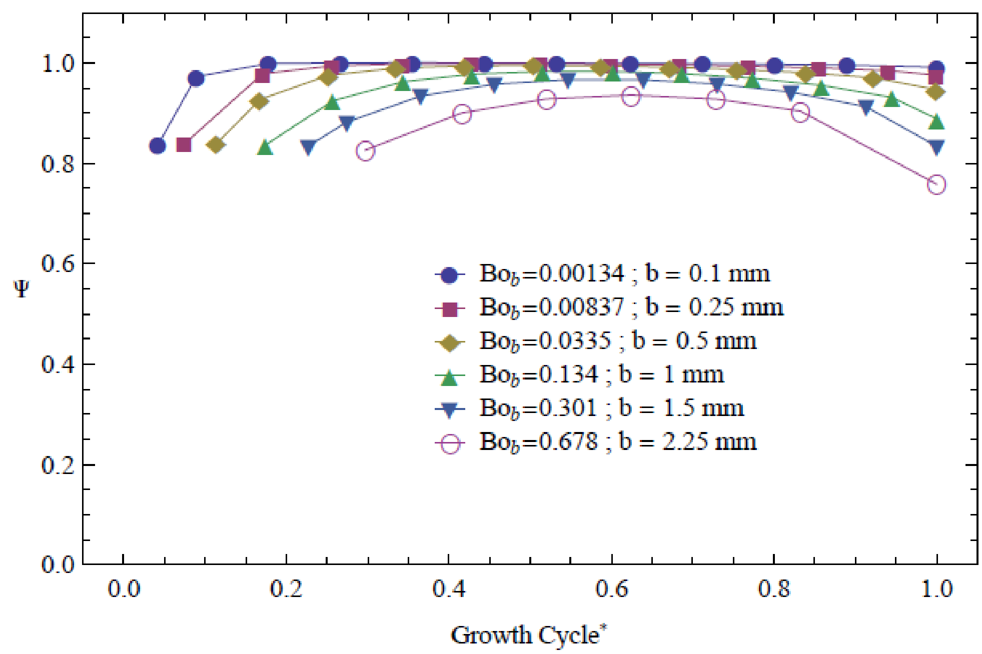

Figure 3-32 : Bubble degree of sphericity evolution from numerical simulations at terrestrial gravity and a Bond number varying with respect to bubble foot radius.

In order to better visualize the spherical evolution quantified in terms of the bubble degree of sphericity in the above figures, two bubble formation sequences are provided below depicting bubble growth for two different Bond numbers. The sequence of images in Figure 3-33 are a sample of the experiments described in section 3.4.

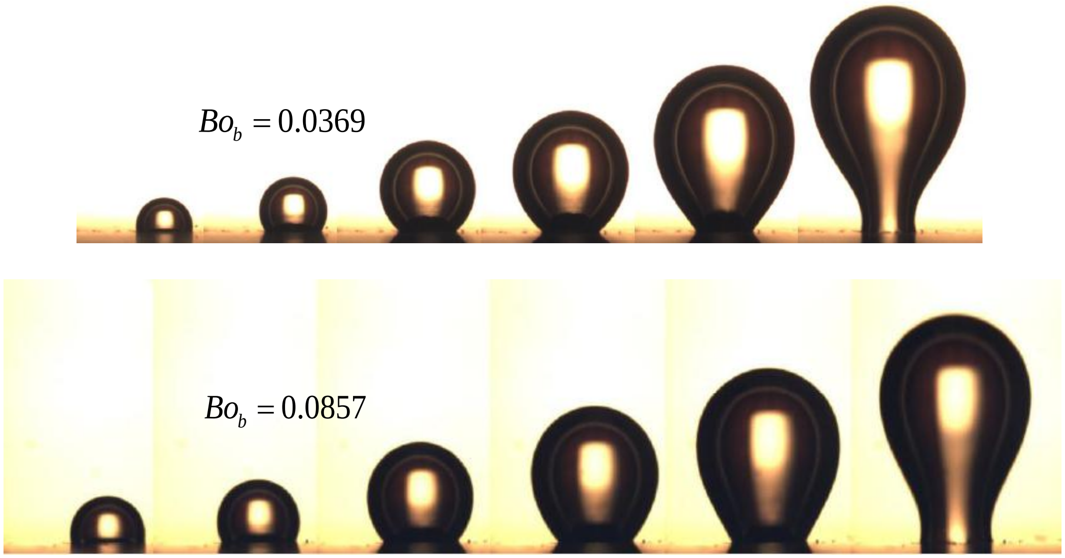

Figure 3-33: *(Top)* Bubble images captured by Sergio Di Bari of air injected into water through a 0.525 mm orifice in which $Bo_b = 0.0369$. *(Bottom)* Bubble images captured by Sergio Di Bari of air injected into water through a 0.8 mm orifice in which $Bo_b = 0.0857$.

The images in the above figure show bubbles transitioning from hemispherical to spherical with an elongation due to neck formation. Indeed, the images above support the sphericity analysis showing that smaller Bond numbers imply a more spherical bubble evolution and that a bubble deviates from a spherical shape near inception and near detachment. This phenomenon is quantified in Figure 3-31 and Figure 3-32 showing that the degree of sphericity is indeed dependent on the Bond number only, even for different gravitational field strengths.

This analysis provides insight into the shape evolution of a bubble during its growth cycle suggesting that a truncated spherical geometry elongated due to neck formation is more appropriate for bubble growth modeling then a spherical assumption. Furthermore, the results suggest that the magnitude with which the bubble neck elongates is also in a one-to-one dependence with the Bond number.

3.7.10. Bubble Degree of Modified sphericity

The results of the bubble degree of sphericity study of the previous section show that a spherical bubble shape assumption in bubble growth modeling, which would correspond to a sphericity of unity, can lead to erroneous results. In light of this, as a starting point in the development of more appropriate bubble geometric modeling, the validity of a truncated spherical geometric bubble shape with a fixed base radius, illustrated in Figure 3-34, is investigated.

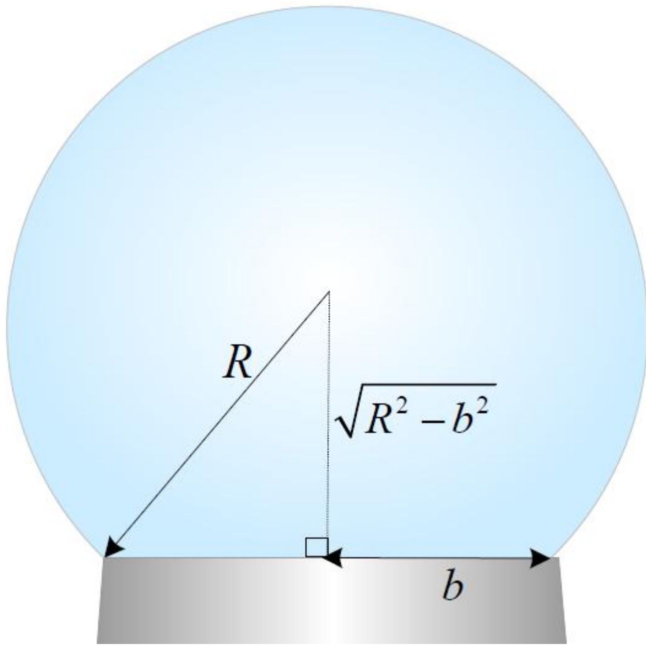

Figure 3-34: Truncated spherical bubble with bubble foot fixed to cavity perimeter.

To this end, the bubble degree of *Modified sphericity*, noted Ψ_{mod}, is introduced. It is defined as the ratio of the area including the base of the bubble's volume equivalent truncated spherical segment with base radius *b* to the bubble's measured area,

3-37 $$\Psi_{\mathrm{mod}} = \frac{A_{tr} \circ V_{tr}^{-1}\left(V_m\right)}{A_m}.$$

In the above, A_m and V_m are the bubble's measured surface area (including the base) and the bubble's measured volume respectively. They are measured from the bubble profile using the frustum method described in section 3.5. From the geometric constraints illustrated in Figure 3-34, the surface area (including the base area) of a truncated spherical segment with base radius *b* is,

3-38 $$A_{tr}(R) = 2\pi\left(R + \sqrt{R^2 - b^2}\right) + \pi b^2$$

and the volume of a truncated spherical segment with base radius *b* is,

3-39 $$V_{tr}(R) = \frac{1}{3}\pi\left(2R - \sqrt{R^2 - b^2}\right)\left(\sqrt{R^2 - b^2} + R\right)^2.$$

It is postulated that, by minimizing the available gas/vapour-liquid surface area, the truncated spherical segment, with base fixed to the perimeter of the cavity from which the bubble emerges, is a more appropriate geometric assumption than a spherical assumption. The accuracy of this postulation is measured in terms of the Modified sphericity in which a Modified sphericity of unity is the validating criterion. That is to say, a Modified sphericity of unity corresponds to a truncated spherical bubble with base radius equal to the orifice radius. Furthermore, the physical mechanism responsible for a deviation from a Modified sphericity of unity is investigated. It is noted that any bubble elongation would yield a bubble degree of Modified sphericity less than unity; during early growth, any inward deformation from hemispherical to a more pyramid shape would result in a bubble degree of Modified sphericity greater than unity.

The procedure of calculating the bubble degree of Modified sphericity first solves for the equivalent radius of the truncated spherical segment with base radius *b* by solving for, $V_{tr}^{-1}\left(V_m\right)$ in which V_{tr}^{-1} is the inverse function of Eq. 3-39. With this equivalent radius and Eq. 3-38, the equivalent truncated spherical area is solved. Subsequently, Eq. 3-37 is used to solve for the bubble degree of Modified sphericity.

In Figure 3-35, the bubble degree of Modified sphericity evolution resulting from the numerically generated bubble profiles is illustrated for a fixed bubble foot radius of 1 mm in which the Bond number is varied by varying the gravitational field strength only. The fluid properties are that of air in water.

In Figure 3-36, the bubble degree of Modified sphericity evolution resulting from the numerically generated bubble profiles is illustrated for terrestrial conditions in which the Bond number is varied by varying the bubble foot radius only. The fluid properties are that of air in water.

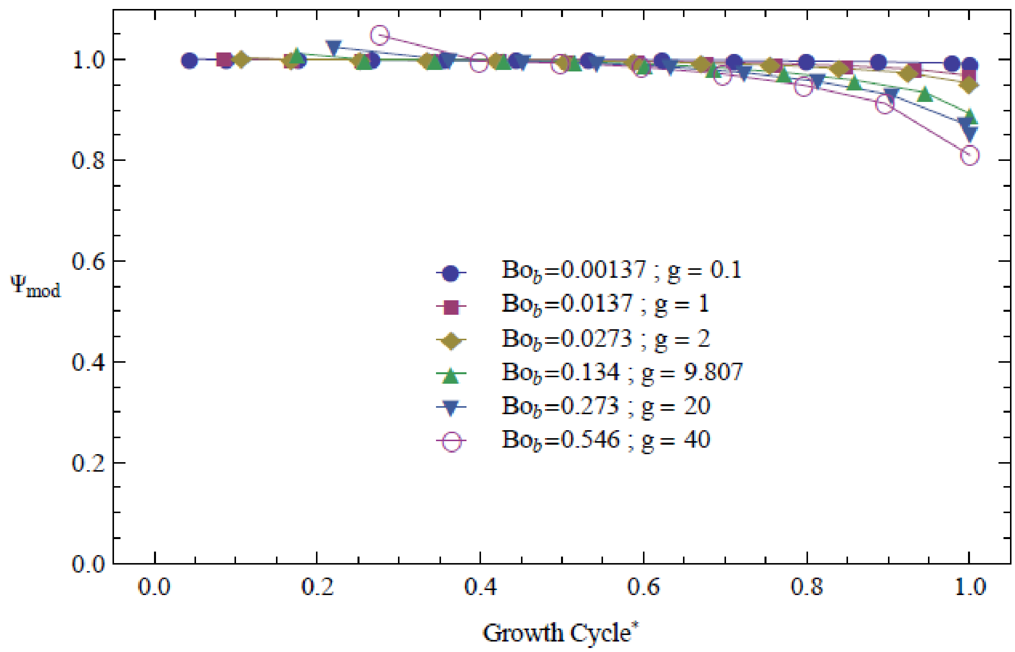

Figure 3-35 : Bubble degree of Modified sphericity evolution from numerical simulations for a fixed foot radius of 1mm and a Bond number varying with respect to the gravitational constant.

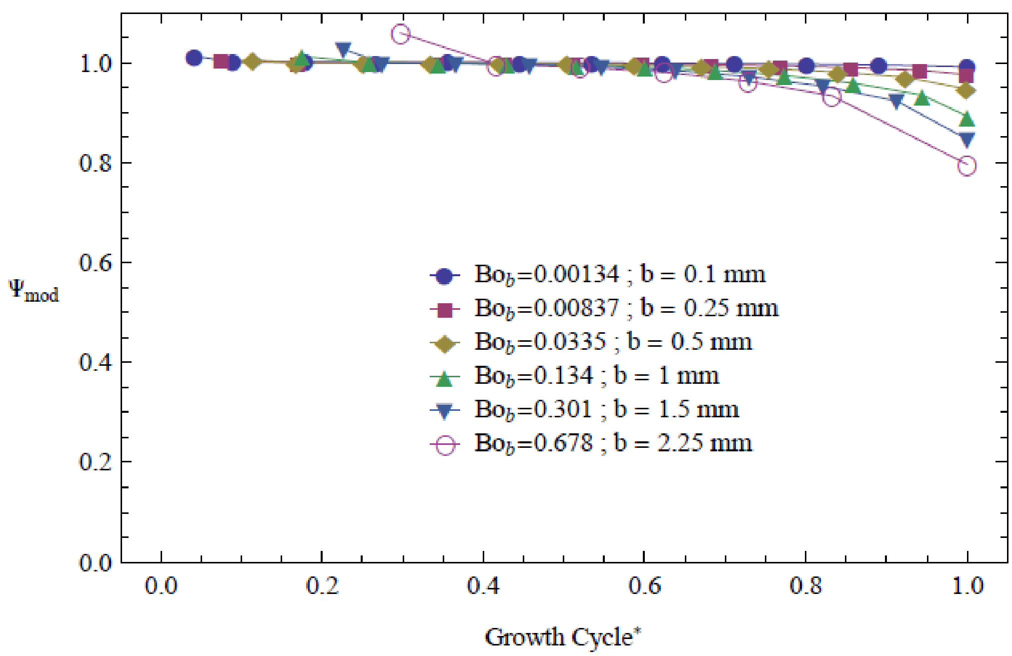

Figure 3-36 : Bubble degree of Modified sphericity evolution from numerical simulations at terrestrial gravity and a Bond number varying with respect to bubble foot radius.

The results illustrated in Figure 3-35 show that during early growth the bubble degree of Modified sphericity is very close to unity for low gravitational field strengths. For the larger gravitational field strengths, the hemispherical shape is altered by inward compressions of the bubble outer walls yielding Modified sphericity degrees greater than unity. After attaining unity, during mid growth, the bubble degree of Modified sphericity begins to decrease; this is attributed to bubble elongation due to neck formation. The deviation from a Modified sphericity of unity is more pronounced for stronger gravitational field strengths corresponding to larger Bond numbers. In addition, the deviation from a Modified sphericity of unity is delayed for weaker gravitational fields corresponding to smaller Bond numbers.

Similarly, the results illustrated in Figure 3-36 show that bubble degree of Modified sphericity during early growth is close to unity for all cavity radii tested with exception to the larger cavity radii in which the bubble degree of Modified sphericity is greater than unity during early growth. Further deviation from unity occurs during mid to late stages in the growth cycle. This deviation from unity is shown to be more pronounced and to occur earlier in the growth cycle for bubbles emmerging from larger cavities corresponding to relatively larger Bond numbers.

Generally, it is shown that in all bubble formations tested, the bubble's degree of *Modified sphericity* remains closer to unity than the bubble's degree of sphericity throughout the growth cycle. This implies that a truncated spherical assumption is more accurate than a spherical assumption.

In addition, it is shown that a bubble deviates from a bubble degree of Modified sphericity of unity with increasing Bond numbers. This is the case when the Bond number increases due to an increase in gravitational field strength; it is also the case when the Bond number increases due to an increase in cavity radius. The deviation to a Modified sphericity of less than unity is attributed to a vertical elongation in the bubble shape. This investigation isolates the Bond number as the quantifier of the physical parameters responsible for bubble elongation due to neck formation.

The results can be summarized as follows: larger Bond numbers imply larger buoyancy to surface tension ratios favouring earlier neck formation and more pronounced neck formation near detachment. It is important to recall that this relation between the bubble profile and the Bond number applies to the bubble shape only. That is to say, two bubbles with the same Bond number will have similar shapes but may have very different size and volume.

The effect of the Bond number on the shape of the bubble may be explained in the following way:

1. Large Bond numbers due to large gravitational field strengths will result in a large buoyancy force countering the hydrostatic forces thereby elongating the bubble and favouring neck formation.

2. Large Bond numbers due to large orifice (or nucleation cavity) radii produce larger bubbles with greater bubble height. These larger bubbles experience weakened countering hydrostatic forces due to their height thereby elongating the bubble and favouring neck formation.

3.7.11. Bubble Shape Dependence on Bond Number

The previous sections have illustrated, through analysis of the bubble Aspect Ratio and the bubble degree of Modified sphericity, that a bubble's shape tendency is dictated by its Bond number. To further illustrate this phenomenon, Figure 3-37 compares the bubble profiles generated by the numerical treatment of the capillary equation in which the Bond number is invariant.

In one case, an air bubble grows in water from an orifice of radius 2.02 mm under terrestrial conditions yielding a Bond number of 0.546. The other bubble profile simulates air bubble growth in water from an orifice of radius 1 mm under a gravitational field strength of 40 m/s^2 also yielding a Bond number of 0.546. The sequence shows the respective bubbles transitioning from *Early* to *Mid* to *Late* growth. The resulting graphical representation shows that the bubbles are of similar shape despite having very different volumes.

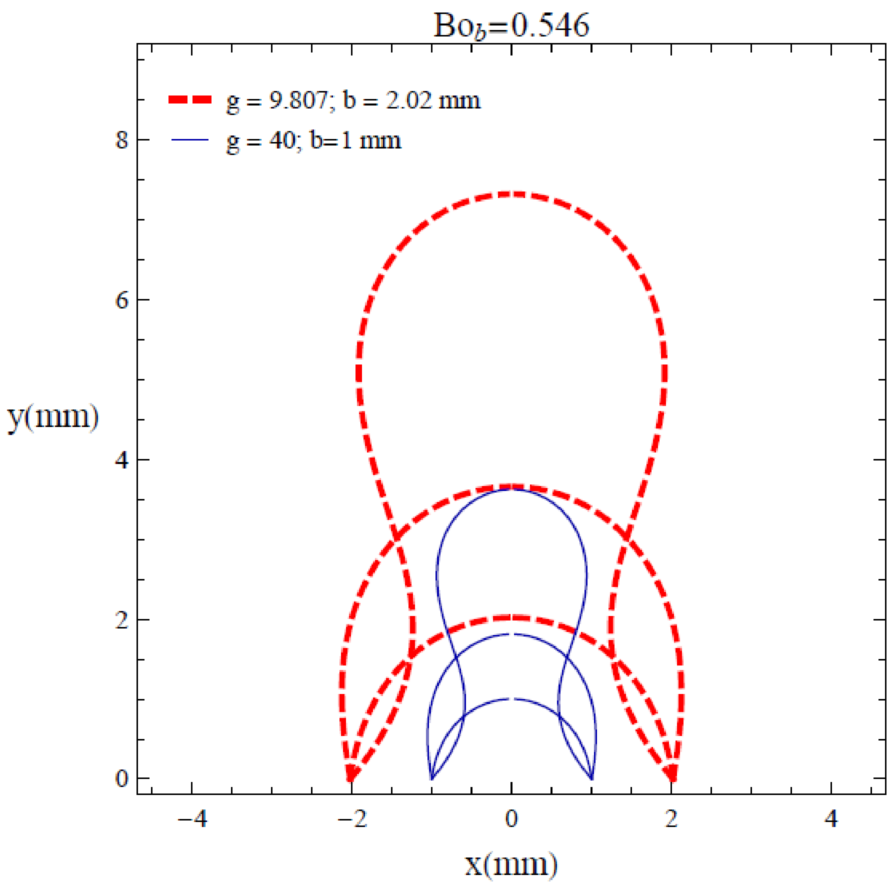

Figure 3-37: Comparison of bubble profiles of a bubble growing under terrestrial conditions from a cavity of radius 2.02 mm with a bubble growing in a gravitational field strength of 40 m/s² from a cavity of radius 1 mm. The Bond number for both sets of conditions is 0.546.

In order to compare the relative bubble shapes of the two growing bubbles considered in Figure 3-37, the bubble profiles are normalized by dividing the horizontal and vertical components by their respective bubble heights, noted h_{bub}. The results illustrated in Figure 3-38 show that the bubble shapes are essentially identical despite having very different size.

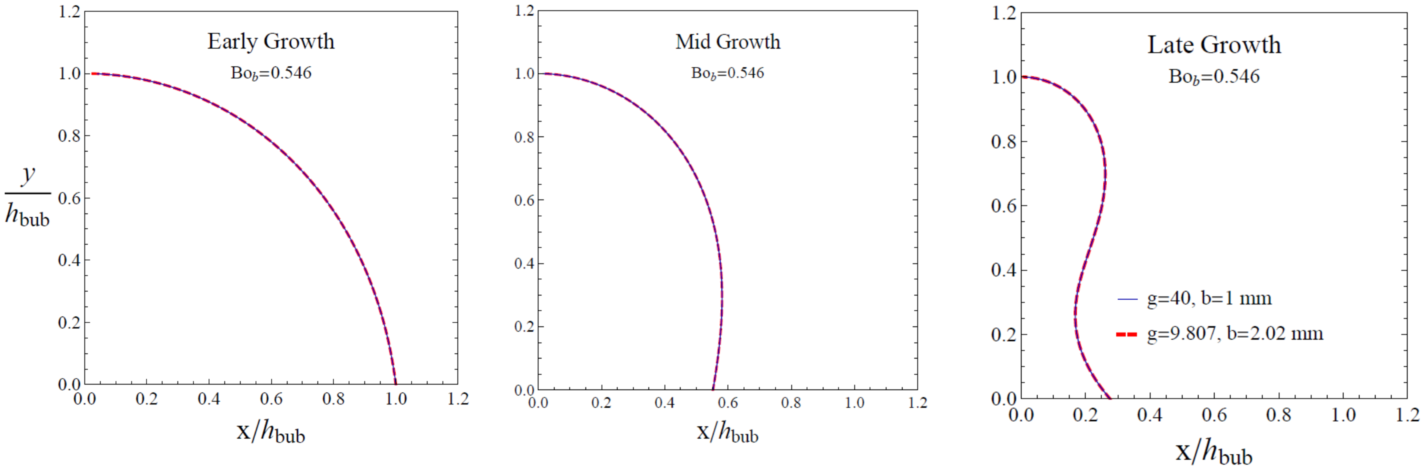

Figure 3-38 : Comparison of normalized bubble profiles of different size bubbles with the same Bond number 0.546 in *Early, Mid* and *Late Growth*.

In light of this result, from this point onward, the only contributing factor considered in the analysis of bubble shape is the Bond number.

3.7.12. Bubble Deformation due to Local Stresses

The following pressure balance analysis investigates the hydrostatic pressure distribution and the capillary pressure distribution over a growing bubble. The capillary equation is numerically solved for different Bond numbers over various stages of the bubble growth cycle. It is carefully noted that the variations in Bond number expose the influence of the gravitational field strength on bubble shape as well as the influence of the cavity radius on bubble shape. Indeed, an increase in Bond number with fixed fluid properties may be considered to be due to an increase in gravitational field strength or to an increase in cavity radius.

In order to further understand the influence of local stresses on bubble shape, the principal radii of curvature resulting in changes in the pressure distribution are also investigated.

The principal radii of curvature at any point on the bubble interface, noted R_1 and R_2, are normalized by the radius of curvature at the bubble apex, noted R_o, such that,

3-40 $$\bar{\bar{R}}_i^{-1} = \frac{R_o}{R_i}\,.$$

Similarly, the hydrostatic pressure and the capillary pressure, noted P_{hydro} and P_c respectively, are normalized by the capillary pressure at the bubble apex, noted $P_{c,o}$, such that,

3-41 $$\bar{\bar{P}} = \frac{P}{P_{c,o}} = \frac{P}{2\sigma / R_o}\,.$$

Recalling from Eq. 3-15 that the capillary equation represents the balance of pressure at a point along the bubble interface,

3-42 $$\underbrace{\frac{2\sigma}{R_o}}_{P_{c,o}} = \underbrace{\sigma\left(\frac{1}{R_1}+\frac{1}{R_2}\right)}_{P_c} + \underbrace{\left(\rho_l-\rho_v\right)gz}_{P_{hydro}}\,,$$

the capillary equation may be conveniently expressed in terms of the normalized pressures,

$$3\text{-}43 \qquad \underbrace{1}_{\bar{\bar{P}}_{c,o}} = \underbrace{\tfrac{1}{2}\left(\bar{R}_1^{-1} + \bar{R}_2^{-1}\right)}_{\bar{\bar{P}}_c} + \underbrace{\tfrac{1}{2}Bo_b z^* R_o^*}_{\bar{\bar{P}}_{hydro}}.$$

Before analysing the results, it is important to recall the physical significance of the principal radii of curvature. Illustrated in Figure 3-39 are the principal radii of curvature R_1 and R_2 at two arbitrarily chosen points along an arbitrary bubble profile. The principal radii of curvature represent the curvature in two planes perpendicular to the surface of the infinitesimal segment neighbouring a chosen point.

An important feature for bubble growth is that $\bar{R}_1^{-1}$ can at no point dissolve to zero since this would imply that R_1 tends to infinity effectively making the bubble width tend to infinity. This can be visualized as a gas bubble which planes over the surface on which it sits as if there were no surface tension forces.

Furthermore, a change in the sign of $\bar{R}_2^{-1}$ implies a change in concavity. In the specific case of the capillary equation, a negative $\bar{R}_2^{-1}$ value implies an outward curvature (relative to the central symmetric bubble axis) causing an inward bubble deformation from spherical. Consequentially, $\bar{R}_2^{-1} = 0$ represents the location of an inflexion point and appears as a straight portion, possibly infinitely short, of the bubble profile and serves to identify the beginning of the necking phenomenon. Therefore, if a negative $\bar{R}_2^{-1}$ occurs and is located along the bubble profile away from the foot of the bubble, the location of the minimum negative value of $\bar{R}_2^{-1}$ would appear as an inward pinching of the neck of the bubble. The inward pinching would be accompanied by smaller values of R_1. For this reason, the minimum negative value of $\bar{R}_2^{-1}$ attained along the bubble profile, paralleled by the maximum value of $\bar{R}_1^{-1}$ attained along the bubble profile, identifies the most inward pinch that will occur along the bubble profile.

To summarize, deformation from a truncated spherical shape can by identified as the moment in which the minimum and maximum values of $\bar{R}_2^{-1}$ and $\bar{R}_1^{-1}$ respectively are located away from the foot of the bubble.

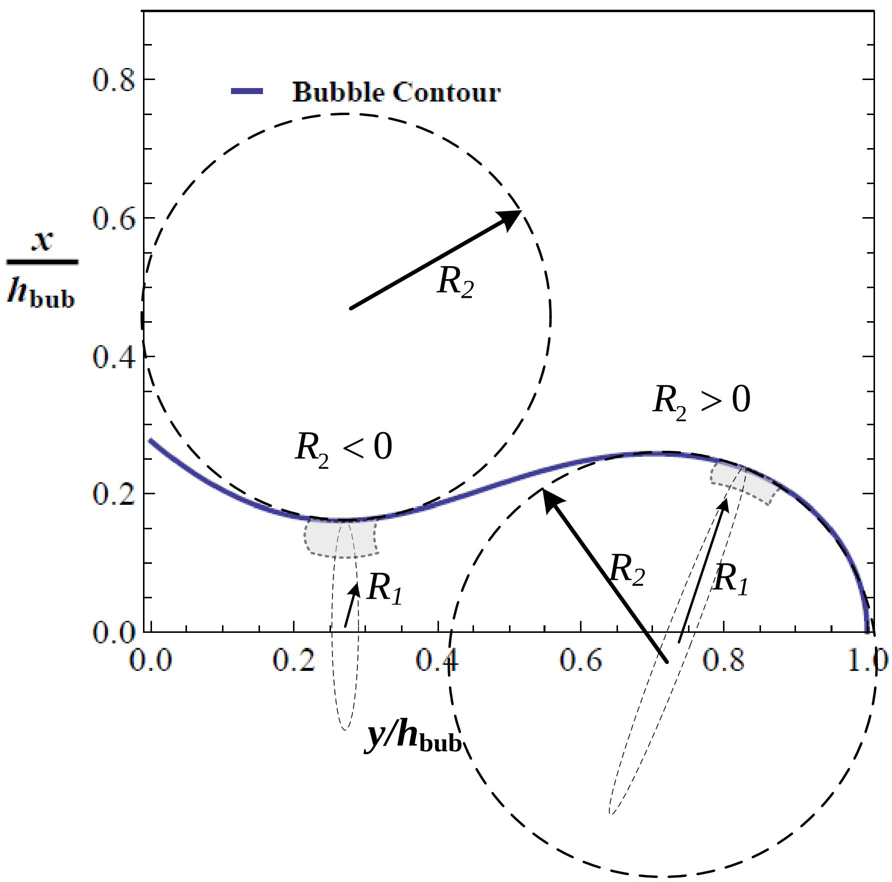

Figure 3-39: Representation of the principal radii of curvature at two arbitrary locations along an arbitrary bubble contour.

The hydrostatic pressure distribution and capillary pressure distribution over a growing bubble analysis begins with bubble shapes at detachment corresponding to the moment in the growth cycle in which deformation from truncated spherical is most apparent. The profiles resulting from three different Bond numbers are compared.

Figure 3-40 illustrates the principal radii of curvature distribution as well as the pressure distribution over a bubble at detachment, noted *Growth Cycle** = 1, for three different Bond numbers: 0.00137, 0.134 and 0.546. Once again, the bubble contour coordinate points are normalized by the bubble height h_{bub}.

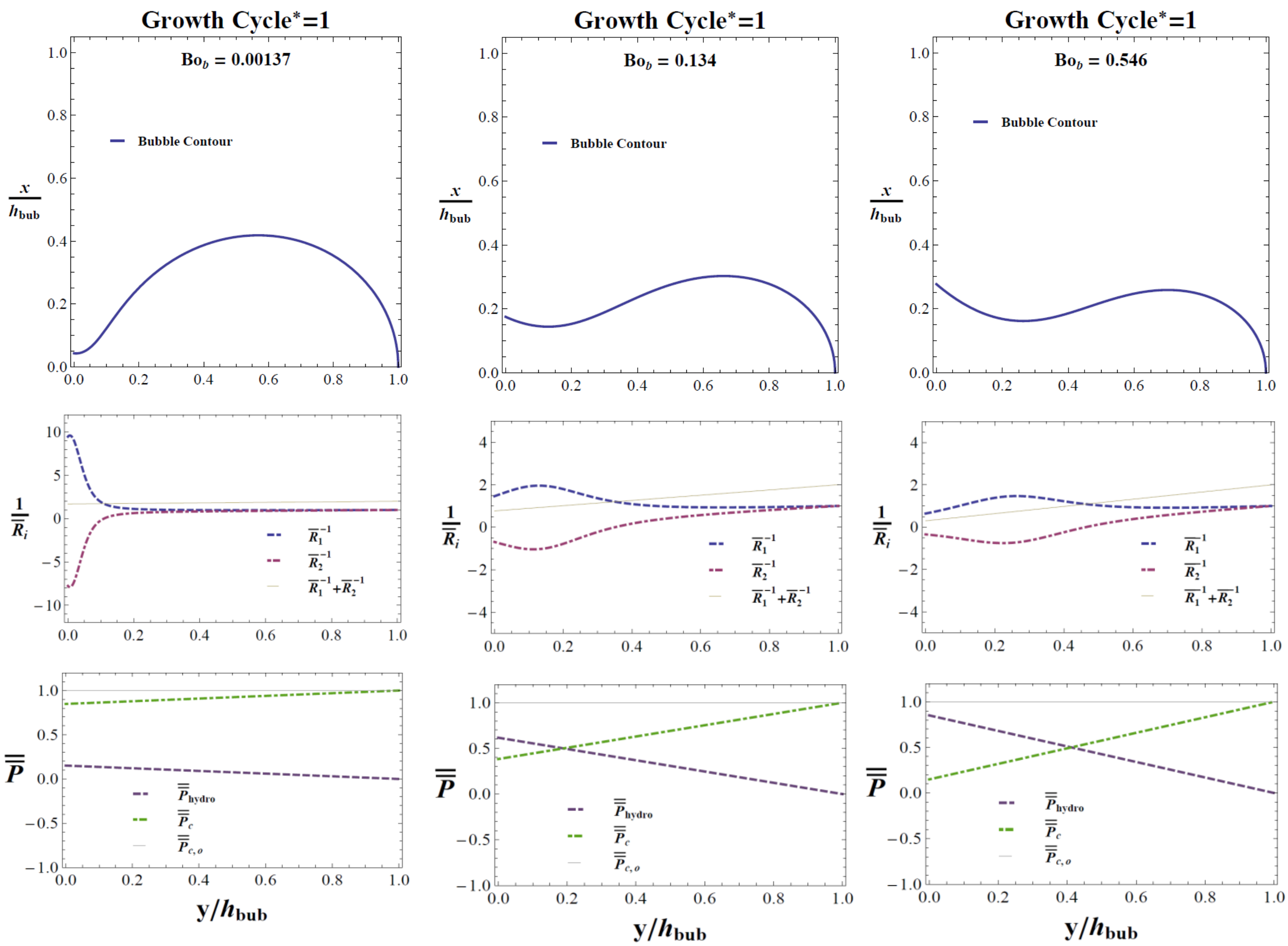

Figure 3-40: *(Top)* Bubble contours near detachment. *(Middle)* Principal radii of curvature profile along the bubble contour. *(Bottom)* Pressure distribution over the bubble.

The results show that a low Bond number favours a spherical bubble shape near detachment. This is demonstrated by the principle radii of curvature being equal to each other over the majority of the bubble contour for the small Bond number simulation. In addition, the absolute maximums values of $\bar{R}_2^{-1}$ and $\bar{R}_1^{-1}$ are located at the bubble foot implying little deformation due to inward pinching. In contrast, the larger Bond number simulation yields principal radii of curvature that are only equal near the bubble apex implying a less spherical bubble at detachment. Furthermore, the maximum value of $\bar{R}_1^{-1}$, paralleled by the minimum negative value of $\bar{R}_2^{-1}$, occurs along the neck of the bubble for larger Bond numbers. This implies that larger Bond numbers favour deformation in the way of inward pinching relative to the central axis. This is attributed to the observation (illustrated in the bottom frames of Figure 3-40) that for larger Bond numbers, in late stage bubble growth the hydrostatic pressure dominates in the lower section of the bubble causing bubble deformation from spherical. In the lower Bond number late stage bubble growth scenario, the hydrostatic pressure does not have such a dominant role at any point along the bubble contour. This defining feature between larger and smaller Bond numbers is found in the forthcoming arguments to provide a pivot between what is considered to be a small or large Bond number at 0.06032.

In order to further understand the influence of the hydrostatic pressure relative to the capillary pressure on bubble shape during the bubble growth cycle, the principal radii of curvature distribution and the pressure distribution over the bubble contour are investigated during bubble growth from inception to detachment.

Figure 3-41 to Figure 3-43 illustrate the evolution of the pressure distribution over a bubble growing from a hemispherical inception to detachment for a Bond number of 0.00137. The simulations are repeated for growing bubbles with larger Bond numbers 0.134 and 0.546, the results of which are illustrated in Figure 3-44 to Figure 3-49.

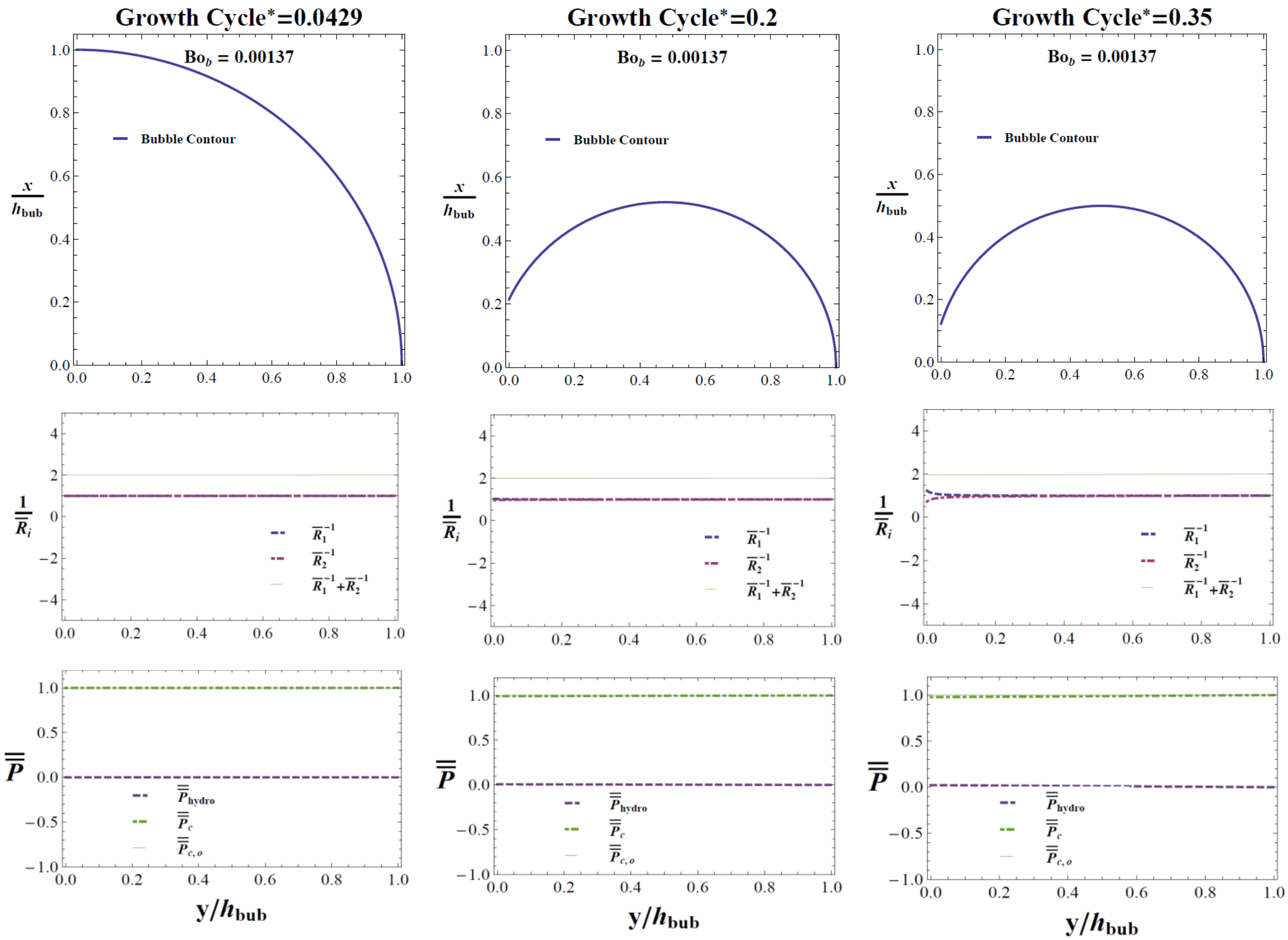

Figure 3-41: *(Top)* Bubble contours during early stage growth for Bond number 0.00137. *(Middle)* Principal radii of curvature profile along the bubble contour. *(Bottom)* Pressure distribution over the bubble.

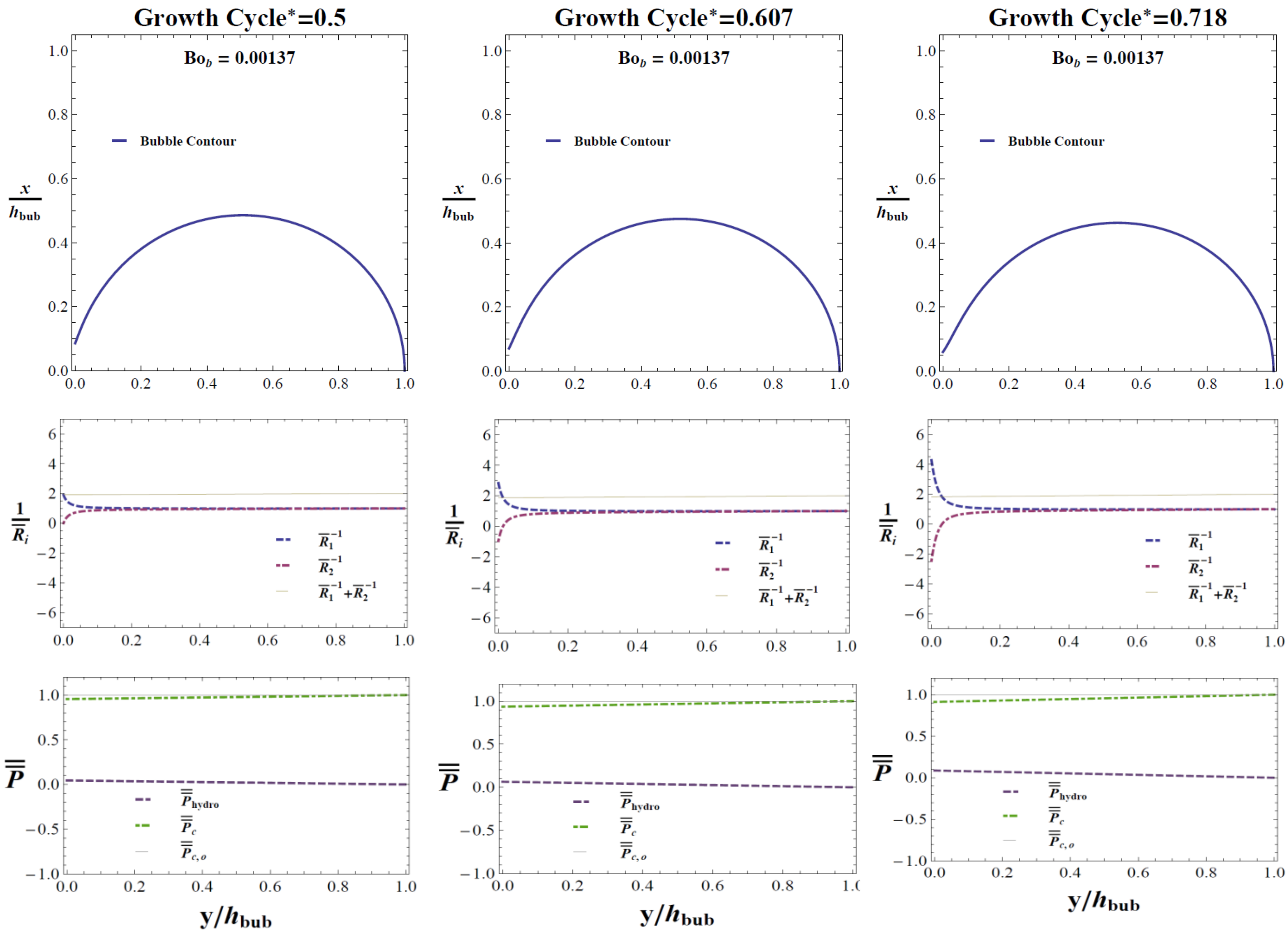

Figure 3-42: *(Top)* Bubble contours during mid stage growth for Bond number 0.00137. *(Middle)* Principal radii of curvature profile along the bubble contour. *(Bottom)* Pressure distribution over the bubble.

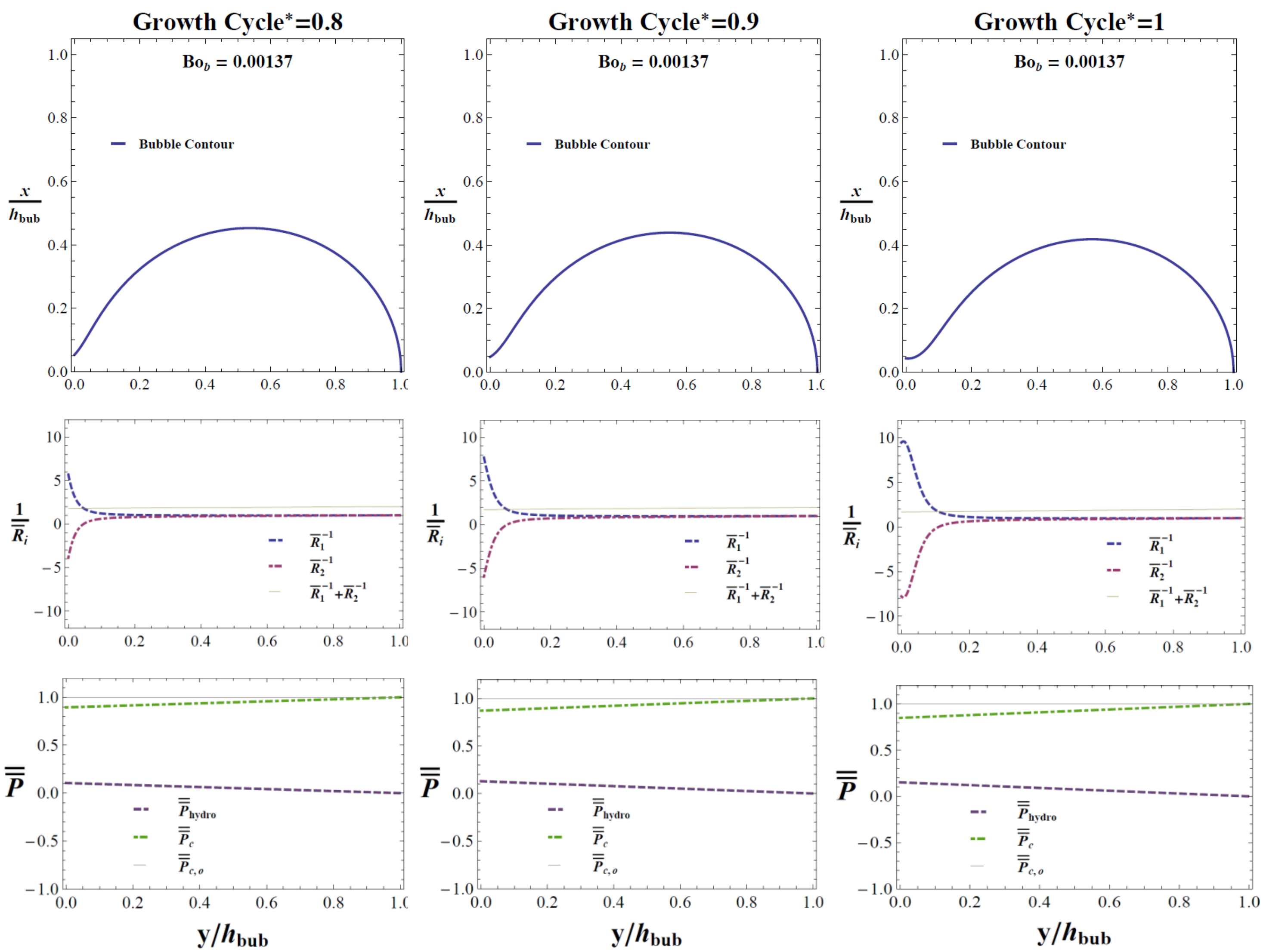

Figure 3-43: *(Top)* Bubble contours during late stage growth for Bond number 0.00137. *(Middle)* Principal radii of curvature profile along the bubble contour. *(Bottom)* Pressure distribution over the bubble.

Figure 3-44 to Figure 3-46 illustrate the evolution of the pressure distribution over a bubble growing from a hemispherical inception to detachment for a Bond number of 0.134. It is important to note that for larger Bond numbers, the hydrostatic pressure plays a more influential role and as such, bubble deformation from spherical is more significant.

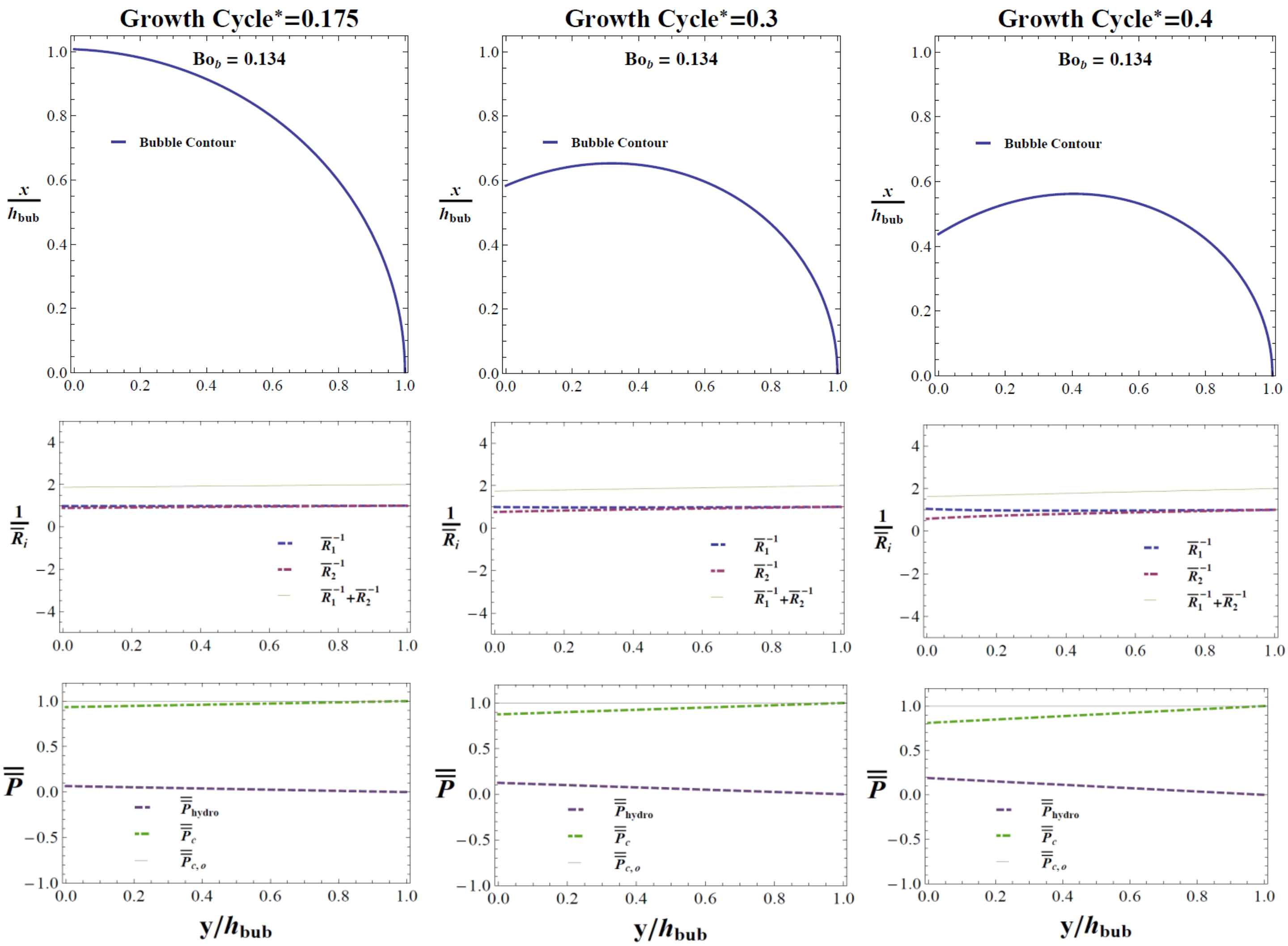

Figure 3-44: *(Top)* Bubble contours during early stage growth for Bond number 0.134. *(Middle)* Principal radii of curvature profile along the bubble contour. *(Bottom)* Pressure distribution over the bubble.

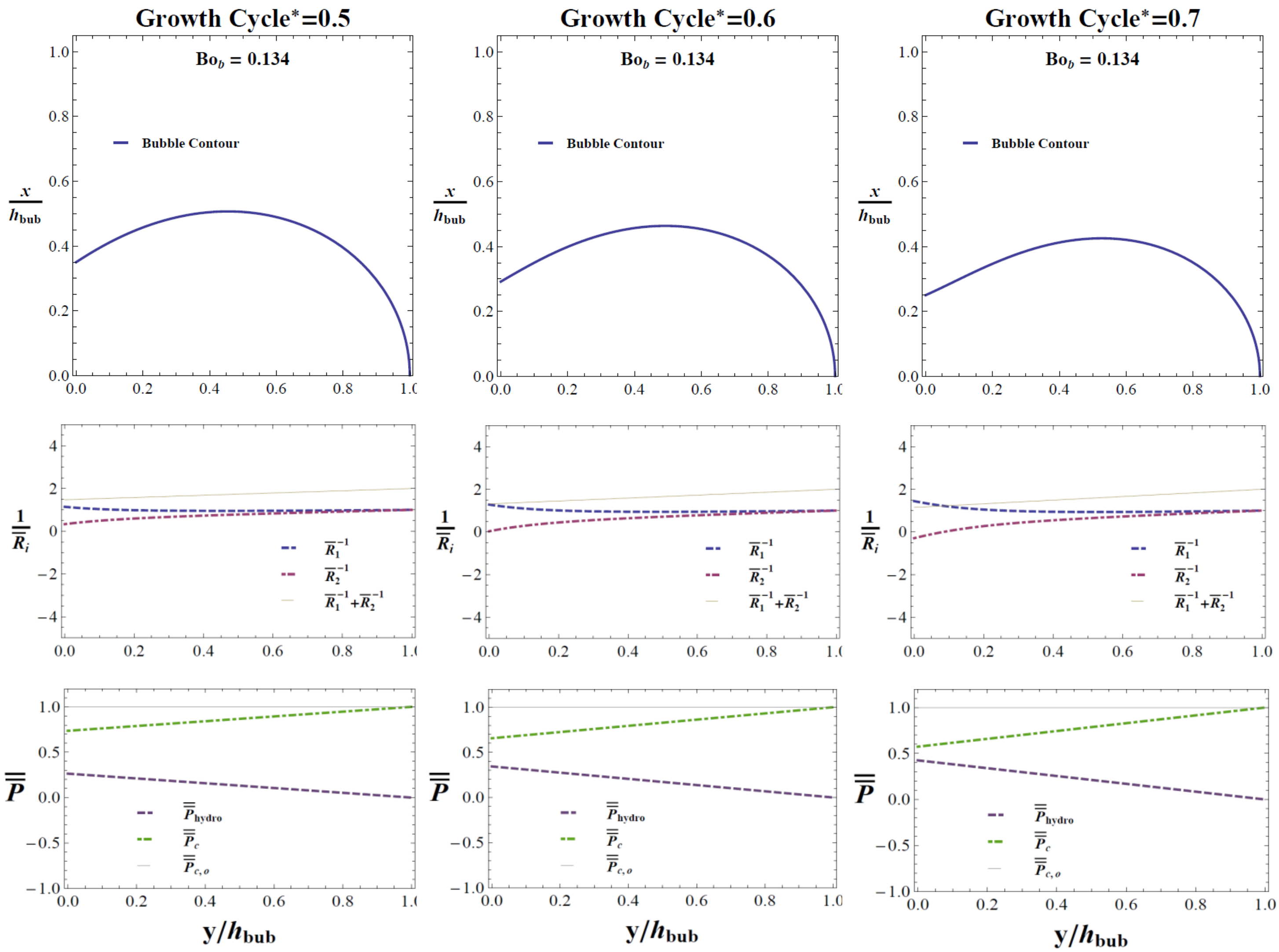

Figure 3-45: *(Top)* Bubble contours during mid stage growth for Bond number 0.134. *(Middle)* Principal radii of curvature profile along the bubble contour. *(Bottom)* Pressure distribution over the bubble.

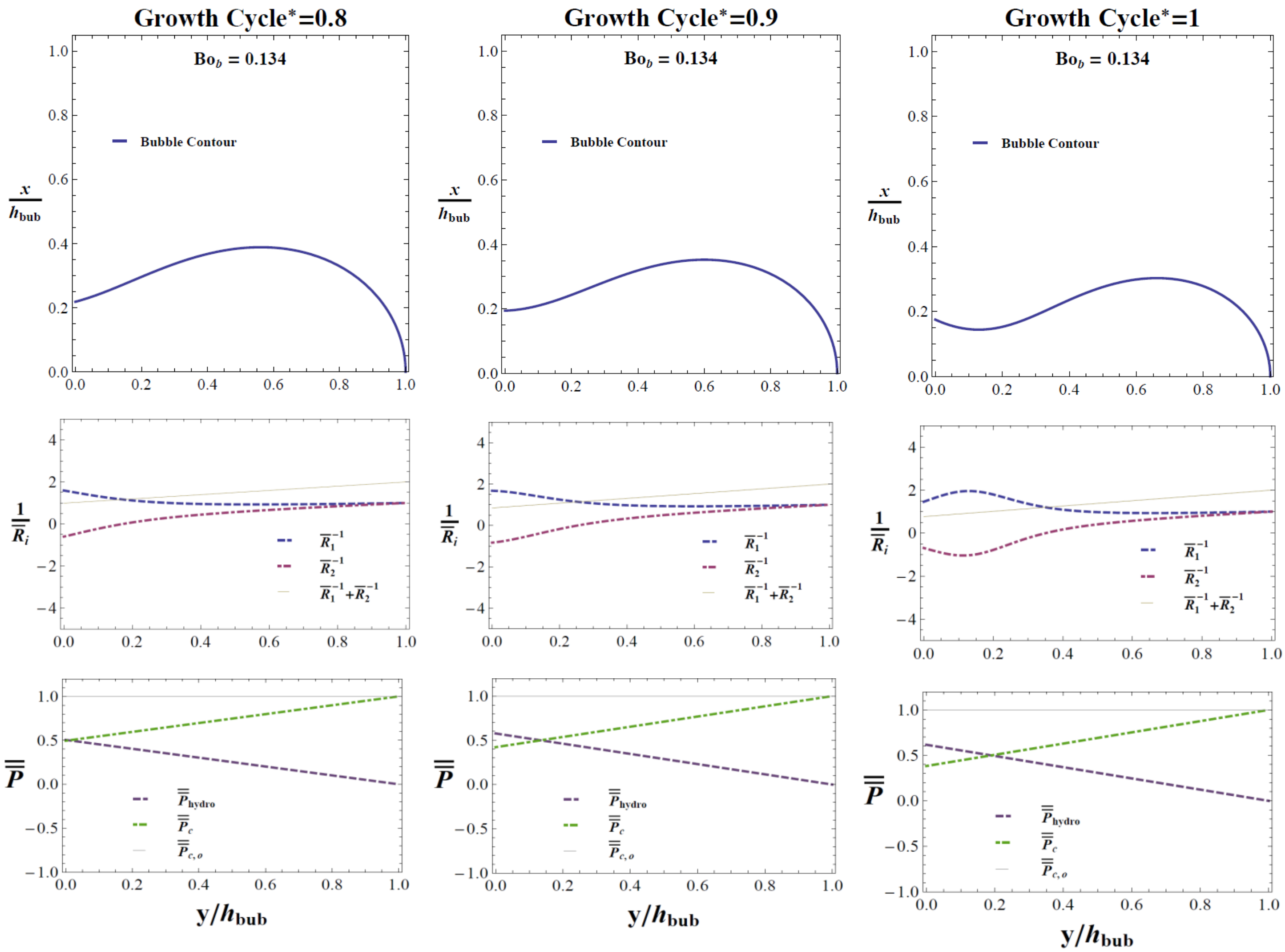

Figure 3-46: *(Top)* Bubble contours during late stage growth for Bond number 0.134. *(Middle)* Principal radii of curvature profile along the bubble contour. *(Bottom)* Pressure distribution over the bubble.

Figure 3-47 to Figure 3-49 illustrate the evolution of the pressure distribution over a bubble growing from a hemispherical inception to detachment for a Bond number of 0.546. Once again, in the analysis of this evolution, it is important to note the role of the hydrostatic pressure. In particular, the hydrostatic pressure is more dominant than the capillary pressure at some point along the bubble profile for the majority of the bubble growth cycle for the larger Bond number of 0.546. As a result, the neck formation is significant in the bubble shape evolution.

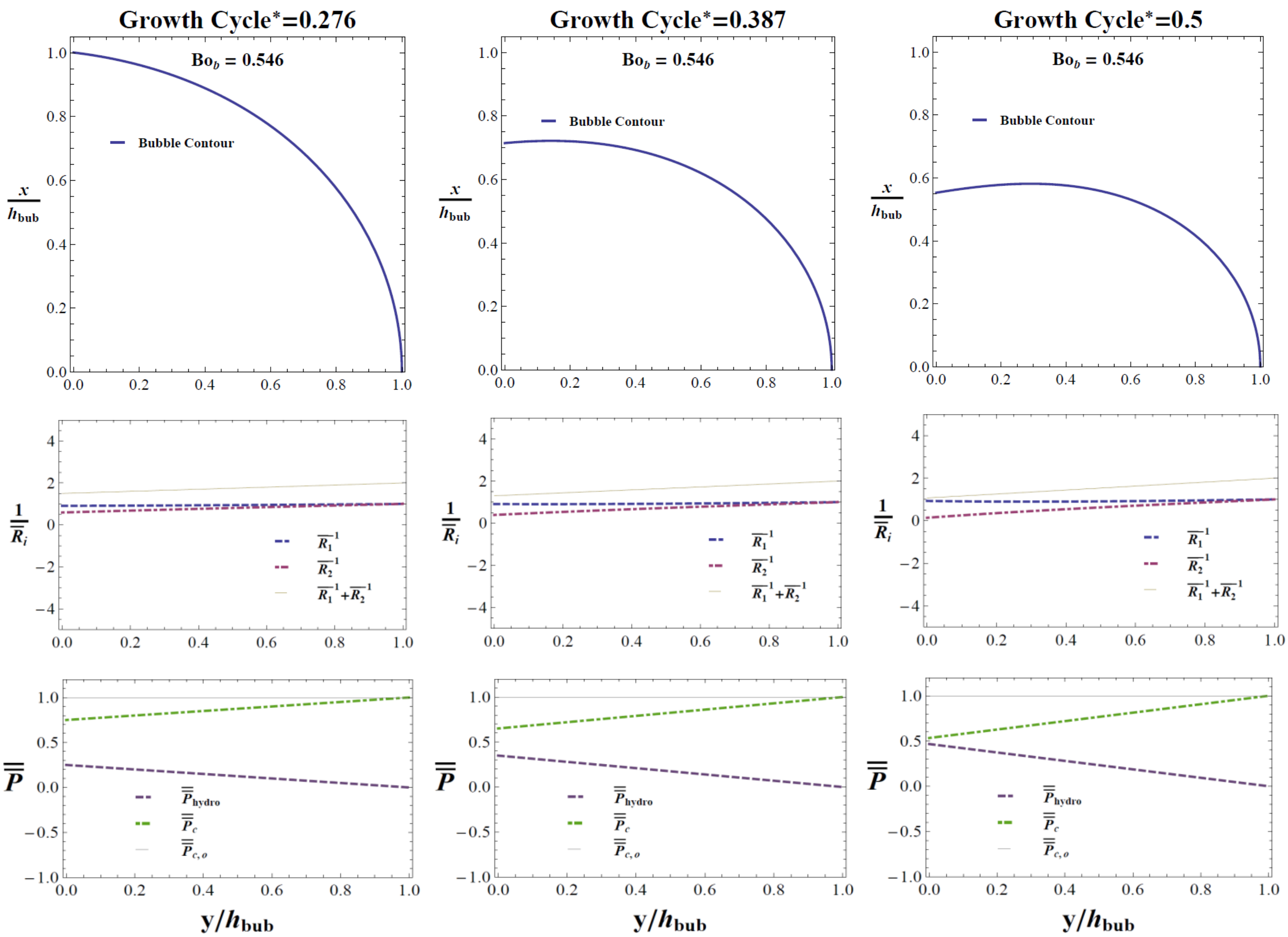

Figure 3-47: *(Top)* Bubble contours during early stage growth for Bond number 0.546. *(Middle)* Principal radii of curvature profile along the bubble contour. *(Bottom)* Pressure distribution over the bubble.

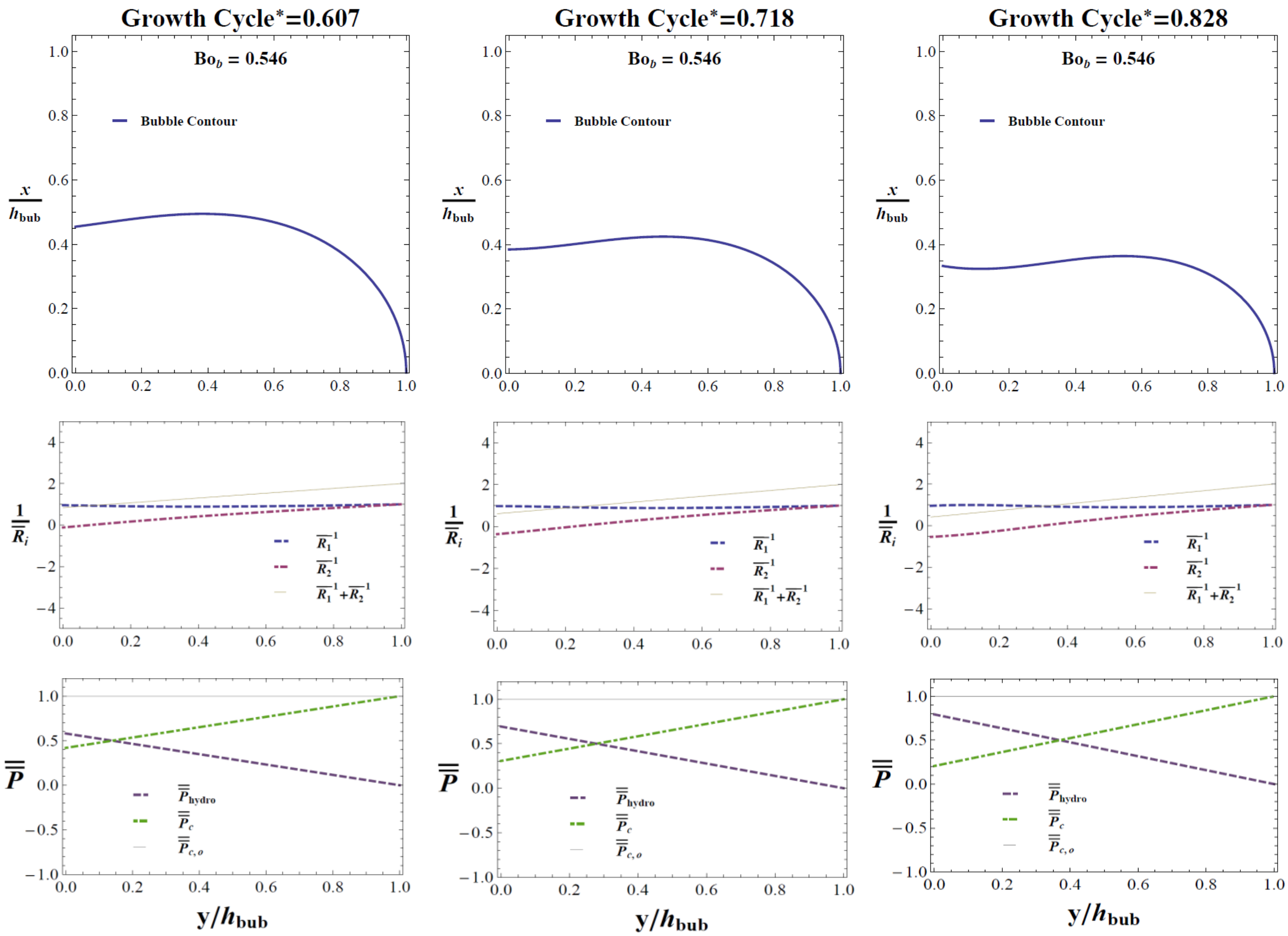

Figure 3-48: *(Top)* Bubble contours during mid stage growth for Bond number 0.546. *(Middle)* Principal radii of curvature profile along the bubble contour. *(Bottom)* Pressure distribution over the bubble.

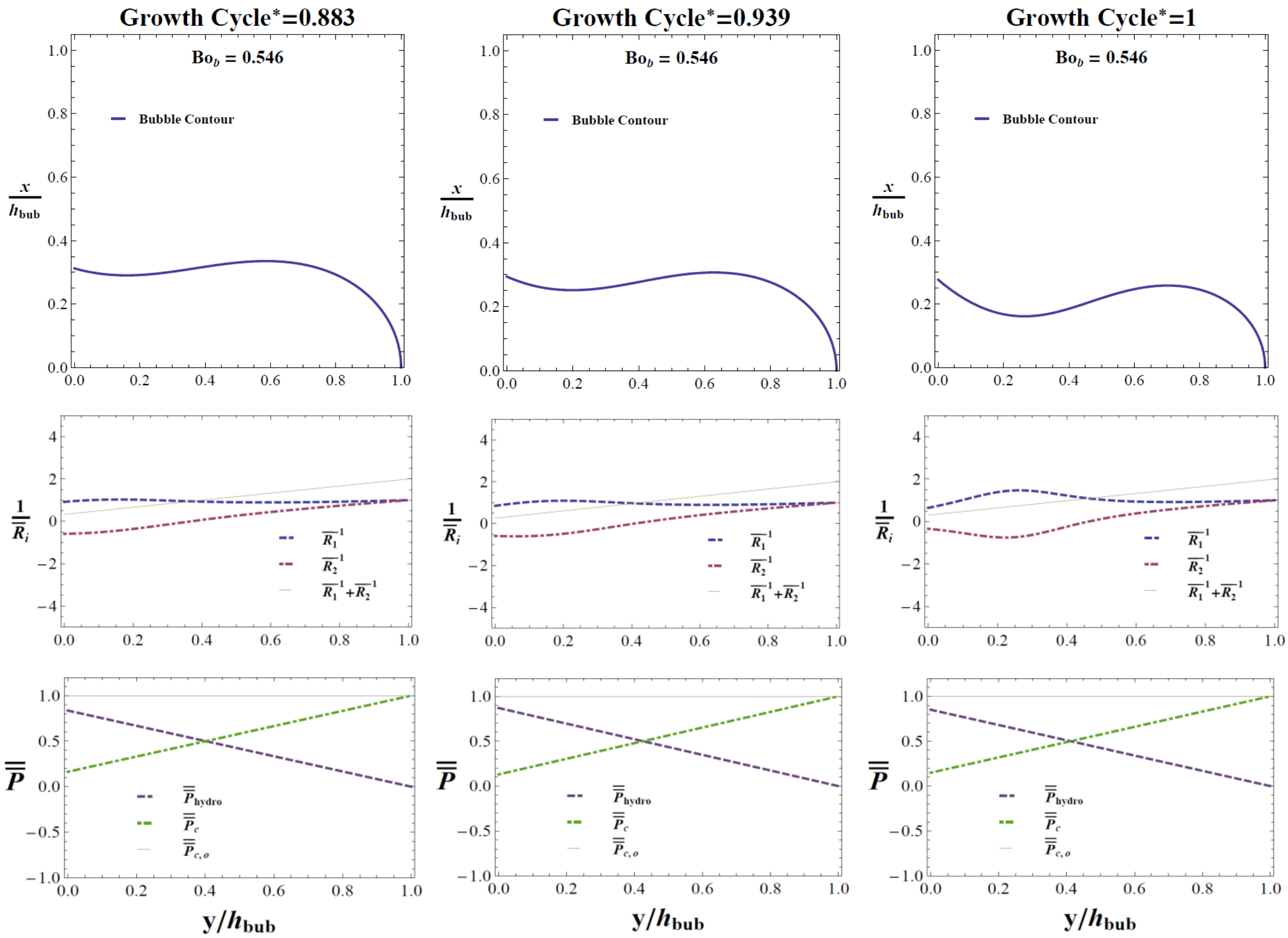

Figure 3-49: *(Top)* Bubble contours during late stage growth for Bond number 0.546. *(Middle)* Principal radii of curvature profile along the bubble contour. *(Bottom)* Pressure distribution over the bubble.

The behaviour of the principal radii of curvature featured in Figure 3-41 to Figure 3-49 parallel the results of the Modified sphericity study. In particular, the inverses of the principal radii of curvature are observed to diverge from each other and obtain their maximum absolute values, interrelated to the inward pinching on the walls of the bubble neck, earlier in the growth cycle for relatively large Bond numbers. This corresponds well with the observed trends of deviation from a Modified sphericity of unity. What the above analysis provides is a closer look at the mechanism that is causing the bubble to deviate from a Modified sphericity of unity. In particular, the slope of $\overline{R}_2^{-1}$ with respect to y/h_{bub} is positive for the entire bubble profile until the hydrostatic pressure becomes dominant. The bubble profile at points in which the slope of $\overline{R}_2^{-1}$ is negative yields an inward pinching trend. For the relatively large Bond numbers, the maximum absolute values of $\overline{R}_1^{-1}$ and $\overline{R}_2^{-1}$ are attained along the neck of the bubble away from the bubble foot during the mid to late growth stages. Prior to this occurrence in the growth cycle, the bubble appears to remain a spherical portion with straightening outer walls near the bubble foot. It is therefore postulated here that, prior to the hydrostatic pressure dominating the capillary pressure, a reasonable bubble shape approximation that would simplify any analytical attempts to solving the bubble growth problem would be to assume the bubble be a truncated spherical portion rising due to a cylindrical neck at its base.

This crucial location in bubble shape transformation in which the hydrostatic pressure becomes dominant can be identified by the following inequality,

3-44 $$\overline{\overline{P}}_{hydro} \geq \overline{\overline{P}}_{c}\,.$$

Recalling the normalized capillary equation (Eq. 3-43),

3-45 $$1 = \bar{\bar{P}}_c + \bar{\bar{P}}_{hydro}$$

and combining with the inequality of Eq. 3-44 yields the following condition for bubble deformation due to a dominant hydrostatic pressure,

3-46 $$\bar{\bar{P}}_{hydro} \geq \frac{1}{2}.$$

The above is easily shown to dissolve to,

3-47 $$R_o^* z^* \geq \frac{1}{Bo_b}$$

in which $z = h_{bub} - y$.

When analysing the above inequality, it is useful to consider its significance at the foot of the bubble when y = 0. This is due to the fact that, if the hydrostatic pressure surpasses the capillary pressure in magnitude, the bubble foot is the first location on the bubble profile during the growth cycle to experience the effects of a dominant hydrostatic pressure on the bubble shape. At the base of the bubble 3-47 becomes,

3-48 $$R_o^* h_{bub}^* \geq \frac{1}{Bo_b}.$$

This result is significant in that it illustrates the dependence of bubble shape on the Bond number. Notably, for very small Bond numbers, the product on the left hand side must be very large to satisfy the inequality making bubble deformation due to hydrostatic pressure dominance less likely.

Since the dominant hydrostatic pressure manifests itself first at the foot of a bubble during the bubble growth cycle, the smallest Bond number for which bubble deformation due to a dominant hydrostatic pressure term occurs is solved for by equating both sides of the inequality of Eq. 3-48 yielding,

3-49 $$R_o^* = \frac{1}{Bo_b h_{bub}^*} .$$

When including Eq. 3-49 into the numerical treatment of the capillary equation for a detaching bubble, the Capillary equation solution procedure provides one possible Bond number: 0.06032.

In this way, it is calculated that for Bond numbers strictly less than 0.06032, bubble deformation due to a dominant hydrostatic pressure term does not occur at any moment during the bubble growth cycle. For bubble growth in which the Bond number is larger than 0.06032, bubble deformation due to a dominant hydrostatic pressure term will occur during the bubble growth cycle. As illustrated in Figure 3-50, for bubble growth in which the Bond number is exactly 0.06032, the hydrostatic pressure is equal to the capillary pressure at the foot of the bubble at the moment of detachment.

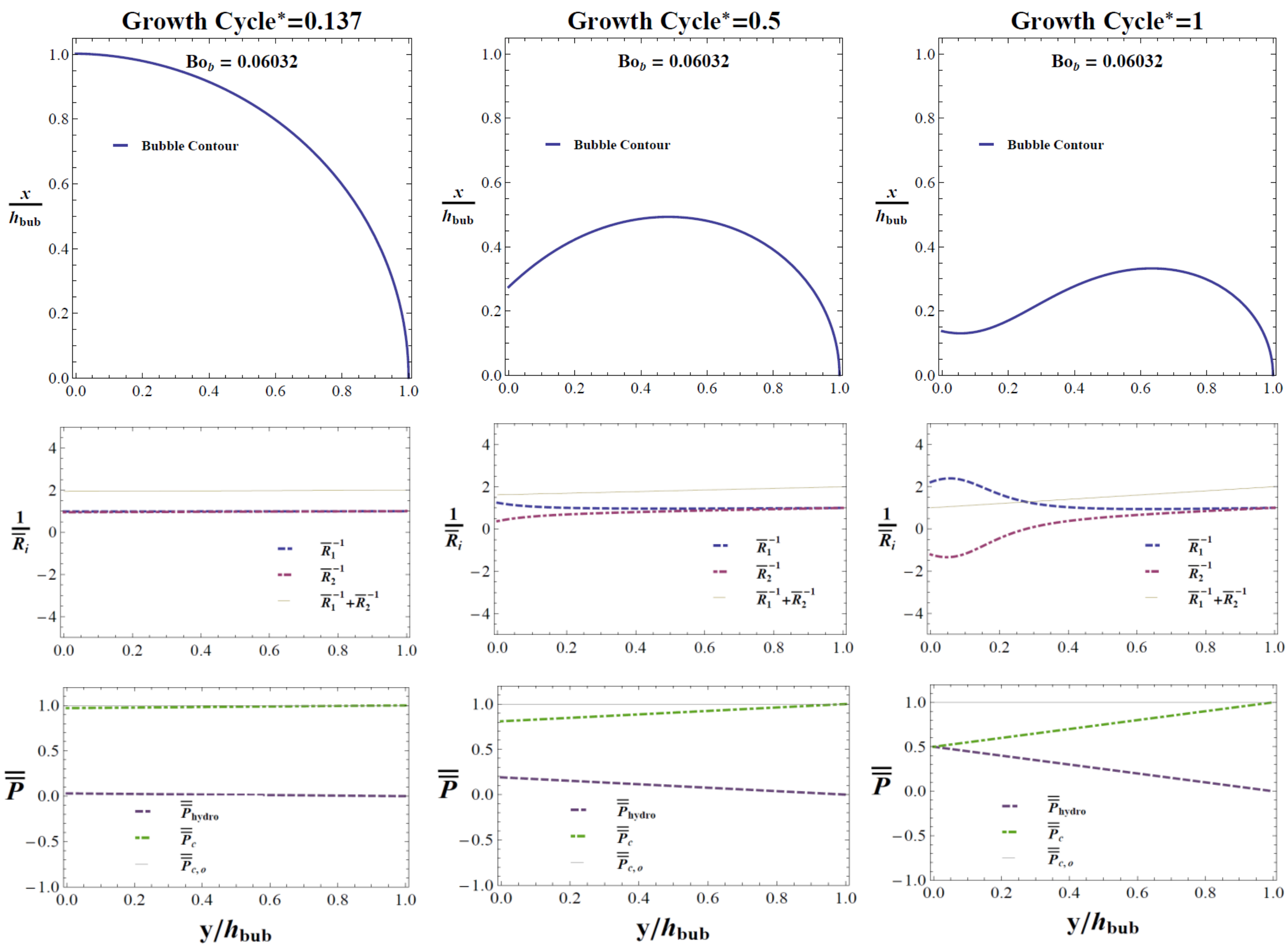

Figure 3-50: Limiting case for a truncated sphere rising due to a growing cylindrical neck assumption. *(Top)* Bubble contours: *Early*, *Mid* and *Late* stage growth for Bond number 0.06032. *(Middle)* Principal radii of curvature profile along the bubble contour. *(Bottom)* Pressure distribution over the bubble.

In light of this result, in the forthcoming chapter, a limiting condition for the proposed geometric model in which a bubble grows as an idealized truncated spherical bubble rising due to a growing cylindrical neck is set to be a Bond number that is less than or equal to 0.06.

To summarize, the results lead to the following generalization. A small Bond number is considered to be less than or equal to 0.06 and results in bubble growth that can be idealized as a truncated sphere transitioning from hemispherical to spherical while rising due an elongated cylindrical neck. In contrast, a large Bond number is considered to be greater than 0.06 and features, at some point in its growth cycle, a hydrostatic pressure that dominates over the capillary pressure causing bubble deformation in the form of an inward pinching of the neck walls.

3.8. Limitations of Numerical Model

The numerical treatment of the Capillary equation can generate bubble profiles in which the hydrostatic pressure is greater than the capillary pressure at the bubble apex, that is to say, it provides solutions for which $\bar{\bar{P}}_{hydro} > \bar{\bar{P}}_{c,o} = 1$. However, this provides a physically unrealistic solution since Eq. 3-43 implies that in this case, the pressure term $\bar{\bar{P}}_c$ would be negative effectively inverting the interfacial pressure balance. For this reason, the applicability of the numerical treatment of the capillary equation is limited to hydrostatic pressures satisfying the following inequality, 3-50 $\bar{\bar{P}}_{hydro} \leq 1$

which dissolves into,

3-51 $R_o^* z^* \leq \dfrac{2}{Bo_b}$.

The limiting case of the applicability of the capillary equation is therefore that in which a hydrostatic pressure $\bar{\bar{P}}_{hydro} = 1$ is included into the solution at the point in which $\bar{\bar{P}}_{hydro}$ unity is first attained: the bubble foot. The equality

3-52 $R_o^* h_{bub}^* = \dfrac{2}{Bo_b}$

is thus included into the numerical treatment of the capillary equation for a detaching bubble. For this restrictive condition, the Capillary equation solution procedure provides one possible Bond number: 0.9941.

In this way, it is calculated that the capillary equation numerical treatment is applicable to bubble shape profiles for Bond numbers less than or equal to 0.9941. This limiting case is illustrated in Figure 3-51 featuring $\bar{\bar{P}}_{hydro} = 1$ and $\bar{\bar{P}}_c = 0$ in the detachment frame.

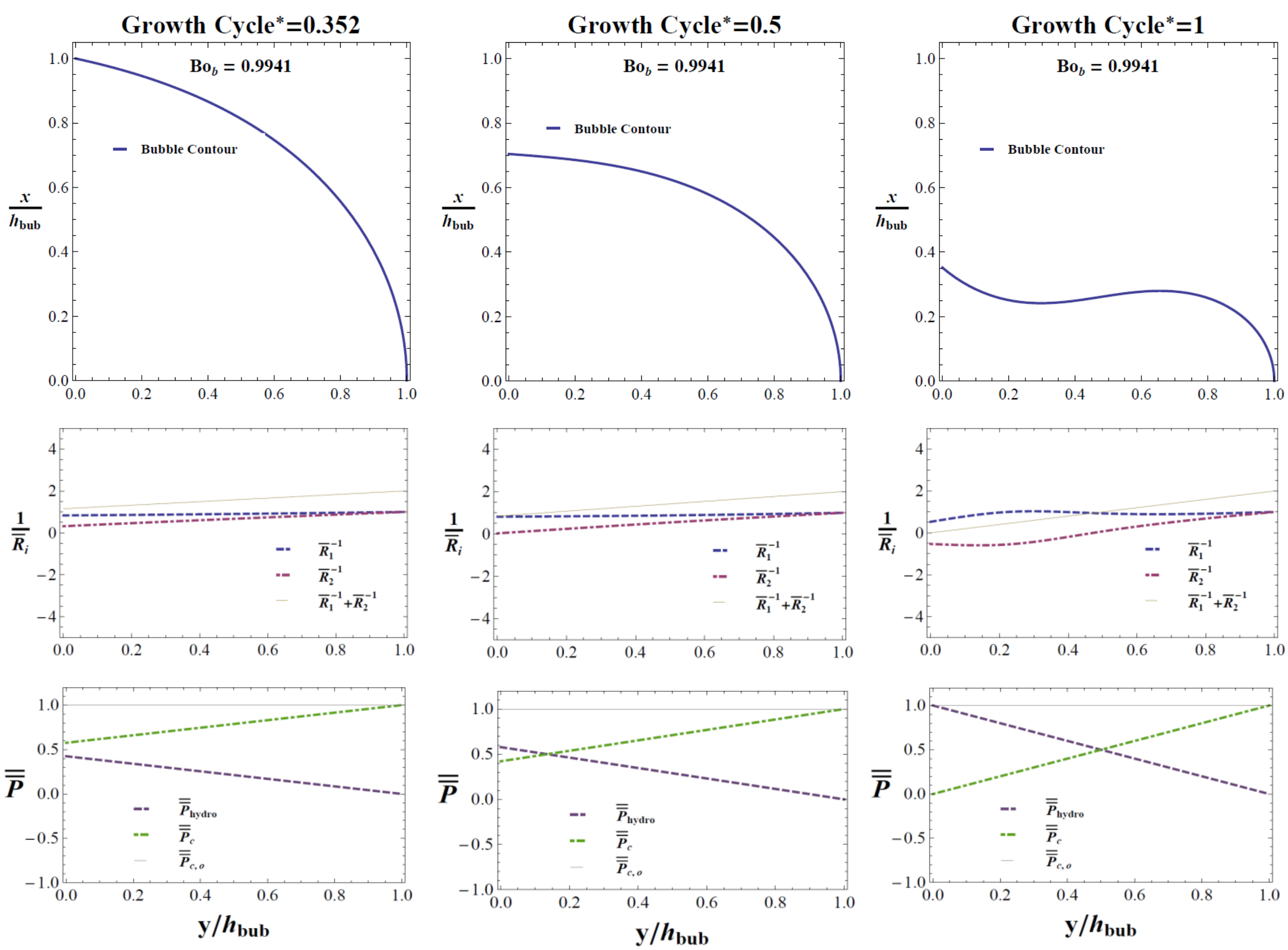

Figure 3-51: Limiting case for the applicability of the capillary equation. *(Top)* Bubble contours: *Early*, *Mid* and *Late* stage growth for Bond number 0.9941. *(Middle)* Principal radii of curvature profile along the bubble contour. *(Bottom)* Pressure distribution over the bubble.

Further model limitations are due to the fact that, in the development of the numerical model, the Young-Laplace equation was used neglecting the viscous term. In order to justify this assumption, it is imperative that bubble growth simulations remain within the quasi-static regime. Furthermore, the capillary equation is deemed valid for bubble profiles transitioning from an *AR* of ½ (approximately hemispherical) to detachment. Indeed, experimentally measured bubble growth from nucleation to hemispherical is not observed as quasi-static and therefore cannot bench mark the capillary equation bubble profiles prior to an *AR* of ½.

3.9. Conclusion

A numerical treatment of the capillary equation is benchmarked against bubble profiles for quasi-static bubble growth due to gas injection and for heat-transfer controlled bubble growth due to vaporization. Due to a limited applicability of the hydrostatic pressure term, the solution procedure is deemed valid for bubble growth applications in which the Bond number with characteristic length equal to the bubble foot radius is less than or equal to 0.9941.

This study of bubble degree of sphericity demonstrates that a fixed base truncated spherical geometry more accurately describes bubble shape during bubble growth than a spherical geometric assumption. Furthermore, it is shown that bubble shape is strictly dependent on the Bond number. The results may be summarized as follows: smaller Bond numbers favour a more spherical bubble shape. The results remain true for Bond numbers varying due to a varying gravitational constant as they do for Bond numbers varying due to a varying bubble foot radius. In particular, bubbles of very different size with the same Bond number are shown to have the same shape profile.

Furthermore, it is shown that for small Bond numbers less than or equal to 0.06 the hydrostatic pressure does not dominate the capillary pressure at any stage during the bubble growth cycle and consequently the bubble behaves as an approximate truncated sphere rising due to the elongation of a cylindrical neck. For large Bond numbers greater than 0.06, this geometric simplification is no longer valid due to inward pinching in the lower section of the bubble attributed to a hydrostatic pressure term that is of greater magnitude than the capillary pressure term.

4. GAS INJECTED ADIABATIC BUBBLE GROWTH

4.1. Introduction

A common shortcoming of analytical attempts to describe bubble growth and/or bubble detachment stem from geometric models which over constrain the shape of the bubble as it transitions from inception to detachment.

In this investigation, a geometric model is proposed in which the bubble evolves from a hemisphere into a truncated sphere with a fixed base radius while rising due to the formation and elongation of a cylindrical neck at its base. An adiabatic bubble growth model is developed in the quasi-static regime in order to validate the bubble geometry. This same bubble shape will then be adopted in a forthcoming chapter to heat-induced vapour bubble growth.

The key assumptions are:

1. Early in the growth cycle the bubble attains a hemispherical shape. This is due to the fact that in this early stage, buoyancy is not a dominant force and the bubble will take a hemispherical shape in order to minimize its free energy.
2. The bubble will grow as a spherical segment rising due to an elongating cylindrical neck with a radius equal to the orifice radius.
3. Subsequent to departure a mass equivalent to that of a hemispherical bubble is left behind. This is depicted in Figure 4-1 in which the centre of curvature of the bulk of the bubble is noted *C*.

The geometric shape assumption is a result of the numerical treatment of bubble shape evolution in chapter 3 for applications in which the Bond number is less than or equal to 0.06.

The incipient hemispherical bubble assumption is due to the relatively instantaneous event that is the transition from an absence of vapour at a nucleation site to the presence of a hemispherical bubble. Indeed, for the relatively slow *n*-pentane vapour bubble growth experiments with a wall superheat of 2.1K carried out by Siedel *et al.* (2008), the transition from an inactive nucleation site to the presence of a hemispherical bubble made up for less than 0.22% of the bubble growth cycle and is therefore inertia driven. The hemispherical inception assumption is deemed appropriate for quasi-static bubble growth analysis.

Recalling that a bubble idealized to be a perfect sphere is fully described by a single parameter - its radius - the proposed geometry of Figure 4-1 requires three shape parameters for its full geometric description: the radius of the truncated spherical segment, the height of the cylindrical neck, and the radius of the base of the cylindrical neck. In this way, the analytical treatment of bubble growth becomes more complex. The advantage of the proposed geometry of Figure 4-1 is that it more accurately describes low Bond number quasi-static bubble formations thereby leading to more accurate bubble characteristic predictions. Furthermore, the proposed geometry of Figure 4-1 alleviates the contradictory notion that a perfect sphere with at most a singularity in contact with a solid surface could have a surface tension capable of opposing the buoyancy of the bubble.

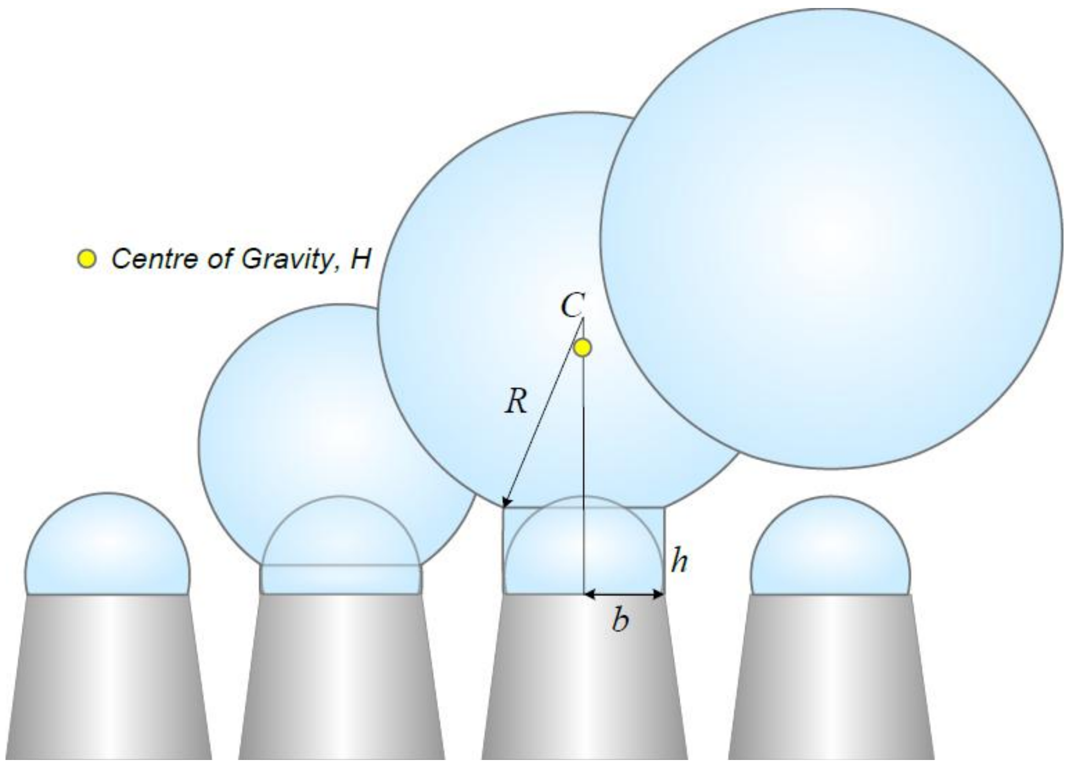

Figure 4-1: Geometry of growing bubble with formation of a cylindrical neck.

Considering the geometry of Figure 4-1, the centre of curvature of the bubble is related to the bubble radius, noted *R*, the orifice radius, noted *b*, and the height of the cylindrical neck, noted *h*, in the following expression,

4-1 $$C = \sqrt{R^2 - b^2} + h \ .$$

Admittedly this is a simple geometry. Even still, the bubble will grow and elongate with the development of the neck resulting in a centre of gravity vertical component that surpasses the magnitude of the radius of the bubble as is observed in reality (Lesage *et al.*, 2009). Conversely, bubble growth that is modeled as a perfect sphere or as a truncated sphere with a fixed base radius has a centre of gravity vertical component that, due to geometric constraints, remains inferior in magnitude to the bubble radius which is contrary to what we know is true .

In what follows, a geometric detachment relation is developed based on a postulated mass balance at the moment of bubble detachment. This relation is dependent on the proposed geometric shape of a bubble. A force balance based on the proposed bubble geometric model is coupled with the geometric detachment relation into a fully analytical bubble growth model for adiabatic gas injected bubble growth from a submerged orifice with a constant volumetric flow rate.

4.2. Geometric Detachment Relation

At the moment of detachment the bubble is assumed to split into two segments such that the first is a detaching spherical bubble and the second is a new hemispherical bubble with radius b fixed to the orifice. This assumption is supported in Figure 4-2; captured bubble images from Sergio Di Bari's experiments described in section 2.4 are presented during the rapid bubble pinch-off at detachment. It is shown that an approximate hemispherical bubble is left at the orifice from which the bubble emerged. The lengths are normalized by the orifice radius and time is normalized by the time of bubble detachment,

$$x^* = x/b$$
$$y^* = y/b \qquad (4\text{-}2)$$
$$t^+ = t/t_d$$

It is noted that in the geometric detachment postulation of this paper, the process of a bubble detaching into two segments is considered to be an instantaneous event. Indeed, the moment of neck formation is often equated with the moment of bubble detachment since the life of the neck portion of the bubble compared with the growth cycle of the bubble makes the formation of the neck and detachment of the bubble nearly simultaneous event (Van der Geld, 2009). Furthermore, bubble pinch-off is only a fraction of the necking phenomenon and is idealized here as instantaneous. Indeed, experimental results of bubble pinch-off illustrated in Figure 4-2 show bubble pinch-off to make up less than 0.2 % of the bubble growth cycle.

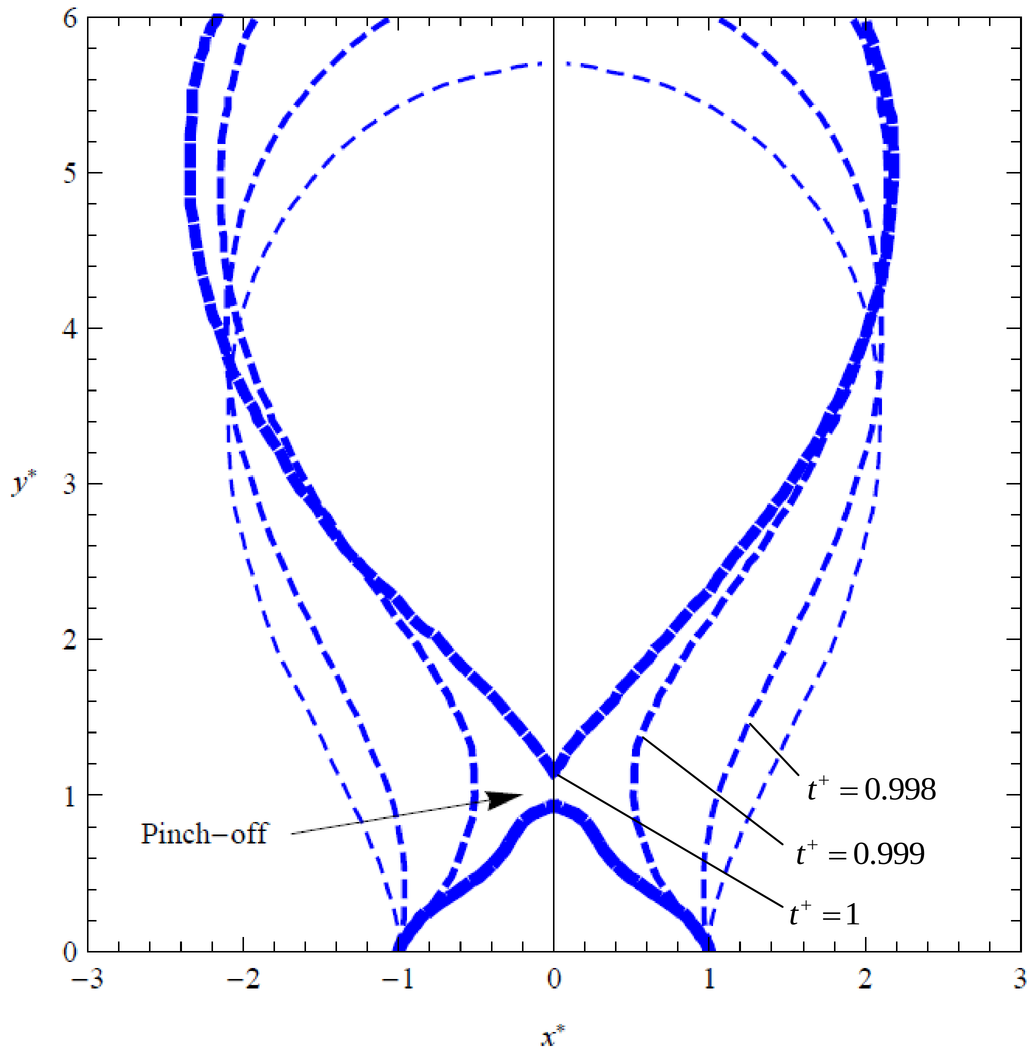

Figure 4-2: Non-dimensional bubble contours of bubble pinch-off. Bubble images providing the profiles captured by Sergio Di Bari.

Similar pinch-off phenomenon's were observed by Buwa *et al.* (2007); in their experimental and numerical study, air was injected into a quiescent liquid at constant flow rates ranging from 100 cm^3/min to 1700 cm^3/min through submerged orifices of diameters ranging from 2 mm to 10 mm. At the moment of bubble detachment, it was consistently observed that the bulk of the bubble detached itself from an approximate hemispherical bubble that remained fixed to the orifice. Further experimental results exposing this detachment phenomenon are detailed in Burten *et al.* (2005), Kiem *et al.* (2006), Thoroddsen *et al.* (2007) and Thoroddsen *et al.* (2008).

The interfacial pressure difference at the apex of the bubble at the moment of detachment is deduced from Eq. 3-11 to be,

4-3 $$\Delta P_{o,d} = \frac{2\sigma}{R_d}$$

in which R_d is the principal radius of curvature of the detaching segment. However, assuming that R_d is larger than b, a greater interfacial pressure difference at the apex of the hemispherical bubble is required,

4-4 $$\Delta P_{o,hemi} = \frac{2\sigma}{b}.$$

Specifically, the difference in the gas pressure at the apex of the detaching bubble to the gas pressure necessary to maintain a hemispherical shape at the orifice is greater than zero. In particular, from Eq. 3-16

4-5 $$P_{v,o,hemi} - P_{v,o,d} = 2\sigma\left(\frac{1}{b} - \frac{1}{R_d}\right) + \rho_l g\left(h_{bub,d} - b\right) > 0$$

in which $h_{bub,d}$ is the height of the bubble at detachment, $P_{v,o,hemi}$ is the vapour pressure at the apex of the incipient hemispherical bubble and $P_{v,o,d}$ is the vapour pressure at the apex of the detaching bubble.

This implies that the pressure in the gas of the detaching bubble is less than the pressure required for the hemispherical bubble: $P_{v,o,hemi} > P_{v,o,d}$. Therefore, post detachment; the hemispherical bubble that is left attached to the orifice will experience a downward force that is dependent on the relative size of the detaching segment's radius to the orifice radius. This can contribute to deformation from a hemispherical shape and to weeping into the cavity. Weeping occurs when liquid flows down the inner walls of a submerged orifice from which gas is issuing (Zhang & Tan, 2000).

It is postulated here that this moment of detachment occurs once there is sufficient vapour mass in the neck of the bubble to complete the spherical portion of the detaching vapour bubble and to leave behind enough vapour mass to also form a hemispherical vapour bubble of radius *b* at the tip of the orifice. Further assuming that the vapour density is uniform, this detachment relation requires the volume of the cylindrical neck portion to be equal to the volume necessary to complete the truncated spherical portion into a sphere and the volume necessary to leave a hemispherical bubble of radius *b* at the tip of the orifice.

Equating these volumes,

$$\underbrace{\pi b^2 h}_{V_{Neck}} = \underbrace{\frac{1}{3}\pi\left(R-\sqrt{R^2-b^2}\right)^2\left(2R+\sqrt{R^2-b^2}\right)}_{V_{\text{Sphere}}-V_{\text{Truncated Sphere}}} + \underbrace{\frac{2}{3}\pi b^3}_{V_{\text{Hemisphere}}} \tag{4-6}$$

yields the following geometric detachment relation relating the height of the cylindrical neck at the moment of detachment with the bubble detachment radius and the orifice radius,

$$h_d = \frac{\left(R_d-\sqrt{R_d^2-b^2}\right)\left(2R_d+\sqrt{R_d^2-b^2}\right)}{\left(R_d+\sqrt{R_d^2-b^2}\right)} + \frac{2}{3}b\,. \tag{4-7}$$

In order to compare this detachment relation to the similar empirically developed detachment relation of Oguz & Prosperetti (1993), the vertical component of the centre of curvature at the moment of detachment, noted C_d, is expressed in terms of the bubble detachment radius of Eq. 4-7. To this end, Eq. 4-7 is substituted into Eq. 4-1 yielding the following centre of curvature vertical component at the moment of detachment which is a result of the geometric detachment relation,

$$C_d = \frac{2R_d^2}{\left(R_d+\sqrt{R_d^2-b^2}\right)} + \frac{2b}{3}\,. \tag{4-8}$$

A comprehensive study of bubble detachment from submerged orifices was performed by Oguz & Prosperetti (1993) in which it was observed that the centre of curvature was of the order of the bubble radius plus the orifice tip radius at bubble detachment. In order to run a numerical treatment of the bubble growth problem, the following detachment relation, resulting from experimental observations, was put forth by Oguz & Prosperetti (1993):

4-9 $C_d = R_d + b$ (Oguz & Prosperetti, 1993).

It can be argued that the geometric detachment relation of Eq. 4-8 dissolves into Eq.4-9 since the ratio of the bubble radius to orifice was commonly large for the experimental conditions of Oguz & Prosperetti (1993). Assuming then that $\sqrt{R_d^2 - b^2} \lesssim R_d$, Eq. 4-8 reduces to,

4-10 $C_d \gtrsim \dfrac{2R_d}{R_d + R_d} = R_d + \tfrac{2}{3}b$.

The above shows that the geometric detachment relation of Eq. 4-8 is of the same order of magnitude as the empirically developed relation of Oguz & Prosperetti (1993).

In order to validate this geometric detachment relation with experimentally measured values, it is compared with bubble detachment radius and bubble detachment centre of gravity coordinates that are the result of measurements from image processed bubbles of Sergio Di Bari's experiments described in section 3.4.

To this end, the geometric detachment relation is presented in terms of the bubble centre of gravity vertical coordinate at the moment of bubble detachment.

The centre of gravity vertical coordinate for the proposed geometry is illustrated in Figure 4-3 below.

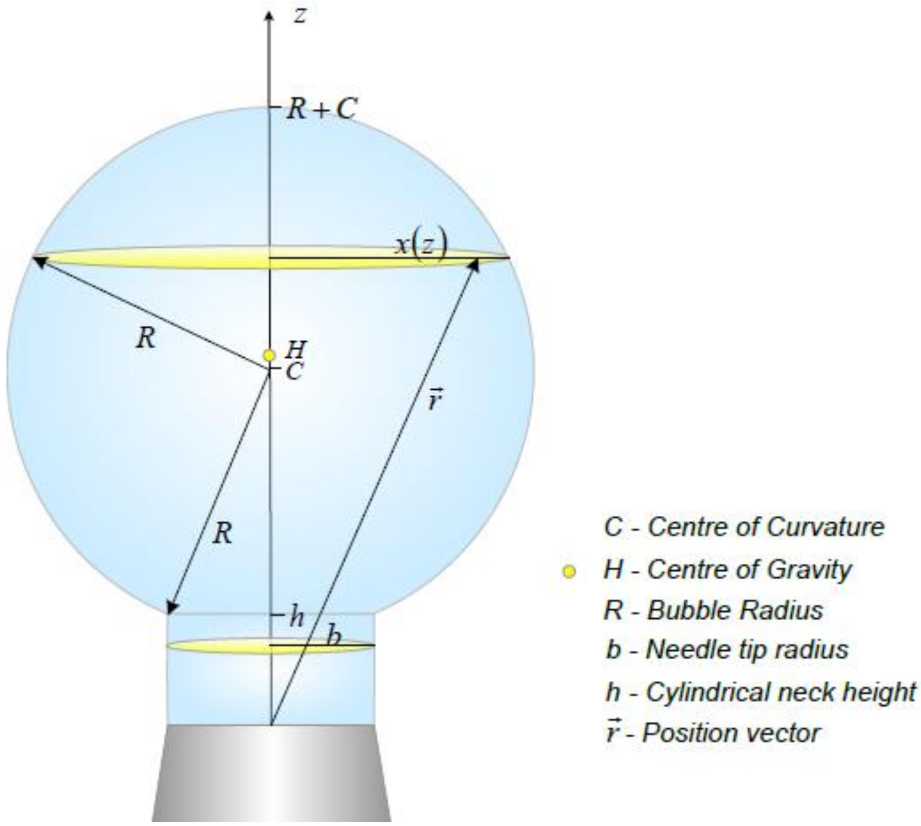

Figure 4-3 : Area of integration for the calculation of the centre of gravity.

Adopting the geometry of Figure 4-3, the centre of gravity vertical component, noted *H*, is deduced from the general vector definition of the centre of gravity,

4-11 $$\vec{H} = \frac{\int_0^{R+C} \vec{r}\rho dV}{\int_0^{R+C} \rho dV}.$$

Assuming the bubble to be symmetric about the vertical axis due to an absence in cross flow, solving 4-11 expresses the centre of gravity vertical component in terms of the height of the cylindrical portion, the radius of the spherical portion and the centre of curvature (refer to Appendix 7.6). The detachment relation in terms of the centre of gravity is expressed as the following condition,

4-12 $$H_d = \frac{(R_d + C_d + h_d)(3R_d - C_d + h_d)(R_d + C_d - h_d) + 2h_d(R_d - C_d + h_d)(R_d + C_d + 2h_d)}{4\left((2R_d - C_d)(R_d + C_d + h_d) + 2h_d^2\right)}.$$

It is important to note that, by substituting Eq.4-7 and Eq. 4-8 into the above, the geometric detachment centre of gravity relation is expressed in terms of the detachment radius and the orifice radius only.

4.2.1. Non-Dimensional Forms of the Geometric Detachment Relation

The geometric detachment relation described in Eq. 4-7, Eq. 4-8 and Eq. 4-12 can be conveniently expressed in non-dimensional terms by defining the orifice radius as the characteristic length thereby defining the normalized parameters as,

4-13 $$\begin{cases} R^* = \dfrac{R}{b} \\ s^* = \dfrac{s}{b} = \sqrt{R^{*2} - 1} \end{cases}.$$

Dividing all terms of Eq. 4-7 by *b* and all terms of the Eq. 4-8 by *b*, the non-dimensional forms of the geometric detachment relation for the neck height and for the centre of curvature are, respectively,

4-14 $$h_d^* = \frac{\left(R_d^* - s_d^*\right)\left(2R_d^* + s_d^*\right)}{\left(R_d^* + s_d^*\right)} + \frac{2}{3}$$

and

4-15 $$C_d^* = \frac{2R_d^{*2}}{\left(R_d^* + s_d^*\right)} + \frac{2}{3}.$$

Finally, the expression of the geometric detachment relation used to compare with the validating data is the non-dimensional form of Eq. 4-12, that is to say, the normalized bubble centre of gravity,

4-16 $$H_d^* = \frac{\left(R_d^* + C_d^* + h_d^*\right)\left(3R_d^* - C_d^* + h_d^*\right)\left(R_d^* + C_d^* - h_d^*\right) + 2h_d^*\left(R_d^* - C_d^* + h_d^*\right)\left(R_d^* + C_d^* + 2h_d^*\right)}{4\left(\left(2R_d^* - C_d^*\right)\left(R_d^* + C_d^* + h_d^*\right) + 2h_d^{*2}\right)}.$$

4.2.2. Geometric Detachment Relation Validation

The experimental validation of the geometric detachment relation is illustrated in Figure 4-4. Experimental measurements from Sergio Di Bari's captured images of adiabatic bubble growth, described in section 3.4 of this document, for all orifice radii tested and all flow rates tested are compared with the geometric detachment relation of this section.

In particular, the normalized bubble detachment radius versus the normalized bubble centre of gravity predicted by the detachment relation is plotted against their experimentally measured values.

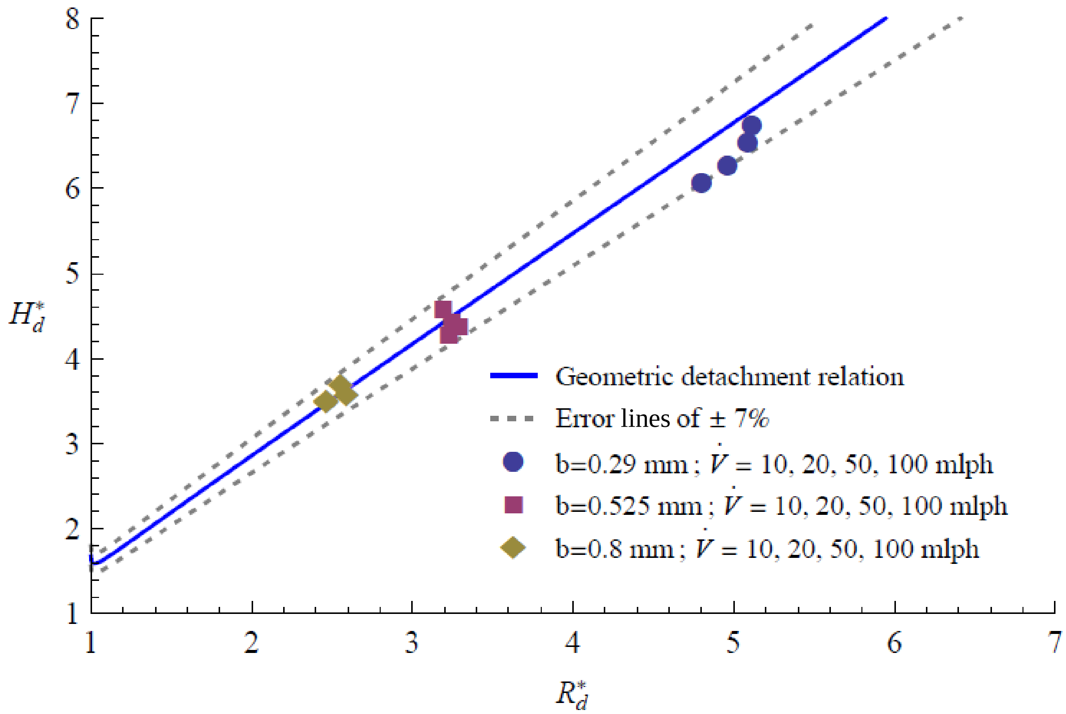

Figure 4-4: Experimental validation of Eq. 4-16 plotting the normalized bubble detachment radius versus the normalized bubble centre of gravity.

The results show that the geometric detachment relation is within the error lines of ±7 % with the experimentally measured values.

4.3. Force Balance Detachment Criterion

A detachment criterion based on a force balance is developed in an attempt to bring analytical closure to the gas injected adiabatic bubble growth problem. To this end, the forces acting on the bubble are identified in consideration of the geometric bubble assumption of this chapter illustrated in Figure 4-3. Once these are quantified, a force balance is applied which predicts the bubble radius at the moment of detachment.

4.3.1. Forces Acting on Growing Bubble

The applicable forces acting on a bubble with the geometric bubble assumption of this chapter are illustrated in Figure 4-5. They are identified as the capillary force, the buoyancy force, the force due to contact pressure, the force due to gas momentum and the force due to drag.

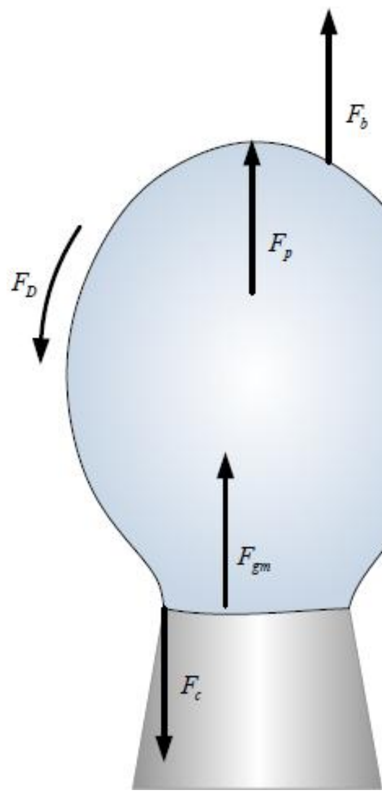

Figure 4-5: Forces acting on a growing bubble.

4.3.1.1. Capillary Force

The downwardly directed capillary force, noted F_c, acts along the triple contact line at the base of the bubble. For an arbitrary injected vapour bubble that is symmetric about the vertical axis, the triple contact line is the perimeter of the orifice from which the bubble is issuing. Integrating about this line, considering the orifice radius to be *b*, yields the capillary force,

4-17 $$\vec{F}_c = -2\int_0^{\pi} b\sigma\vec{t}\left(\varphi\right)d\varphi \, .$$

In the above equation $\vec{t}$ is a unit vector tangent to the interface of the bubble and normal to the contact line for which the negative sign represents the inward direction of the force (Klausner *et al.*, 1993; Duhar & Colin, 2006). This vector and the resultant capillary force are illustrated in Figure 4-6 for an arbitrary bubble issuing from an orifice of radius *b*.

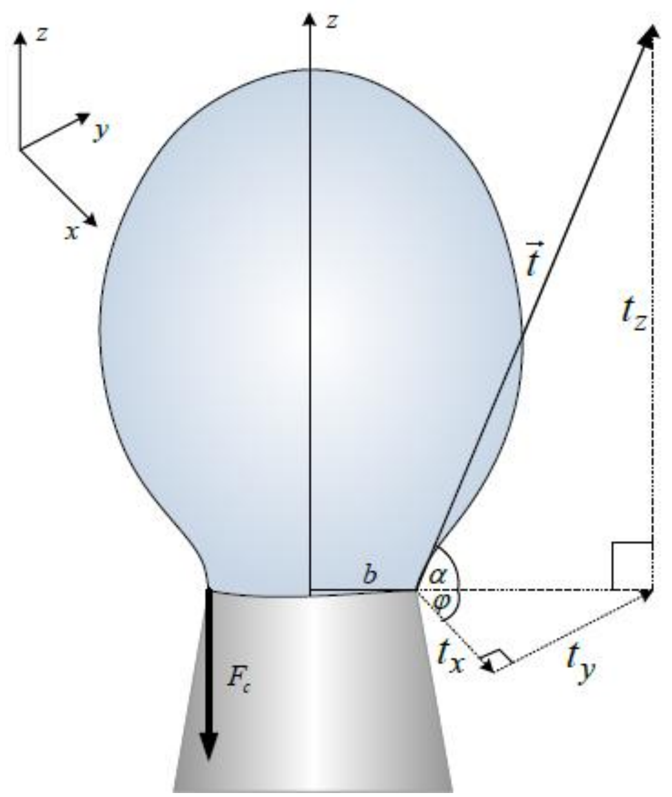

Figure 4-6: Capillary force representation.

The components of $\vec{t}$ are defined by the magnitude of the vector, the contact angle, noted α, and an angle φ in the *x*-*y* plane:

4-18 $$\begin{cases} t_x = \left\|\vec{t}\right\| \cos\alpha \cos\varphi \\ t_y = \left\|\vec{t}\right\| \cos\alpha \sin\varphi \\ t_z = \left\|\vec{t}\right\| \sin\alpha \end{cases}.$$

When integrating over the contact line, the resulting *x* and *y* directional components of the capillary force vector have zero magnitude leaving only the *z* directional component. In light of the spherical symmetry, the *z* component is independent of φ, it is unchanged along the perimeter of the orifice. Therefore, only the vertical component of the Capillary force is non-zero. Equation 4-17 reduces to the following *z*-directional force,

4-19 $$F_c = -2\int_0^{\pi} b\sigma \left\|\vec{t}\right\| \sin\alpha d\varphi = -2\pi b\sigma \left\|\vec{t}\right\| \sin\alpha .$$

Applying this to the geometric assumption of this chapter (Figure 4-3), in which the contact angle is a right angle at the triple contact line, and recalling that $\vec{t}$ is a unit vector, the capillary force is reduced to its final form representing a downward force,

4-20 $$F_c = -2\pi b\sigma .$$

4.3.1.2. Buoyancy Force

The upwardly directed buoyancy force, noted F_b is obtained by integrating the hydrostatic component of the liquid pressure over the bubble cap only, 4-21 $$F_b = \int (\rho_l - \rho_v) g dV \ .$$

For the spherical segment of the proposed geometric model, this implies the volume of the region with liquid both above and below it. This region is illustrated in Figure 4-7.

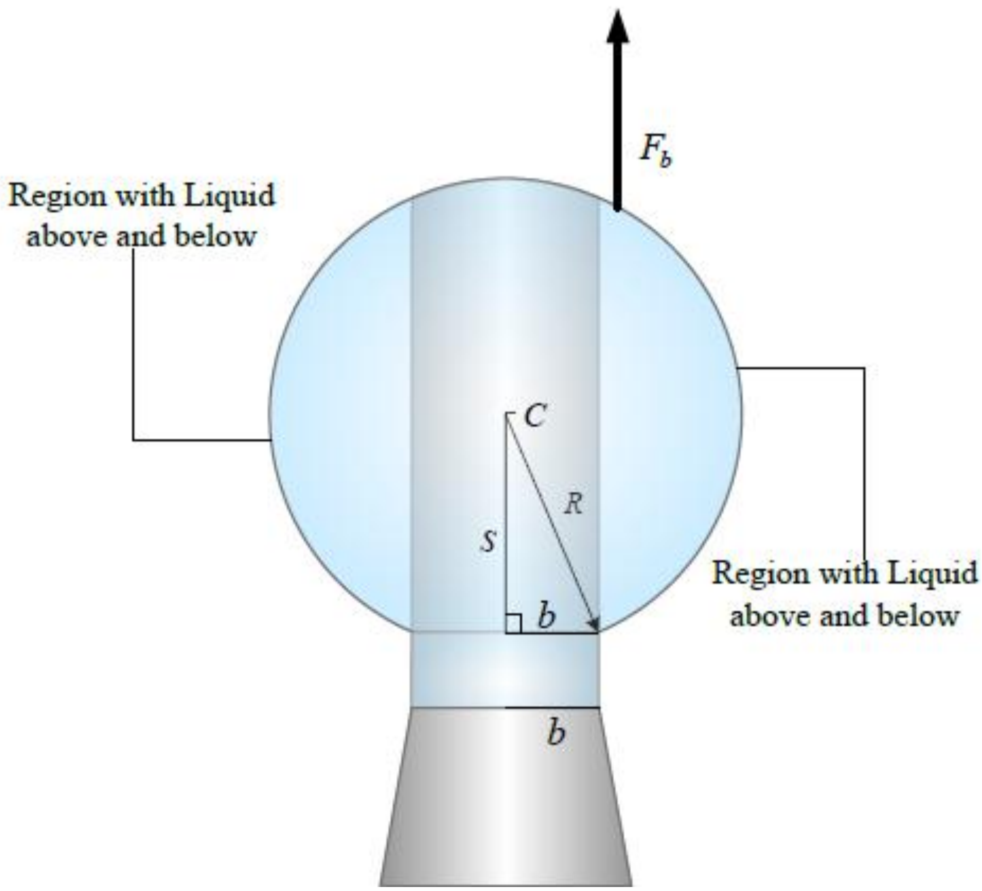

Figure 4-7: Representation of volume of region on which the buoyancy force is acting.

The volume of the bubble that has liquid above and below it is simply the volume of the spherical segment minus the volume of the central silo segment illustrated in Figure 4-7. In particular,

4-22 $$V_{bub} - V_{silo} = \frac{\pi}{3}(R+s)^2(2R-s) - \frac{\pi}{3}\left(2R^3 + 3sR^2 - 5s^3\right) = \frac{4}{3}\pi s^3$$

in which $s = \sqrt{R^2 - b^2}$.

The buoyancy force acting on a truncated spherical bubble is therefore the upward force,

4-23 $$F_b = (\rho_l - \rho_v)g\left(\frac{4\pi\left(R^2 - b^2\right)^{3/2}}{3}\right).$$

It is noted that the buoyancy force correctly approaches zero for a hemispherical bubble, that is to say, when *R* approaches *b*.

4.3.1.3. Force due to Contact Pressure

The upwardly directed force due to contact pressure, noted F_p, sometimes referred to as a buoyancy correction force (Cohran and Aydelott, 1966), is obtained by integrating along the bubble base,

4-24 $$\vec{F}_p = \int \vec{n} \cdot (-pI)\, dS.$$

In the above, I is an identity matrix such that pI is a tensor making the product $\vec{n}\cdot pI$ a vector.

Due to the symmetry about the vertical z-axis, only the z directional component of the force vector is considered reducing 4-24 to,

4-25 $$F_p = \int \left(n_z p \right) dS = (p_v - p_l)\pi b^2 .$$

The negligible dynamic actions on the gas-liquid interface within the quasi-static regime permit the application of the Young-Laplace equation for a truncated sphere, $p_v - p_l = 2\sigma / R$ (Eq. 3-11).

Applying the Young-Laplace equation to the above yields the final form of the upward force due to contact pressure,

4-26 $$F_p = \frac{2\pi\sigma b^2}{R} .$$

It is noted that for a bubble model that retains the shape of a spherical segment without any necking phenomenon, the force due to contact pressure and the capillary force are equal yet opposite and thus have exactly offsetting effects on the growth of the bubble. This is due to the fact that, for a truncated sphere without necking, the term $\sin\alpha$ of Eq. 4-19 is equal to the ratio of the orifice radius to bubble radius.

4.3.1.4. Force due to Gas Momentum

For a bubble growing due to gas injection, the momentum of the injected gas, and its resultant force, noted F_{gm}, may not be negligible (Kasimsetty *et al.*, 2007). It is defined as,

4-27 $$F_{gm} = \dot{m} v_g \, .$$

For bubble growth due to gas injection at a constant volumetric flow rate, the conservation of mass principle applies such that the flow rate is expressed in terms of the velocity of the injected gas, noted v_g, issuing from the orifice,

4-28 $$\dot{V} = \pi b^2 v_g \, .$$

Assuming the gas density to be constant with respect to time, the force due to gas momentum entering the bubble is expressed in terms of the gas injection flow rate, the gas density and the orifice radius. The resulting upward force due to gas momentum is,

4-29 $$F_{gm} = \dot{m} v_g = \rho_v \dot{V} v_g = \frac{\rho_v}{\pi b^2} \dot{V}^2 \, .$$

4.3.1.5. Force due to Drag

The force due to drag on an object in a steady stream, which, in the case of bubble growth in a quiescent liquid would be the fluid velocity adjacent to the bubble induced by the bubble formation, is defined as (White, 2008),

$$F_D = \frac{1}{2}\rho_l u^2 C_D A. \tag{4-30}$$

In the above, u is the stream velocity, C_D is the drag coefficient and A is the characteristic area identified as the projected area normal to the flow direction. Considering that the bubble is being injected into a motionless fluid and that the above definition is for an object that is not growing, the radial expansion shall account for the stream velocity that is creating the drag force, that is to say $u = \dot{R}$.

Without resorting to solving the fully viscous governing equations for the flow around the bubble, an approximate approach is typically used to calculate the influence of the drag force (Kasimsetty *et al.*, 2007). Due to the symmetry about the vertical axis of the bubble, the resultant drag force is in the negative z-direction only. For a truncated sphere with a cylindrical neck whose neck radius is less than the bubble radius, as for a sphere, the characteristic area is the cross sectional area πR^2. For this reason, Eq. 4-30 can be expressed as,

$$F_D = \frac{1}{2}\rho_l C_D \pi R^2 \dot{R}^2. \tag{4-31}$$

The drag force is generally quite small and often inviscid liquids are assumed in the theoretical modelling of quasi-static bubble growth (Buyevich & Webben, 1996). In this force balance, in light of the quasi-static assumption, the force due to drag shall be deemed negligible.

4.3.1.6. Sum of the Forces

The sum of the vertical directional forces acting on the bubble influencing its upward momentum is approximately,

4-32 $$\sum F = \underbrace{F_D + F_c}_{\substack{downward \\ forces}} + \underbrace{F_p + F_b + F_{gm}}_{\substack{upward \\ forces}} \quad .$$

Bubble detachment is postulated to take place at the moment in which the sum of the above forces is zero since this is when it would be transitioning from a negative sum holding the bubble to the cavity to a positive sum translating the bubble vertically away from the cavity (Fritz, 1935). The detachment radius can therefore be deduced by solving the following equation for R_d,

4-33 $$-2\pi b\sigma + \frac{2\pi\sigma b^2}{R_d} + (\rho_l - \rho_v) g \left(\frac{4\pi\left(R_d^2 - b^2\right)^{3/2}}{3} \right) + \frac{\rho_v}{\pi b^2}\dot{V}^2 = 0 \, .$$

4.3.2. Quasi-static Bubble Growth Regime

In the case of bubble growth due gas injection, it is postulated here that the quasi-static regime can be identified as the regime for which the force due to gas momentum is negligible. For an orifice radius *b*, the magnitude of this upward force due to gas momentum (detailed in section 4.3.1.4) is

4-34 $$F_{gm} = \frac{\rho_v}{\pi b^2}\dot{V}^2 .$$

In this study, the influence due to gas momentum shall be deemed negligible when it is sufficiently opposed by the downward capillary force (detailed in section 4.3.1.1)

4-35 $$F_c = 2\pi b\sigma .$$

The condition for quasi-static bubble growth is set here to be such that the ratio of the force due to gas momentum to the capillary force be less than 10^{-5}. That is to say, the quasi-static regime in this document shall be identified by the following inequality,

4-36 $$\frac{\frac{\rho_v}{\pi b^2}\dot{V}^2}{2\pi b\sigma} < 10^{-5} .$$

This inequality places the critical volumetric flow rate at, 4-37 $$\dot{V}_{cr} = \frac{\pi}{100}\sqrt{\frac{b^3\sigma}{5\rho_v}}.$$

The critical volumetric flow rate implies that any gas injected flow below the critical volumetric flow rate will yield bubble growth within the quasi-static regime. A normalized flow rate in terms of the critical flow rate is defined,

4-38 $$\dot{V}' = \frac{\dot{V}}{\dot{V}_{cr}}.$$

Bubble growth is therefore deemed within the quasi-static regime if the following inequality holds,

4-39 $$\dot{V}' < 1.$$

This critical flow rate is validated in the following section.

4.3.3. Force Balance Detachment Criterion Validation

The predicted detachment radius resulting from the force balance detachment criterion is compared with measurements from Sergio Di Bari's captured bubble images detailed in section 3.4 for all flow rates tested and all orifice radii tested. It is further compared with experimentally measured values for different fluids, different injection rates and different orifice radii that are available in the literature. In particular, experimentally measured data of bubble detachment radii for air bubbles growing in water through an orifice of 2mm radius (Oguz & Prosperetti, 1993), for air bubbles growing in silicon through an orifice of radius 0.15 mm (Duhar & Colin, 2006) and for nitrogen bubbles growing in ethanol, FC-72, water and HFE (Di Marco *et al.*, 2005) are compared with the model's force balance bubble detachment criterion. These comparisons are compiled in Figure 4-8 in which $R_{d,m} / R_{d,pr}$ unity shows agreement between predicted and measured detachment radii and in which values of $\dot{V}^{¢}$ less than unity indicate that the bubble formation is taking place within the quasi-static regime.

The results show that within the quasi-static regime, the force balance detachment criterion yielding the bubble detachment radius of Eq. 4-33 is within the error lines of ± 7% of the experimental results.

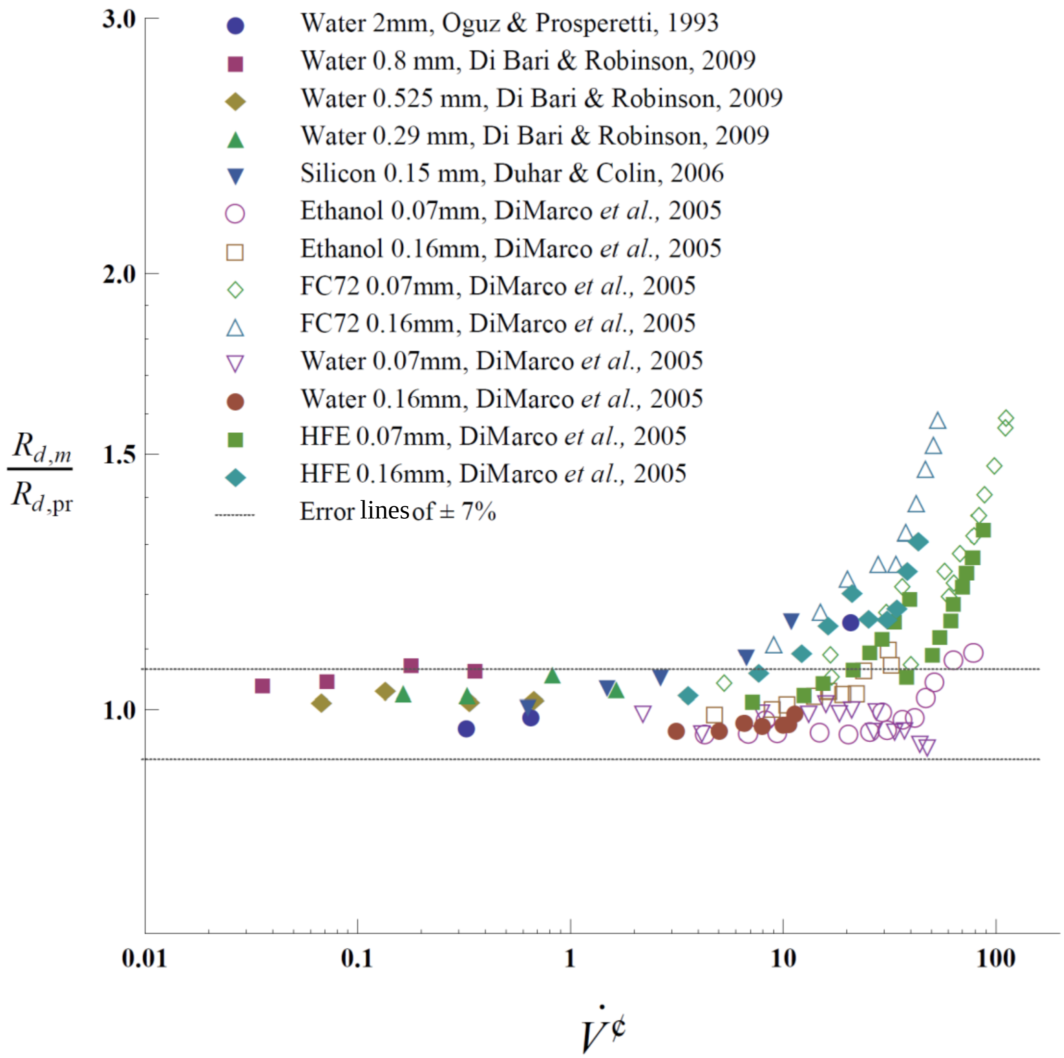

Figure 4-8: Experimental validation of Eq. 4-33. Comparison of the ratio of measured detachment radius to predicted detachment radius for different fluids and orifice radii.

The results illustrated in Figure 4-8 show that beyond the critical flow rate, the predicted values generally underestimate the bubble detachment radius for all fluids and orifice radii tested. This is attributed to the inertia from the gas momentum expanding the bubble walls, thereby creating larger bubbles prior to detachment and to the presence of the force due to drag delaying detachment thereby allowing the bubble to grow larger.

4.3.4. Non-dimensional Form of Detachment Criterion

For the present work, the viscous and inertial dynamic forces are assumed negligible which limits the applicability to very low gas injection rates such that buoyancy and capillary forces are dominant (Gerlach *et al.*, 2007). These low rates are categorized as the quasi-static regime. Physically, this regime is such that the dynamical actions are negligible when defining the gas-liquid interface making the Young-Laplace equation viable. Analytically, this regime is dependent on the gas flow rate, fluid characteristics and the orifice radius from which the bubble is issuing.

Experimental results have shown that the volumetric flow rate has little influence on bubble detachment radius within the quasi-static regime (Nahra & Kamotani, 2003; Di Marco *et al.*, 2005). Recalling that the quasi-static regime is identified by assuming the force due to gas momentum negligible relative to the capillary force, this phenomenon is now considered in the force balance detachment criterion of Eq. 4-33 without a significant change in the resulting detachment radius within the quasi-static bubble growth regime. It is simplified by neglecting the force due to gas momentum and by defining the normalized detachment radius $R_d^* = R_d / b$ as the ratio of the detachment radius and the orifice radius. Dividing all terms by b and neglecting the force due to gas momentum, Eq. 4-33 reduces to,

$$\frac{R_d^* - 1}{R_d^*\left(R_d^{*2} - 1\right)^{3/2}} = \frac{2}{3} Bo_b \ . \qquad \text{4-40}$$

Equation 4-40 implies that the force balance bubble detachment criterion is dependent only on the Bond number and not the volumetric flow rate, which, as earlier mentioned, is justifiable within the quasi-static bubble growth regime.

Figure 4-9 compares the measured normalized detachment radius parameter R_d^* to its predicted value generated by Eq. 4-40. The experimentally measured bubble detachment radii used in the comparison of Figure 4-9 are those among the experimental data used in the earlier validation of the force balance criterion of Figure 4-8 for which the bubble formation was deemed to be within the quasi-static regime.

The results show that, for quasi-static bubble growth, the detachment criterion of Eq. 4-40 predicts the measured detachment radii within the ± 7% error lines.

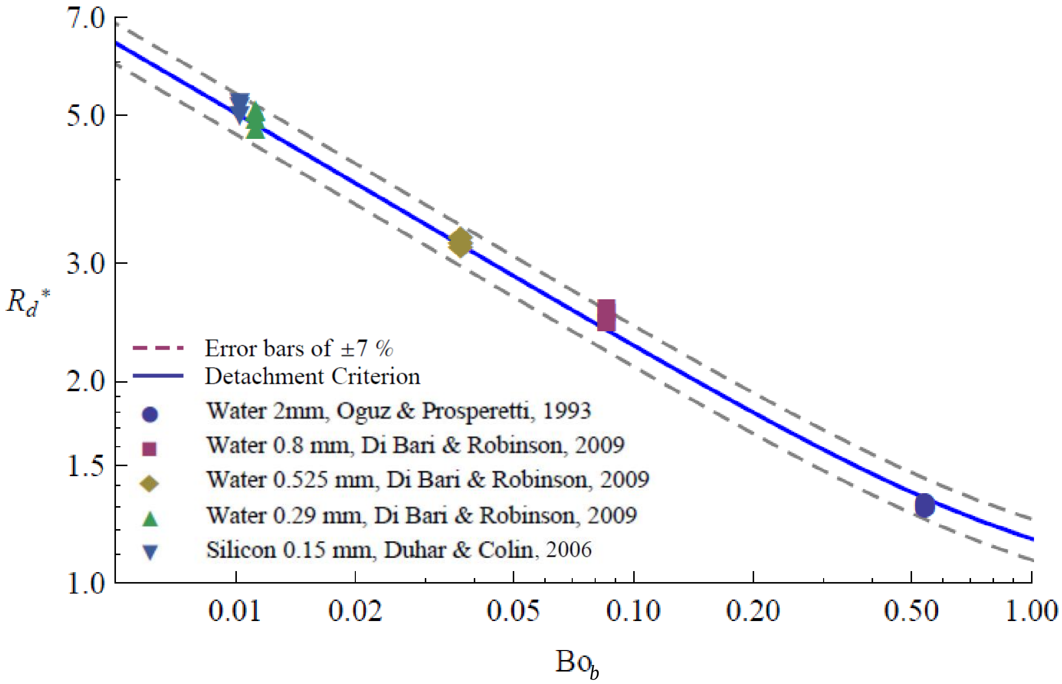

Figure 4-9: Normalized detachment radius with respect to Bond number for quasi-static bubble growth.

4.4. Bubble Detachment Volume

The bubble detachment volume is calculated by coupling the geometric detachment relation and the force balance detachment criterion with the postulated bubble growth geometry illustrated in Figure 4-1. The detachment volume is easily shown to be related to the normalized detachment radius, calculated with Eq. 4-40, and the normalized detachment neck height, calculated with Eq. 4-14, such that,

4-41 $$ {}^{*}V_d = \frac{1}{2}\left(R_d^* + s_d^*\right)\left(2R_d^* - s_d^*\right) + \frac{3}{2}h_d^* . $$

In this document, bubble volumes are normalized by the initial hemispherical volume such that,

4-42 $$ {}^{*}V = \frac{V}{\frac{2}{3}\pi b^{3}}. $$

Figure 4-10 compares the model predicted bubble detachment volume of Eq. 4-41 with the numerically generated detachment volumes from the numerical treatment of the Capillary equation described in chapter 3.

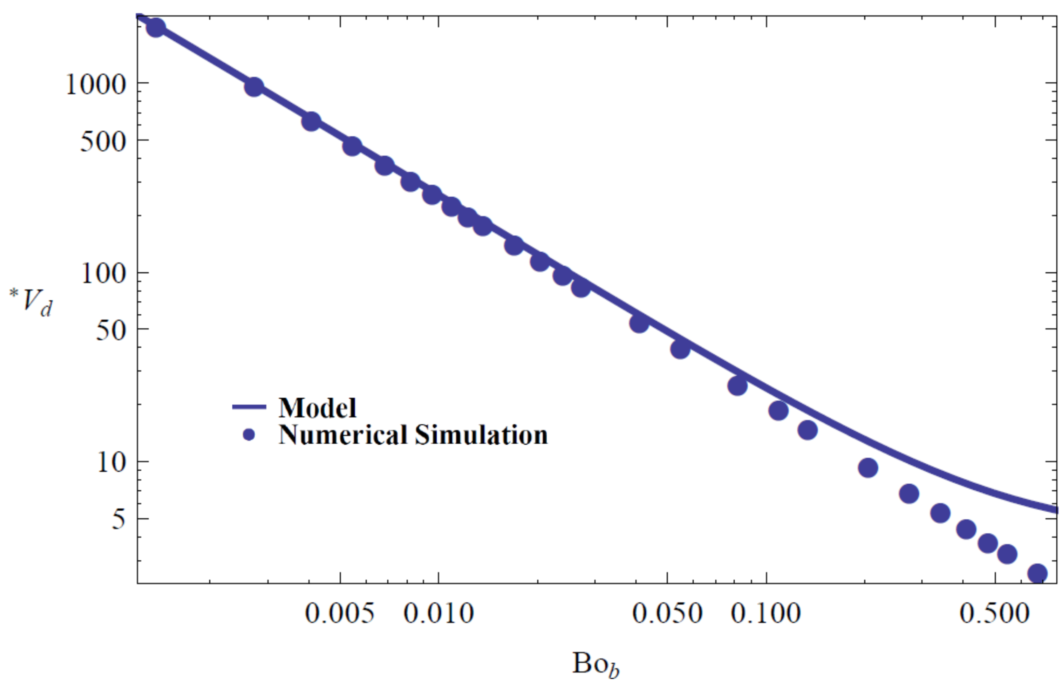

Figure 4-10: Model predicted versus numerically simulated bubble detachment volume for varying Bond numbers.

Figure 4-10 shows that the proposed geometric model coupled with the geometric detachment relation and the force balance detachment criterion is in good agreement with the numerical solutions for bond numbers less than or equal to 0.06; it is within ± 7% of the numerical solution for these Bond numbers.

As was previously discussed in chapter 3, for Bond numbers larger than 0.06, the hydrostatic pressure near the base of the detaching bubble overcomes the capillary pressure causing the neck walls to pinch inwards thereby making the cylindrical neck assumption no longer valid. Once again, the geometric model proposed in this chapter is deemed suitable in describing bubble growth for Bond numbers less than or equal to 0.06.

4.5. Model Development

A fully analytical bubble growth model for quasi-static gas injected bubble growth from a submerged orifice is developed; the model is based on the geometric detachment relation and the force balance detachment criterion of the previous section. The model is applicable to adiabatic quasi-static bubble growth for which the working conditions are such that the Bond number is less than or equal to 0.06. The model's bubble detachment conditions are summarized in the following table.

Table 4-1 : Bubble Detachment		
	Equation	Description
Geometric Detachment Relation Eq. 4-14	$h_d^* = \frac{\left(R_d^* - s_d^*\right)\left(2R_d^* + s_d^*\right)}{\left(R_d^* + s_d^*\right)} + \frac{2}{3}$	Relates bubble neck height to bubble detachment radius.
Force Balance Detachment Criterion Eq. 4-40	$\frac{R_d^* - 1}{R_d^*\left(R_d^{*2} - 1\right)^{3/2}} = \frac{2}{3} Bo_b$	Relates bubble detachment radius to Bond number.

4.5.1. Bubble Radius Growth Curve

In the particular case of constant flow rate gas injected adiabatic bubble growth, a simple mass balance is used to dictate the bubble volumetric growth rate. That is to say, for a fixed injection rate $\dot{V}$, assuming that there is no mass diffusion through the bubble interface and that the injected gas feeds the truncated spherical segment of the bubble directly, the time in which the bubble radius has a magnitude R is,

4-43 $$t = \frac{V_{tr}(R) - V_{tr}(b)}{\dot{V}} \; .$$

The time t is expressed explicitly in terms of R by considering the volume of a truncated spherical segment with radius R and base radius b, $V_{tr} = \frac{\pi}{3}\left(R+\sqrt{R^2-b^2}\right)^2\left(2R-\sqrt{R^2-b^2}\right)$, yielding,

4-44 $$t = \frac{\pi}{3\dot{V}}\left(\left(2R-\sqrt{R^2-b^2}\right)\left(\sqrt{R^2-b^2}+R\right)^2 - 2b^3\right).$$

4.5.1.1. Non-dimensional Form of Bubble Radius

The bubble radius growth curve takes on its non-dimensional form by defining the characteristic length to be the orifice radius, noted b, the characteristic volume to be the incipient hemispherical bubble, noted $V_o = \frac{2}{3}\pi b^3$, and the characteristic time to be the inverse of the normalized volumetric flow rate, thereby defining the non-dimensional parameters as,

4-45 $$\begin{cases} {}^*V = \dfrac{V}{V_o} \\ {}^*\dot{V} = \dfrac{\dot{V}}{V_o} \\ t' = {}^*\dot{V}\cdot t \\ R^* = \dfrac{R}{b} \\ s^* = \dfrac{s}{b} = \sqrt{R^{*2}-1} \end{cases}.$$

Multiplying both sides of the equality of Eq. 4-44 by ${}^{*}\dot{V}$ yields its non-dimensional form,

4-46 $$t' = \frac{1}{2}\left(2R^{*} - s^{*}\right)\left(s^{*} + R^{*}\right)^{2} - 1.$$

4.5.2. Bubble Centre of Gravity

In order to develop a centre of gravity growth curve, it is necessary to account for the rise of the spherical segment of the bubble due to neck formation at its base. The rise of the centre of gravity during bubble growth is therefore considered in this chapter to be due to the growing spherical segment with radius *R* described by Eq. 4-46 coupled with the rise of the bulk of the bubble due to the necking phenomenon.

To this end, the bubble shape of Figure 4-1 is adopted geometrical relating the centre of gravity of the bubble, noted *H* and detailed in Appendix 7.6, to the bubble radius, the orifice radius and the height of the bubble neck, noted *h*,

4-47 $$H = \frac{(3R-s)(R+s)(2h+R+s) + 2h(R-s)(3h+R+s)}{4\big(3h(R-s) + (2R-s)(R+s)\big)}.$$

Once again, the term $s = \sqrt{R^2 - b^2}$ represents the centre of curvature position of the spherical segment above the neck of the bubble placing the centre of curvature of the bubble at a height $C = s + h$.

Recalling that throughout this document all length terms divided by the orifice radius are noted $\zeta^* = \zeta / b$, the centre of gravity is normalized,

$$4\text{-}48 \qquad H^* = \frac{\left(3R^* - s^*\right)\left(R^* + s^*\right)\left(2h^* + R^* + s^*\right) + 2h^*\left(R^* - s^*\right)\left(3h^* + R^* + s^*\right)}{4\left(3h^*\left(R^* - s^*\right) + \left(2R^* - s^*\right)\left(R^* + s^*\right)\right)}.$$

4.5.2.1. Bubble Neck Growth Curve

The only term on the right hand side of Eq. 4-48 not accounted for by Eq. 4-46 is the normalized height of the cylindrical neck, h^*. This term is solved for by coupling the neck growth trend illustrated in Figure 3-36 with the geometric detachment relation and the force balance detachment criterion of this chapter.

Throughout this document, all bubble characteristics during the growth cycle can be normalized by its value at bubble detachment and are noted $\zeta^+ = \zeta / \zeta_d$ in which ζ_d is the value of an arbitrary bubble characteristic ζ at detachment. In what follows, the neck height h^+ is solved for in terms of t^+ by first postulating a neck height growth trend from the results of chapter 3.

In particular, Figure 3-36 of chapter 3 demonstrated that the phenomenon of bubble deviation from a truncated spherical shape is more pronounced, and manifests itself earlier, for larger Bond numbers. This deviation from a Modified sphericity of unity during bubble growth is attributed to neck formation.

Illustrated in Figure 4-11 are the findings of Figure 3-36 with a postulated bubble neck growth trend that would account for the bubble elongation as a function of the Bond number. The non-dimensional bubble neck growth curve,

h^+ is postulated to have the growth trend of a monomial function dependent on the non-dimensional time t^+.

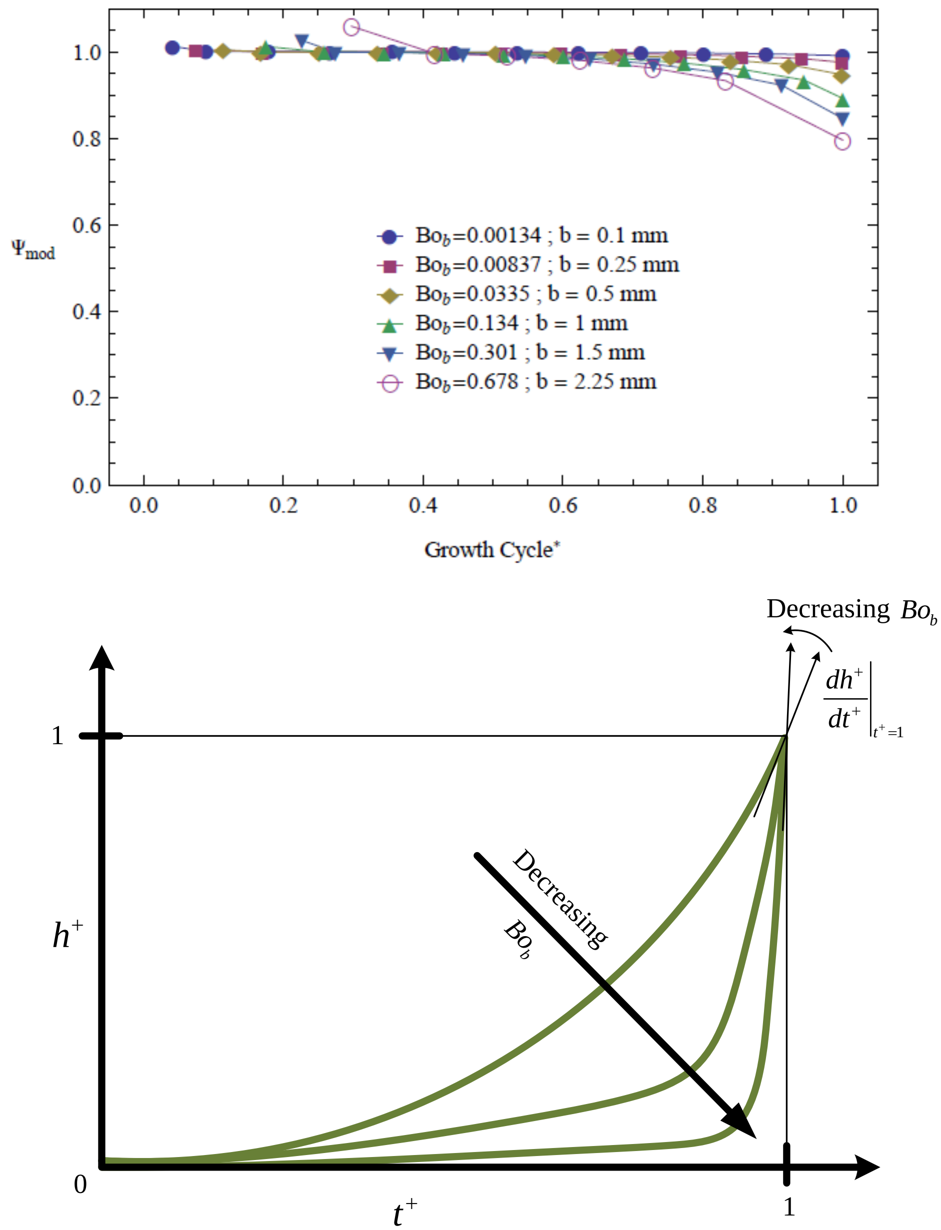

Figure 4-11 : *(Top)* Modified sphericity quantification of shape deviation from a truncated spherical segment relative to Bond number. *(Bottom)* Postulated bubble neck formation accounting for the necking phenomenon relative to Bond number.

The described bubble neck monomial growth curve in Figure 4-11 is represented symbolically with the arbitrary constants C_1 and C_2,

4-49 $$h^+ = C_1 t^{+C_2}.$$

In the above, C_1 is clearly 1 since unity for h^+ and t^+ coincide. A distinguishing feature of the proposed bubble neck growth curve is that the slope of h^+ at detachment, for which $t^+ = 1$ and which is noted $\left.\frac{dh^+}{dt^+}\right|_{t^+=1}$, increases with decreasing Bond number Bo_b. Furthermore, $\left.\frac{dh^+}{dt^+}\right|_{t^+=1}$ tends towards infinity as Bo_b approaches zero. A term exhibiting such trends while being in a one-to-one functional relation with Bo_b is R_d^* as is shown by Eq. 4-40. For this reason, the following equality is established,

4-50 $$\left.\frac{dh^+}{dt^+}\right|_{t^+=1} = R_d^*.$$

With this, a derivation of Eq. 4-49 with respect to t^+ and solving for C_2 yields an expression of h^+ in its final form,

4-51 $$h^+ = t^{+R_d^*}.$$

In Eq. 4-51, R_d^* is solved for with Eq. 4-40 of the force balance detachment criterion. In Figure 4-12, Eq. 4-51 is shown to yield the desired growth trend accounting for the more prominent bubble elongations associated with larger Bond numbers.

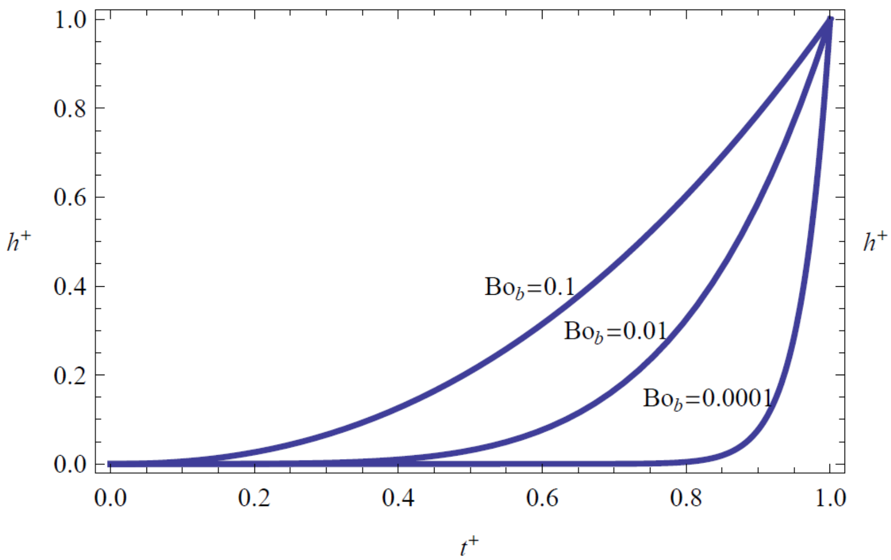

Figure 4-12: Normalized predicted growth histories of bubble neck formation for different Bond numbers.

4.5.2.2. Centre of Gravity Growth Curve

Recalling that it is h^* that will provide closure to the bubble centre of gravity growth curve of Eq. 4-48, Eq. 4-51 is expressed in non-dimensional terms relative to the orifice radius,

4-52 $$h^* = h_d^* \left(\frac{t'}{t_d'} \right)^{R_d^*}.$$

From the geometric detachment relation Eq. 4-14, h_d^* is expressed in terms of R_d^*, from Eq. 4-46, t_d' is expressed in terms of R_d^* and from the force balance detachment criterion R_d^* is solved for in terms of the Bond number. This implies that coupling Eq. 4-52 with Eq. 4-48 yields the centre of gravity growth curve with only the Bond number as an input value. The model therefore predicts the centre of gravity growth curve with the following inputs: fluid densities, surface tension, gravitational constant and orifice radius.

The following table describes the equation set solving for the centre of gravity growth curve.

Table 4-2 : Bubble Centre of Gravity Growth Curve

Equation	Description
$H^* = \dfrac{6h^{*2}\left(R^* - s^*\right) + \left(s^* + 4h^* - R^*\right) + 4h^* R^*\left(s^* + R^*\right)}{4\left(3h^*\left(R^* - s^*\right) + R^*\left(s^* + R^*\right) + 1\right)}$	*Geometric constraint,* Eq. 4-48
$h^* = h_d^*\left(\dfrac{t'}{t_d'}\right)^{R_d^*}$	*Neck height modeling,* Eq. 4-52
$t' = \dfrac{1}{2}\left(2R^* - s^*\right)\left(s^* + R^*\right)^2 - 1$	*Mass balance for constant volumetric flow,* Eq. 4-46
$h_d^* = \dfrac{\left(R_d^* - s_d^*\right)\left(2R_d^* + s_d^*\right)}{\left(R_d^* + s_d^*\right)} + \dfrac{2}{3}$	*Geometric detachment relation,* Eq. 4-14
$\dfrac{R_d^* - 1}{R_d^*\left(R_d^{*2} - 1\right)^{3/2}} = \dfrac{2}{3} Bo_b$	*Force balance detachment criterion,* Eq. 4-40

4.5.3. Results and Discussion

The model described in the preceding sections is compared with the bubble growth characteristics generated by the numerical treatment of the Capillary equation detailed in chapter 3. These benchmarked numerical simulations are used to provide validating curves of bubble growth characteristics. In this way, a wide range of conditions that are not easily tested experimentally, such as a very small Bond number due to a weak gravitational field strength and/or a small cavity radius, are compared with the analytical models ability to predict bubble growth characteristics. Indeed the low flow rates required to inject a gas through a small orifice while maintaining a bubble growth rate within the quasi-static regime are increasingly difficult to attain for increasingly small orifice radii. Similarly, extreme gravitational field strengths are not easily simulated in laboratory experiments.

The model predicts the bubble volume to be that of a truncated sphere with a foot radius equal to the cavity radius rising due to a cylindrical neck such that,

4-53 $$ {}^{*}V = \frac{1}{2}\left(R^{*}+s^{*}\right)^{2}\left(2R^{*}-s^{*}\right)+\frac{3}{2}h^{*}. $$

The model predicts the bubble Aspect Ratio to be,

4-54 $$ AR = \frac{R^{*}+s^{*}+h^{*}}{2R^{*}} $$

and the Modified sphericity as it is defined in Eq. 3-37. The normalized radius and neck height, R^* and h^* respectively, are detailed in Table 4-2; the volume has been normalized by the incipient hemispherical bubble, ${}^*V = \frac{V}{\frac{2}{3}\pi b^3}$ and the normalized bubble centre of gravity H^* is calculated from Eq. 4-48.

In Figure 4-13 to Figure 4-15, analytical model predicted bubble growth characteristics for Bond numbers ranging from 0.00137 to 0.06032 are compared with numerically generated growth curves. The normalized time parameter used as an input value for the analytical model is quantified from the numerically generated bubble volume such that,

4-55 $$t' = {}^*V_{NG} - 1$$

in which ${}^*V_{NG}$ is the normalized numerically generated bubble volume.

The results show that the analytical model predicted bubble growth curves are in agreement with the growth trends generated from the numerical treatment of the Capillary equation for Bond numbers less than or equal to 0.06. In particular, from inception to detachment for a small Bond number of 0.00137, the analytical treatment is within 0.05%, 11%, 15% and 1% with the numerical treatment of the bubble volume, centre of gravity, *AR*, and Modified sphericity growth curves respectively. It is also shown that the centre of gravity increases in a root function trend to a certain point during mid growth at which time it transitions to an exponential growth curve. This transition is attributed to the formation of the bubble neck and is accounted for in the analytical model.

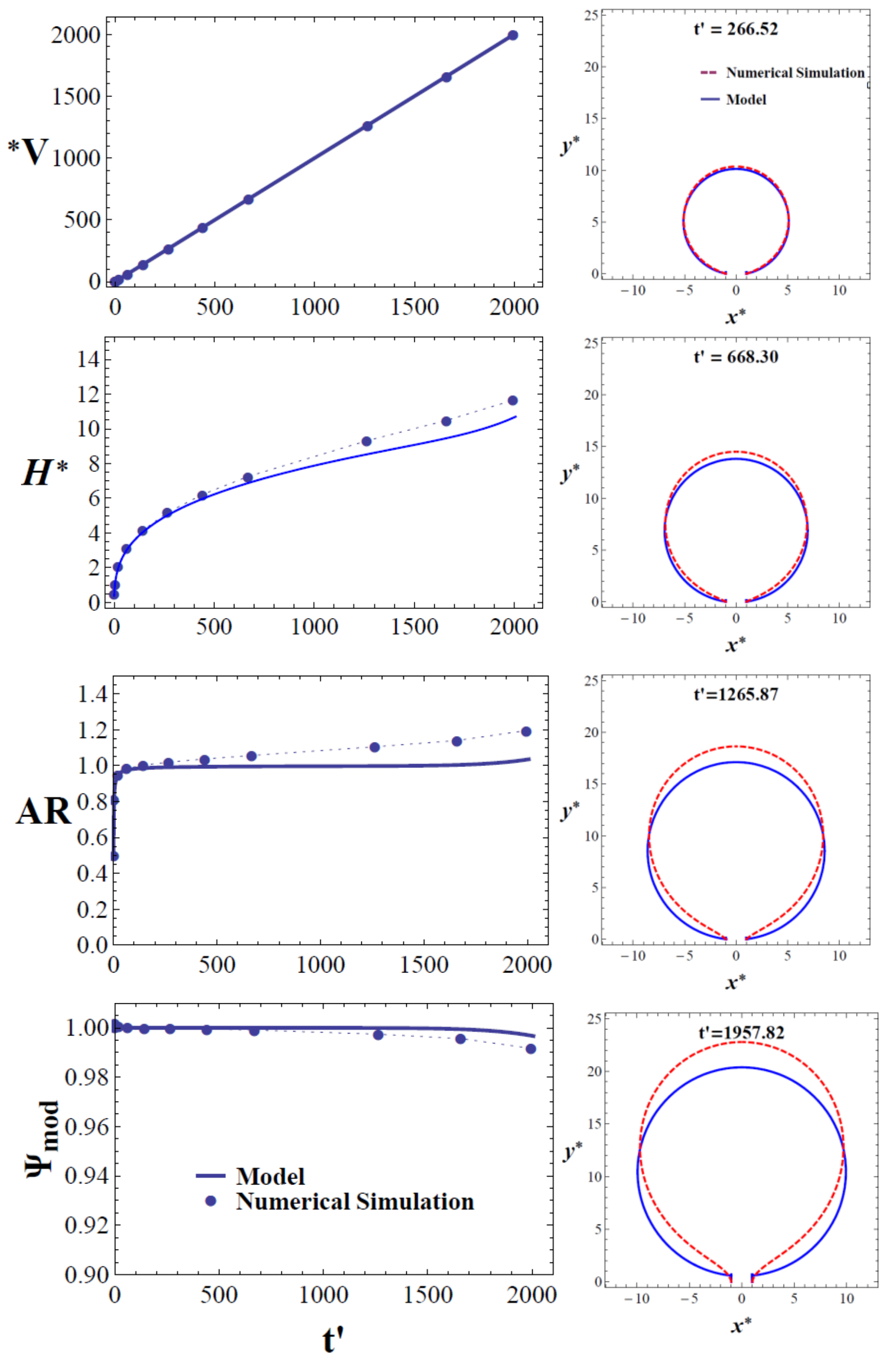

Figure 4-13: Model predicted versus numerically simulated bubble growth characteristics for conditions in which the Bond number is 0.00137.

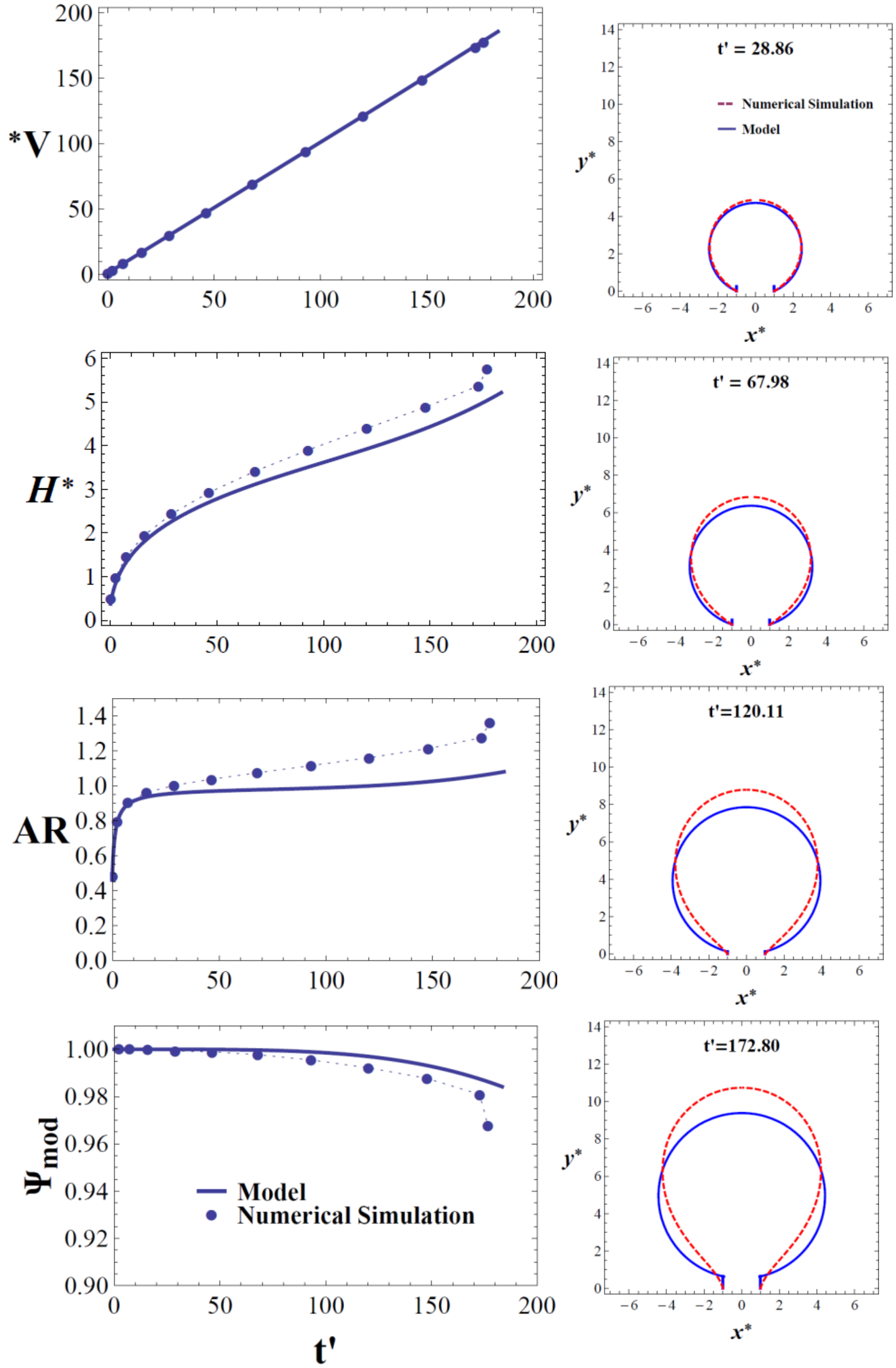

Figure 4-14: Model predicted versus numerically simulated bubble growth characteristics for conditions in which the Bond number is 0.0137.

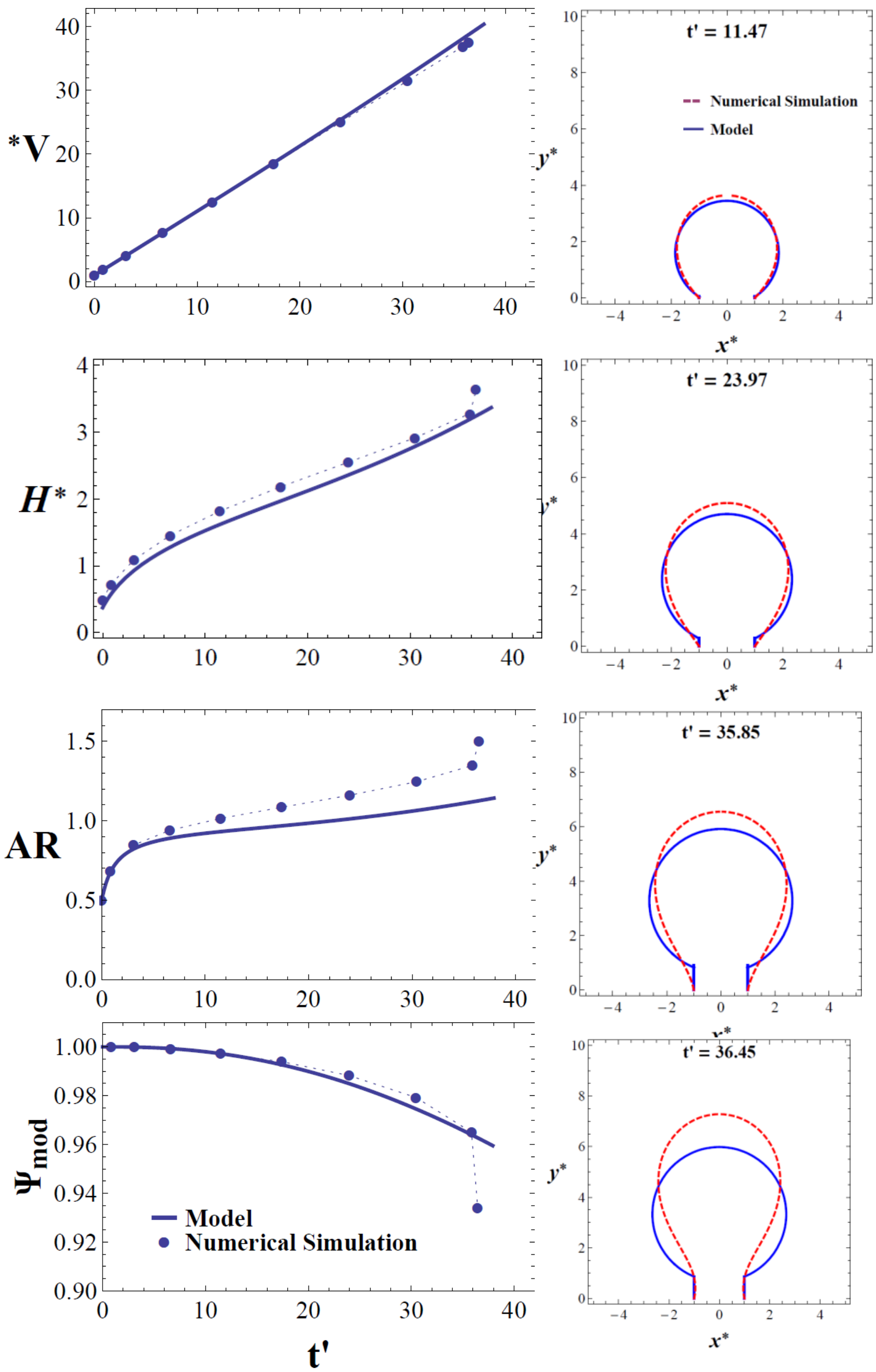

Figure 4-15: Model predicted versus numerically simulated bubble growth characteristics for conditions in which the Bond number is 0.06032.

4.6. Model Limitations

4.6.1. Bond number

As previously discussed, a bubble growing as a spherical segment that is rising due to a growing cylindrical neck is limited to applications in which the Bond number is less than or equal to 0.06. Indeed, it was shown in chapter 3 that for larger Bond numbers, the hydrostatic pressure becomes more dominant than the capillary pressure near the base of the bubble at some point during the bubble growth cycle. This causes the outer walls of the cylindrical bubble neck to pinch inwards making the cylindrical neck assumption inadequate for larger Bond numbers.

As an illustrative example of this limitation, Figure 4-16 compares the model predicted bubble growth characteristics to the numerically generated results for bubble growth in which the Bond number is 0.546, much larger than 0.06. It is important to recall that this is still within the numerical treatments Bond number limitation of 0.9941.

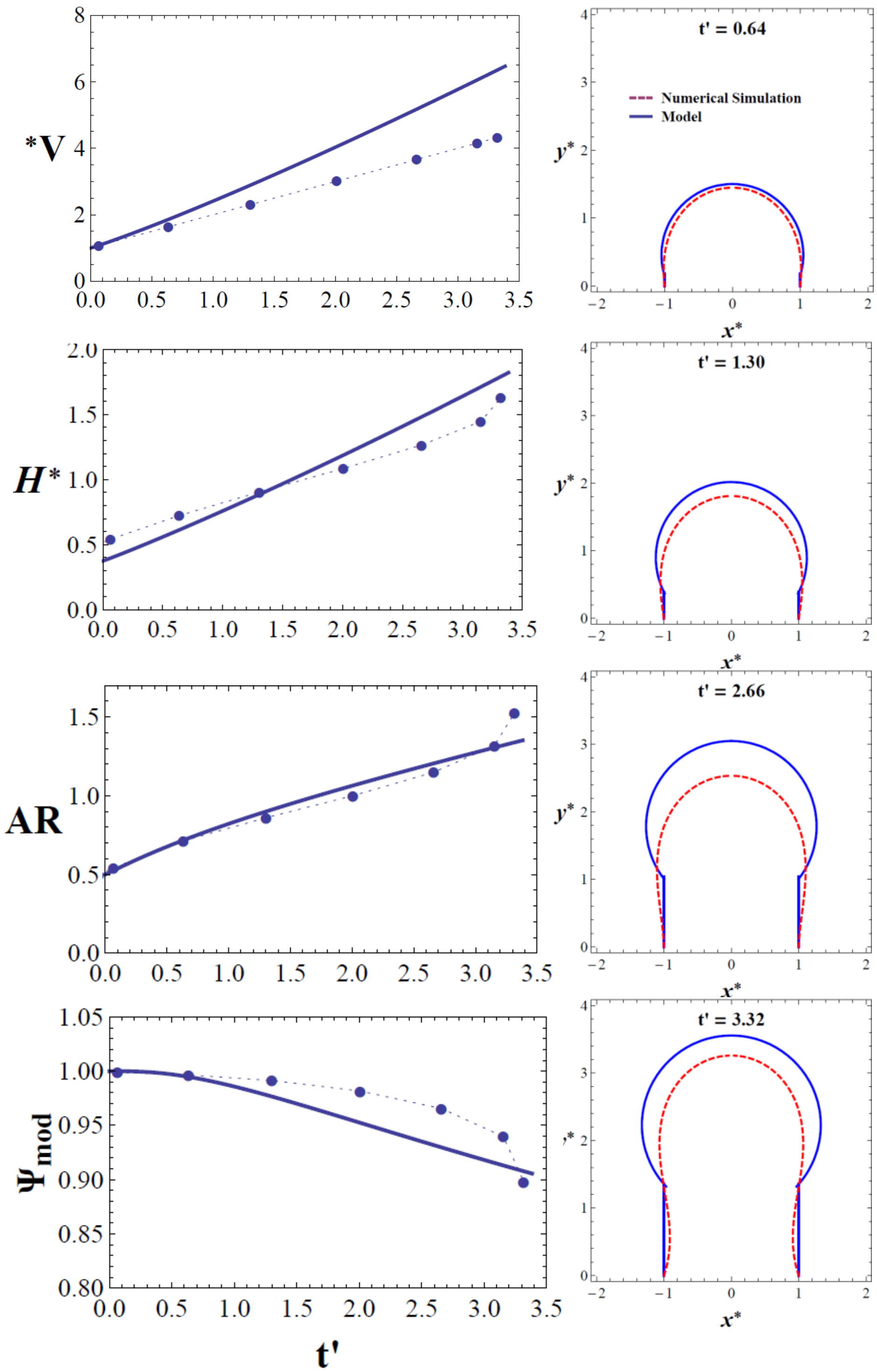

Figure 4-16: Model predicted versus numerically simulated bubble growth characteristics for conditions in which the Bond number is 0.546.

4.6.2. Quasi-static Bubble Growth Regime

The proposed model is limited to the quasi-static regime defined by the normalized critical flow rate such that $\dot{V}' = \dfrac{\dot{V}}{\dot{V}_{cr}} < 1$ in which $\dot{V}_{cr} = \dfrac{\pi}{100}\sqrt{\dfrac{b^3\sigma}{5\rho_v}}$. Indeed, Figure 4-8 shows that beyond this critical flow rate, the force balance detachment criterion of the model is no longer valid thereby limiting the model to the quasi-static bubble growth regime. The erroneous results produced by the model once outside the quasi-static bubble growth regime are well illustrated in the following Figure 4-17 which considers bubble formation due to gas injection at a constant flow rate of 100 ml/h through an orifice of radius 0.29 mm in which the measured data is a result of the experiments of Sergio Di Bari described in section 3.4. The ratio of flow rate to resulting critical flow rate yields a normalized critical flow rate of $\dot{V}' = 1.64$ which is greater than 1 placing the bubble growth outside the quasi-static regime.

Figure 4-17 illustrates that the model predicted growth trend, for this non quasi-static bubble formation, is not in agreement with the experimentally measured growth curve. For this case, the model appears to under-predict the experimental data and does not account for any oscillation in the bubble radius during growth. This is attributed to the added inertia driven growth that the bubble is experiencing in which its momentum helps to drive the adjacent liquid outwards.

It is carefully noted that the first frame in the sequence of captured images during the bubble formation at 100 ml/h through an orifice radius of 0.29 mm yielded a bubble radius greater than the orifice radius. In light of the hemispherical assumption of this chapter's model, the experimental comparison of Figure 4-17 was rendered difficult and should be understood as approximate.

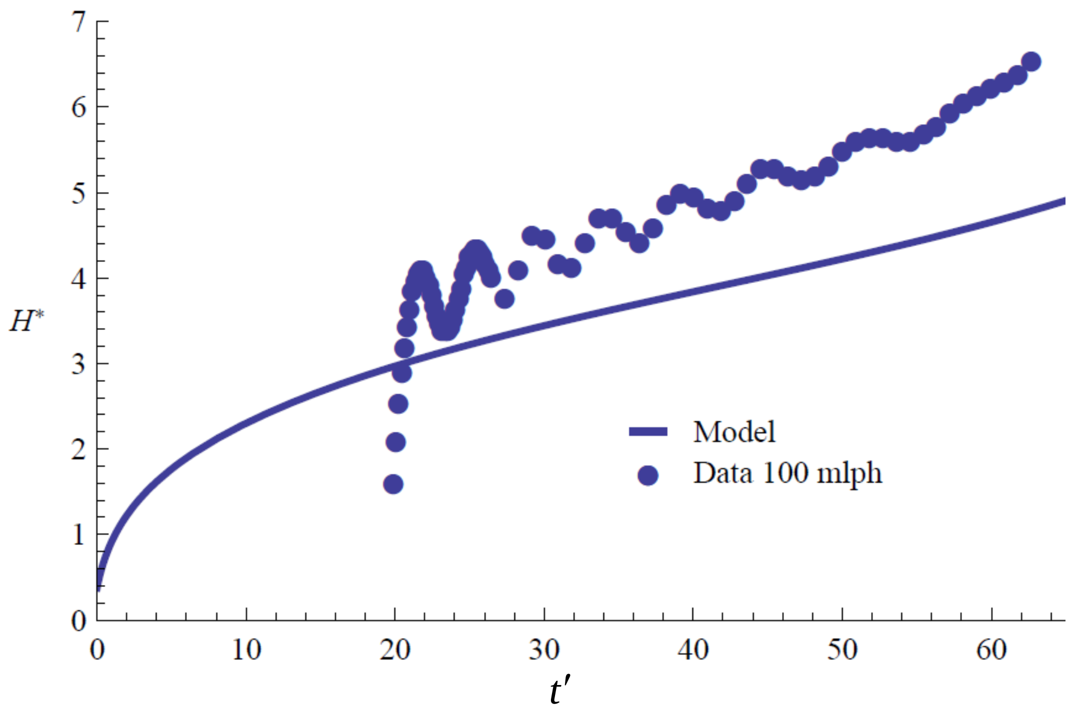

Figure 4-17: Theoretical versus measured bubble centre of gravity normalized growth curves from an orifice of radius 0.29 mm. The flow rate is 100 ml/h and the bubble growth is subsequently not quasi-static, $\dot{V}^* = 1.64$.

4.7. Conclusion

An analytical model is presented that describes the observed geometries of bubble growth in the quasi-static regime for low Bond number applications thereby contributing to the understanding of the fundamental mechanics behind pool boiling heat transfer.

In particular, a geometric model including the necking phenomenon for applications in which the Bond number is less than or equal to 0.06 is adopted; the geometric model is a consequence of the analysis of the results of chapter 3. Subsequently, a bubble geometric detachment relation and a force balance bubble detachment criterion are validated by showing them to be within ± 7% of the available experimental data for quasi-static adiabatic bubble growth. An analytical model based on the proposed geometry, the geometric detachment relation, and the force balance detachment criterion is developed and compared to bubble growth characteristics generated from the benchmarked numerical treatment of the problem thereby enabling a comparison of small Bond number applications.

The model has been validated against the following numerically generated bubble growth characteristics: bubble volume during the growth cycle and at detachment; bubble centre of gravity; bubble *AR* and bubble Modified sphericity. The model is deemed valid for quasi-static adiabatic bubble growth applications in which the Bond number is less than or equal to 0.06.

5. BUBBLE GROWTH DYNAMICS IN A NON-UNIFORM TEMPERATURE FIELD

5.1. Introduction

Boiling is an effective means of heat transfer. Despite many studies yielding numerical models and empirical correlations, the mechanism that governs bubble growth during nucleate boiling is not fully understood. Such an understanding would facilitate the optimization of industrial heat exchangers rendering them more cost effective.

To this end, many studies have brought insight to bubble formation mechanisms by investigating the idealized case of spherical bubble growth in an extensive pool of uniformly superheated liquid. In particular, for spherical bubble formation in an extended pool of superheated liquid, Forster and Zuber (1954), Plesset & Zwick (1954) and Scriven (1959) provided extended versions of Raleigh's equation (Raleigh, 1917) in describing the momentum balance driving bubble growth during the inertia-controlled growth regime. Plesset & Zwick (1954) and Scriven (1959), with an energy balance analysis, provide analytical solutions to spherical bubble growth within the heat-transfer controlled growth regime. Bubble growth may transition from one regime to another, and for this reason, Mikic *et al.* (1970) developed a relation that is applicable for the entire bubble growth cycle. Riznic *et al.* (1999) examined the influence of the curved vapour-liquid interface on the temperature field during heat-induced bubble growth. In these studies, it was globally shown that during the inertia-controlled growth regime, the bubble radius growth curve is approximately linear relative to time, while in the heat-transfer growth regime, the radius growth curve is an approximate root function relative to time. Prosperetti & Plesset (1978) showed that large superheats are required for inertia-controlled bubble growth and that otherwise, the heat-transfer controlled regime dominated bubble growth. Robinson & Judd (2004) identified the working parameters for which bubble growth would be inertia controlled or heat-transfer controlled for spherical bubble growth such that,

5-1 $$I_R = \frac{b\sigma}{3\rho_l}\left(\frac{2}{3\alpha Ja}\right)^2 \begin{cases} \ll 1 \Rightarrow \text{ Inertia controlled} \\ \gg 1 \Rightarrow \text{ Heat-transfer controlled} \end{cases}.$$

The heat-transfer controlled regime favours bubble growth due to a mass transfer at the interface rather than the inertia driven bubble expansion of the inertia controlled regime. The commonality between quasi-static adiabatic gas injected bubble growth in which the momentum is considered negligible and heat-transfer vapour bubble growth is that in both of these regimes, bubble growth is dictated by mass transfer.

In application, industrial heat exchangers exploiting the thermal transport due to the phase change boiling phenomenon generally favour nucleate pool boiling issuing from cavities on heated planes rather than spherical bubble growth in an extended pool of superheated liquid. Despite this, these previously mentioned studies are useful in investigating bubble growth from a heated plane since, despite noteworthy differences, bubble growth in an infinite pool of superheated liquid exhibits similar growth regimes (Carey, 1992). In the particular case of bubble growth from a heated plane in a non-uniform temperature field, Mikic & Rohsenow (1969) developed a model based on a one-dimensional analysis of the heat equation for the waiting period and then again for the growth period in assuming that the bubble's interface is at saturation temperature. The resulting Mikic & Rohsenow (1969) model contains a shape factor, accounting for the moving and curved interface, which is solved for by considering the limiting case of a spherical bubble in an extended pool of superheated liquid put forth by Plesset & Zwick (1954). In the treatment of the problem, the calculation of the waiting time is necessary and is done so by Han & Griffith (1965) in considering a thin isothermal layer adjacent to the bubble interface that acts as a conduction layer for the bubble. Mikic *et al.* (1970) provide a unified relation for both regimes, inertia-controlled and heat-transfer controlled, that is dependent on a Kinetic Energy balance containing an empirical constant. Further vapour bubble growth correlations depending on empirical results are detailed in chapter 2.

A common feature of these studies is a restrictive bubble geometry, which in the case of bubble growth on a heated plane, unrealistically simplifies bubble growth to spherical. The resulting models often compensate for this by including empirical correction terms in order to match validating data thereby impeding our understanding of the mechanisms responsible for bubble growth.

In order to validate a bubble shape proposition, either spherical or not, a bubble growth experiment was necessary that reduces the number of varying parameters, while still producing growing vapour bubbles due to the phase change phenomenon. This was accomplished by Samuel Siedel of INSA Lyon (Siedel *et al.*, 2008; Siedel *et al.*,2011) in which boiling conditions are tailored such that a single bubble grows from an artificial nucleation site while the bubble foot remains fixed to the perimeter of the cavity throughout its growth cycle.

In this study, a geometric model, validated for adiabatic bubble growth in the previous chapter 4, is adapted to heat-transfer controlled bubble formation. In a collaborative effort with Samuel Siedel of INSA Lyon, the validating experiments are idealized to favour the conditions of the model featuring a bubble foot that is fixed to the perimeter of an artificial nucleation site; the experiments are described in detail in section 3.4. The experiments feature heat-induced low saturation temperature *n*-pentane vapour bubbles growing from an artificial nucleation cavity of 90 μm on a heated plane; the wall superheat is between 2K and 6K since outside of this range the nucleation site deactivates or bubble coalescence occurs; the heat flux is low (ranging from 6 to 9 kW/m^2) in order to minimize microlayer vaporization and to maintain bubble growth within the heat-transfer controlled regime (Siedel *et al.*, 2008; Siedel *et al.*, 2011).

5.2. Saturated Bulk Fluid Temperature

In this study, the particular case of bubble growth due to vaporization in which the bulk fluid is at saturation temperature is investigated.

For this scenario, Eq. 2-57, combined with the initial boundary layer thickness provided by Eq. 2-75, reduces the temperature profile adjacent to the heated plane to,

$$5\text{-}2 \qquad \theta(y,t)=\left(T_{wall}-T_{sat}\right)\left(erf\left(\frac{y}{\sqrt{4\alpha t}}\right)-erf\left(\frac{y}{\sqrt{4\alpha\left(t+\delta_o^2/(\pi\alpha)\right)}}\right)\right).$$

The above is the temperature profile for the liquid adjacent to the heated plane for a constant wall temperature of T_{wall}.

It is carefully noted that the bubble interface and the heated plane positions have coincided in the modeling of the temperature field. The fact that the bubble interface is in fact moving away from the heated plane is addressed in the forthcoming section 5.3.

Strictly for illustrative purposes, Figure 5-1 shows the predicted temperature profile during the growth period of Eq. 5-2 for a fluid at saturation temperature. The input conditions are that of *n*-pentane with a wall superheat of 2.1 K. This graphical representation of the temperature profile during the growth period illustrates that the thermal boundary layer's peak temperature diminishes in time corresponding to the energy absorbed during bubble formation. Furthermore, the temperature near the wall decreases and the boundary layer's peak temperature advances away from the plate with time. Arbitrary initial normalized boundary layer thicknesses of 0.1 and 10 are used in the illustration in which the nucleation cavity radius is the characteristic length.

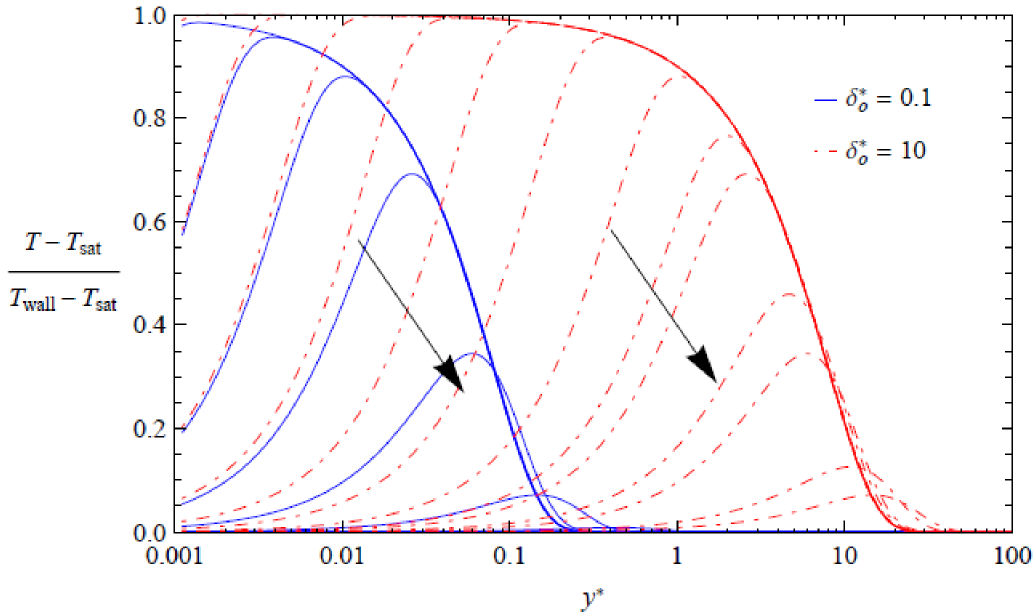

Figure 5-1: Graphical representation of the predicted temperature profile during the growth period, $0 < t < t_d$. The arrows indicate the advancement of time.

5.3. Moving Interface

As previously mentioned, the temperature profile assumes the boundary condition $T(0,t) = T_{sat}$ during the growth period to be located at position $y = 0$ corresponding to the bubble interface location. Since the bubble is growing, is curved and is expanding, the boundary is therefore moving. This phenomenon has not yet been accounted for in the model. It does however have an influence on bubble growth rate since the mass balance at the bubble interface requires that the mass flow rate of vapour be proportional to the heat transfer rate at the bubble interface,

$$\text{5-3} \qquad h_{lv}\rho_v \frac{dV}{dt} = k_l \int \nabla \cdot \vec{T}\, dA \; .$$

In particular, accounting for the variable interfacial area in the temperature profile will have an effect on the temperature gradient of the above Eq. 5-3.

In an attempt to account for the moving boundary, Mikic & Rohsenow (1969) proposed a shape factor value of $\sqrt{3}$. In assuming the bubble to be spherical throughout its growth, they solved the interfacial mass-energy balance Eq. 5-3 with the temperature profile of Eq. 2-57 and included an unknown constant, noted *C*, into the solution,

$$\text{5-4} \qquad \rho_v h_{lv} \frac{dR}{dt} = Ck\left(\frac{T_{wall} - T_{sat}}{\sqrt{\alpha\pi t}} - \frac{T_{wall} - T_{\infty}}{\sqrt{\alpha\pi\left(t + \delta_o^2/\left(\pi\alpha\right)\right)}} \right).$$

The initial thermal boundary layer thickness δ_o is a function of the waiting time (Eq. 2-75). The unknown *C* was solved for by equating the above with the limiting solution of spherical bubble growth in an infinite uniformly superheated liquid Plesset & Zwick (1954),

$$\text{5-5} \qquad h_{lv}\rho_v \frac{dR}{dt} = \sqrt{3}k \frac{T_{\infty} - T_v}{\sqrt{\alpha\pi t}} \, ,$$

and by setting the bubble vapour temperature to the liquid saturation temperature.

In the Mikic & Rohsenow (1969) analysis, the bubble volume is calculated by integrating Eq. 5-4 which solves for the bubble radius and by assuming the bubble to be a perfect sphere.

5.3.1. Shape factor

The thickness of the thermal boundary layer above and near the bubble is altered by the presence of the bubble. This has a direct consequence on the temperature gradient effectively scaling down the vertical position by the shape factor. This increases the temperature gradient as if the medium were reduced in thickness. It is postulated here that this reduction in thickness is due to a movement upwards of the thermal boundary layer initiated by the bubble itself making the $\sqrt{3}$ shape factor of Mikic & Rohsenow (1969) a simple ratio of the calculated thermal boundary thickness δ and the thermal boundary thickness affected by the bubble interface, noted *d*. Indeed, Han & Griffith (1965) observed that during the rapid expansion of early bubble growth, a large portion of the thermal layer is translated vertically upwards.

Illustrated in Figure 5-2 are the thermal boundary thickness, noted δ, as conceptualized by the temperature field model and the adjusted thickness, noted *d*, that is reduced in thickness due to bubble formation. The position term *y* is the perpendicular distance from the heated plane and the position term ζ is the perpendicular distance from the bubble interface.

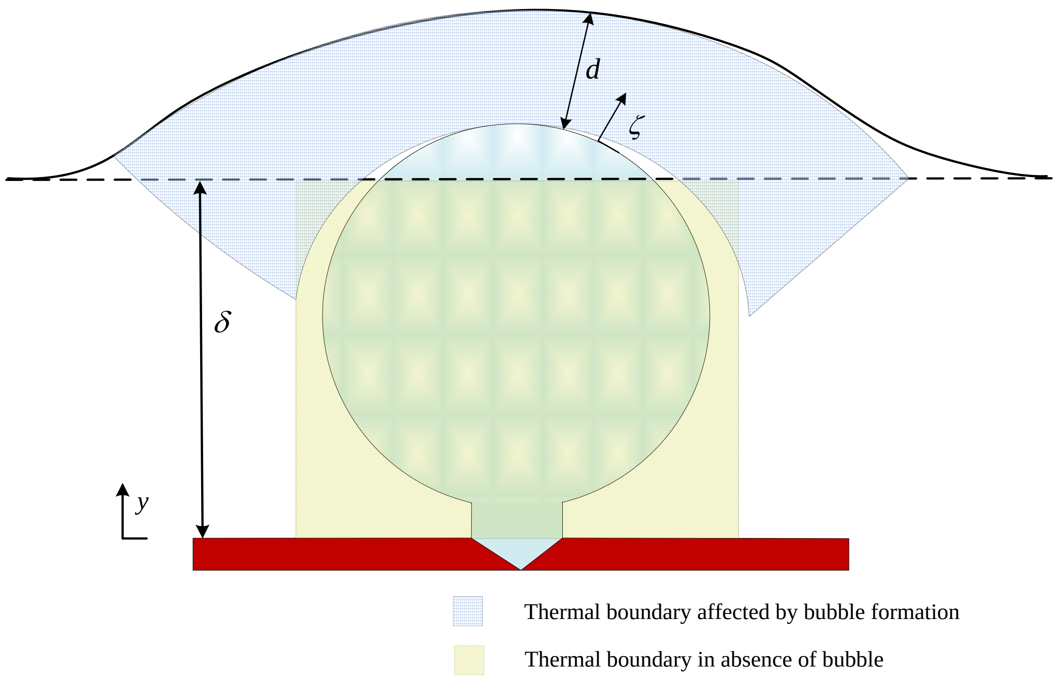

Figure 5-2 : Effects of bubble growth on the thermal boundary layer.

The shape factor $\sqrt{3}$ is therefore the ratio δ / d and is incorporated into the temperature profile with the following change of variable.

5-6 $$y = \frac{\delta}{d}\zeta = \sqrt{3}\zeta \, .$$

The temperature profile described by Eq. 5-2 can therefore be expressed in terms of ζ ,

5-7 $$\theta(\zeta, t) = \left(T_{wall} - T_{sat}\right)\left(erf\left(\frac{\sqrt{3}\zeta}{\sqrt{4\alpha t}}\right) - erf\left(\frac{\sqrt{3}\zeta}{\sqrt{4\alpha\left(t + \delta_o^2 / (\pi\alpha)\right)}}\right)\right).$$

Equation 5-7 represents the temperature profile adjacent to the heated plane in which a shape factor $\sqrt{3}$ is included and ζ is the distance from the bubble interface.

5.4. Radius Growth Curve

The temperature profile of Eq. 5-7 is applied to the energy-mass balance of Eq. 5-3. Due to the symmetry of the problem, the temperature profile is one dimensional. Furthermore, in light of the numerical study on bubble sphericity of chapter 3, truncated spherical bubble geometry is adopted, illustrated in Figure 3-34, in which the bubble vapour-liquid surface area and bubble volume are

5-8 $$A_{tr}(R) = 2\pi\left(R + \sqrt{R^2 - b^2}\right)$$

and Eq. 3-39 respectively. It is also assumed that the temperature gradient at the interface is uniform over the interface. With these conditions, Eq. 5-3 is expressed as,

5-9 $$h_{lv}\rho_v \frac{dV}{dR}\frac{dR}{dt} = k_l A \left.\frac{dT}{d\zeta}\right|_{\zeta=0}$$

which reduces to,

5-10 $$\int \frac{h_{lv}\rho_v}{A_{tr}}\frac{dV_{tr}}{dR}dR = \int k_l \left.\frac{d\theta}{d\zeta}\right|_{\zeta=0} dt\,.$$

The importance in Eq. 5-10 lies in that the evolving shape of the bubble is considered in the integration of the interfacial mass-energy balance equation. Typically, the bubble shape is fixed to spherical and the bubble only changes in size. However, the interfacial mass-energy balance is greatly affected by the shape of the bubble and therefore requires accurate bubble geometry for an accurate account of interfacial mass and energy transfer.

From Eq. 5-7, the one dimensional temperature gradient is calculated to be,

5-11 $$\left.\frac{d\theta}{d\zeta}\right|_{\zeta=0} = \left(T_{wall} - T_{sat}\right)\left(\frac{1}{\sqrt{\alpha\pi t/3}} - \frac{1}{\sqrt{\alpha\pi t/3 + \delta_o^2}}\right)$$

The integrand of the left hand side of Eq. 5-10 is calculated to be,

5-12 $$\frac{h_{lv}\rho_v}{A_{tr}}\frac{dV_{tr}}{dR} = \frac{1}{2}h_{lv}\rho_v\left(1 + \frac{R}{\sqrt{R^2 - b^2}}\right).$$

Integrating Eq. 5-10 fully with the initial condition that the bubble radius equals the cavity radius at the beginning of the growth period yields an equation which implicitly solves for the bubble radius during the growth cycle as a function of time,

5-13 $$\frac{1}{2}h_{lv}\rho_v\left(R + \sqrt{R^2 - b^2} - b\right) = \frac{2k_l\left(T_{wall} - T_{sat}\right)}{\sqrt{\alpha\pi/3}}\left(\sqrt{t} - \sqrt{t + \frac{\delta_o^2}{\alpha\pi/3}} + \sqrt{\frac{\delta_o^2}{\pi\alpha/3}}\right).$$

Simplifying with the use of the Jakob number, noted *Ja*, and defined relative to the wall superheat,

5-14 $$Ja = \frac{c_p \rho_l \left(T_{wall} - T_{sat}\right)}{\rho_v h_{lv}},$$

reduces Eq. 5-13 to,

5-15 $$\begin{aligned} &R + \sqrt{R^2 - b^2} - b \\ &\quad = 4\alpha^{1/2}\pi^{-1/2} Ja\sqrt{3}\left(\sqrt{t} - \sqrt{t + \frac{\delta_o^2}{\alpha\pi/3}} + \sqrt{\frac{\delta_o^2}{\alpha\pi/3}}\right). \end{aligned}$$

Equation 5-15 is conveniently expressed in non-dimensional terms by identifying the cavity radius, noted *b*, as the characteristic length and the characteristic time as,

5-16 $$t_{Ja} = \frac{\pi}{\alpha}\left(\frac{b}{4Ja}\right)^2.$$

The non dimensional terms are defined as,

5-17 $$\begin{aligned} R^* &= \frac{R}{b} \\ s^* &= \sqrt{R^{*2} - 1} \\ \hat{t} &= \frac{t}{t_{Ja}} \\ \bar{\delta}_o &= \frac{\delta_o}{\sqrt{\alpha\pi t_{Ja}/3}} \end{aligned}.$$

With these parameters, Eq. 5-13 is reduced to,

5-18 $$R^* + s^* - 1 = \sqrt{3}\left(\sqrt{\hat{t}} - \sqrt{\hat{t} + \bar{\delta}_o^2} + \bar{\delta}_o\right).$$

Equation 5-18 is the governing equation for nucleate bubble growth in a non-uniform temperature field with a bubble foot that is fixed to the perimeter of the nucleation cavity. It is dependent on the fluid properties, the initial thermal boundary layer thickness, the wall superheat and the nucleation site radius.

5.5. Results and Discussion

In a collaborative effort with Samuel Siedel of INSA-Lyon, the model is tested against bubble growth experiments from an artificial nucleation site of cavity radius 90 μm. The working fluid is *n*-pentane due to its low saturation temperature at 1 bar of 35.7 ^{o}C. These experiments are particularly well adapted to such a model since the ratio of heat flux transmitted directly from the heated plane to the bubble is very low (approximately 1%) making any microlayer vaporization contribution negligible. The wall temperature can then be assumed to be kept constant allowing it to be used as a reference. This is a key component in the testing of the model as a constant surface temperature had been assumed. With this and heat flux measurements, a range of initial thermal boundary layer thickness is generated from the uncertainties in the measurements. Despite the non-uniform temperature field, the *n*-pentane experiments provide a heat-transfer controlled environment. This is due to the low wall superheat (2.1 K and 4.7 K), a low imposed heat flux, a moderate contact angle (33 degrees which is a result of the wetting properties of *n*-pentane) and a high latent heat of evaporation 25.9 kJ/mole. Such conditions result in slower bubble growth minimising the effects of inertia thereby requiring heat and mass transfer at the bubble interface for bubble growth. Furthermore, mass transfer due to microlayer vaporization is considered negligible. This is due to several factors: the low Bond number value implies a more spherical shape (refer to chapter 3) thus minimizing the microlayer; microlayer contribution to vapour bubble growth is negligible in the heat-transfer controlled regime (Carey, 1992); Judd & Huang (1976) showed that microlayer evaporation is negligible for low heat fluxes.

Shape and size of bubbles are recorded with a high speed camera, and computed by an automatic processing of the images. Rather than measuring the volume of the bubble from an equivalent radius measurement requiring that the measurements themselves impose some type of bubble geometry, the volume is measured from the image processed bubble contours using a conical frustum geometric analysis described in section 3.5; the volume is therefore identified as the varying parameter.

5.5.1. Model Bubble Volume

The model's bubble volume is calculated assuming that the bubble grows as a truncated spherical segment rising due to an elongating cylindrical neck. Furthermore, the foot of the bubble is assumed to be fixed to the perimeter of the nucleation site. For this geometric constraint, as described in chapter 4, the volume is related to the bubble radius and bubble neck height in the following way,

$$5\text{-}19 \qquad {}^{*}V = \frac{1}{2}\left(R^{*}+s^{*}\right)^{2}\left(2R^{*}-s^{*}\right)+\frac{3}{2}h^{*}.$$

Once again, the normalized terms used in the above are such that, for an arbitrary value ζ, $\zeta^{*}=\zeta/b$ and the volume is normalized by the incipient hemispherical bubble with volume $V_o=(2/3)\pi b^3$ such that ${}^{*}V=V/V_o$.

The neck height represented in the last term on the right hand side of Eq. 5-19 is related to the detachment radius and the growth time in the same formulation as in chapter 4 such that,

$$5\text{-}20 \qquad h^{*}=h_d^{*}\left(\frac{\hat{t}}{\hat{t}_d}\right)R_d^{*}$$

in which the geometric detachment relation of section 4.2 requires that,

$$5\text{-}21 \qquad h_d^{*}=\frac{\left(R_d^{*}-s_d^{*}\right)\left(2R_d+s_d^{*}\right)}{\left(R_d^{*}+s_d^{*}\right)}+\frac{2}{3}.$$

The detachment radius is calculated by setting the sum of the forces acting on the bubble is quasi-static growth identified in section 4.3 to zero, 5-22 $$\underbrace{-2\pi b\sigma Sin\alpha}_{F_c}+\underbrace{\frac{2\pi\sigma b^2}{R_d}}_{F_p}+\underbrace{(\rho_l-\rho_v)g\left(\frac{4\pi\left(R_d^2-b^2\right)^{3/2}}{3}\right)}_{F_b}=0\,.$$

Equation 5-22 is normalized by the cavity radius reducing Eq. 5-22 to,

5-23 $$\frac{\sin\alpha-R_d^{*-1}}{\left(R_d^{*2}-1\right)^{3/2}}=\frac{2}{3}Bo_b\,.$$

The model's ability to accurately predict bubble volume during bubble formation for the vapour bubble experimental conditions described in section 3.4 is illustrated in Figure 5-3 to Figure 5-6. The working fluid is *n*-pentane, the wall superheats are 2.1 K and 4.7 K, the nucleation cavity radius is 90 µm and the contact angle for *n*-pentane is measured to be 33 degrees. From Eq. 5-1, bubble growth is deemed within the heat-transfer controlled regime for working conditions in which the following inequality is satisfied,

5-24 $$Ja\ll\frac{2}{3\alpha}\sqrt{\frac{b\sigma}{3\rho_l}}\approx 237\,.$$

The above inequality is easily satisfied for the low wall superheats of the working conditions. The bubble growth is therefore deemed entirely within the heat-transfer controlled regime due to the low Jakob numbers which are 2.83 and 6.32 corresponding to wall superheats of 2.1 K and 4.7 K respectively. The model is also compared with those of Han & Griffith (1965), Van Stralen (1966), Mikic & Rohsenow (1969) and Zhao *et al.* (2002) detailed in chapter 2.

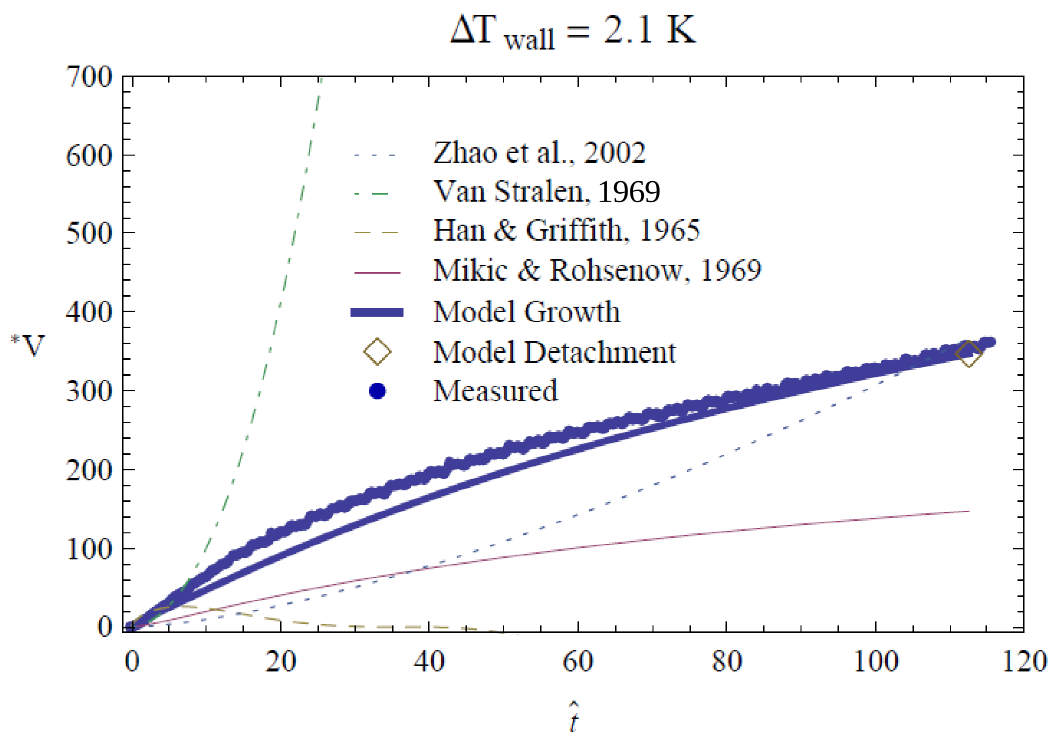

Figure 5-3: Predicted versus measured bubble volume growth histories. The wall superheat is 2.1 K, the bulk liquid is saturated *n*-pentane and the artificial nucleation cavity radius is 90 μm. The wall superheat Jakob number is 2.83.

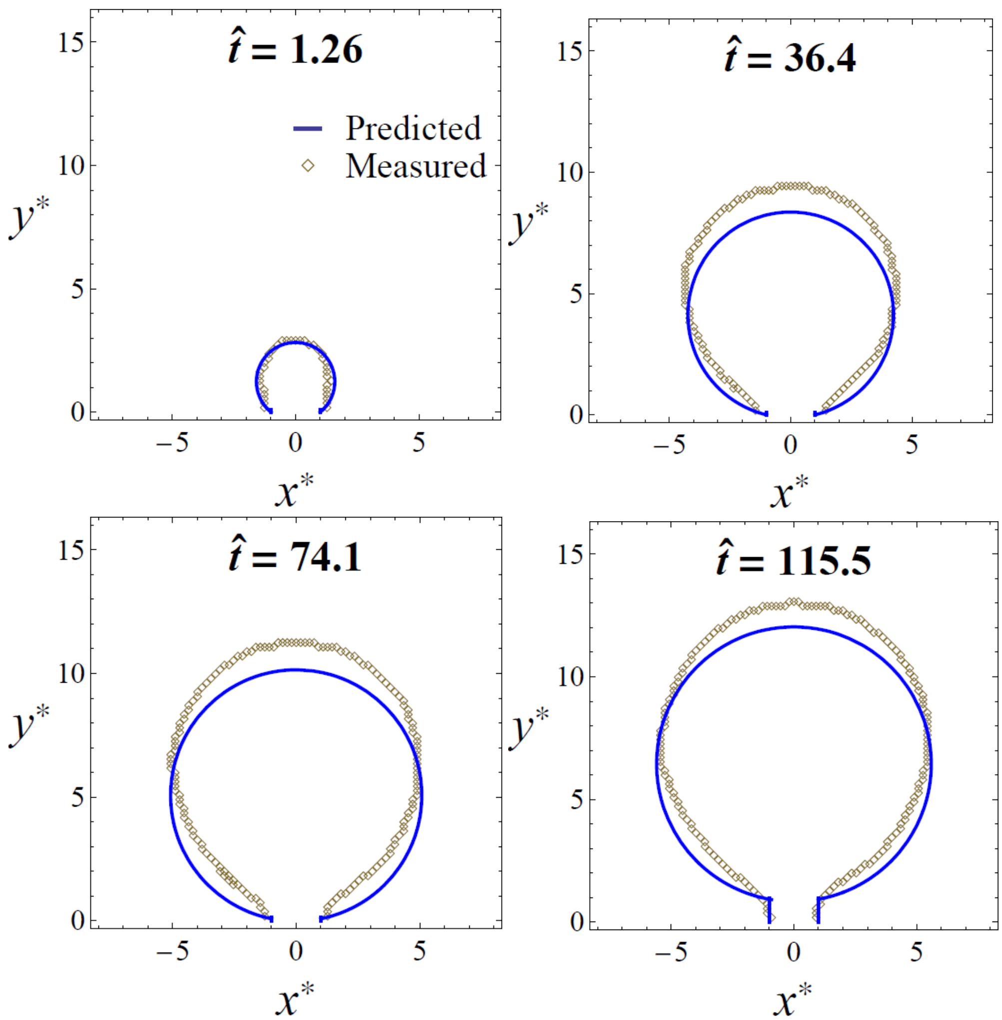

Figure 5-4: Predicted versus measured bubble contour growth histories. The wall superheat is 2.1 K, the bulk liquid is saturated *n*-pentane and the artificial nucleation cavity radius is 90 μm. The wall superheat Jakob number is 2.83.

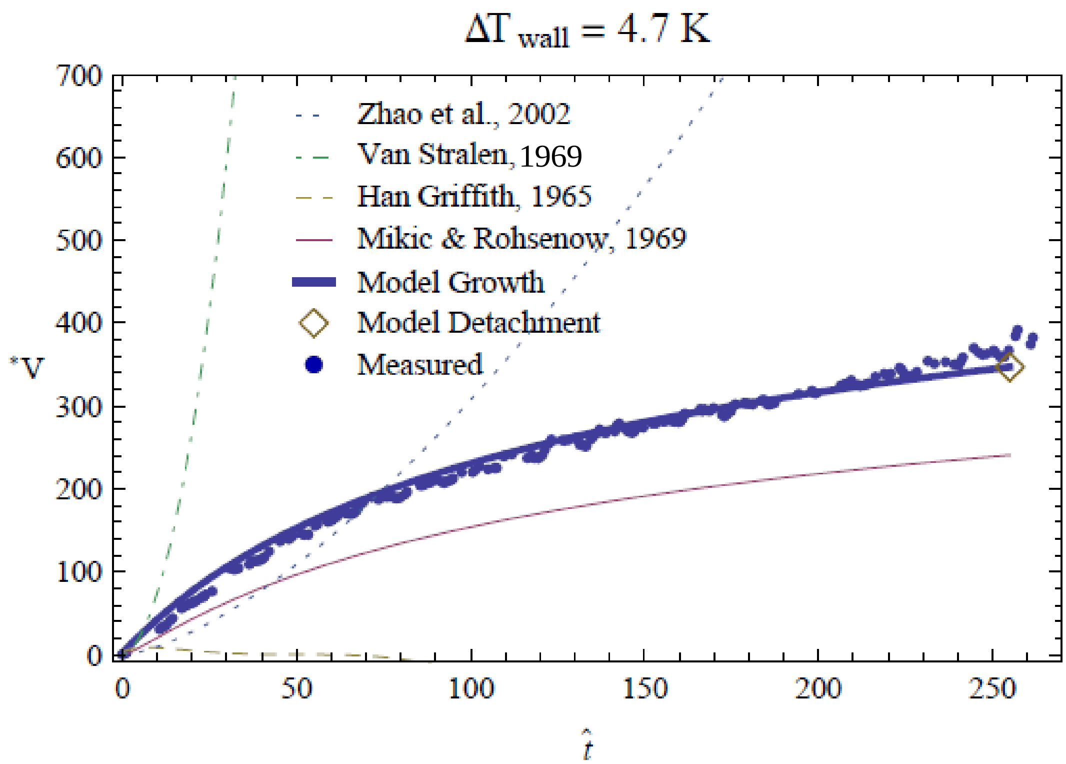

Figure 5-5: Predicted versus measured bubble volume growth histories. The wall superheat is 4.7 K, the bulk liquid is saturated *n*-pentane and the artificial nucleation cavity radius is 90 μm. The wall superheat Jakob number is 6.32.

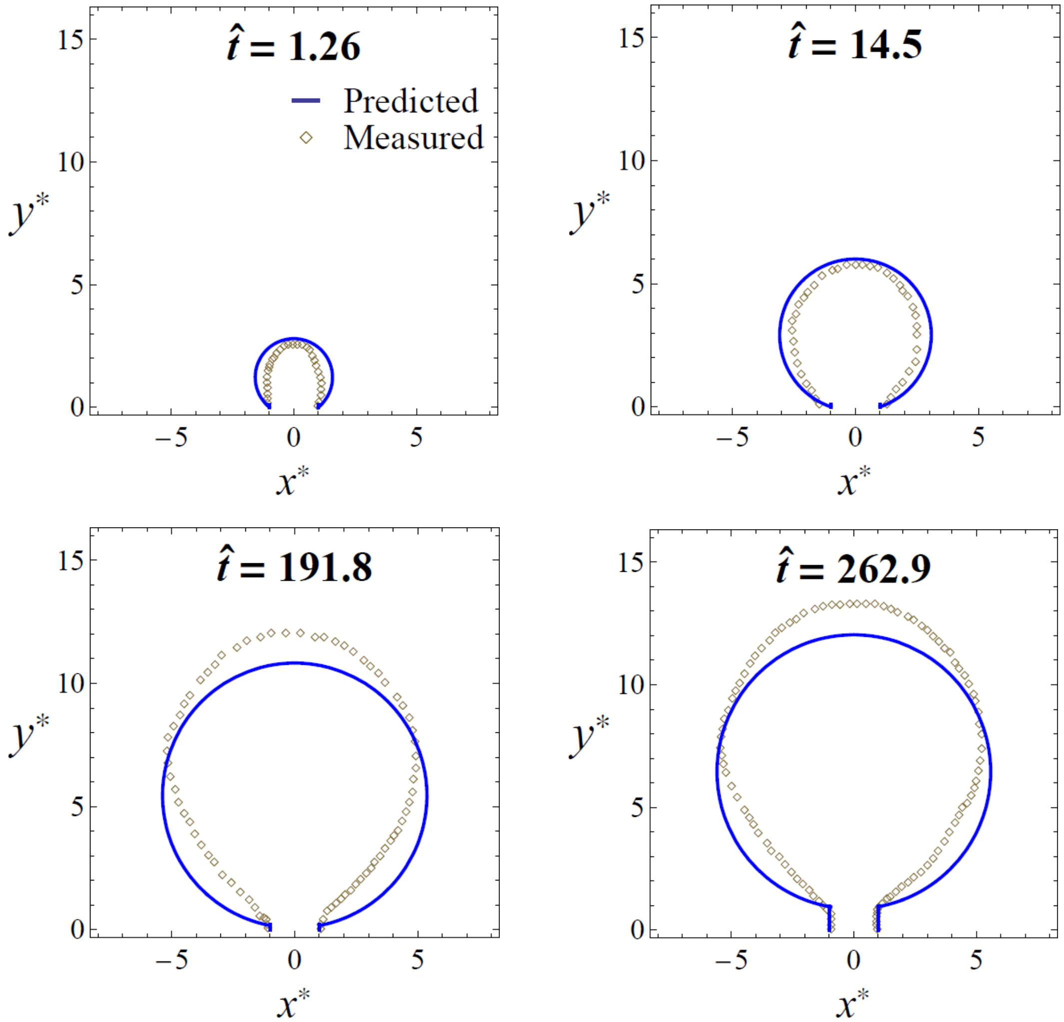

Figure 5-6: Predicted versus measured bubble contour growth histories. The wall superheat is 4.7 K, the bulk liquid is saturated *n*-pentane and the artificial nucleation cavity radius is 90 μm. The wall superheat Jakob number is 6.32.

The initial thermal boundary layer is a required input parameter for the present model, the Mikic & Rohsenow (1969) model and the Han & Griffith (1965) model. From the validating data, the maximum initial thermal boundary layer possible is calculated from the heat flux measurements for the wall superheat of 2.1 K and the wall superheat of 4.7 K detailed in Siedel *et al.* (2011). The most appropriate initial thermal boundary layer within the limit was inputted into the models. The table below details the initial thermal boundary layers used in generating the growth curves for the respective models. The initial thermal boundary layer is normalized by the bubble foot radius such that $\delta_o^* = \delta_o / b$. It is noted that the best fit thermal boundary layer thickness for the Han & Griffith (1965) and Mikic & Rohsenow (1969) models was the maximum resulting from the Siedel *et al.* (2011) heat flux measurements.

Table 5-1 : Initial thermal boundary layer

	$\Delta T_{wall} = 2.1K$	$\Delta T_{wall} = 4.7K$
Present Model	$\delta_o^* = 1.526$	$\delta_o^* = 0.553$
Mikic & Rohsenow (1969)	$\delta_o^* = 1.559$	$\delta_o^* = 0.739$
Han & Griffith (1965)	$\delta_o^* = 1.559$	$\delta_o^* = 0.739$

5.5.2. Centre of gravity

The rise of the centre of gravity provides insight into the elongation of the bubble. The model predicted bubble centre of gravity is once again deduced from the bubble geometry of chapter 4, illustrated in Figure 4-3, in which the centre of gravity is shown to be geometrically related to the vertical position of the bubble neck height and the bubble radius,

$$\text{5-25}\quad H^* = \frac{\left(3R^* - s^*\right)\left(R^* + s^*\right)\left(2h^* + R^* + s^*\right) + 2h^*\left(R^* - s^*\right)\left(3h^* + R^* + s^*\right)}{4\left(3h^*\left(R^* - s^*\right) + \left(2R^* - s^*\right)\left(R^* + s^*\right)\right)}.$$

The model's ability to accurately predict the bubble centre of gravity during bubble formation is illustrated in Figure 5-7 and Figure 5-8 below for the same experimental conditions as in Figure 5-3 and Figure 5-5 respectively.

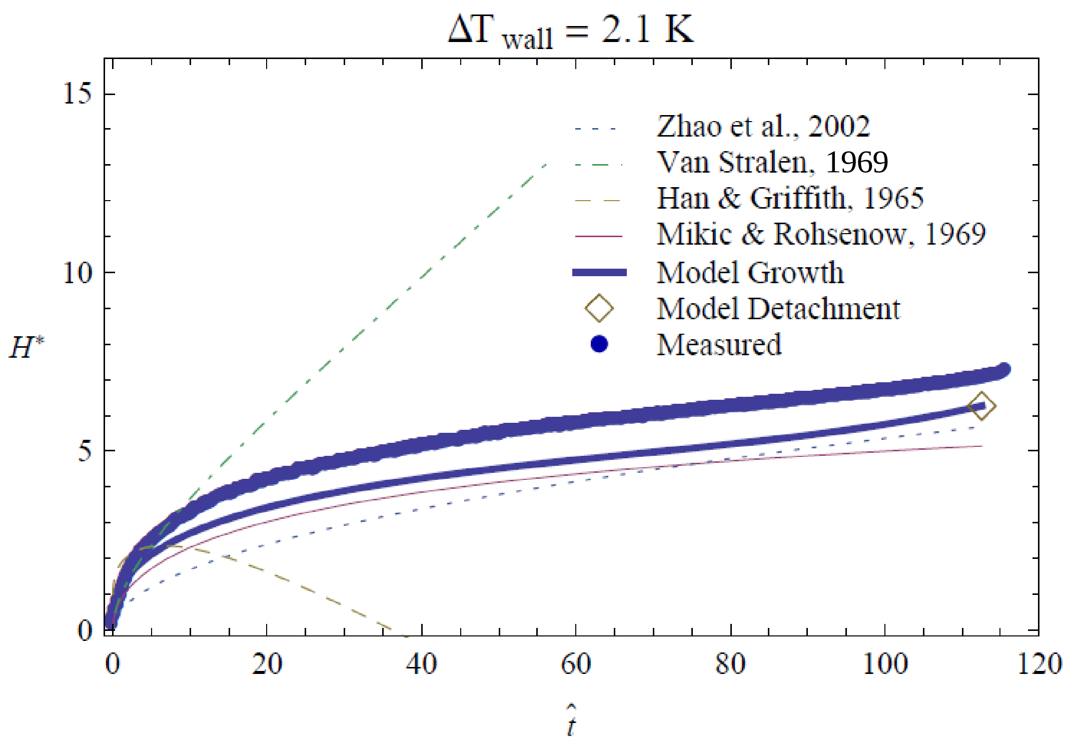

Figure 5-7: Predicted versus measured bubble centre of gravity growth histories. The wall superheat is 2.1 K, the bulk liquid is saturated *n*-pentane and the artificial nucleation cavity radius is 90 μm. The wall superheat Jakob number is 2.83.

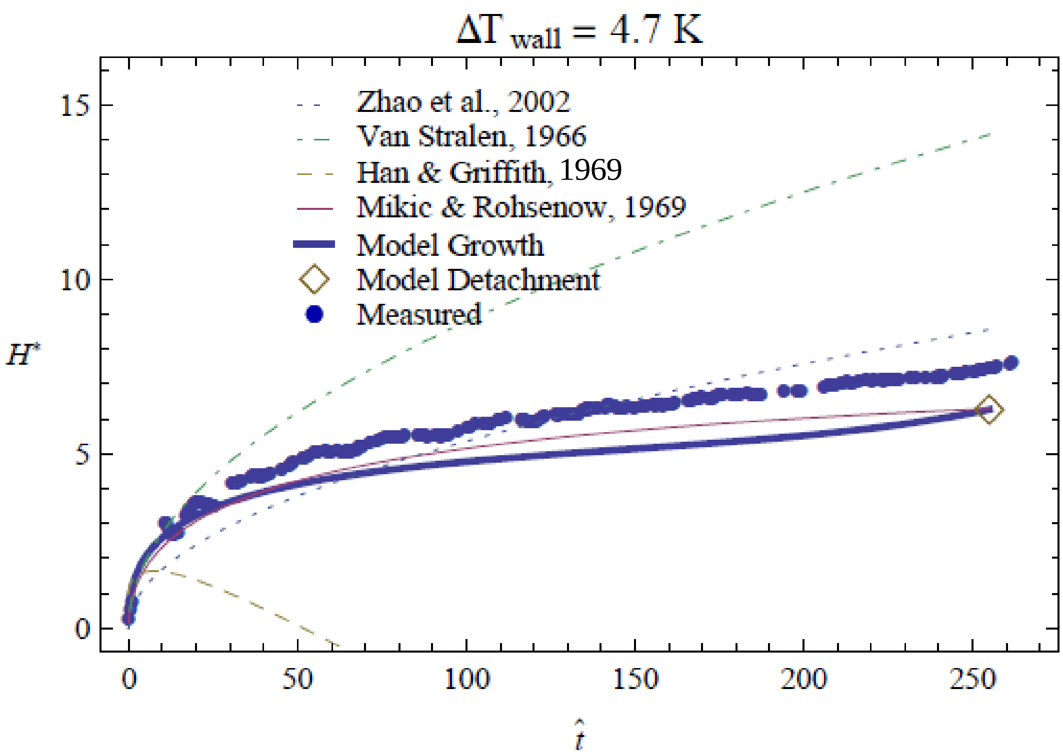

Figure 5-8: Predicted versus measured bubble centre of gravity growth histories. The wall superheat is 4.7 K, the bulk liquid is saturated *n*-pentane and the artificial nucleation cavity radius is 90 μm. The wall superheat Jakob number is 6.32.

The results show that the model under predicts the centre of gravity position. It does however correctly predict the centre of gravity growth trend. In particular, a common short coming of a spherical assumption or a truncated spherical assumption that does not include the necking phenomenon, is that the centre of gravity vertical position plateaus near the end of the growth cycle. However, it is experimentally observed that the centre of gravity vertical position increases near the end of the growth cycle as the bubble prepares to detach. The model proposed in this chapter correctly predicts this trend yet under predicts the magnitude of the centre of gravity vertical position.

5.5.3. Aspect Ratio

The rise of the centre of gravity in this document has been attributed to the asymmetric growth of the bubble which is responsible for its changing shape. The bubble has been assumed to transition from hemispherical to spherical with its bulk rising due to the necking phenomenon. The combination of the rise and transforming shape of the bubble can be described in a simple term as bubble elongation. A convenient method of quantifying bubble elongation is the bubble Aspect Ratio, noted *AR* and detailed in section 3.7.7, which is defined as the ratio of bubble height to bubble width.

The model predicts the bubble height, illustrated in Figure 4-3, to be,

5-26 $$h^*_{bub} = R^* + s^* + h^* .$$

The model's ability to accurately predict the bubble *AR* during bubble formation is illustrated in Figure 5-9 and Figure 5-10. The predictive capabilities of the Han & Griffith (1965), Van Stralen (1966), Mikic & Rohsenow (1969) and Zhao *et al.* (2002) models are represented by an *AR* of unity due to the spherical assumptions of these models.

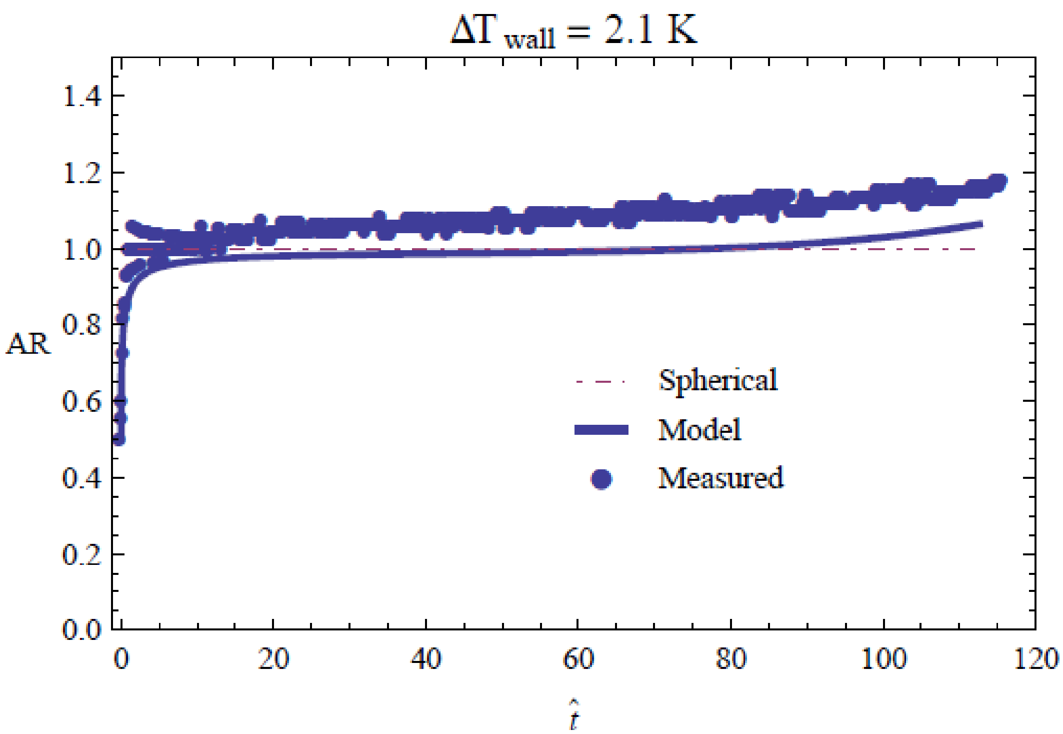

Figure 5-9: Predicted versus measured bubble *AR* growth histories. The wall superheat is 2.1 K, the bulk liquid is saturated *n*-pentane and the artificial nucleation cavity radius is 90 μm. The wall superheat Jakob number is 2.83.

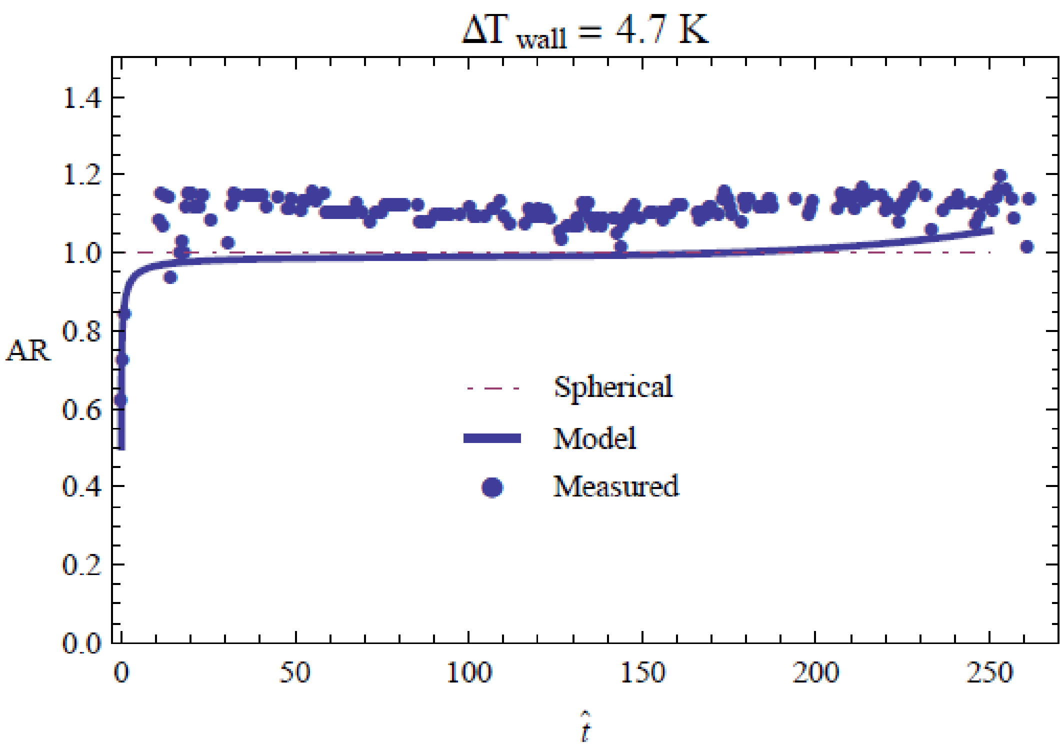

Figure 5-10: Predicted versus measured bubble *AR* growth histories. The wall superheat is 4.7 K, the bulk liquid is saturated *n*-pentane and the artificial nucleation cavity radius is 90 μm. The wall superheat Jakob number is 6.32.

The results show that the model correctly predicts the *AR* trend of sharply increasing during early growth (attributed to the bubble's transition from hemispherical to spherical) to a stabilized value of *AR* that is close to unity (corresponding to a more spherical bubble during mid growth) and finishing with a sharp increase in *AR* near the end stage (attributed to neck formation prior to detachment). Figure 5-10 shows that the model of this chapter correctly predicts the bubble elongation trends.

5.6. Conclusion

The results show that the presented model provides bubble growth curves that follow the observed bubble growth trends for a vapour bubble growing on a heated plane. In contrast, these experimentally measured growth trends are not produced from the previous analytical models that were limited by the spherically geometric bubble assumption.

The novelty of the presented model lies in that it assumes the bubble to change in size as well as in shape while maintaining a fixed bubble foot to the nucleation cavity. The force balance calculation subsequently becomes non contradictory and the interfacial mass-energy balance (Eq. 5-3) is solved for considering the transitioning bubble rather than an unrealistic fixed spherical shape. Indeed, the interfacial mass-energy balance is sensitive to the adopted geometric form when integrating over the vapour-liquid surface; as such, spherical assumptions lead to erroneous growth trends. Furthermore, no empirical correction factors have been used in the presented model thereby providing insight into the physical mechanisms responsible for bubble growth.

The presented model applies to low Bond number heat-transfer controlled bubble growth in which inertial effects from accelerating fluids are negligible and in which the hydrostatic pressure is less than the capillary pressure at all points along the bubble interface. The model is restricted to working conditions yielding Bond numbers that are less than or equal to 0.06 and in which the bubble foot remains fixed to the nucleation cavity.

The comparison between the experimentally measured growth curves and the presented analytical model is made possible by Samuel Siedel's novel experimental results in which a heat-induced vapour bubble grows in a pool of *n*-pentane from a nucleation site on a heated plane such that the bubble foot remains fixed to the cavity perimeter.

5.7. Model Limitations

The proposed model is deemed suitable for low Jakob numbers, as defined by Eq. 5-14, which, for fixed fluid properties, entails low wall superheats. Physically, the Jakob number represents the ratio of sensible energy to latent energy transfer at the bubble interface. Since the model was built on an interfacial mass-energy balance and not on an inertia driven momentum balance, the model will deviate from measured values for higher Jakob numbers. That is to say, high Jakob numbers favour the inertia-controlled bubble growth regime where as low Jakob numbers favour the heat-transfer controlled regime which, in this study, is the bubble growth regime investigated. In particular, for higher wall superheats, the bubble experiences growth due to the bubble's momentum-induced ability to do work on the neighbouring fluid rather than growth due to a heat-induced mass transfer. Subsequently, for higher Jakob numbers, the bubble interface temperature is not necessarily at the fluid's saturation temperature rendering the model's assumption of such non valid. Specifically, the model is limited to working conditions yielding a Jakob number that satisfies the inequality of Eq. 5-24.

The geometric constraint proposed in which the bubble grows as a truncated spherical segment rising due to an elongating cylindrical neck with a foot fixed to the cavity perimeter is limited to applications in which the Bond number is less than or equal to 0.06. This restriction is detailed in chapter 3 and is attributed to the fact that for Bond numbers larger than 0.06, the hydrodynamic force becomes more dominant than the capillary force near the base of the bubble causing the neck walls to pinch inwards and thereby deviate from the model's geometric assumption of a cylindrical neck.

Further limitations require the bubble foot to stay fixed to the perimeter of the nucleation cavity, the wall superheat to be constant, and the micro layer vaporization to be negligible. In the case of the Siedel *n*-pentane experiments described earlier, the experiments conform well to the model for wall superheats between 2 K and 6 K. For superheats less than 2 K the nucleation site deactivates and for superheats greater than 6K bubble coalescence occurs (Siedel *et al.*, 2008).

The ensemble of these limiting conditions make the Siedel *n*-pentane experiments with wall superheats of 2.1 K and 4.7 K the only available validating data for the presented model at the time of this writing.

6. CONCLUSION

6.1. Discussion

A mathematical model is presented that more accurately describes the observed geometries of bubble growth in the quasi-static regime and the heat-transfer controlled regime than previous analytical models and without empirical correction factors thereby contributing to the understanding of the fundamental mechanics behind pool boiling heat transfer.

Bubble shape behaviour is first investigated by considering the bubble degree of sphericity of numerically generated bubble contours for both adiabatic bubble growth and for bubble growth due to vaporization. The numerical treatment of the capillary equation generating bubble profiles is benchmarked with image processed bubble contours for gas injected bubble growth. Furthermore, the novel benchmarking of the capillary equation with bubble growth due to vaporization from an artificial nucleation cavity is made possible by the unique bubble growth experiments of Samuel Siedel in which a vapour bubble grows from a nucleation cavity in a quasi-static manner while its bubble foot remains fixed to the cavity perimeter.

The analysis of the numerical results shows a strict dependence of bubble shape on the Bond number. In particular, bubble elongation due to the necking phenomenon begins earlier and is more pronounced for bubble formation with a larger Bond number. This result can be summarized in saying that a bubble with a small Bond number is more spherical than a bubble with a larger Bond number regardless of the bubble's size.

Subsequently, a geometric model for low Bond number applications in which the bubble changes in size and in shape and which includes the necking phenomenon, is introduced in conjunction with a newly developed geometric detachment relation. A novel feature of the presented geometric model is that the tendency of the bubble to elongate, an observed bubble growth phenomenon, is dictated by the physical mechanisms quantified by the Bond number. The geometric detachment relation is validated with quasi-static adiabatic bubble growth experiments.

In addition, the adopted low Bond number geometry allows for a force balance calculation in which the surface tension and buoyancy force each employ the same bubble geometry. This alleviates the contradictory statement in the much used Fritz (1935) buoyancy-surface tension balance bubble detachment criterion in which the bubble is assumed spherical for the buoyancy force calculation (and thus having at most an infinitesimal in contact with the heated plane) while having a bubble foot in contact with the nucleation site for the surface tension calculation.

Bubble growth curves predicting bubble volume, centre of gravity, aspect ratio and contours are generated from the resulting geometric model and are validated with the benchmarked numerical solution for quasi-static bubble growth in which the Bond number is less than or equal to 0.06.

The geometric model is applied to heat-induced vapour bubble growth in which the bubble foot is fixed to the cavity perimeter. It is validated with *n*-pentane heat-transfer controlled vapour bubble growth from a heated plane of low wall superheat.

The presented models tell a complete analytical story of bubble growth characteristics such as bubble volume, centre of gravity, centre of curvature, height, neck height, truncation, contour, sphericity and aspect ratio.

6.2. Contribution

The notion of the bubble degree of Modified sphericity is introduced showing that it is necessary to consider the asymmetric shape of a bubble throughout its growth cycle when predicting bubble characteristics. In particular, the bubble degree of bubble Modified sphericity is shown to be close to unity during the bubble growth cycle with a deviation from unity near detachment; this deviation is attributed to bubble neck formation near the base of the bubble. It is shown, in a novel result, that this behaviour is dictated by a Bond number for which the characteristic length is the cavity radius.

In addition, the numerical solution to the capillary equation is benchmarked with bubble formation due to vaporization. Indeed, The validation of the bubble profiles generated from the numerical treatment of the capillary equation was made possible by the novel vapour bubble experiments of Siedel *et al.* (2008) in which a heat-induced bubble grows due to vaporization within the heat-transfer controlled growth regime with the bubble foot fixed to the perimeter of the cavity. At the time of this writing, to the best of the author's knowledge, the numerical solution of the capillary equation had only been validated for gas injected bubble growth (Gerlach *et al.*, 2005; Di Marco *et al.* 2005) and for bubble growth due to gas diffusion (Mori & Baines, 2001).

A geometric detachment relation links bubble growth characteristics, such as bubble detachment radius and bubble detachment centre of gravity, which can provide closure to problems that are one relation away from solving a system of equations associated with bubble growth. Such use of this geometric detachment relation resulting in a more accurate bubble growth model than previous analytical models appears in this study for both adiabatic bubble growth and bubble growth due to vaporization for applications in which the Bond number with characteristic length equal to the cavity radius is less than or equal to 0.06.

6.3. Recommended Future Work

Further validation of the numerical treatment of the capillary equation for bubble growth due to vaporization is recommended. In particular, there is very little model validation of the postulation that bubble detachment occurs when the numerical treatment no longer provides a solution (Mori & Baines, 2001; Gerlach *et al.* 2005).

Incorporating the phenomenon of bubble pinch-off at detachment is recommended. This process is very rapid and is often left as an instantaneous event; however, there are a growing number of numerical studies on the subject (Quan & Hua, 2008) and an analytical model would provide insight into the physical mechanisms responsible for bubble pinch-off.

Finally, a natural continuation of this work would be to develop a similar bubble shape model for Bond numbers greater than 0.06 thereby including the inner neck pinching resulting from a dominant hydrostatic pressure.

7. Appendix

7.1. Capillary Equation as a function of *z*

In order to express Eq. 3-18 as a function of *z* rather than as a function of *x*, the respective first order derivatives are related in the following way. Implicitly differentiating $x = x(z)$ with respect to *z* yields,

7-1 $$1 = x'(z)\tfrac{dz}{dx} \;.$$

The above in turn implies Eq. 3-21. Implicitly differentiating Eq. 7-1 yields,

7-2 $$0 = x''(z)\left(\frac{dz}{dx}\right)^2 + x'(z)\frac{d^2z}{dx^2}$$

yielding,

7-3 $$\frac{d^2z}{dx^2} = -\frac{x''(z)\left(\frac{dz}{dx}\right)^2}{x'(z)}$$

which when combined with Eq. 3-21 yields Eq. 3-22.

7.2. Mathematica Code

To measure the bubble volume, vapour-liquid surface area and bubble centre of gravity from the image processed bubble profiles, a *Mathematica* code is written using a conical frustum geometric analysis described in Figure 3-12. The input *data* is a set of coordinates representing half of the bubble contour for a bubble that is symmetric about the vertical axis as illustrated in Figure 3-12.

Input data:

```
data= ...
n=Length[data];
r[i_]:=data[[i+1]][[1]]
R[i_]:=data[[i]][[1]]
h[i_]:=data[[i+1]][[2]]-data[[i]][[2]]
v[i_]:=(1/3)π*h[i](r[i]^2+r[i]*R[i]+R[i]^2)
a[i_]:=π(r[i]+R[i])Sqrt[(R[i]-r[i])^2+h[i]^2]
z[i_, data_] := (hi[i,data] (r[i, data]^2 + 2r[i, data]*R[i, data]
+ 3 R[i, data]^2))/(4 (r[i, data]^2 + r[i, data]*R[i, data] +
R[i, data]^2));
```

Volume: `Sum[v[i],{i,1,n-1}]`

Surface Area: `Sum[a[i],{i,1,n-1}]`

Centre of Gravity: `Sum[z[i, data], {i, 1, n[data] - 1}]`

7.3. Leibniz's Theorem

Let *R* be a region with surface area *S* and a surface velocity of $\vec{w}$. If φ is a scalar, vector or tensor function with time parameter *t*, then

7-4 $$\frac{d}{dt}\int_{R(t)}\phi dV=\int_R \frac{d\phi}{dt}dV+\int_S \vec{n}\cdot\vec{w}\phi dS\ .$$

7.4. Gauss's Theorem

Let R be a region that is bound by the closed surface S. Let $\vec{v}$ be a vector function with continuous partial derivatives. Gauss' Theorem states that,

7-5 $$\int_R div\vec{v}dV=\int_S \vec{n}\cdot\vec{v}dS\ .$$

7.5. The Continuity Equation

The continuum assumption states that the time rate of change of mass of a Material Region is zero. Symbolically,

7-6 $$\frac{d}{dt}\int_{MR}\rho dV=0\ .$$

Applying Leibniz's Theorem to the Material Region with $\vec{v}=\vec{w}$ (Recalling that for a Material Region the surface velocity $\vec{w}$ is equal to the fluid velocity $\vec{v}$),

7-7 $$\int_{MR}\frac{\partial\rho}{\partial t}dV+\int_{MR}\left(\vec{n}\cdot\vec{v}\right)\rho dS=0\ .$$

Applying Gauss' Theorem,

7-8 $$\int \left(\frac{\partial \rho}{\partial t} + \vec{\nabla} \cdot \rho \vec{v}\right) dV = 0 .$$

The above integrand must be zero since the Material Region was chosen arbitrarily yielding the differential form of the continuity equation which for a Material Region with fluid velocity $\vec{v}$ is stated as,

7-9 $$\frac{\partial \rho}{\partial t} + \vec{\nabla} \cdot \rho \vec{v} = 0 .$$

7.6. Prinipal Radius of Curvature at the Apex Evolution

The bubble principal radius of curvature at the apex origin, noted R_o, is investigated with the numerical treatment detailed in chapter 3.

In Figure 7-1, the principal radius of curvature at the apex origin evolution resulting from the numerically generated bubble profiles is illustrated for a fixed bubble foot radius of 1 mm in which the Bond number is varied by varying the gravitational constant only. The fluid properties are that of air in water.

In Figure 7-2, the principal radius of curvature at the apex origin evolution resulting from the numerically generated bubble profiles is illustrated for terrestrial conditions in which the Bond number is varied by varying the bubble foot radius only. The fluid properties are that of air in water.

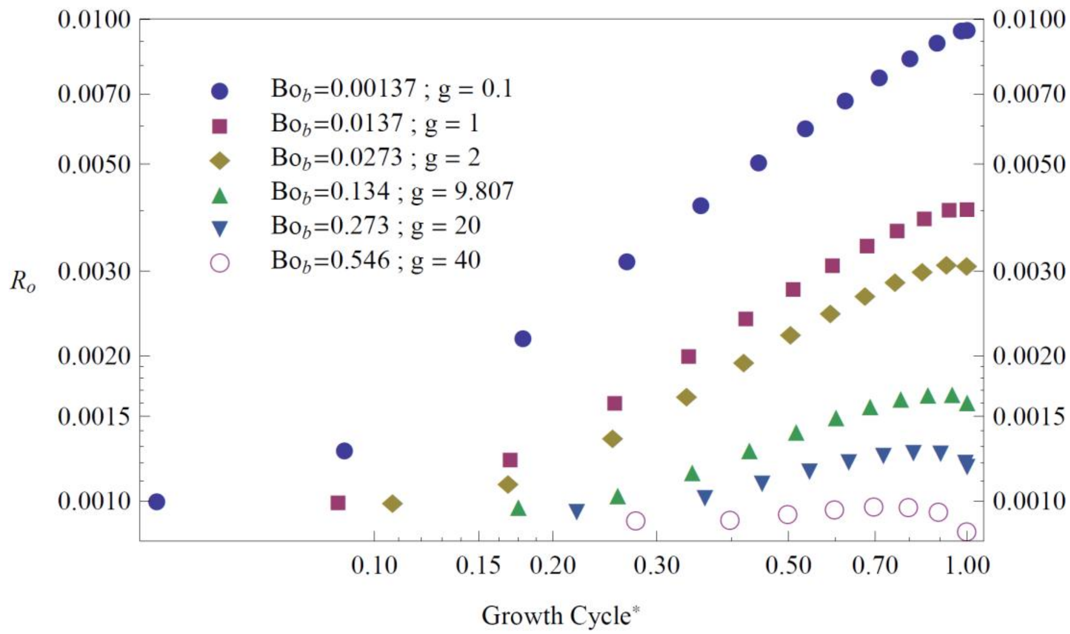

Figure 7-1 : Bubble principal radius of curvature at the apex origin evolution from numerical simulations for a fixed foot radius of 1mm and a Bond number varying with respect to the gravitational constant.

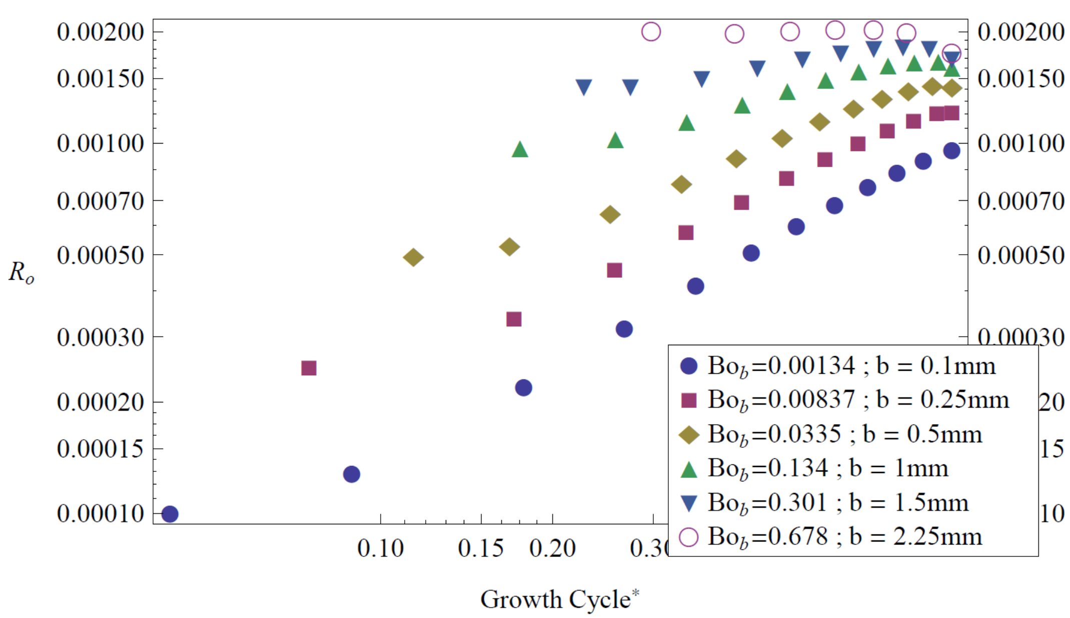

Figure 7-2 : Bubble principal radius of curvature at the apex origin evolution from numerical simulations at terrestrial gravity and a Bond number varying with respect to bubble foot radius.

Figure 7-3 illustrates the dependence of the normalized principal radius of curvature at the apex origin on the Bond number.

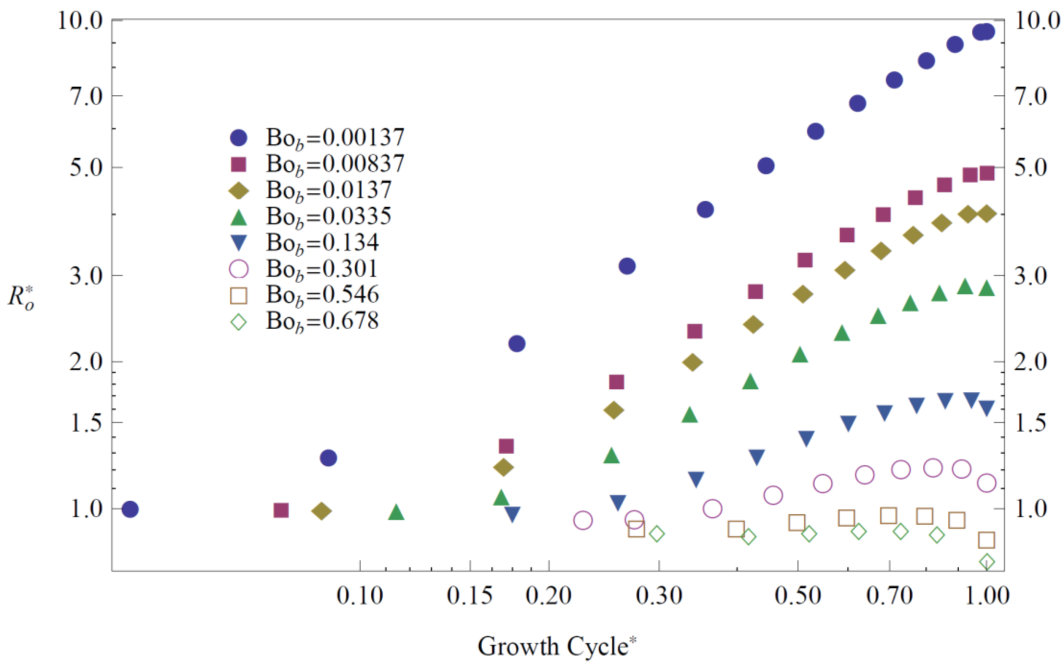

Figure 7-3 : Normalized bubble principal radius of curvature at the apex origin evolution from numerical simulations relative to Bond number.

7.7. The Centre of Gravity of a Truncated Sphere with Cylindrical Neck at its Base

The centre of gravity of the geometric form represented in Figure 4-3 is solved for in the following sequence beginning with the definition of the centre of gravity,

7-10 $$\vec{H} = \frac{\int_0^{R+C} \vec{r}\rho dV}{\int_0^{R+C} \rho dV}.$$

Since the density is assumed uniform and the geometry of the growing bubble is symmetric about the vertical *z* axis, the *z* component of the centre of gravity can be expressed as an integration of the *z* component of the position vector $\vec{r}$. The centre of gravity in terms of the centre of curvature and the bubble radius is calculated in which *A(z)* is the cross sectional surface perpendicular to the *z* axis:

7-11 $$H_z = \frac{1}{V}\int_0^{R+C} r_z dV$$

$$= \frac{1}{V}\int_0^{R+C} zA(z)\,dz$$

$$= \frac{\pi}{V}\left[\int_0^h zb^2 dz + \int_h^{R+C} z\left(x(z)\right)^2 dz\right]$$

$$= \frac{\pi}{V}\left[\int_0^h zb^2 dz + \int_h^{R+C} z\left(R^2 - (z-C)^2\right)dz\right]$$

$$= \frac{\pi}{12V}\left[h^3(4C-3h) + (R+C)^3(3R-C)\right].$$

The volume, noted *V*, of the geometric form illustrated in Figure 4-3 is,

7-12 $$V = \frac{\pi}{3}(R+s)^2(2R-s) + \pi b^2 h\,.$$

Rearranging the above and expressing the volume of the bubble in terms of the bubble centre of curvature, bubble neck height and bubble radius yields,

7-13 $$V=\frac{\pi}{3}\left(R+C-h\right)\left(\left(2R-C\right)\left(R+C+h\right)+2h^2\right).$$

Substitution yields the final expression for the centre of gravity of the bubble,

7-14 $$H=\frac{\left(R+C+h\right)\left(3R-C+h\right)\left(R+C-h\right)+2h\left(R-C+h\right)\left(R+C+2h\right)}{4\left(\left(2R-C\right)\left(R+C+h\right)+2h^2\right)}$$

in which $C=\sqrt{R^2-b^2}+h$.

7.8. Solution to $\int_0^\infty e^{-\zeta^2}d\zeta$

In what follows, a numerical value of the integral *I*, defined as $I=\int_0^\infty e^{-\zeta^2}d\zeta$, is solved for. By definition of *I*, for two arbitrary variables ζ_1 and ζ_2,

7-15 $$I=\int_0^\infty e^{-\zeta_1^2}d\zeta_1=\int_0^\infty e^{-\zeta_2^2}d\zeta_2.$$

I^2 is expressed as a double integral,

7-16 $$I^2=\int_0^\infty e^{-\zeta_1^2}d\zeta_1\int_0^\infty e^{-\zeta_2^2}d\zeta_2=\int_0^\infty\int_0^\infty e^{-\left(\zeta_1^2+\zeta_2^2\right)}d\zeta_1 d\zeta_2.$$

Setting the variables ζ_1 and ζ_2 to $\zeta_1=\lambda\cos\omega$ and $\zeta_2=\lambda\sin\omega$, the above is solved for in terms of λ and ω, 7-17 $$I^2 = \int_0^{\frac{\pi}{2}} \int_0^{\infty} e^{-\lambda^2 \overbrace{\left(\cos^2\omega + \sin^2\omega\right)}^{1}} \lambda d\lambda d\omega = \frac{\pi}{4}\left(-e^{-\lambda^2}\right)\Big|_0^{\infty} = \frac{\pi}{4}.$$

Therefore,

7-18 $$I = \int_0^{\infty} e^{-\zeta^2} d\zeta = \frac{\sqrt{\pi}}{2}.$$

Bibliography

Bai, Q., & Fujita, Y. (2000). Numerical simulation of bubble growth in nucleate boiling - Effects of system parameter. *Multiphase Sci. Tech. , 12* (3-4), 195-214.

Brenn, G., Kolobaric, V., & Durst, F. (2006). Shape oscillations and path transition of bubbles rising in a model bubble column. *Chemical Engineering Science , 61*, 3795-3805.

Brennen, C. E. (2005). Fundamentals of Multiphase Flow. Cambridge University Press.

Buwa, V. V., Gerlach, D., Durst, F., & Schülcker, E. (2007). Numerical simulations of bubble formation on submerged orifices: Period-1 and period-2 bubbling regimes. *Chemical Engineering Science*, *62*, 7119-7132.

Burton, J. C., Waldrep, R., & Taborek, P., (2005). Scaling and instabilities in Bubble Pinch-off. *Physical Review Letters, 94*, 184502-1-4.

Buyevich, Y. A., & Mankevich, V. N. (1995). Interaction of dilute mist flow with a hot body. *Int. J. Heat Mass Transfer , 38*, 731-744.

Buyevich, Y. A., & Webben, B. (1996). Dynamics of vapour bubbles in nucleate boiling. *Int. J. Heat Mass Transfer , 39*, 2409-2426.

Carey, V. P. (1992). Liquid-Vapor Phase-change Phenomena: An introduction to the Thermophysics of Vaporization and Condensation Processes in Heat Transfer Equipment. Taylor and Francis.

Carrera, J., Parthasarathy, R. N., & Gollahalli, S. R. (20006). Bubble formation from a free-standing tube in microgravity. *Chemical Engineering Science , 61*, 7007-7018.

Chen, F., Peng, Y., Song, Y. Z. & Chen, M. (2007). EHD behaviour of nitrogen bubble in DC electric fields. *Experimental Thermal and Fluid Science*, *32,* 174-181.

Cochran, T., & Aydelott, J. (1966). The effect of subcooling and gravity level on boiling in discrete bubble regime. *NASA Technical Note* , TN D-3449.

Cole, R. (1967). Bubble frequencies and bubble departures at subatmospheric pressures. *AIChE Journal., 13*, 779-783.

Cole, R., & Rohsenow, W. M. (1969). Correlation of bubble departure diameters for boiling saterated liquids. *Chem. Eng. Progr. Symp. Ser. A. I. Ch. E. , 65*, 211-213.

Cole, R., & Shulman, H. L. (1966). Bubble departure diameters and subatmospheric pressures. *Chem. Eng. Progr. Symp. Ser. A. I. Ch. E. , 62*, 6-16.

Cole, R., & Shulman, H. L. (1972). Bubble growth rates at high Jakob numbers. *Int. J. Heat Mass Transfer., 15*, 655-664.

Cooper, M. G., Judd, A. M., Malcotsis, G., & Pike, R. A. (1975). Shape and departure of single bubbles growing at a wall. *Letters in Heat and Mass Transfer, 2*, 207-212.

Cooper, M. G., Judd, A. M., & Pike, R. A. (1978). Shape and departure of single bubbles growing at a wall. *Proceedings of the 6th International Heat Transfer Conference*, 115-120.

Davidson, J. F., & Schuler, B. O. (1960). Bubble formation at an orifice in an inviscid liquid. *Trans. Inst. Cham. Engrs , 38*, 335-342.

Di Bari, S., & Robinson, A. J. (2009). Experimental Study of Bubble Growth from a Submerged Orifice considering the Dynamic Pressure Field. *7th International Conference on Boiling Heat Transfer.* Florianopolis, Brazil.

Di Marco, P., Forgione, N., & Grassi, W. (2005). Quasi-static formation and detachment of gas bubbles at a submerged orifice: Experiments, theoretical prediction and numerical calculations. *XXII Congresso Nazionale UIT sulla Trasmissione deel Calore,Parma,* 20-22 Guigno.

Dhir, V. (1991). Nucleate and transition boiling heat transfer under pool and external flow conditions. *Int. J. Heat and Fluid Flow , 12* (4), 290-314.

Dhir, V. (2006). Mechanistic Prediction of Nucleate Boiling Heat Transfer– Achievable or a Hopeless Task? *J. Heat Trans. , 128*, 1-12.

Duhar, G., & Colin, C. (2006). Dynamics of bubble growth and detachment in a viscous shear flow. *Phys. Fluids , 18*, 077101-1-13.

Faghri, A., & Zhang, Y. (2006). Transport Phenomena in Multiphase Systems. Elsevier.

Forster, H. K. & Zuber N. (1954). Growth of a Vapor Bubble in Superheated Liquids. *J. of Applied Physics , 25*, 474-478.

Fritz, W. (1935). Berechnung des Maximalevolumens von Dampfblasen. *Physikalische Zeitschrift , 36*, 379-384.

Fritz, W., & Ende, W. (1936). Verdampfungsvorgang kinematographischen aufnahmen und dampflbasen. *J. Appl. Phys., 25*, 391.

Fuchs, T., Kern, J., & Stephan, P. (2006). A transient nucleate boiling model including microscale effects and wall heat transfer. *J. Heat Transfer , 128* (12), 1257-1265.

Genske, P., & Stephan, K. (2006). Numerical simulation of heat transfer during growth of single vapor bubbles in nucleate boiling. *Int. J. Thermal Science , 45* (3), 299-309.

Gerlach, D., Biswas, G., Durst, F. & Kolobaric, V. (2005). Quasi-static bubble formation on submerged orifices. *Int. J. Heat and Mass Transfer*, 48, 425-438.

Gerlach, D., Alleborn, N., Buwa, V., & Durst, F. (2007). Numerical simulation of periodic bubble formation at a submerged orifice with constant gas flow rate. *Chemical Engineering Science , 62*, 2109-2125.

Han C. and Griffith P. (1965). The mechanism of heat transfer in nucleate pool boililng, *Int. J. Heat Transfer,* Vol. 8, pp. 887-904.

Hutter Y., Kenning, D. B. R., Serfiane, K., Karayiannis, T. G., Lin, H., Cummins, G., & Walton, A. J. (2010). Experimental pool boiling investigations of FC-72 on silicon with artificial cavities and integrated temperature microsensors, *Experimental Thermal and Fluid Science*, 34, 422-433.

Iacona, E., Herman, C., Chang, S. & Liu, Z. (2006). Electric field effect on bubble detachment in reduced gravity environment. *Experimental Thermal Fluid Science, 31*, 121-126.

Incropera, F. J., Dewitt, D. P., Bergman, T. L., & Lavine, A. S. (2007). Introduction to Heat Transfer (5^{th} edition). John Wiley and Sons.

Jensen, M. K., & Memmel, G. J. (1986). Evalution of Bubble Diameter Correlations. *Proceedindings 8^{th} Int. Heat Transfer Conference, 4*, 1907-1912.

Joosten, J. G. H., Zijl, W., & Van Stralen, S. J. D. (1978). Growth of a vapour bubble in combined gravitational and non-uniform temperature fields. *Int. J. Heat Mass Trans, 21*, 15-23.

Judd, R. L., & Hwang, K. S. (1976). A comprehensive model for nucleate pool boiling heat transfer including microlayer evaporation. *J. Heat Trans , 98*, 623-629.

Kasimsetty, S. K., Subramani, A., Manglik, R. M., & Jog, M. A. (2007). Theoretical modelling and experimental measurements of single bubble dynamics from a submerged orifice in a liquid pool. *Proc. ASME-JSME Thermal Engineering Summer Heat Transfer Conference*, (pp. HT2007-32088).

Keim, N. C., Moller, P., Zhang, W. W., & Nagal, S. R. (2006). Breakdown of air bubbles in water: Memory and breakdown of cylindrical symmetry. *Physical Review Letters, 97*, 144503-1-4.

Kiper, A. M. (1971). Minimum Bubble Departure Diameter in Nucleate Pool Boiling. *Heat Mass Transfer, 14*, 931-937.

Klausner, J. F., Mei, R., Hernhard, M. D., & Zeng, L. Z. (1993). Vapour bubble departure in forced convection boiling. *Int. J. Heat Mass Transfer, 36,* 651-662.

Kulkarni, A. A., & Joshi, J. B. (2005). Bubble formation and bubble rise velocity in gas-liquid systems: A review. *Ind. Eng. Chem. Research , 44* (16), 5873-5931.

Lee, H. S., & Merte, H. J. (1996). Spherical vapour bubble growth in uniformly superheated liquids. *Int. Journal Heat Mass Transfer, 39* (12), 2427-2447.

Lee, H. S., & Merte, H. J. (1996). Hemispherical vapor bubble growth i microgravity: experiments and model. *Int. Journal Heat Mass Transfer, 39* (12), 2449-2461.

Lesage, F. J., Cotton, J. S., & Robinson, A. J. (2009). An Equation of Motion for Bubble Growth. *7th International Conference on Boiling Heat Transfer.* Florianopolis, Brazil.

Li, H. Z., Mouline, Y., & Midoux, N. (2002). Modelling the bubble formation dynamics in non-Newtonian fluids. *Chemical Engineering Science, 57* (3), 339-346.

Loubière, K., & Hébrard, G. (2003). Bubble formation from a flexible hole submerged in an inviscid liquid. *Chemical Engineering Science*, *58*, 135-148.

Mikic, B. B. And Rohsenow, W. M. (1969). Bubble growth rates in non-uniform temperature field, *Progress in Heat and Mass Transfer* Vol. 2, pp. 283-293.

Mikic, B. B., Rohsenow, W. M., & Griffith, P. (1970). On bubble growth rates. *Int. J. Heat Mass Transfer , 13*, 657-665.

Mori, B. K., & Baines, D. W. (2001). Bubble departure from cavities. *Int. J. Heat Mass Trans., 44*, 771-783.

Mukherjee, A., & Kandlikar, S. G. (2007). Numerical study of single bubbles with dynamic contact angle during nucleate pool boiling. *Int. J. Heat Mass Trans., 50* (1-2), 127-138.

Nahra, H. K., & Kamotani, Y. (2000). Bubble formation from wall orifice in liquid cross-flow under low gravity. *Chemical Engineering Science*, *55*, 4653-4665.

Nahra, H. K., & Kamotani, Y. (2003). Prediction of bubble diameter at detachment from a wall orifice in liquid cross-flow under reduced and normal gravity conditions. *Chemical Engineering Science, 58*, 55-69.

Nam Y., Wu J., Warrier G. and Ju S. (2009). Experimental and Numerical Study of Single Bubble Dynamics on a Hydrophobic Surface, *J. Heat Transfer, 131* 121004-1-7.

Nam Y., Aktinol E., Dhir V. K. and Ju Y. S. (2011). Single bubble dynamics on a superhydrophilic surface with artificial nucleation sites, *Int. J. Heat MassTransfer*, 54, 1572-1577.

Nieuland, J. J., Veenendaal, M. L., Kuipers, J. A. and Vanswaaij, W. P. M. (1996). Bubble Formation at a Single Orifice in Gas-fluidised Beds, *Chemical Engineering Science*, *51(17)*, 4087-4102.

Oguz, H. N., & Prosperetti, A. (1993). Dynamics of bubble growth and detachment from a needle. *J. Fluid Mech.*, *257*, 111-145.

Panton, R. L. (1996). Incompressible Flow (2nd edition). John Wiley & Sons.

Plesset, M. S., & Zwick, S. A. (1954). The growth of vapor bubbles in superheated liquids. *J. Appl. Phys.*, *25*, 493.

Plesset, M. S., & Prosperretti, A (1977). Annual Review of Fluid Mechanics. *Palo Alto, 9*, 145.

Prosperetti, A. (1982). A generalization of the Rayleigh-Plesset equation of bubble dynamics, *Physics of Fluids*, *25*(3), 409-410.

Prosperetti, A & Plesset, M. S. (1978). Vapour-bubble growth in a superheated liquid, *Int. J. Fluid Mech*., *85* (2), 349-368.

Quan, S. & Hua, J. (2008). Numerical studies of bubble necking in viscous liquids, *Physical Review, 77*, 0663030-1-11.

Rayleigh, Lord (1917). On the pressure developed in a liquid during collapse of a spherical cavity. *Phil. Mag., 34*, 94-98.

Riznic, J., Kojasoy, G., & Zuber, N. (1999). On the Spherically Symmetric Phase Change Problem. *International Journal of Fluid Mechanics Research, 26*, 110-145.

Robinson, A. J. (2002). *Bubble growth dynamics in uniform and non-uniform temperature fields.* Ph.D. Thesis, McMaster University, Mechanical Engineering, Hamilton, Ontario, Canada.

Robinson, A. J., & Judd, R. L. (2001). Bubble growth in a uniform and spatially distributed temperature field. *Int. J. Heat Mass Transfer , 44*, 2699-2710.

Robinson, A. J., & Judd, R. L. (2004). The dynamics of spherical bubble growth. *Int. J. Heat Mass Transfer , 47*, 5101-5113.

Robinson, A. J., Lesage, F., & Judd, R. L. (2010). Numerical method for spherical bubble growth in superheated liquids. *Computational Thermal Sciences , 2* (1), 19-31.

Rohsenow, W. (1985). Boiling. *Handbook of Heat Transfer Fundamentals* , 12-94.

Scriven, L. E. (1959). On the dynamics of phase growth. *Chemical Engineering Science, 10,* 1-13.

Serway, R. A. (1982). Physics for Scientists and Engineers with Modern Physics (4th edition). Saunders College Publishing.

Siedel, S., Cioulachtjian, S., & Bonjour, J.(2008). Experimental analysis of bubble growth, departure and interactions during pool boiling on artificial nucleation sites, *Experimental Thermal and Fluid Science,* Vol. 32, pp. 1504-1511.

Siedel, S., Cioulachtjian, S., Robinson, A. J., & Bonjour, J.(2011). Electric field effects during nucleate boiling from an artificial nucleation site, *Experimental Thermal and Fluid Science*, Vol. 35, pp. 762-771.

Stephan, P., & Fuchs, T. (2009). Local heat flow and temperature fluctuations in wall and fluid in nucleate boiling systems. *Heat and Mass Transfer/Waerme- und Stoffuebertragung*, 45, 919-928.

Terasaka, K., Oka, J., & Tsuge, H. (2002). Ammonia absorption from a bubble expanding at a submerged orifice into water. *Chemical Engineering Science , 57*, 3757-3765.

Thoroddsen, S. T., Etoh, T. G., & Takehara, K. (2007). Experiments on bubble pinch-off. *Physics of Fluids, 19*, 042101-1-29.

Thoroddsen, S. T., Etoh, T. G., & Takehara, K. (2008). High-Speed Imaging of Drops and Bubbles. *Annual Review of Fluid Mechanics, 40,* 257-285.

Van der Geld, C. W. (2009). The dynamics of a boiling bubble before and after detachment. *Heat and Mass Transfer/Waerme- und Stoffuebertragung, 45*, 831-846.

Van Stralen, S. J. D., & Sluyter, W. M. (1969). Local temperature fluctuations in saturated pool boiling of pure liquids and binary mixtures. *Int. J. Heat Mass Transfer , 12*, 187-198.

Van Stralen, S. J. D., Sohal M. S., Cole, R., & Sluyter, W. M. (1975). Bubble growth rates in pure and binary systems: Combined effect of relaxation and evaporation microlayers. *Int. J. Heat Mass Transfer , 18,* 453-467.

Van Helden, W. G., Van Der Geld, C. W., & Boot, P. G. (1995). Forces on bubbles growing and detaching in flow along a vertical wall. *Int. J. Heat Mass Transfer , 38* (11), 2075-2088.

White, F. M. (2008). Fluid Mechanics (6^{th} edition). McGraw-Hill.

Wu, J., Dhir, V. K., & Qian, J. (2007). Numerical simulation of subcooled nucleate boiling by coupling level-set method with moving-mesh method. *Numerical Heat Transfer, Part B: Fundamentals , 51* (6), 535-563.

Yoon, H. Y., Koshizuka, S., & Oka, Y. (2001). Direct calculation of bubble growth, departure, and rise in nucleate pool boiling. *Int. J. Multiphase Flow , 27*, 277-298.

Zhao, Y., Masuoka, T., & Tsurata, T. (2002). Unified theoretical prediction of fully developed nucleate boiling and critical heat flux based on a dynamic microlayer model. *Int. J. Heat Mass Transfer , 45*, 3189-3197.

Zhao, Y., Masuoka, T., & Tsurata, T. (2002). Theoretical studies on transient pool boiling based on microlayer model. *Int. J. Heat Mass Transfer , 45*, 4325-4331.

Zhang, L., & Shoji, M. (2001). A periodic bubble formation from a submerged orifice. *Chemical Engineering Sciences , 56*, 5371-5381.

Zhang, W., & Tan, R. B. H. (2000). A model for bubble formation and weeping at a submerged orifice. *Chemical Engineering Sciences , 55*, 6243-6250.

Zuber, N. (1959). Hydrodynamic aspects of boiling heat transfer, U S AEC report AECU 4439, June.